THE UNIVERSITY *of* EDINBURGH

This thesis has been submitted in fulfilment of the requirements for a postgraduate degree (e.g. PhD, MPhil, DClinPsychol) at the University of Edinburgh. Please note the following terms and conditions of use:

This work is protected by copyright and other intellectual property rights, which are retained by the thesis author, unless otherwise stated.
A copy can be downloaded for personal non-commercial research or study, without prior permission or charge.
This thesis cannot be reproduced or quoted extensively from without first obtaining permission in writing from the author.
The content must not be changed in any way or sold commercially in any format or medium without the formal permission of the author.
When referring to this work, full bibliographic details including the author, title, awarding institution and date of the thesis must be given.

Antenna and Rectifier Designs for Miniaturized Radio Frequency Energy Scavenging Systems

THE UNIVERSITY *of* EDINBURGH

Yi Ding

A thesis submitted for the Degree of Doctor of Philosophy

The University of Edinburgh

May 2015

Declaration

I hereby declare that this thesis was composed and originated entirely by myself; work contained herein is my own except where explicitly stated in the text, and it has not been submitted for any other degree or professional qualification.

Yi Ding

May 2015

Edinburgh, U.K.

To my parents

Acknowledgements

First of all, I express my sincere appreciation to my supervisor Prof. Tughrul Arslan, for giving me the opportunity to do this project, who has given me consistent help and unceasing guidance, with his profound knowledge, kindness and patience extended to me.

I also would like to give my gratitude to my second supervisor Dr. Alister Hamilton, for his invaluable assistance in this research. I am also grateful and indebted to Dr. Ahmet T. Erdogan and Mrs. Susan Kivlin, who have given me important assistance in my academic procedures.

To the members of the System Level Integration Group (SLIG) and Advanced Smart Antenna Technologies (ASAT) research group, I owe sincere and earnest thankfulness for the unforgettable and unique experience of my life.

Most of all, I take this opportunity to record my deepest gratitude and best wishes to my parents, who have made everything possible during my whole life.

Abstract

With ample radio transmitters scattered throughout urban landscape, RF energy scavenging emerges as a promising approach to extract energy from propagating radio waves in the ambient environment to continuously charge low power electronics. With the ability of generating power from RF energy, the need for batteries could be eliminated. The effective distance of a RF energy scavenging system is highly dependent on its conversion efficiency. This results in significant limitations on the mobility and space requirement of conventional RF energy scavenging systems as they operate only in presence of physically large antennas and conversion circuits to achieve acceptable efficiency. This thesis presents a number of novel design strategies in the antenna and rectifier designs for miniaturized RF energy scavenging system.

In the first stage, different energy scavenging systems including solar energy scavenging system, thermoelectric energy scavenging system, wind energy scavenging system, kinetic energy scavenging system, radio frequency energy scavenging system and hybrid energy scavenging system are investigated with regard to their principle and performance. Compared with the other systems, RF energy scavenging system has its advantages on system size and power density with relatively stable energy source. For a typical RF energy scavenging system, antenna and rectifier (AC-DC convertor) are the two essential components to extract RF energy and convert to usable electricity.

As the antenna occupies most of the area in the RF energy scavenging system, reduction in antenna size is necessary in order to design a miniaturized system. Several antennas with different characteristics are proposed in the second stage. Firstly, ultra-wideband microstrip antennas printed on a thin substrate with a thickness of 0.2 mm are designed for both half-wave and full-wave wideband RF energy scavenging. Ambient RF power is distributed over a wide range of frequency bands. A wideband RF energy scavenging system can extract power from different

frequencies to maximize the input power, hence, generating sufficient output power for charging devices. Wideband operation with 4 GHz bandwidth is obtained by the proposed microstrip antenna. Secondly, multi-band planar inverted-F antennas with low profile are proposed for frequency bands of GSM 900, DCS 1800 and Wi-Fi 2.4 GHz, which are the three most promising frequency bands for RF energy scavenging. Compared with previous designs, the triple band antenna has smaller dimensions with higher antenna gain. Thirdly, a novel miniature inverted-F antenna without empty space covering Wi-Fi 2.4 GHz frequency band is presented dedicated for indoor RF energy scavenging. The antenna has dimensions of only 10 × 5 × 3.5 mm^3 with appreciable efficiency across the operating frequency range.

In the final stage, a passive CMOS charge pump rectifier in 0.35 μm CMOS technology is proposed for AC to DC conversion. Bootstrapping capacitors are employed to reduce the effective threshold voltage drop of the selected MOS transistors. Transistor sizes are optimized to be 200/0.5 μm. The proposed rectifier achieves improvements in both power conversion efficiency and voltage conversion efficiency compared with conventional designs.

The design strategies proposed in this thesis contribute towards the realization of miniaturized RF energy scavenging systems.

Table of Contents

List of Figures

List of Tables

List of Acronyms and Abbreviations

RF	Radio Frequency
WSN	Wireless Sensor Network
MS	Microwave Studio
HESS	Hybrid Energy Scavenging System
DC	Direct Current
AC	Alternating Current
VNA	Vector Network Analyzer
PCB	Printed Circuit Board
KISS	Keep It Simple, Stupid
RFID	Radio Frequency Identification
FSPL	Free Space Path Loss
MPPT	Maximum Power Point Tracking
TEG	Thermoelectric Generator
TE	Thermo-Electric
FSPL	Free Space Path Loss
UHF	Ultra High Frequency
FCC	Federal Communication Commission
ETSI	European Telecommunications Standards Institute
ADC	Analogy / Digital Converter
FPGA	Field Programmable Gate Array
MCU	Micro Control Unit
RFIC	Radio Frequency Integrated Circuit
EM	Electromagnetic
LC	Inductor-Capacitor
UHF	Ultra High Frequency
PMM	Power Management Module
CPS	Coplanar Stripline
HPBW	Half-Power Beamwidth
FNBW	First Null Beamwidth

BE	Beam Efficiency
RHCP	Right-Hand Circular Polarization
LHCP	Left-Hand Circular Polarization
CPW	Coplanar Waveguide
FDTD	Finite Difference Time Domain
UWB	Ultra Wide Band
SMA	Subminiature A
BW	Band Width
RLC	Resistor- Inductor-Capacitor
SCR	Silicon Controlled Rectifier
SC	Switched-Capacitor
DBB	Dynamic Bulk Biasing
ESD	Electrostatic Discharge
PCE	Power Conversion Efficiency
VCE	Voltage Conversion Efficiency
AR	Aspect Ratio
EVC	External – V_{th} – Cancellation
IVC	Internal –V_{th} – Cancellation
SVC	Self –V_{th} – Cancellation
DVC	Differential –V_{th} – Cancellation
VNA	Vector Network Analyser
DTV	Digital Television
WLAN	Wireless Local Area Network
IFA	Inverted – F Antenna
PIFA	Planar Inverted – F Antenna
ICNIRP	International Commission on Non-Ionizing Radiation Protection
MSA	Microstrip Antenna
SC-MSA	Short-Circuit Microstrip Antenna

Chapter 1

Introduction

In this introductory chapter, I present some of the background for this dissertation. In other words, I try to establish a context for the research which is discussed in the later chapters.

1.1 Motivation

In recent years, there has been a growing demand for wireless devices such as mobile phones and wireless sensor networks. With the trends in technology that allow the decrease in both size and power consumption of electronics, it is possible for small devices to perform complex task while run on low voltage portable batteries. However, traditional power supply batteries for remote devices have certain limitations on wireless applications to date: (1) the lifetime of the batteries is quite limited, which requires periodical battery replacement that may be either economically or practically infeasible under some situations; (2) the use of commercial batteries gives rise to environmental pollution due to the disposal of batteries; (3) the large size and weight of batteries compared with the more advanced electronic increase the difficulty of device miniaturization. Therefore, energy

scavenging emerges as an environmentally friendly alternative as it serves as a long term solution to replace the conventional primary batteries. By implementing the ability of scavenging energy from ambient energy sources to partly or fully charge wireless devices, the functionality and performance of the devices can be improved by providing a low maintenance cost with extended battery life and enabling further miniaturization.

The feasibility of scavenging energy from a variety of natural and artificial energy sources such as radio frequency (RF) energy [1, 2], thermal energy[3, 4], vibration energy [5, 6] and solar energy [7, 8] has been explored for years to power devices directly or store the energy in batteries or capacitors for later use. These sources can be categorized into five categories [9]: photonic; thermal; kinetic; electromagnetic; autophagous (self-consuming) structure–power. Photonic sources include solar radiation and artificial lighting. Thermal energy sources include objects heated by sun, ground terrain, ambient air, exhaust vents and utility piping etc. Kinetic sources include wind, flowing fluids, and vibrational or oscillatory motion generated by moving structures or machinery. Electromagnetic energy is available in the form of oscillating magnetic fields surrounding AC power lines, or radio waves emitted by nearby transmitters. Autophagous structure–power is a multifunctional concept that involves the "transformation" of mechanical structure into an "internal" source of energy.

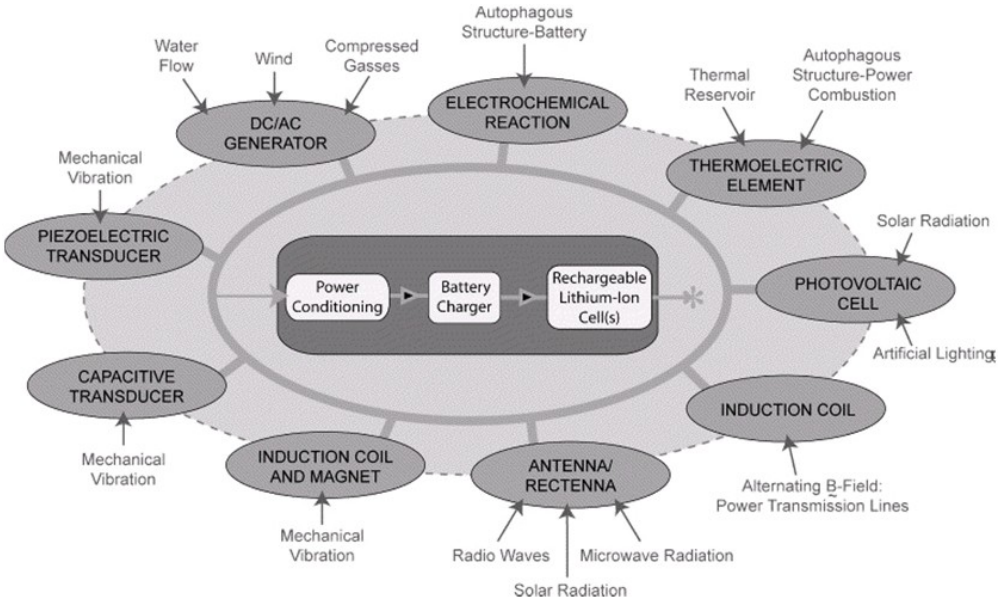

Figure 1.0.1 Various scavengable energy (non-biological) [9]

Figure 1.0.1 shows various ambient energy sources with their respective energy conversion systems. As seen from the figure, energy scavenging systems generally consist of energy transducer elements and power conditioning hardware. Scavenged energy should be converted into electrical energy and then conditioned to an appropriate form to charge system batteries.

Among all the available sources for energy scavenging, RF energy has recently captured significant interest because of the increased availability of free RF energy. RF energy scavenging extracts power from ambient propagating radio waves and converts into usable electrical energy. A basic RF energy scavenging system is shown in Figure 1.0.2. Ambient RF energy is collected and converted into alternating current (AC) by antenna and then rectified to direct current (DC) for charging system batteries. Impedance load matching between the antenna and rectifying circuit is necessary to maximize the scavenged power.

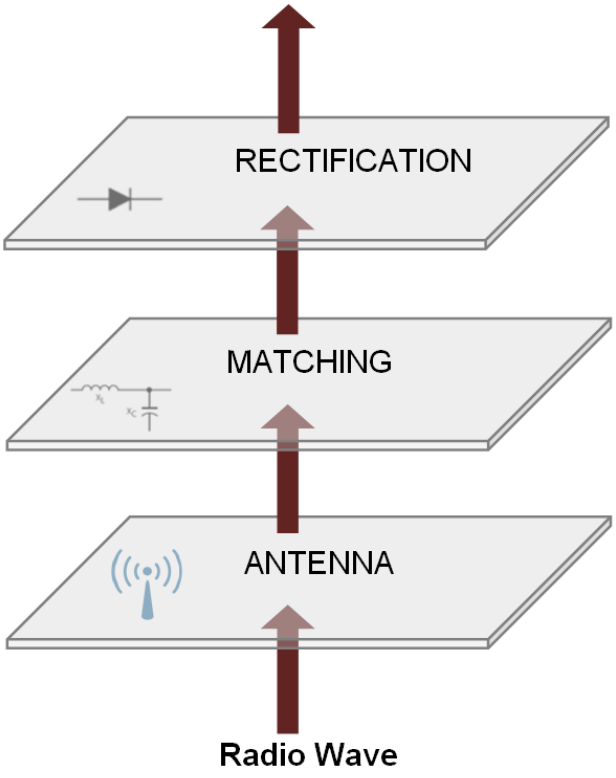

Figure 1.0.2 A basic RF energy scavenging system

1.2 Global Design Consideration

1.2.1 Robustness

Our designs have to be robust to different environmental conditions and device performance has to be maintained over a wide range of humidity and temperature to meet various application requirements. An effective way to enhance device robustness is *simplicity*. The design principle of KISS (Keep It Simple, Stupid) states that when other factors are equal, most systems work best if they are kept simple rather than made complicated. In other words, simple systems are more likely to work properly under adverse conditions than complicated ones. Therefore *simplicity* should be key goal in design and unnecessary complexity should be avoided. The KISS philosophy is widely applied to engineering design, but with caveats. Although complexity without function benefits is valueless, it is frequently desirable for ingenious use of a certain amount of complexity. A minimum level of complexity is necessary for any system to be efficient and robust in a noisy environment. In a word, function and robust enhancements for the designs have to be achieved without significantly increasing system complexity.

1.2.2 Cost

Another reason for simple design is to keep costs down. Engineering design should be kept as cheap as possible to be attractive to retailers. Usually, the complexity and size of a system decide its fabrication cost. Take RFID tag for example, the fabrication cost is primarily set by the embedded circuit, whose cost scales as the die size. Hence, the occupied die size needs to be as small as possible to reduce the cost. The smaller size places heavy penalties on increased circuit complexity, which accords with KISS design principle.

1.2.3 Performance

The main challenge faced in RF energy scavenging is to extract power from the air at very low power density since RF energy drops off rapidly with the increased distance from the transmitter [10]. In free space (i.e., with no environmental effects and far

away from the source) the electric field and propagation power density diminishes with the square of distance according to *Friis Transmission Formula* [11]:

$$P_r = P_t G_t G_r [\lambda / (4\pi R)]^2 \quad (1.1)$$

Where,

P_r = Power available at the output terminals of the receiving antenna

P_t = Power fed into the transmitting antenna at its input terminals

G_r = Antenna gain of the receiving antenna

G_t = Antenna gain of the transmitting antenna

R = Distance between the transmitting and receiving antennas

λ = Electromagnetic wavelength in the transmission medium

For every doubling of distance from the source, the available power to the receiver decreases by 6.02 dB. What's more, for multipath situations with environmental reflections and losses, the power density drops off at a much faster rate. It is therefore critical for the system to operate at low receive power with high conversion efficiency. This also ties in well with the KISS philosophy mentioned previously since the more complicated system has more lossy elements that reduce the power conversion efficiency.

1.2.4 Physical Size

With the continuous miniaturization of electrical devices, our designs should be as small and inconspicuous as possible so that it can be easily embedded in small electronics. However, the physical size of antennas scales as the free space wavelength [12]. In 1975, Harold Wheeler proposed the theory of small antennas whose size is a small fraction of a wavelength. Wheeler's theory predicts the efficiency and / or bandwidth of an antenna is ultimately limited by size relative to the wavelength for any antenna configuration [13]. For small antennas, most of the energy is stored in reactive near fields instead of radiated to far field. So there is a minimum size limit on the antenna at a given operating frequency. Thus, attention should be devoted to reduce antenna volume without sacrificing radiation performance.

1.3 Design Challenges

The principle components of a RF energy scavenging system are the antenna for power extraction and the rectifier for power conversion. Therefore, the research presented in this thesis focus on the design of these two components, aiming at the realization of miniaturized RF energy scavenging systems. Several challenges related to the component design are addressed in this section.

1.3.1 Antenna design

Most of the area of a RF energy scavenging system is occupied by the antenna. In order to achieve effective and miniature RF energy scavenging system, a well designed antenna effective in both radiation characteristic and space requirement is critical. According to the impedance bandwidth, antenna designs for RF energy scavenging can be categorized to three categories: wideband antenna, multiband antenna and antenna operating at single frequency band.

1.3.1.1 Wideband Antenna

As ambient RF power is distributed over a wide range of frequency bands, wideband antenna for RF energy scavenging [14-19] were designed in order to scavenging RF energy from broad frequency range for generating enough power to charge electronic devices. However, wideband antenna designs present challenges include limited bandwidth and large antenna size.

This research investigates the design of a coplanar waveguide fed microstrip antenna with thin substrate. Rectangular slot is etched on the radiating patch for wider bandwidth. The aim is to develop an antenna with ultra-wideband operation while maintaining relatively small size.

1.3.1.2 Multiband Antenna

Although wideband RF energy scavenging is capable of extracting more power than multiband or single band RF energy scavenging, it requires complex conversion and controlling circuit due to its wideband characteristic. This also results in larger system size and more power consuming devices. Hence, most of the current RF

energy scavenging research focus on multiband [20-24] or single band [25-29]. The challenges associated with multiband antenna designs for RF energy scavenging is to realize multiband operation while maintaining certain radiation characteristics. Besides, the dimensions of the antenna also need to be considered.

Planar-Inverted F antenna (PIFA) with multiple frequency bands is investigated in this research. In the first stage, a dual-band PIFA with low profile is designed at operating frequency bands of GSM 900 and GSM 1800. These two communication bands are selected as they demonstrate the largest power density in the urban environment. Various feeding and shorting strip configurations are considered. In the second stage, the antenna is modified in order to obtain a third operating frequency at Wi-Fi 2.4 GHz for RF energy scavenging at indoor environment. Antenna gain, efficiency and radiation patterns are evaluated and analyzed.

1.3.1.3 Single Band Antenna

RF energy scavenging at single frequency band is the most widely used. In this thesis, our single band antenna design is aimed at short range indoor RF energy scavenging in the crowed 2.4 GHz spectrum (Wi-Fi / Bluetooth / ZigBee / RFID) to power wireless sensor networks. Due to the fact that RF energy experience much more losses during transmission at frequencies around 2.4 GHz than lower frequencies, more than one antenna element is needed for the RF energy scavenging system to generate enough power for wireless sensors. Therefore, it is crucial for the antenna to have small dimensions to reduce the system size. Moreover, acceptable radiation performance for antenna bandwidth, efficiency and radiation pattern is necessary.

This research investigates miniaturized Inverted-F antenna (IFA) for indoor Wi-Fi energy scavenging. Meandering structure with thick substrate is adopted to reduce the antenna dimensions. The aim is to design a miniature IFA covering Wi-Fi 2.4 GHz with suitable antenna efficiency and radiation patterns. Test board and ground plane effects on antenna radiation performance are also explored.

1.3.2 Rectifier Design

With low forward voltage and high switching speed, Schottky diode is considered as an ideal component for rectifier to obtain high power conversion efficiency (PCE). However, with its particularity of manufacturing, Schottky diode cannot be implemented in normal CMOS process [30]. Usually CMOS integration is realized by utilizing diode-connected MOS transistors. Nevertheless, PCE of a rectifier using diode-connected MOSFET is generally lower than Schottky diode based rectifier due to its large threshold voltage. Static-V_{th}-Cancellation scheme [31] is proposed, which however requires an external power supply and clocking. In [32] floating-gate transistors are used as diodes to achieve high efficiency for low-voltage input. However, external programming is required to control the floating gates, which has slow processing speed and potentially impacts circuit reliability. Moreover, floating-gate transistor trades off low threshold voltage with increased input capacitance and layout area [33]. Comparator is applied as switch in [34] to control MOS transistors to improve power efficiencies. This design is reported to generate less heat [35] while it can only be used in semi passive or active circuits.

This research investigates the design of passive half-wave CMOS charge pump rectifier. Transistors equipped with reduced effective threshold voltage technique are employed to yield high power conversion efficiency. Multiple stage configurations are also studied to obtain high voltage conversion efficiency.

1.4 Outline of the Thesis

The reminder of the thesis is structured as follows:

Chapter 2 – Literature Review

This chapter presents a brief overview of energy scavenging. Various energy scavenging techniques including solar, thermoelectric, wind, piezoelectric, radio frequency energy scavenging and hybrid energy scavenging are investigated. With a focus on RF energy scavenging, system architecture and power conversion

performance of these techniques are introduced. Summary of existing RF energy scavenging systems is also illustrated in this chapter.

Chapter 3 - UWB Microstrip Antenna for RF Energy Scavenging

This chapter proposes a UWB microstrip antenna for half-wave RF energy scavenging. The antenna is fed by a coplanar waveguide transmission line. Enhancement techniques including partial ground plane, tapered structure and etched slot are adopted. Broad bandwidth of 4 GHz is achieved with compact dimensions of $35 \times 80 \times 0.2$ mm^3. Based on the design, a dual antenna array is also proposed for wideband full-wave RF energy scavenging. Separation between two adjacent antenna elements is 15 mm. Parametric analysis is performed to optimize antenna bandwidth.

Chapter 4 – Multi-Band PIFA for RF Energy Scavenging

In this chapter, firstly a low profile dual-band PIFA is presented. With a coupled feeding line and a bended shorting strip, operation at GSM 900 and GSM 1800 is achieved. Then, the bended shorting strip is replaced by a meandered shorting strip to obtain a third operating band covering Wi-Fi 2.4 GHz. The triple-band PIFA has a compact structure of $15 \times 40 \times 0.8$ mm^3 with efficiencies all above 70% across the operating range. Maximum power extracted by the antenna is also estimated.

Chapter 5 – Miniature IFA for Indoor Wi-Fi Energy Scavenging

This chapter presents the design of a novel miniature IFA without empty space for indoor Wi-Fi energy scavenging. The antenna configuration is designed based on planar inverted-F antenna with meandered line structure for antenna size miniaturization. Various antenna configurations are considered to achieve operation covering the whole Wi-Fi 2.4 GHz band with miniature and compact structure. The proposed antenna has dimensions of only 10 (L)$\times$ 5 (W) $\times$ 3.5 (H) mm^3 to be integrated into miniaturized RF energy scavenging systems. Variations of radiation characteristics when the antenna is placed at different positions of the test board with various sizes are also evaluated.

Chapter 6 – Passive CMOS Charge Pump Rectifier

This chapter presents an efficiency enhanced CMOS charge pump rectifier for AC to DC conversion in the RF energy scavenging systems. The proposed rectifier designed in 0.35 μm CMOS technology utilizes bootstrap capacitors to reduce the threshold voltage drop of selected MOS transistors. Design strategies are introduced in the chapter. Effects of main path transistor size on power conversion efficiency are also investigated. Improvements on both power conversion efficiency and voltage conversion efficiency are observed compared with conventional designs.

Chapter 7 – Conclusion

This chapter draws the main conclusions of the thesis and points towards future work.

1.5 Novelty and Contributions

The novel aspects of the work presented in this thesis include:

i. UWB microstrip antenna for wideband half-wave RF energy scavenging

ii. UWB dual antenna array for wideband full-wave RF energy scavenging

iii. Low profile dual band PIFA operating at GSM 900 and GSM 1800

iv. Low profile triple band PIFA operating at GSM 900, GSM 1800 and Wi-Fi 2.4 GHz

v. Miniaturized Inverted-F Antenna without empty space for indoor Wi-Fi energy scavenging

vi. Efficient passive CMOS charge pump rectifier with reduced effective MOSFET threshold voltage

1.6 Publications Arising from This Research

In the course of this research, the following journals and conference papers have been submitted and published:

2012

Y. Ding, T. Arslan, and A. Hamilton, "Broadband antenna for RF energy scavenging system," in *Antennas and Propagation Conference (LAPC)* Loughborough, 2012, pp. 1-4.

2013

Y. Ding and T. Arslan, "Broadband differential antenna for full-wave RF energy scavenging system," in *2013 Loughborough Antennas and Propagation Conference (LAPC)*, 2013, pp. 325-328.

Y. Ding and T. Arslan, "Compact planar inverted-F antenna for mobile RF energy scavenging system," in *2013 Loughborough Antennas and Propagation Conference (LAPC)*, 2013, pp. 329-332.

Y. Ding and T. Arslan, "Miniaturized antenna for RF energy scavenging systems," in *University of Edinburgh Postgraduate Research Conference*, 2013.

2014

Y. Ding and T. Arslan, "Miniature IFA without empty space for Wi-Fi energy scavenging," in *2014 Loughborough Antennas and Propagation Conference (LAPC)*, 2014, pp. 592-595.

Y. Ding and T. Arslan, "A triple bands printed inverted-F antenna for mobile RF energy scavenging," in *2014 Loughborough Antennas and Propagation Conference (LAPC)*, 2014, pp. 218-221.

Y. Ding and T. Arslan, "Efficiency enhanced rectifier for RF energy scavenging," in *University of Edinburgh Postgraduate Research Conference*, 2014.

2015

Y. Ding and T. Arslan, "Efficiency Enhanced Passive CMOS Rectifier for RF Energy Scavenging System," *IEEE Transactions on Circuits and Systems - II,* 2015 (under review)

Y. Ding and T. Arslan, "Miniaturized Inverted-F Antenna without Empty Spcae for Indoor Wi-Fi Energy Scavenging," *IEEE Transactions on Antennas and Propagation,* 2015 (under review)

1.7 Summary

This thesis presents the research of miniaturized RF energy scavnging systems, where particular attention is given to:

i. Ultra wideband microstrip antenna design

ii. Low profile multi-band planar Inverted-F antenna design

iii. Miniaturized Wi-Fi Inverted-F antenna design

iv. Efficiency enhanced passive CMOS charge pump rectifier design

Chapter 2

Literature Review

The literature review contains three major parts. The first part briefly introduces the principles of energy scavenging. The second part begins with a broad review on several common energy scavenging techniques, and is followed by a comparison on the range of scavengable energy under various environmental conditions. Six energy scavenging techniques of interest: solar, thermoelectric, wind, piezoelectric, radio frequency energy scavenging as well as hybrid energy scavenging technique are studied and discussed in terms of their operating principle and performance. The second part of this chapter focus on the investigated technique: RF energy scavenging. A further review on the current RF energy scavenging technology is presented.

2.1 Energy Scavenging Principles

Energy scavenging, also known as energy harvesting or power harvesting, is defined as the process of extracting energy from nearby sources and converting it to storable electrical energy [36]. In general, an energy scavenging system consists of the following components:

- Available energy source;
- Energy collection element;

- Conversion hardware;
- Conditioning / process control electronic;

Although "energy scavenging" and "energy harvesting" are frequently used in the literature, they are actually different with respect to the uncertainty of the ambient energy sources. Energy scavenging refers to environments where the ambient sources are unknown or highly irregular, whereas energy harvesting is usually referred to situations where the ambient sources are well characterized or regular [37]. Table 2.1 provides some examples of the differences.

Table 2.1 Comparison of energy scavenging and harvesting [37]

	Scavenging	**Harvesting**
Electromagnetic	GSM / WLANs	Dedicated Transmitters
Kinetic flow	Winds	Air-conditioning ducts
Mechanical	Foot traffic	Motors, ductwork
Thermal	Forest fires	Furnace covers

2.2 Comparison of Energy Scavenging Techniques

2.2.1 Solar Energy Scavenging

Solar energy can be converted into electrical energy via photovoltaic effect or by heating of fluid to create steam that can be used for electrical energy generation. Defined as full sunlight, the solar irradiance at noon on the equinox can achieve 100 mW/cm^2 or equivalently 1000 W/m^2 at equator [38]. Depending on the design material, solar conversion efficiencies range from a low of approximately 7% to state-of-art values of 38% or more measured under the global AM1.5 spectrum (1000 W/m^2) at 25 ℃ [39].

Solar cells based on photovoltaic effect have been widely employed for solar energy scavenging. A solar cell is basically a semiconductor diode consisting of a large-area p-n junction in the plane of the cell close to the top surface [40]. When exposed to

solar radiation having energy greater than the bandgap energy of the semiconductor diode, an electrical potential is formed between the p-type and n-type materials due to the electron-hole pairs generated by the absorption of photons. This process is known as the photovoltaic effect. The equivalent circuit of a solar cell model is shown in Figure 2.1. The characteristic equation for this solar cell model is given by [41]

$$I_L = I_{LG} - I_{os}\left\{exp\left[\frac{q}{AkT}(V + I_L R_s)\right] - 1\right\} - \frac{V_L + IR_S}{R_{sh}} \quad (2.1)$$

where I_L and V_L are cell output load current and voltage; I_{LG} is the light-generated current that depends on the incident radiation and temperature; I_{os} is the cell reverse saturation current; q is the electronic charge; A is diode ideality factor; k is the Boltzmann's constant; T is the cell temperature; R_s is the series resistance; R_{sh} is the shunt resistance.

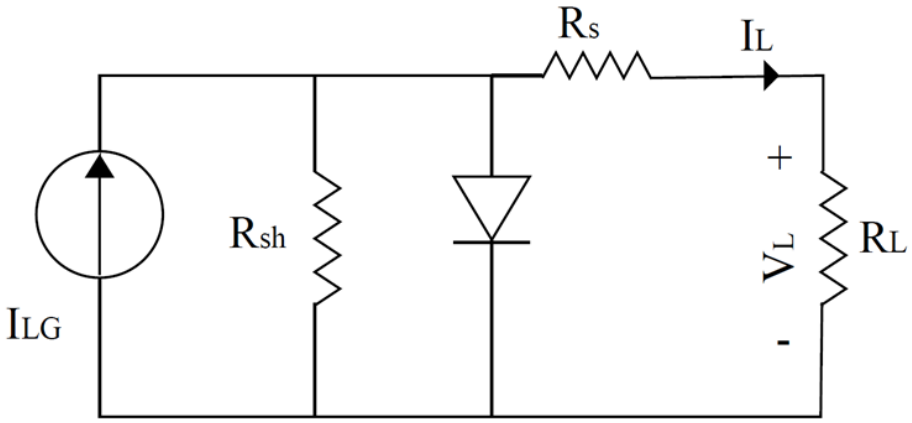

Figure 2.1 The equivalent circuit of a solar cell [42]

Figure 2.2 shows the current versus voltage (I-V) plot of a typical solar cell with and without incident radiation. The performance of a solar cell can be characterised by two parameters: I_{SC} (short circuit current at zero voltage) and V_{OC} (open circuit voltage at zero current). For a given level of light intensity and temperature, maximum output power can be achieved when operating at an optimum operating point which exists on the I-V curve between the two shaded region in the figure.

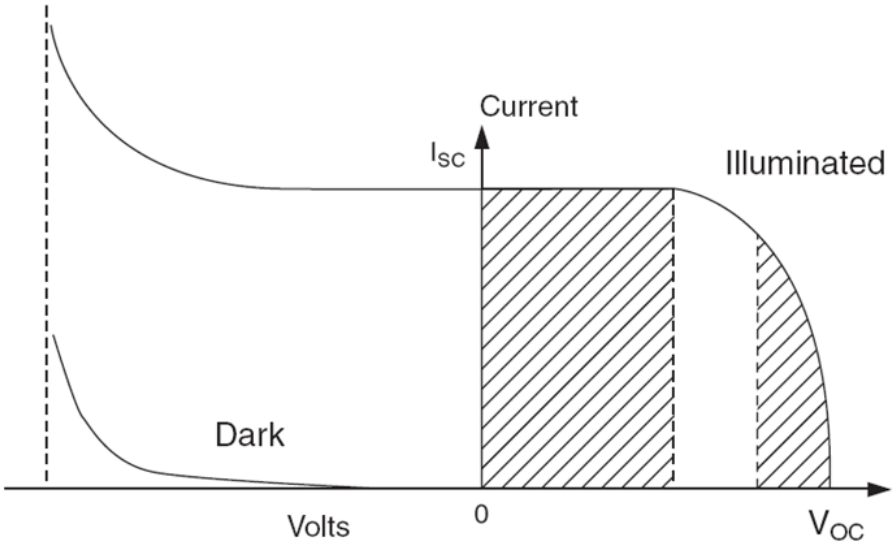

Figure 2.2 I-V characteristics of a typical solar cell [43]

The short circuit current (I_{SC}) and open circuit voltage (V_{OC}) together with the maximum output power (P_{max}) are used to define the fill factor (FF), which is a measure of solar cell quality ranging from 0 (poor) to 1 (excellent) [44]. For commercial solar cells, the fill factors commonly have values in the range of 0.7-0.8. (see Table 2.2)

$$\boldsymbol{FF} = \frac{\boldsymbol{P_{max}}}{\boldsymbol{I_{SC}V_{OC}}} \tag{2.2}$$

Table 2.2 Manufacturer specifications for several commercially available photovoltaic cells with 100mW/cm^2 incident radiation [9]

Cell	Dimensions (cm^2)	Thickness (μm)	Weight (g)	V_{OC}	I_{SC}	FF	Efficiency (%)
Schott® EFG 1030	100	330	8.2	0.595	3.15	0.77	14.5
Photowatt® Af	102	300 ± 50	NA	0.606	3.57	0.73	15.4
SunPower® A-300	156	270 ± 40	12.5	0.67	5.9	0.78	21.5
SunPower® Pegasus	21.9	160	0.88	0.68	0.88	0.82	22.5
Spectrolab® UT J[a]	32	140	2.7	2.66	0.41	0.83	28.3

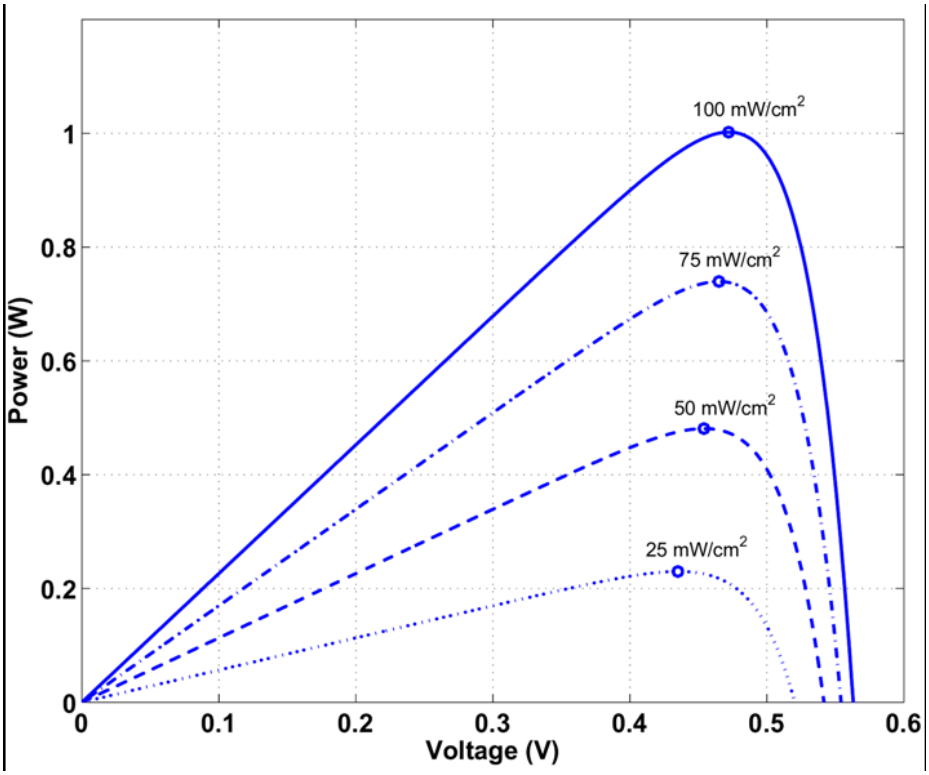

Figure 2.3 P-V characteristics of a typical 1-W solar cell for different lighting conditions (at 25 ℃) [32]

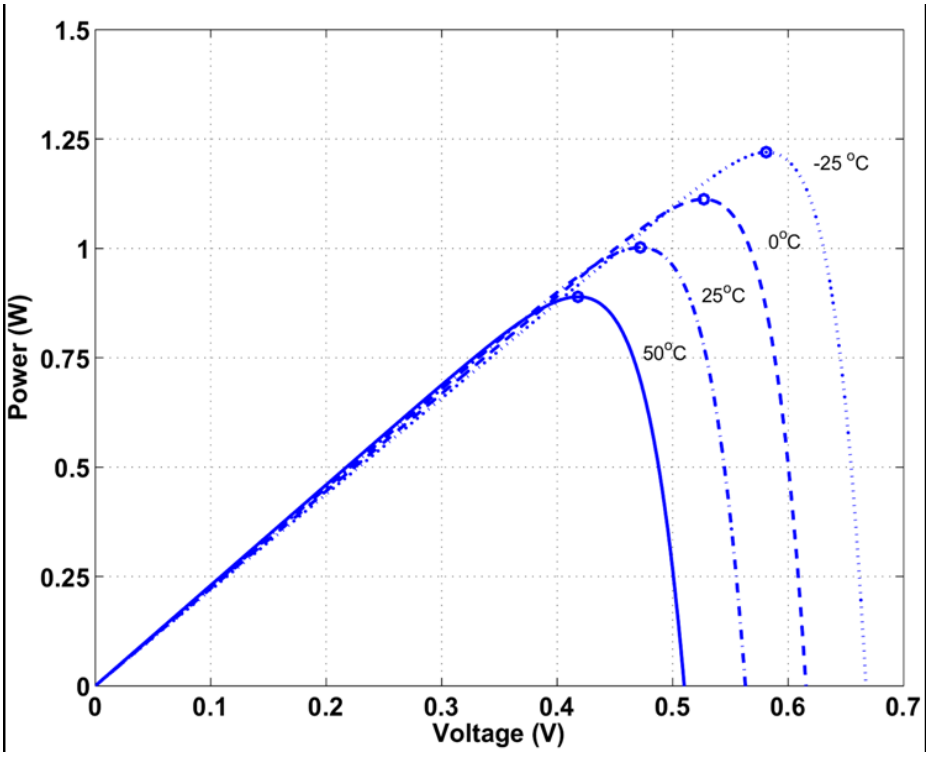

Figure 2.4 P-V characteristics of a typical 1-W solar cell at different temperatures (at 100 mW/cm^2) [32]

Simulated variations of the output P-V characteristics of a commercial solar cell as a function of irradiation and temperature are illustrated in Figure 2.3 and Figure 2.4. The solar cell has dimensions of 3 x 3 inches with an energy conversion efficiency of 17%.

It can be observed that the maximum power point of the solar cell is strongly affected by the light intensity and temperature. To ensure the solar cell continuously operates with maximum power transfer efficiency between the cell and the load, regardless of temperature and lighting change, maximum power point tracking (MPPT) circuit is required to properly match the current and voltage characteristics of the solar cell with the system load.

Discussion

Being a readily and abundant accessible energy source in a typical outdoor environment, solar energy is considered as one of the most popular energy sources for energy scavenging. Compared with the other sources, power scavenged from solar energy has the highest power density. However, the output power of solar cells is highly dependent to the environmental conditions, i.e. temperature and lighting conditions. The first and most obvious is that, on a cloudy day or in an office environment, the level of light intensity upon the cells decreases significantly. Other environmental factors, such as shadowing, could also affect the light intensity. Sonnenenergie reported that the incident solar energy on the cells is reduced by approximately 60-80% for a core shadow cast by nearby object, and up to 50% for a partial shade [45].

Except for the load matching mentioned previously, the incident angle of radiation also needs to be taken into consideration for maximum output power. The power incident drops with the cosine of the incident angle of the sun's ray [46]. To maximise the output power, dynamic solar tracking are commonly used to make sure the angle of incidence remains close to zero at all times. However, this comes with the expense of added cost, weight and complexity, which is undesirable according to the KISS philosophy mentioned in chapter 1.

2.2.2 Thermoelectric Energy Scavenging

Thermoelectric energy scavenging extracts energy from naturally occurring temperature variations in the environment to generate a small amount of electricity. The term thermoelectric effect (direct conversion of thermal gradient to electrical voltage and vice verse) comprises of three separately identified effects: the Seebeck effect, Peltier effect and Thompson effect. A thermocouple, which is widely used in thermoelectric energy generators, is based on the Seebeck effect [42]. A basic structure of a thermocouple made of p-type and n-type semiconductors connected in series is depicted in Figure 2.5. When the temperatures of the two junctions of each semiconductor are different, an open-circuit voltage (known as Seebeck Voltage) proportional to the temperature difference is produced. Numerous thermocouples are usually connected thermally in parallel and electrically in series to obtain a practical output at small thermal gradient. Figure 2.6 illustrates a thermoelectric generator (TEG) formed by three thermocouples.

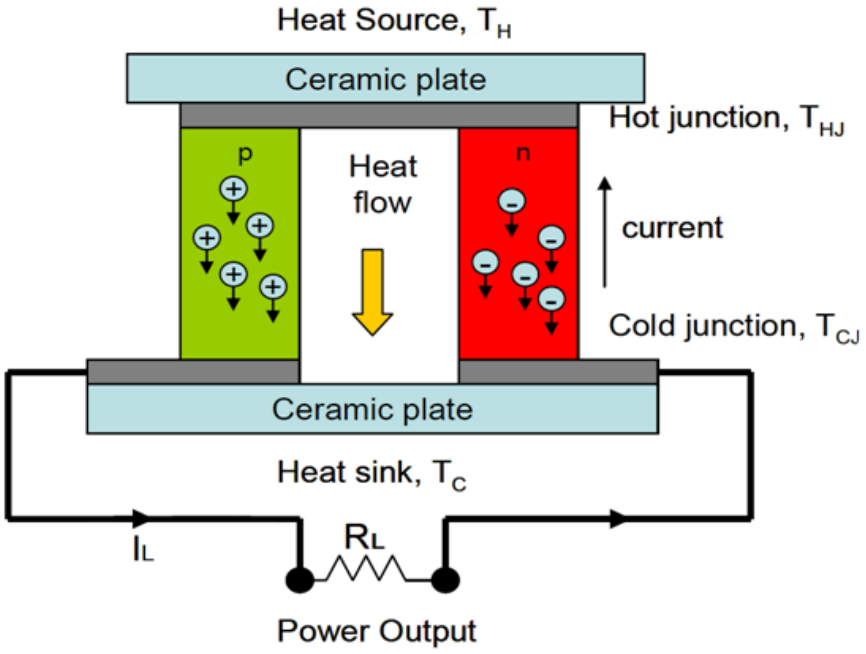

Figure 2.5 Basic structure of a semiconductor thermoelectric couple [40]

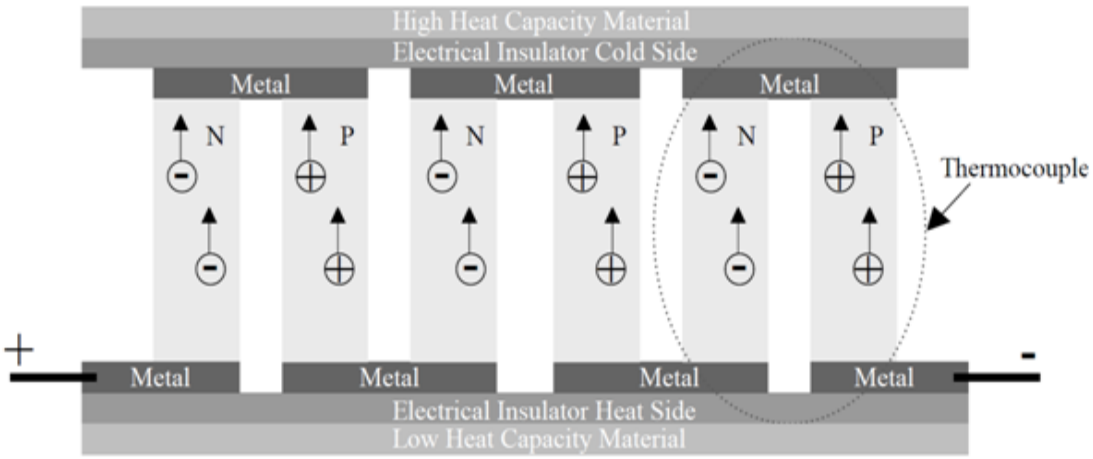

Figure 2.6 Diagram of Thermoelectric Generator with Thermocouple Unit [42]

The Seebeck voltage V_G of a TEG with N stages of thermocouple is expressed as [47]:

$$\boldsymbol{V_G = NS_{PN}\,(T_{HJ} - T_{CJ})} \tag{2.3}$$

where $S_{PN} = S_P - S_N$ is the Seebeck coefficient between the p-type and n-type semiconductors, and $T_{HJ} - T_{CJ}$ is the temperature difference across the hot and cold junctions taking into account of the thermal losses. When connecting to a load resistance R_L, a current I_L flows, which is given by [47]

$$\boldsymbol{I_L = \frac{V_G}{R_{in}+R_L} = \frac{NS_{PN}\,(T_{HJ}-T_{CJ})}{R_{in}+R_L}} \tag{2.4}$$

where R_{in} is the internal electrical resistance of the thermocouple. The output power P_L to the load R_L is simply the product of voltage and current across the load [47]:

$$\boldsymbol{P_L = V_L I_L = N^2 S_{PN}{}^2 (T_{HJ} - T_{CJ})^2 \frac{R_L}{(R_{in}+R_L)^2}} \tag{2.5}$$

Maximum output power is generated when the TEG is on matched-load conditions with the load resistance equals to the internal electrical resistance.

Table 2.3 Manufacturer specifications for three commercially available thermoelectric modules [9]

Manufacturer (Model no.)	Dimensions (mm)	Weight (g)	Power (W)	Voltage (V)	Efficiency, η_{TE} (%)
Hi-Z (HZ-2)	29 × 29 × 5.1	13.5	2.5	3.3	4.5
Kryotherm (TGM-127-1.0-1.3)	30 × 30 × 3.6	10.5	1.9	2.6	3.8
Tellurex (CZ1-1.0-127-1.27 HT)	34 × 31 × 3.3	7.5	2.5	3.5	4.5 (est.)

Discussion

For thermoelectric generation, the following efficiency factor is normally used [48]:

$$\eta_{TE} = \eta_{Carnot} \frac{M-1}{M+T_C/T_H} \tag{2.6}$$

where $M = (1 + ZT_m)^{1/2}$, Z is a dimensionless "figure-of-Merit" quantity for the thermocouples and $T_m = (T_H + T_C)/2$ is the mean temperature. η_{TE} is the maximum theoretical efficiency of a heat engine, known as Carnot efficiency.

Although a thermoelectric generator is a robust and highly reliable energy scavenging system, its application is limited, especially for low power occasions, due to the relatively low conversion efficiency - typically less than 5% for most of the commercial TEGs (see Table 2.3). As seen from Equation 2.6, thermoelectric conversion efficiency is constrained by the Carnot efficiency. Figure 2.7 presents the plot of Carnot efficiency and thermoelectric conversion efficiency as a function of temperature. As observed from the figure, for small to modest temperature differences, the Carnot efficiency is very low, which limits the maximum theoretically possible thermoelectric conversion efficiency. What's more, for real world conversion, the thermoelectric conversion efficiency is much lower than the Carnot efficiency. Current commercial TEGs operate below 40% of the Carnot efficiency [46].

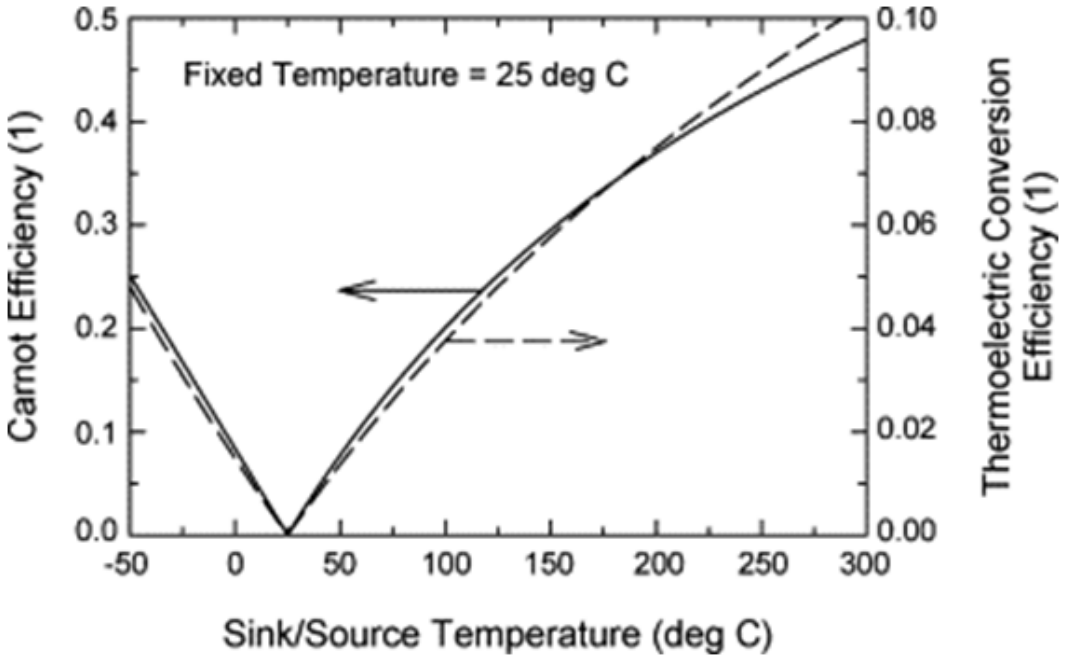

Figure 2.7 Carnot efficiency for a heat engine and the thermoelectric conversion efficiency as a function of temperature [9]

2.2.3 Wind Energy Scavenging

Energy scavenging from wind flow is realized through a wind turbine. The flow of wind is transformed to the rotation of a shaft by a rotor which consists of one or more airfoil blades that rotate with the shaft. The shaft is attached to a generator which has coils and magnets inside. As the magnets rotate around the coils, electrical current is induced from the changing magnetic fields. Theoretically, the available power from wind flow is equal to the rate of flow of kinetic energy per second [9]:

$$P_{wind} = \frac{1}{2}\frac{dm}{dt}V^2 = \frac{\rho A V^3}{2} \tag{2.7}$$

where ρ is the air density, A is the cross-section area of flow, and V is the upstream velocity. However, a wind turbine cannot extract all of this power. The amount of power that can be extracted from the wind is defined as the difference in upstream and downstream wind powers [49]:

$$P_{shaft} = \frac{1}{2}\frac{dm}{dt}(V^2 - V_{down}^2) = C_P P_{wind} \quad (2.8)$$

$$C_p = \frac{\left(1+{}^{V_{down}}/_{V}\right)\left[1-\left({}^{V_{down}}/_{V}\right)^2\right]}{2} \quad (2.9)$$

C_p is the fraction of upstream power given by the Betz's coefficient [50] (analogous to Carnot's efficiency) with a theoretical maximum value of 16/27 or 59.26%. For a small scale wind turbine, C_p is expected to be about 10% [51]. Assuming that the turbine is coupled to a transmission with efficiency η_m which drives a generator having efficiency η_g, the electrical power generated P_e will be [50]

$$P_e = \eta_m \eta_g C_p P_{wind} \quad (2.10)$$

Discussion

Similar to solar energy, wind energy is an attractive alternative for energy scavenging for the fact that wind flow is abundant and readily accessible in outdoor environment. However, since the wind is a variable energy source dependent to the environmental conditions (i.e. wind speed and direction change with weather from season to season), its application for energy scavenging is restricted to the locations which are subjected to constant wind, usually an open field. Wind speed and, consequently, wind energy potential are heavily influenced by the surface roughness of the surrounding area of nearby obstacles, such as trees or buildings, and by the contours of the local terrain [52]. In addition, the wind velocity varies with the height above the ground. It decreases from its free-stream value high above the ground to zero at ground-level [9]. An approximate estimation on the average flow velocity, V_h, at height h above "rough" ground, is given by [49]:

$$V_h = V_{ref}\left(\frac{h}{h_{ref}}\right)^{\alpha} \quad (2.11)$$

where V_{ref} is the wind velocity at height h_{ref}, and the exponent α is the friction coefficient which accounts for terrain roughness effects.

2.2.4 Piezoelectric Energy Scavenging

There are plenty of vibration sources in the environment ranging from industry machinery to human motions. Three typical conversion mechanisms can be applied to convert vibration to electrical power: electromagnetic, electrostatic and piezoelectric. Electrostatic converter has a primary disadvantage that a separate voltage source is required to initiate the process. Moreover, the implementation of electrostatic converter is practically difficult. Electromagnetic converter presents a serious problem of low output voltage. The drawback of piezoelectric convertor is the difficulty of implementation on the micro-scale, which is also common to electromagnetic converter. With high output voltage and energy density, piezoelectric converter is discussed in this thesis for vibration energy scavenging.

The piezoelectric effect is a reversible process defined as the linear electromechanical interaction between the mechanical and the electrical state in crystalline materials with no inversion symmetry [53]. Piezoelectric energy scavenging capitalizes on piezoelectric materials such as crystals and certain ceramics to generate an electrical potential in response to an applied mechanical stress [53]. One of the most common piezoelectric ceramic in use today is Lead Zirconate Titanate, also known as PZT. When a mechanical stress is placed on a piezoelectric material, an open circuit voltage is produced. Figure 2.8 shows the equivalent circuit of a piezoelectric element. The open circuit voltage generated by the piezoelectric generator is expressed as [54]:

$$V_{OC} = \frac{-dt}{\varepsilon}\sigma \tag{2.12}$$

where t is the thickness of the piezoelectric material, ε is the dielectric constant of the piezoelectric material and σ is the mechanical stress.

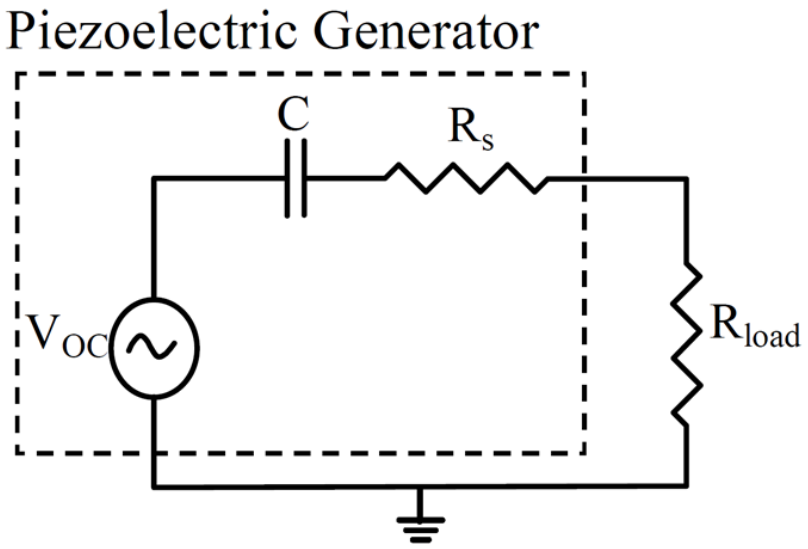

Figure 2.8 Equivalent circuit for a piezoelectric generator [54]

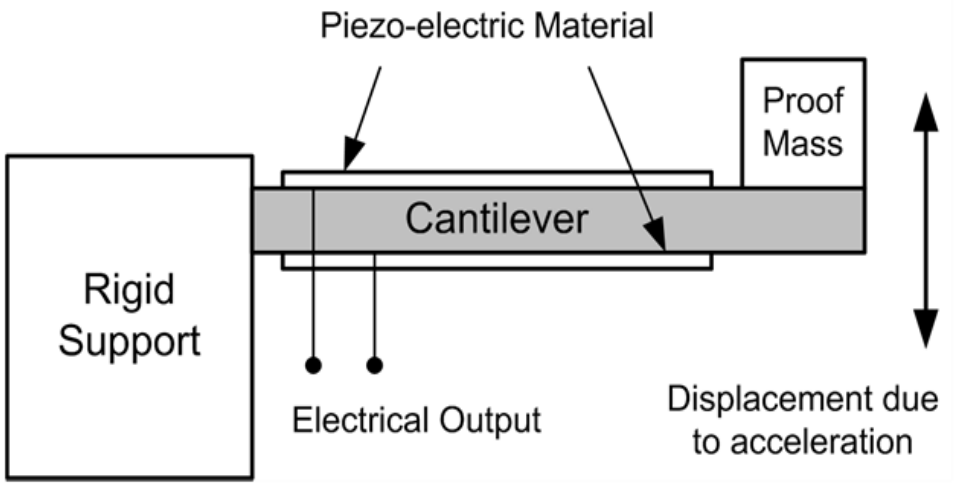

Figure 2.9 Mechanical setup of piezoelectric power generator [32]

The mechanical setup of a piezoelectric power generator with a cantilever is demonstrated by Figure 2.9. A proof mass is placed on the end of the cantilever for vibration enhancement. The power generated is proportional to the square of acceleration, to the proof mass, and inversely proportional to the resonant and excitation frequency [55].

Discussion

Piezoelectric energy scavenging is one of the most widely used energy scavenging techniques for micro-power generation that converting vibrational energy to electrical energy. It is possible to achieve a power density of 10mW/cm^3 at excitation frequency of 50 Hz and acceleration of 10m/s^2 [32]. Nevertheless, both the frequency and amplitude of vibrations in the ambient environment are very low, which have limited the output power generated. Another disadvantage of piezoelectric energy scavenging is that its micro-fabrication process is not compatible with standard CMOS technology. Although it is true that we can integrate piezoelectric thin films into MEMS fabrication, this will result in significant reduction of piezoelectric coupling.

2.2.5 Radio Frequency (RF) Energy Scavenging

Another possible approach to scavenge energy from ambient environment is by RF energy scavenging. In urban and semi-urban environment, the background propagating radio waves emitted by wireless local networks, cell phone towers or broadcast transmitters could serve as a potential source for RF energy scavenging. In this context, "Radio Frequency" (RF) refers to electromagnetic waves in the frequency range of around 3 kHz to 300 GHz. RF energy scavenging converts ambient microwave energy into DC electricity using rectenna, which is a rectifying antenna that consists of antenna and rectifying circuit. The amount of available RF energy in the ambient environment is dependent to the power density of the location, power extracting capability of energy collection device, and efficiency of power conversion.

Power density is one of the most important parameters for energy scavenging. In the far field region, the incident power density can be calculated based on the electric field strength:

$$P = \frac{E^2}{Z_0} \tag{2.13}$$

where P is the incident power density in W/m^2, E is the electric field strength in V/m, and Z_0 is the characteristic impedance of the free space. The incident power density can also be expressed as a function of distance from the source:

$$P = \frac{N}{4\pi d^2} \tag{2.14}$$

where N is assumed to be the effective power radiated from an isotropic radiator. It can be observed from the equation, the RF power density drops off as $1/d^2$. In free space, the path loss of the RF signal with wavelength of λ, is given by [11]:

$$L_p = \left(\frac{4\pi d}{\lambda}\right)^2 \tag{2.15}$$

At a distance of 20 meters, the path loss for RF signal transmission exceeds 55 dB at frequency of 900 MHz and 65 dB for 2.4 GHz. Therefore, with this high propagation loss, RF energy scavenging is best designed for short range application with highly efficient power conversion system.

Discussion

RF energy scavenging is an emerging technology with the popularization of wireless communication. However, due to its characteristic of high transmission loss, RF energy scavenging is an approach with limited applicability. The current application of RF energy scavenging requires either a large collection device or close range. Another disadvantage of RF energy scavenging is the random and uncontrollable sources. A number of study [14, 56] shows other than the location, available power level also changes with time and traffic density. Also, regulations on the permissible radiated RF power level have been imposed by the governing institutions around the world, such as Federal Communications Commission (FCC) and European Telecommunications Standards Institute (ETSI) [40]. This restriction, in another way, has limited the amount of available RF power in the ambient environment.

2.2.6 Hybrid Energy Scavenging

As has been introduced, electrical energy can be scavenged from various ambient energy sources. Common drawbacks for ambient energy scavenging are the low output power and the dependence on environmental conditions. An approach to reduce or eliminate the effect of environmental variation to produce continues and practical output is hybrid energy scavenging. Hybrid energy scavenging is a concept that integrates two or more different energy scavenging modules to generate electrical energy from multiple energy sources for enhanced performance. Researches [57, 58] on hybrid energy scavenging have proved its feasibility. Figure 2.10 demonstrates the implementation of a hybrid energy scavenging system (HESS) to power wireless sensor network (WSN). Energy is extracted from ambient thermal, radio frequency, vibration and solar sources through different transducers. The scavenged energy is stored in batteries or capacitors to power up different modules in a wireless sensor network.

Discussion

Hybrid energy scavenging is a promising approach to scavenging energy from ambient environment with relatively high output power. The implementation of a hybrid energy scavenging design, however, has practical difficulties. The compatibility of different scavenging systems regarding operating principles and manufacture process needs to be taken into consideration. Moreover, the integration of multiple energy scavenging systems with increased complexity results in larger system volumes and higher fabrication costs. Another fact needs to be bore in mind is that although hybrid energy scavenging gives the capability to accommodate with the change of environmental conditions, the overall efficiency of the whole system is reduced since in most cases it is practically impossible for all the energy scavenging modules to operate efficiently at the same time in the ambient environment. .

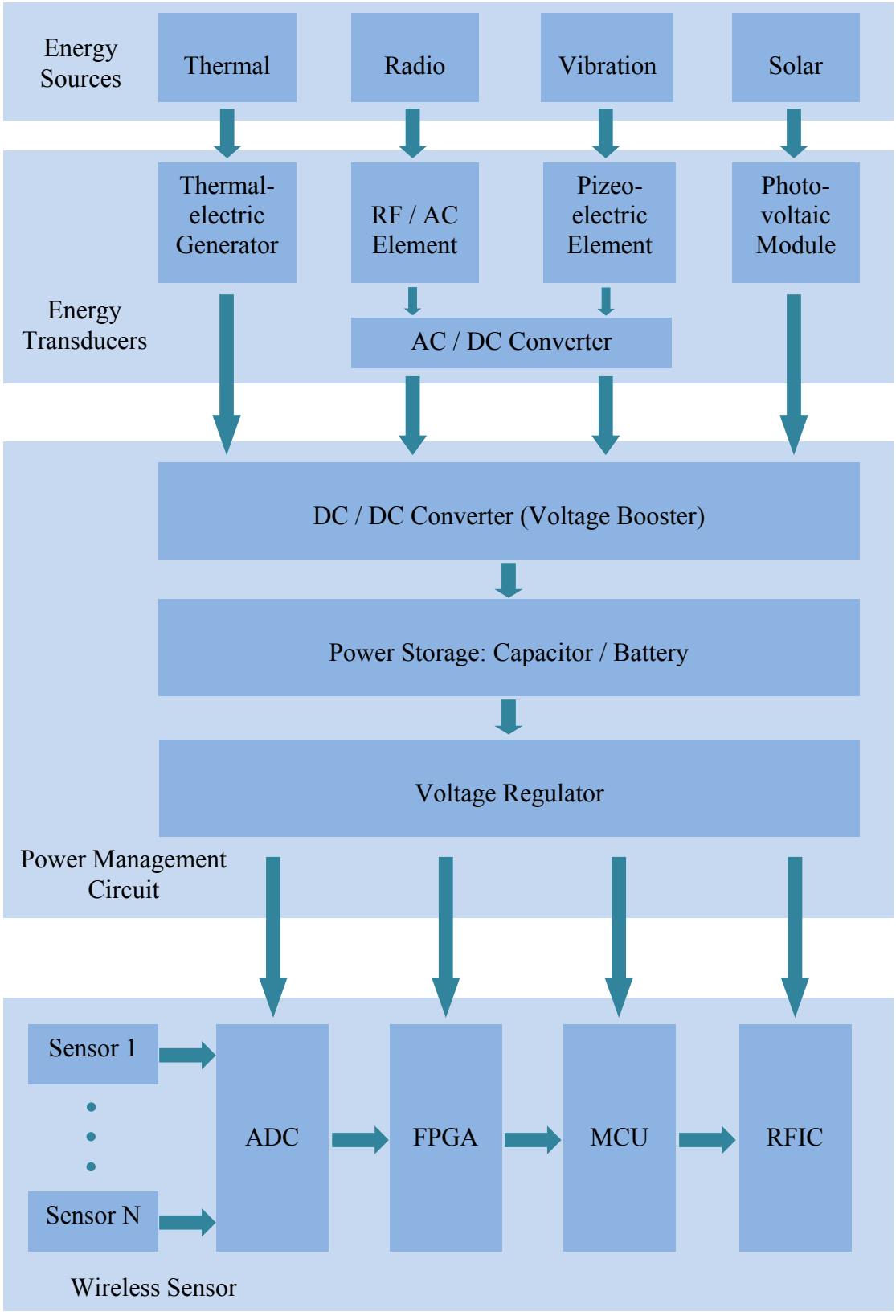

Figure 2.10 Block diagram of HESS for Wireless Sensor Network (WSN)

2.2.7 Summary of Energy Scavenging Methods

Energy scavenging emerges as an attractive alternative to replace the conventional primary batteries. Varieties of energy scavenging techniques have been reviewed and analyzed. The output power of an energy scavenging system depends on the availability of scavengable energy in the ambient environment, the size/weight of the energy collection elements, the efficiency of collection, as well as the efficiency of conversion to electrical energy [9].

It is worth noting that, energy scavenging is extremely source dependent, which makes the direct comparison of these techniques difficult. Due to the variation in source characteristic, it is not useful to compare the efficiency of energy scavenging systems. Instead, they are usually discussed in terms of their power density. Table 2.4 summarises the power density of different energy scavenging techniques. The power density of the energy scavenging methods is presented for various environmental conditions. Clearly, solar energy has the highest power density in the most ideal situation but drops off as a linear function of light intensity. It can be observed that the energy scavenged from solar energy on a cloudy day or in an office environment is significantly lower compared with other means of energy extraction. RF energy scavenging, on the other hand, has relatively higher power density compared with other means of energy extraction.

Unlike solar and wind energy scavenging, RF energy scavenging doesn't not require extraction system of large size, and further size reduction is allowed for RF energy scavenging system with respect to energy scavenging system based on the other sources (e.g. large size of a photovoltaic cell / wind turbine) [59]. As for energy scavenging from thermal and vibrational energy, applications are limited due to low temperature difference and vibration frequency/amplitude in the ambient environment. RF energy, however, is more human dependent rather than natural environment dependent. Because of the widespread usage of RFID systems and wireless portable devices, plenty of RF energy can be found in densely populated areas. Moreover, RF sources are always available throughout the day, both indoor and outdoor. From the summary of different energy scavenging methods, it is clear

that energy scavenging by radio frequency is one of the most attractive approaches for small size, low power applications.

Table 2.4 Comparison of various energy scavenging methods [32]

Energy Source	Power Density ($\mu W/cm^2$)	Source of Information
RF (900 MHz)	450 @ 5m 113 @ 10m 28 @ 20m 7 @ 40m	Le, et al., 2006 [60]
RF (2.4 GHz)	63.3 @ 5m 15.8 @ 10m 4.0 @ 20m 1.0 @ 40m	Le, et al., 2006 [60]
Solar (Outdoors)	15,000 (direct sun) 150 (cloudy day)	Roundy, et al., 2003 [61]
Solar (Indoors)	6 (office desk)	Roundy, et al., 2003 [61]
Vibration	4 (human motion - Hz)	Paradiso, et al., 2005 [62]
Acoustic	0.003 @ 75 dB 0.96 @ 100 dB	Theory
Thermal	100	Venkasubramanian, et al., 2007 [63]
Wind	200 (wind speed at 4 m/s)	Federspiel, et al., 2003 [64]

2.3 Further Review on RF Energy Scavenging

There is increasing research interest in development of rectenna as it is a key component of a RF energy scavenging system. The rectenna, which consists of an antenna and a rectifier, is used to convert high frequency EM (Electromagnetic) energy into DC power. Most of the rectennas are designed based on similar architecture with six main components as described in Figure 2.11.

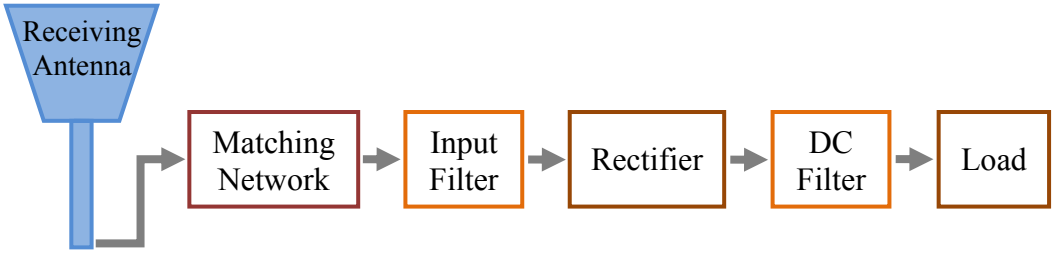

Figure 2.11 Typical rectenna architecture

The first component is the receiving antenna, which commonly operates as an efficient RF radiator in a rectenna to capture the incident RF energy. Secondly, a matching network such as LC circuit is required for impedance matching. The third component is an input filter, normally a low-pass or band-pass filter. The input filter is functioned to reject higher order harmonics generated by the following rectifier circuit from radiating through the antenna. The high efficiency rectifier for AC to DC conversion, which is the fourth component, is one of the most important components in a rectenna. The fifth component, DC pass filter, is basically a decoupling capacitor to remove unwanted voltage transient and passes the DC power. The final component is the load that consumes the output power.

As rectenna is an application dependent device, therefore, generally there is no restriction on the selection of rectifying components. However, the current rectenna design for energy scavenging can be basically divided into two groups based on the types of rectifying components: Schottky diode based rectenna and rectenna with CMOS based rectifier.

2.3.1 Schottky Diode based Rectenna

Schottky diode, also known as hot carrier diode, is named after German physicist Walter H. Schottky. The Schottky diode is preferred for low power RF applications due to its low forward voltage drop which can provides higher switching speed and better system efficiency. There is a small voltage drop across the diode when current flows through. For a normal silicon diode the voltage drop is 0.6-0.7 volts, while it's only 0.15-0.45 volts for a Schottky diode. Therefore, the low series resistance Schottky diode is most suitable for RF energy scavenging. There is a variety of Schottky diodes available in the market. Usually, for RF rectenna designs, Schottky diodes with zero bias are used. A detailed summary of current researches on Schottky diode based rectenna for RF energy scavenging is demonstrated in Table 2.5. As can be observed, the zero biased SMS 7630 diode is frequently selected as an optimal solution for RF energy scavenging as it is the most sensible among zero bias Schottky diodes.

In 2013, Pinuela et al. [1] assessed the power density levels in urban and semi-urban environments to explore the potential for RF energy scavenging by undertaking a citywide RF spectrum survey within UHF (0.3-3 GHz) from outside all of the 270 London Underground stations at street level. The spectral bands for DTV (470-610 MHz), GSM 900 (925-960 MHz), GSM 1800 (1805-1880 MHz) and 3G (2110-2170 MHz) were selected for their RF energy scavenging design. Single band rectennas with PMM (Power Management Module) were investigated individually as well as in multiband array architectures. It was demonstrated that the single band rectennas can start to operate at power level as low as -25 dBm with efficiency up to 40%, while multiband RF energy scavenging is achieved at minimum power level of -29 dBm. Nevertheless, the maximum output power density of the rectennas is lower than $8\mu W/cm^3$.

Olgun et al. [65] developed an ambient Wi-Fi energy harvester for energy scavenging in an office environment. In their design, a 3×3 rectenna array with multilayer structure was proposed to generate sufficient output power. The threshold operating power level of their design is as low as -40 dBm. A prototype was built and

used to demonstrate the ability of driving an off-the-shelf temperature and humidity meter with an LCD display. However, the proposed system requires a period of time ranging from 3 to 20 minutes for initialization before it starts to operate. Also, the multilayer structure increases the difficulty for fabrication.

A high efficiency rectenna operating at 2.45 GHz was presented by Sun et al. [66] for RF energy scavenging with low input power. The proposed rectenna is a two-element dipole array connected to a HSMS-2852 diode through a coplanar stripline (CPS). The antenna was designed to match the rectifier at resonant frequency while missmatch it at the second and third hramonics to eliminat the need for input filter. The overall efficiency of the rectenna can achieve 80% and 50% respectively at power density of 1.95 and 0.22μW/cm^2. However, the rectenna requires a relatively large area for implementation.

Kanaya et al. [25] designed a rectenna with a energy scavenging circuit mounted on the back side of a one-sided directional flexible antenna. They presented a LED light-up demonstration at a distance of 0.2m. However, the proposed antenna gain is only -0.7 dBi, which means the proposed rectenna is limited for applications of extremely close range.

Masotti et al. [67] proposed a rectenna designed based on genetic algorithms to scavenging energy from ambient RF energy. Their target frequency bands were GSM 900 (900 MHz), GSM 1800 (1750 MHz), UMTS (2150 MHz) and Wi-Fi (2450 MHz). The proposed rectenna was validated to provide a DC output voltage of 2.5V with the source consisting of a GSM900 phone call at a distance of 0.5 m. Nevertheless, due to its tetra-band characteristic with increased system complexity, maximum power point tracking (MPPT) is required.

Table 2.5 Summary of Schottky diode based rectenna for RF energy scavenging

YEAR	REFERENCE	FREQUENCY BAND	TYPE OF RADIATOR	POLARISATION	SCHOTTKY DIODE	SUBSTRATE	PERFORMANCE
2013	[1]	DTV GSM 900 GSM 1800 3 G	Dipole Antenna	Linear	SMS 7630	FR4	Minimum Operating Power: -29 dBm
2012	[65]	Wi-Fi	Patch Antenna	Circular	SMS 7630	Rogers RO6010 (Antenna) Rogers RO3206 (Rectifier)	Minimum Operating Power: -40 dBm
2012	[66]	2.45 GHz	Dipole Antenna	Linear	HSMS 2852	RT/Duroid 6002	Efficiency: 80 % @1.95μW/cm^2 50% @0.22μW/cm^2
2013	[25]	900 MHz	Slot Antenna	Linear	HSMS 286Y	Rogers RT6010	Efficiency: 44% @ -10dBm
2013	[67]	GSM 900 GSM 1800 UMTS Wi-Fi	Annular Ring Antenna	Circular	SMS 7630	TLP-5-Taconic (Antenna) RF-60A-Taconic (Rectifier)	Output Voltage: 2.5V @ 0.5m from GSM 900 cell phone

2.3.2 Rectenna with CMOS based Rectifier

Despite the advantages of Schottky diodes in RF energy scavenging, research has been done for years with a focus on the realization of RF energy scavenging in standard CMOS process using regular MOSFETs. Recently, Li et al. [20] proposed a dual-band energy scavenging system with CMOS circuit to scavenging RF energy in two frequency bands simultaneously. A dual-band monopole antenna with operating frequencies of 900 MHz and 2000MHz was used in their design. Two separate scavenging circuit designed in CMOS process were employed for these two bands with different stages. The output voltage was measured to achieve 1.15V and 1.05V for 900 MHz and 2000 MHz, respectively, at an input power as low as -19 dBm. But the overall efficiency is only 9%.

In [2], Le et al. designed a 36-stage floating gate rectifier to convert power extracted from a two-port meander line antenna which was tuned for maximum received power at 916 MHz. The proposed floating gate rectifier was fabricated in a 0.25μm five-metal single-poly CMOS process with active die area of 400μm × 1000μm. A maximum efficiency of 60% is reached by the RF energy scavenging system. However, special programming is required to control the floating-gate devices.

The studies in [68] and [69] focus on the CMOS circuit design for RF energy scavenging. A 915 MHz harvester implementing an integrated input matching network followed by a 17-stage self-compensated rectifier in a 90-nm CMOS technology was presented by Papotto et al. [68]. 1.2V output is generated by the device at input power of -18.8 dBm. Salter et al. demonstrated an RF energy scavenging circuit comprising a power matched Villard voltage doubler and a switched capacitor DC-DC converter in [69]. The proposed circuit can produce output voltage of 1V across a 5 MΩ load from input RF energy as low as -25.5 dBm. Summary of RF energy scavenging studies with rectifier circuit designed in CMOS process is illustrated in Table 2.6.

Table 2.6 Summary of RF energy scavenging with CMOS based rectifier

YEAR	REFERENCE	FREQUENCY BAND	TYPE OF RADIATOR	CMOS TECHNOLOGY	PERFORMANCE
2013	[20]	870-940 MHz 1920-2030 MHz	Monopole Antenna	0.13 μm	Efficiency: 9.1% @ 900 MHz -19.3dBm 8.9% @ 2000 MHz -19 dBm
2008	[2]	902-928 MHz	Meander Line Antenna	0.25 μm	Max. Efficiency: 60%
2011	[68]	915 MHz	N/A	90 nm	Efficiency: 11.75% @ -14dBm
2009	[69]	2200 MHz	N/A	0.13 μm	Output Voltage: 1 V @ -25.5 dBm

2.4 Summary

In this chapter, the concept of energy scavenging has been presented. Different energy scavenging techniques including solar, thermoelectric, wind, piezoelectric, radio frequency energy scavenging as well as hybrid energy scavenging have been explored regarding their operating principles and transducer performance. A detailed review on current RF energy scavenging techniques has also been illustrated. The rectenna is an essential component to convert the RF energy to electrical energy. This chapter has introduced the fundamental components of rectenna and reviewed several recent reported designs.

Chapter 3

UWB Microstrip Antenna for RF Energy Scavenging

A main challenge in RF energy scavenging is capturing sufficient output power. Previous researches on RF energy scavenging design mostly focused on scavenging RF energy in single band [2, 25, 70, 71]. However, the output power is limited with a single band antenna. What's more, ambient RF power is distributed over a wide range of frequency bands. Figure 3.1 illustrates measured RF energy density in the frequency range from 680 MHz to 3500 MHz in an urban environment. Depending on the frequency band, the power density variation was measured to be between -60 dBm/m^2 and -14.5 dBm/m^2 (1 nW/m^2 and 35.5 μW/m^2). Therefore, broadband RF energy scavenging becomes a possible approach to obtain enough output power for charging electronic devices. To cover the frequency bands of available signals in the ambient environment and maximize the received power, a well-designed broadband antenna is necessary. In this chapter, an ultra-wideband (UWB) microstrip antenna designed on ultra-thin substrate is proposed for compact half-wave RF energy scavenging systems. A dual-antenna array is also developed based on this design for full-wave application. The array covers most of the communication bands including DCS (1710 - 1880 MHz), PCS (1850 - 1990 MHz), UMTS (1920 - 2170 MHz), WiFi / WLAN / Hiper LAN /

IEEE 802.11 2.4 GHz (2412 - 2484 MHz), 3.6 GHz (3657.5 - 3690.0 MHz), Bluetooth (2400 - 2484 MHz), WiMAX 2.3 GHz (2.3 - 2.5 GHz), 2.5 GHz (2500 - 2690 MHz), 3.3 GHz, 3.5 GHz (3400 - 3600 MHz) & LTE applications.Simulations were carried out using finite-difference time-domain (FDTD) method based software, namely CST Microwave Studio. The simulation results have been validated by the measurement of fabricated prototypes.

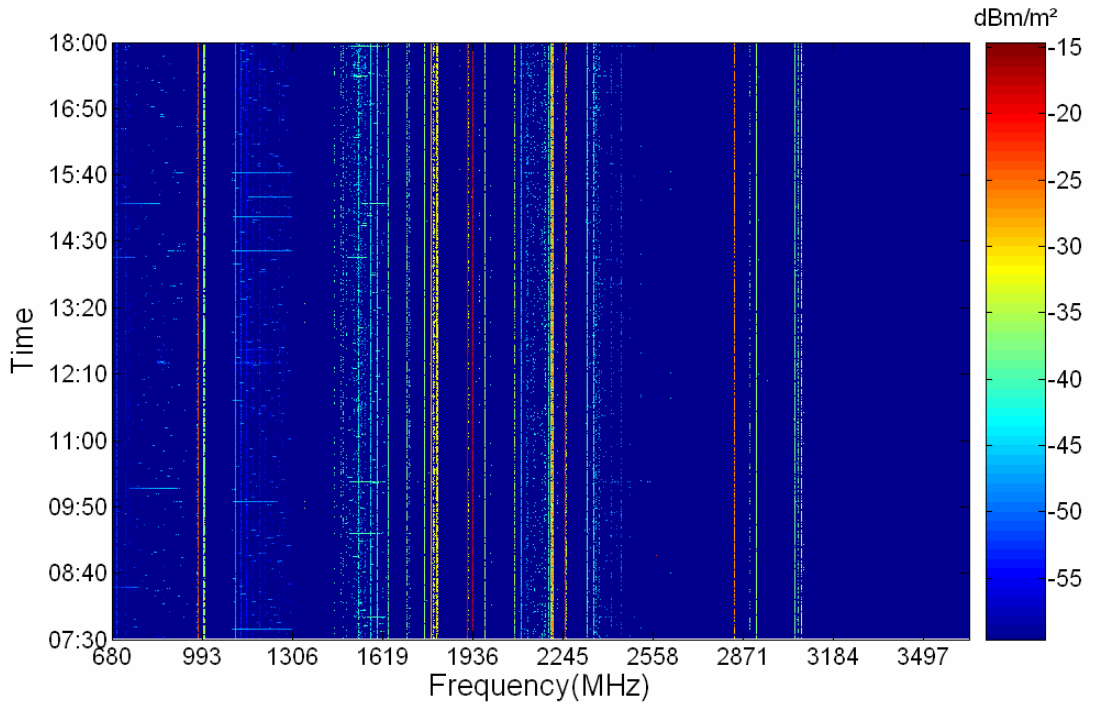

Figure 3.1 Measured RF power density over time (680 MHz-3500 MHz) [14] © IEEE

3.1 Antenna Theory

3.1.1 Introduction to Antenna

An antenna is a transitional device (as shown in Figure 3.2) between free-space and a guiding device for radiating or receiving radio waves. The guiding device, also known as transmission line, is used to transport electromagnetic energy from the source to the antenna or from the antenna to the receiver. Various types of antennas, including wire antennas, travelling wave antennas, aperture antennas and microstrip antennas, are presented in Figure 3.3.

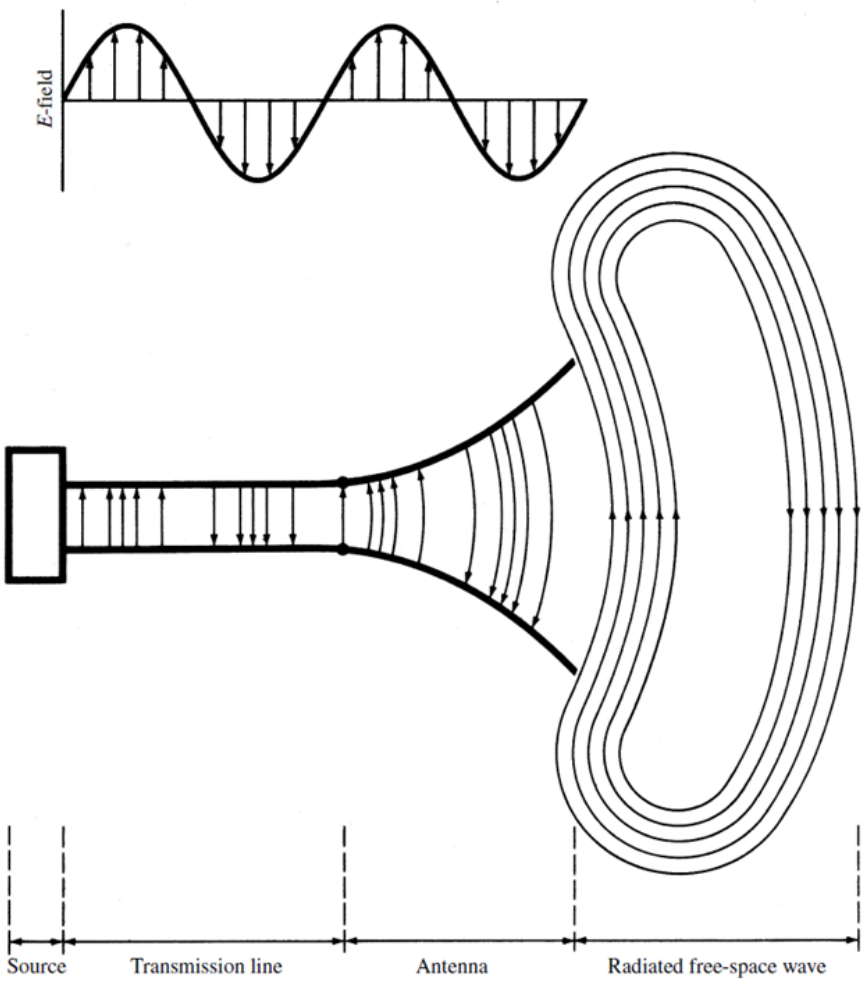

Figure 3.2 Antenna as a transition device [72]

(a) Wire antenna configurations: dipole antenna and loop antenna

(b) Travelling wave antenna configurations: helical antenna and Yagi antenna

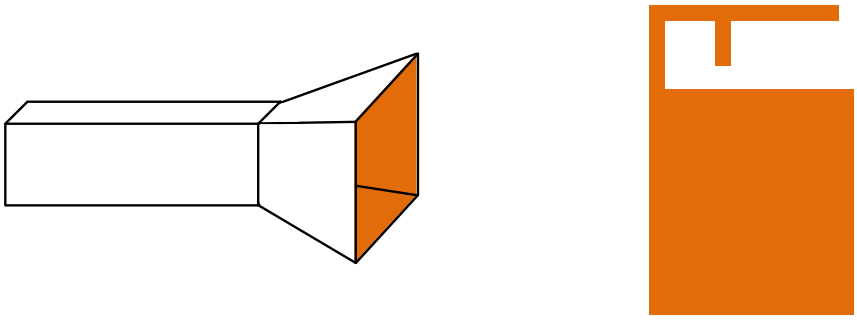

(c) Aperture antenna configurations: horn antenna and inverted-F antenna

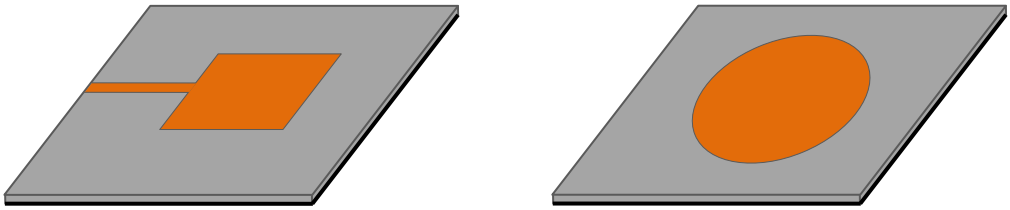

(d) Microstrip antenna configurations: rectangular patch antenna and circular patch antenna

Figure 3.3 Various types of antennas: (a) wire antennas, (b) travelling wave antennas, (c) aperture antennas, (d) microstrip antennas

The transmission-line Thevenin equivalent circuit of the transmitting system (Figure 3.2) is demonstrated in Figure 3.4, where V_g is the source voltage of an ideal generator, Z_g is the impedance of the generator, R_L is the loss resistance which relates to the conduction and dielectric losses associated with the antenna structure, R_r is the radiation resistance and X_A is the antenna reactance which represents the imaginary part of the impedance associated with antenna radiation. The antenna impedance Z_A is given by:

$$\boldsymbol{Z_A = (R_L + R_r) + jX_A} \tag{3.1}$$

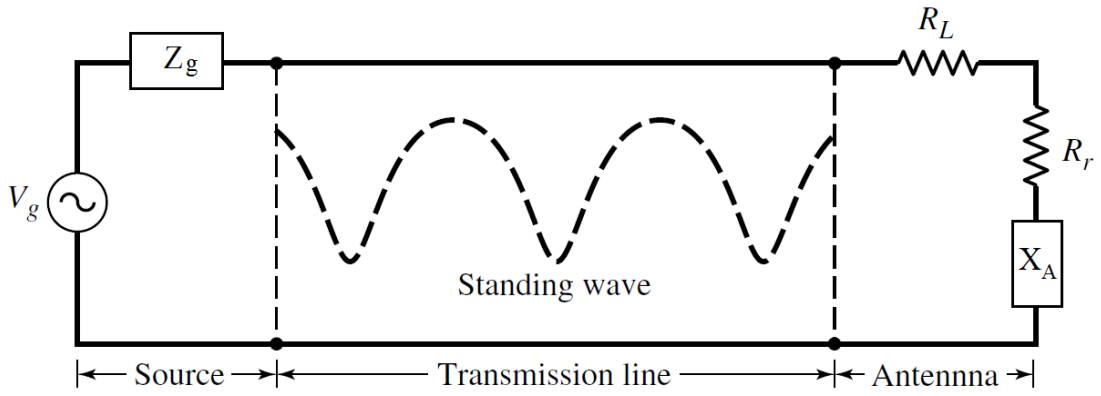

Figure 3.4 Transmission-line Thevenin equivalent of antenna system in transmitting mode [72]

In practical, the power generated by the source can't be totally delivered to the radiation resistance R_r due to the conduction-dielectric loss of the transmission line and the antenna as well as the reflection (mismatch) loss at the interface between the line and the antenna [72]. Taking into account the internal impedance of the source and neglecting the line and reflection losses, maximum power is transferred to the antenna under conjugate matching:

$$\boldsymbol{R_g = R_r + R_L} \tag{3.2}$$

$$\boldsymbol{X_g = -X_A} \tag{3.3}$$

where R_g is the source resistance and X_g is the source reactance.

3.1.2 Fundamental Parameters of Antenna

3.1.2.1 Radiation Pattern

The radiation pattern of an antenna is a graphical representation as a function of spherical coordinates to describe the antenna's radiation properties which include field strength, power flux density, directivity, radiation intensity and polarization [72]. Generally the radiation pattern can be categorized into three categories: isotropic, directional and omni-directional. A pattern is isotropic when uniform radiation is achieved in all directions. Isotropic antenna does not exist in practice, but is usually utilized as a reference for expressing the directive properties of actual antennas. An antenna which has more effective radiation in one direction than in others is defined as a directional antenna. The omni-directional pattern is a special type of the direction pattern, and is defined as one "having an essentially nondirectional pattern in a given plane and a directional pattern in any orthogonal plane" [72].

For a directional radiation pattern, radiation lobes are referred to indicate various parts of the radiation pattern bounded by regions of relatively weak radiation intensity. As depicted in Figure 3.5, the radiation lobes can be classified into main lobes, minor lobes, side lobes and back lobes. The radiation lobe in the direction of maximum radiation is defined as the main lobe, or major lobe. And the axis of maximum radiation, passing through the centre of the main beam, is called the beam axis. In some antennas more than one main lobe may exits. The minor lobe is any radiation lobe other than the main lobe. The other radiation lobes in the directions of undesired radiation are defined as side lobes, which are normally the largest of the minor lobes. The side lobe whose axis makes an angle of approximately 180° with respect to the beam axis is the back lobe.

There are two commonly quoted beamwidth in antenna radiation pattern: HPBW and FNBW. The half-power beamwidth (HPBW) is the angular separation of the main beam at the half-power (-3 dB) points while the first null beamwidth (FNBW) is the angular width between the first nulls on either side of the main beam.

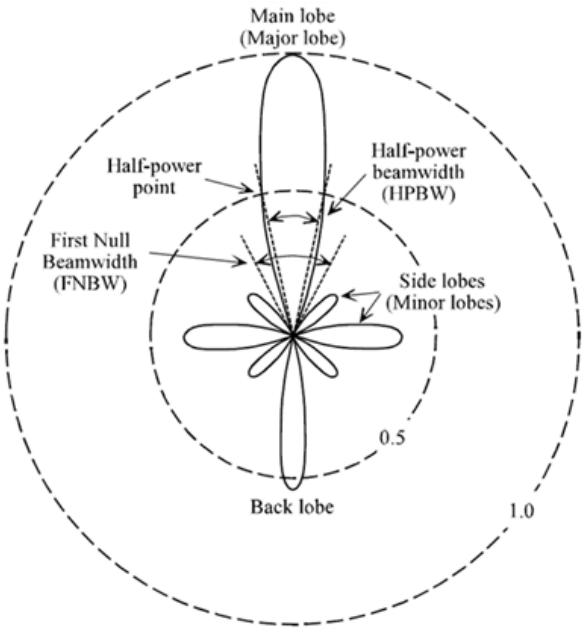

Figure 3.5 Normalized radiation pattern

3.1.2.2 Field Regions

The radiation space surrounding an antenna is divided into three regions: reactive near-field region, radiating near-field (Fresnel) region and far-field (Fraunhofer) region as presented in Figure 3.6.

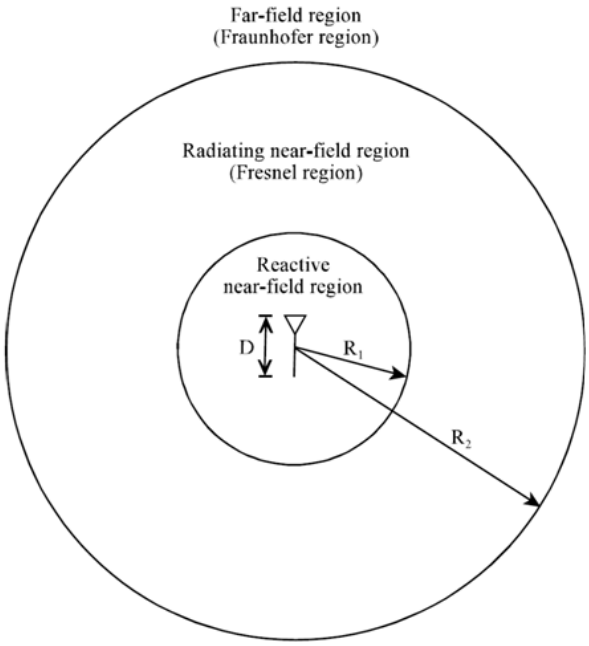

Figure 3.6 Antenna field regions

Reactive near-field region is the region immediately surrounding the antenna where the reactive field (stored energy – standing waves) is dominant. Radiating near-field (Fresnel) region is the region of the field of an antenna between the reactive near-field region and the far-field region where the radiation fields are dominant and the field distribution is dependent on the distance from the antenna. And far-field (Fraunhofer) region is the region farthest away from the antenna where the field distribution is essentially independent of the distance from the antenna. The boundaries (R_1, R_2) of these three regions are defined as a function of the maximum antenna dimension D and the wave length λ:

$$R_1 = 0.62\sqrt{D^3/\lambda} \tag{3.4}$$

$$R_2 = 2\,D^2/\lambda \tag{3.5}$$

3.1.2.3 Radiation Power Density

The average power radiated by an antenna, or radiation power density, is estimated by the time average Poynting vector, which is given by:

$$P_r = \frac{1}{2}\,Re[E \times H^*] \tag{3.6}$$

where E is the electric field intensity and H is the magnetic field intensity.

3.1.2.4 Radiation Intensity

Radiated power per solid angle (radiated power normalized to a unit sphere) is called radiation intensity. The radiation intensity, U, is a far-field parameter expressed as:

$$U = r^2 P_r \tag{3.7}$$

where r is the distance and P_r is the radiation power density described before. The total radiated power is therefore obtained by integrating the radiation intensity over the area of the unit sphere (4π):

$$P_{rad} = \oiint U\,d\Omega = \int_0^{2\pi}\int_0^{\pi} U \sin\theta\, d\theta\, d\phi \tag{3.8}$$

where $d\Omega = \sin\theta\, d\theta\, d\phi$ is the element of solid angle.

3.1.2.5 Directivity

From the field point of view, the most important quantitative parameter of an antenna is the directivity, which is a measure of the concentration of radiated power in a specific direction. It is defined as the ratio of the radiation intensity in a given direction from the antenna to the radiation intensity averaged over all directions [73]. That is to say, the directivity of a nonisotropic antenna equals to the ratio of its radiation intensity in a particular direction over that of an isotropic antenna. Mathematically, the directivity can be written as:

$$\boldsymbol{D} = \frac{\boldsymbol{U}}{\boldsymbol{U_0}} = \frac{\boldsymbol{4\pi U}}{\boldsymbol{P_{rad}}} \tag{3.9}$$

where U_0 is the radiation intensity of isotropic source. The antenna directivity usually implies the directivity in the direction of maximum radiation intensity (maximum directivity) if the direction is not specified.

3.1.2.6 Gain

The definitions of antenna directivity and antenna gain are essentially the same except for the power terms used in the definitions. The antenna gain in a given direction is defined as the ratio of the radiation intensity, in the given direction, to the radiation intensity obtained if the total antenna input power (instead of total antenna radiated power for the definition of directivity) were radiated isotropically. Thus, the antenna gain, being dependant on the total power delivered to the antenna input terminal, is a measure that takes into account the ohmic losses in the antenna. In equation form the antenna gain can be calculated as:

$$\boldsymbol{G} = \boldsymbol{4\pi}\frac{\boldsymbol{radiation\ intensity}}{\boldsymbol{total\ input\ power}} = \frac{\boldsymbol{4\pi U}}{\boldsymbol{P_{in}}} \tag{3.10}$$

3.1.2.7 Antenna Efficiency

The overall antenna efficiency is employed to take into account the conduction-dielectric loss within the antenna structure and the reflection (mismatch) loss at the input terminal. The reflection, conduction and dielectric losses as well as the terminals of an antenna are illustrated in Figure 3.7.

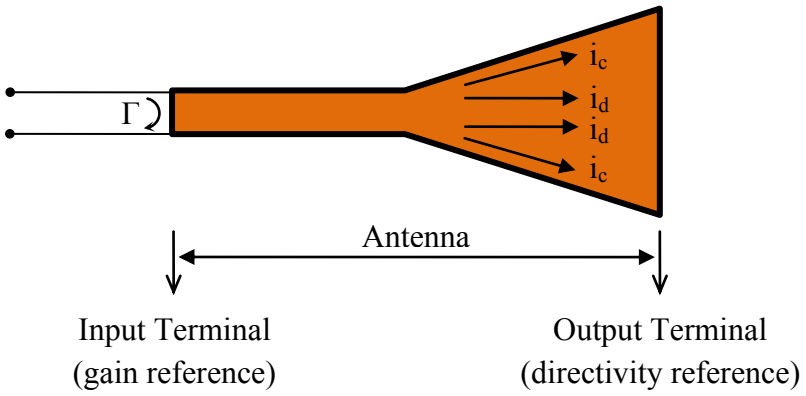

Figure 3.7 Reference terminals and losses of an antenna

The total antenna efficiency e_0 is generally given by:

$$e_0 = e_r e_{cd} \tag{3.11}$$

$$e_r = 1 - |\Gamma|^2 \tag{3.12}$$

$$e_{cd} = e_c e_d \tag{3.13}$$

where e_r, e_c and e_d are the reflection, conduction and dielectric efficiencies, respectively. $\Gamma = (Z_{in} - Z_0) / (Z_{in} + Z_0)$ refers to the voltage reflection coefficient at the input terminal. Z_{in} is the antenna input impedance and Z_0 is the characteristic impedance of the transmission line.

And e_{cd}, the product $e_c \times e_d$, is defined as the antenna radiation efficiency. It is usually applied to relate the gain and directivity:

$$e_{cd} = \frac{P_{rad}}{P_{in}} = \frac{G}{D} \tag{3.14}$$

3.1.2.8 Polarization

Polarization of a radiated wave is defined by the figure traced as a function of time by the instantaneous electric field at a fix observation point. And polarization of an antenna in a given direction is therefore defined as the polarization of the electromagnetic wave radiated by the antenna. Figure 3.8 demonstrates a typical trace as a function of time.

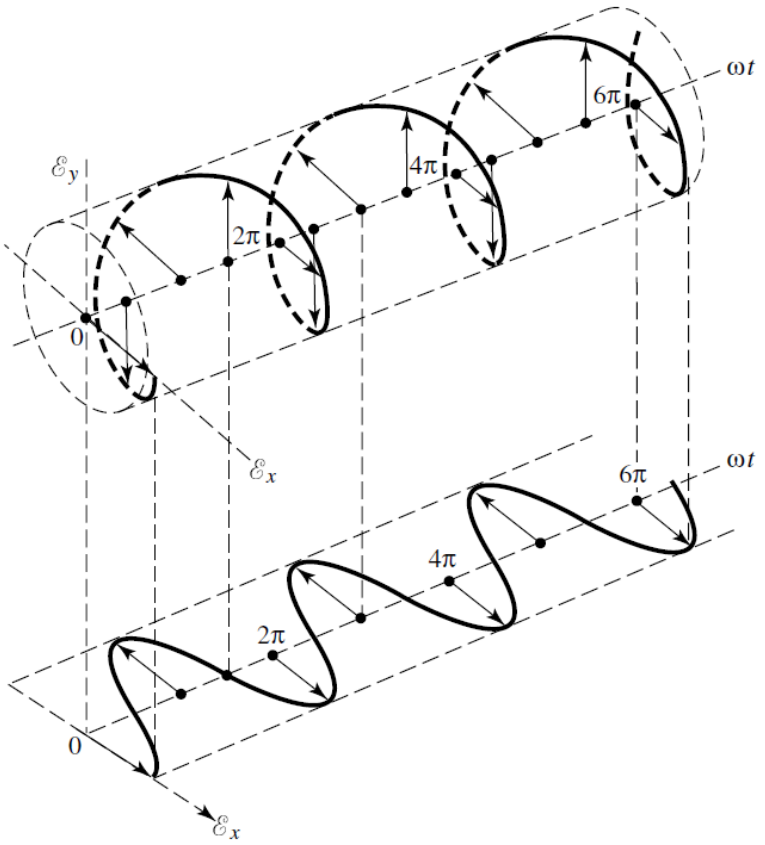

Figure 3.8 Rotation of a plane electromagnetic wave

Polarization can be generally classified as linear, circular and elliptical. An antenna is linearly polarized if the electric field vector of the radiated wave is always oriented along the same straight line at every instant of time. If an antenna radiates an electromagnetic wave whose electric field vector traces a circle as a function of time, the antenna is then defined as circularly polarized. If the rotation of the traced electric field figure is clockwise, the antenna is right-hand (or clockwise) circularly polarized. On the other hand, an antenna is left-hand circularly polarized if the rotation is counter clockwise. An antenna is elliptically polarized if it is not linearly or circularly polarized. Linear and circular polarizations are special cases of elliptical, and they can be obtained when the electric field figure traced changes from ellipse to a straight line or a circle, respectively.

3.2 UWB Microstrip Antennas on Ultra-Thin Substrate for RF Energy Scavenging

3.2.1 Single UWB Microstrip Antenna

3.2.1.1 Antenna Geometry Design

A coplanar waveguide (CPW) fed antenna printed on an inexpensive FR4 dielectric substrate with relative electric permittivity of 4.55 and loss tangent of 0.0175 is proposed. An initial design was created using Antenna Magus Software and then imported into CST Microwave Studio for modification, optimization and simulation. In order to be easily integrated into miniature devices and systems, thickness of the substrate is selected to be 0.2 mm. Geometry of the proposed antenna is illustrated in Figure 3.9 and detailed dimensions are tabulated in Table 3.1.

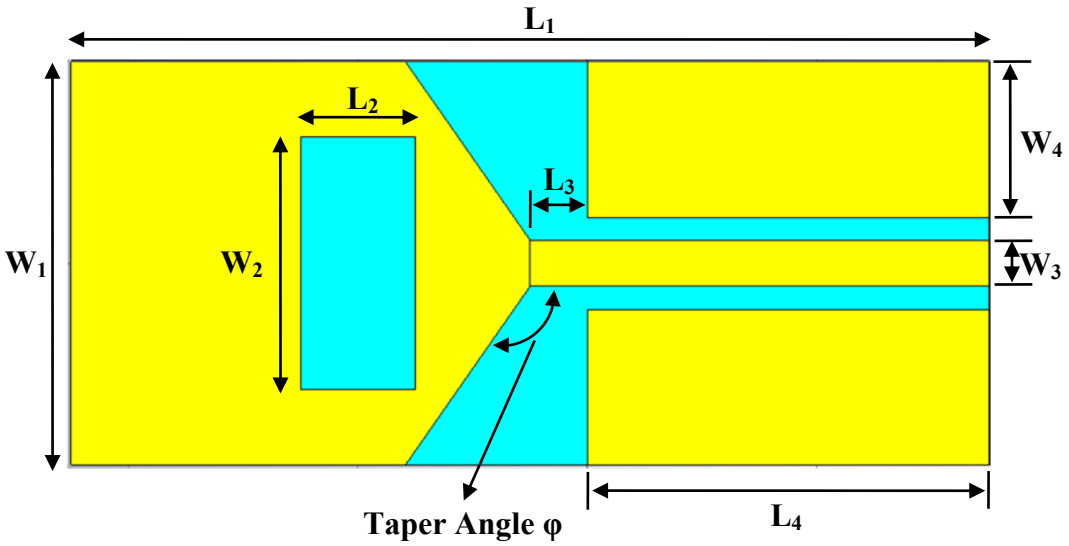

Figure 3.9 Geometry of the proposed single broadband antenna (Copper: yellow, FR4 substrate: blue)

Table 3.1 Dimensions of the proposed single broadband antenna

Parameter	Value	Parameter	Value
L_1	80 mm	W_1	35 mm
L_2	10 mm	W_2	22 mm
L_3	5 mm	W_3	4 mm
L_4	35 mm	W_4	13.5 mm
Taper Angle φ	35°		

The proposed antenna is developed from rectangular patch antenna. A rectangular radiator is fed by a CPW transmission line terminated with a SMA connector for measurement purpose. Since the antenna and the feeding are implemented on the same plane, only one layer of substrate with single-sided metallization is used, which makes the manufacture of the antenna very easy and extremely low cost [74]. Moreover, good circuit isolation can be achieved with the CPW configuration [73]. To broaden the antenna bandwidth, partial ground plane technique is introduced [75]. Tapered structure on the radiating patch is applied for smooth transition from one resonate mode to another and good impedance matching over a broad frequency range [76]. A rectangular slot is etched on the radiating patch to obtain the other resonate mode operating near the one of conventional rectangular patch antenna for bandwidth enhancement. The length of the rectangular slot can be roughly determined by [77]:

$$W_s = \frac{c}{2f\sqrt{\varepsilon_{reff}}} \tag{3.15}$$

where W_s is the length of the slot, c is the free-space velocity of light, f is the resonate frequency and ε_{reff} is effective dielectric constant given by [72]:

$$\varepsilon_{reff} = \frac{\varepsilon_r + 1}{2} + \frac{\varepsilon_r - 1}{2}\left[1 + 12\,\frac{h}{W}\right]^{-1/2} \tag{3.16}$$

where ε_r is the actual dielectric constant, h is the substrate thickness and W is the width of radiation edge.

The formulas used to calculate the dimensions of the radiating patch are shown below [72]:

$$W = \frac{c}{2f}\sqrt{\frac{2}{\varepsilon_r + 1}} \tag{3.17}$$

$$\Delta L = 0.412\,h\,\frac{(\varepsilon_{reff} + 0.3)\left(\frac{W}{h} + 0.264\right)}{(\varepsilon_{reff} - 0.258)\left(\frac{W}{h} + 0.8\right)} \tag{3.18}$$

$$L = \frac{c}{2f\sqrt{\varepsilon_{reff}}} - 2\Delta L \tag{3.19}$$

where is ΔL is the extension of the length due to the fringing effects.

3.2.1.2 Equivalent Circuit Model

To discuss the mechanism of the UWB properties, the equivalent circuit model of the proposed antenna is investigated. Conceptually, CPW is treated as a transmission line with characteristic impedance Z_0. The radiating patch is modelled as several series connected RLC parallel cells for simplicity. And the rectangular slot is described in terms of an equivalent series inductance.

3.2.1.2.1 Transmission Line Model for CPW

CPW can be simply modelled as a transmission line with characteristic impedance of Z_0 in the equivalent circuit model. Properties of the CPW are decided by four geometric parameters: the conductor width and thickness, the gap, and the substrate thickness. Closed-form expressions for the characteristic impedance and effective dielectric constant of CPW with conductor thickness neglected is given in [78].

3.2.1.2.2 Impedance Model for Radiating Patch

As the last component of a transmission system, the antenna is simply represented by a 50 Ω load resistance in most cases [79]. This approximation is valid when the antenna is well matched. However, the hypothesis is not fulfilled for antennas with large bandwidth. A simple RLC parallel circuit is usually used to model an antenna with narrow bandwidth since the resonances are separate with target frequency located in only one resonance. For UWB antennas, matching bandwidth can be considered as the result of several adjacent resonances and each one can be represented by an RLC parallel circuit [80]. Therefore, the radiating patch of the

UWB antenna can be modelled approximately as several parallel resonant sections connected in series as shown in Figure 3.10.

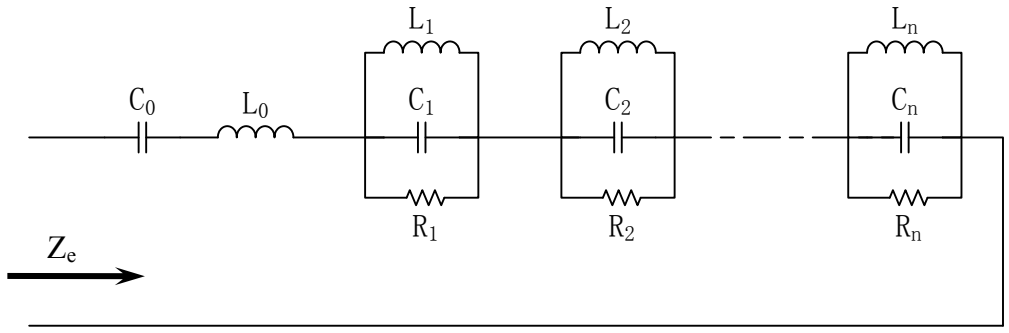

Figure 3.10 Equivalent circuit of radiating patch

An impedance transformation circuit due to the antenna static capacitance (C_0) and self probe (L_0) is represented by the first cell C_0-L_0 serie [80]. The input impedance of the equivalent circuit Z_e is given by:

$$\boldsymbol{Z_e = j \times \frac{L_0 C_0 \omega^2 - 1}{C_0 \omega} + \sum_{k=1}^{n} \frac{j R_k L_k \omega}{R_k (1 - L_k C_k \omega^2) + j L_k \omega}} \tag{3.20}$$

The different parameters (L_0, C_0, R_k, L_k, C_k) can be calculated using an iterative method and curve-fitting method with Z_e obtained from simulated or measured impedance data [79].

3.2.1.2.3 Equivalent Circuit Model for Rectangular Slot

A microstrip antenna can be considered as an open circuit resonator with electrical current flowing along the length direction. Thus, the resonant frequency of the microstrip antenna can be obtained by:

$$\boldsymbol{k L_e = \pi} \tag{3.21}$$

where k is the number of waves in the substrate and L_e is the equivalent path length of current flow. With a rectangular slot etched on the radiating patch, the current flow path is cut off, and the current has to flow around the slot. It increases the equivalent path length of the electrical current, hence, decreases the resonant frequency. This effect can be modelled as an equivalent inductance (L_s) in series [81] as shown in Figure 3.11.

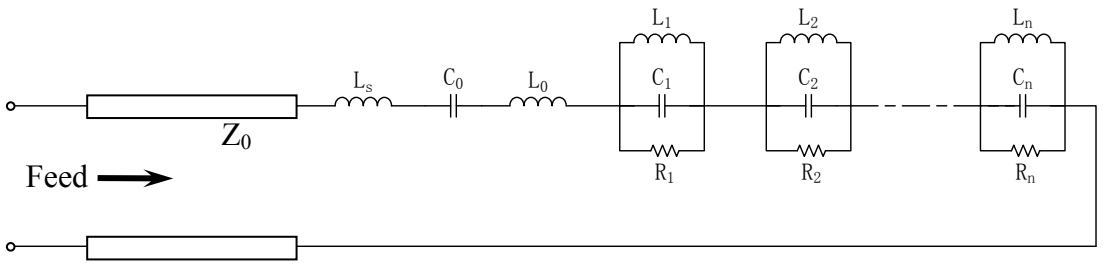

Figure 3.11 Equivalent circuit of the proposed UWB antenna

The quality factor of the microstrip antenna decreases with the increase of inductance due to the presence of the rectangular slot. The correlation of bandwidth (BW) and quality factor Q is expressed as [82]:

$$\boldsymbol{BW} = \frac{1}{Q\sqrt{2}} \tag{3.22}$$

As can be seen, the decrease of Q-factor results in the increase of bandwidth accordingly.

3.2.1.3 Simulation Performance and Discussion

The simulated reflection coefficient of the proposed antenna is presented in Figure 3.12. The antenna has an impedance bandwidth of 4.5 GHz, from 1 GHz to 5.5 GHz. And the lowest value of reflection coefficient reaches -45dB at frequency of 1.27 GHz. As the general definition of UWB is given by the relative bandwidth [83]:

$$\boldsymbol{BW} = 2\frac{f_H - f_L}{f_H + f_L} > 0.2 \tag{3.23}$$

where f_H and f_L are the upper and lower band limits, respectively. Therefore, the proposed antenna can be considered as a UWB antenna.

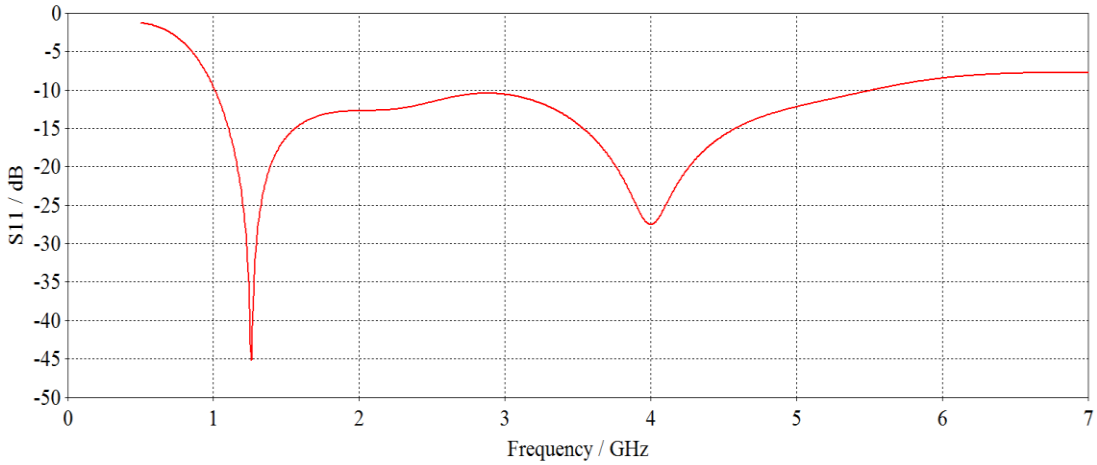

Figure 3.12 Simulated reflection coefficient

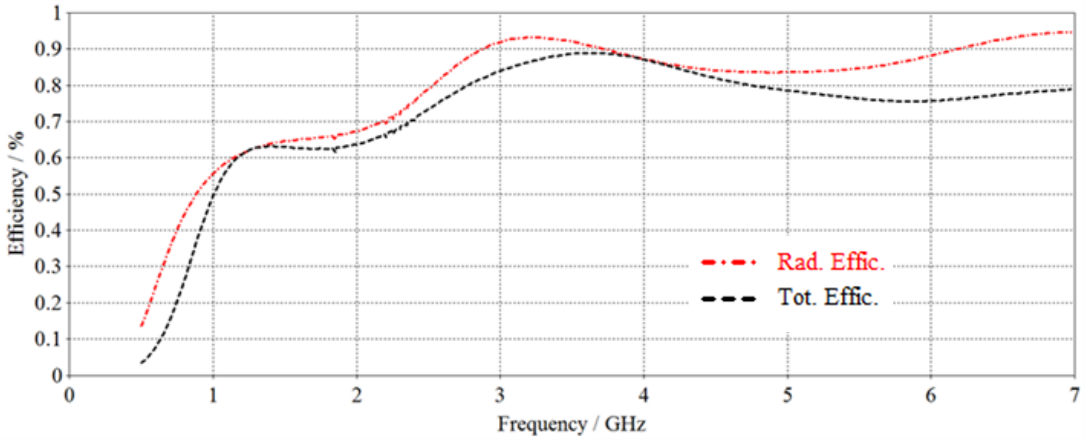

Figure 3.13 Simulated antenna efficiency

Figure 3.13 illustrates the simulated radiation efficiency and total efficiency. At the lowest operating frequency of 1 GHz, the radiation efficiency and total efficiency are the lowest, which are 56% and 50%, respectively. The maximum radiation efficiency within operating frequencies is 93% at 3.2 GHz while the maximum total efficiency is approximately 89% at 3.7 GHz. The computed radiation characteristic at 1.26 GHz and 4 GHz in E-plane and H-plane, which correspond to x-z plane (Phi = 0°) and y-z plane (Phi = 90°), respectively, are illustrated in Figure 3.14.

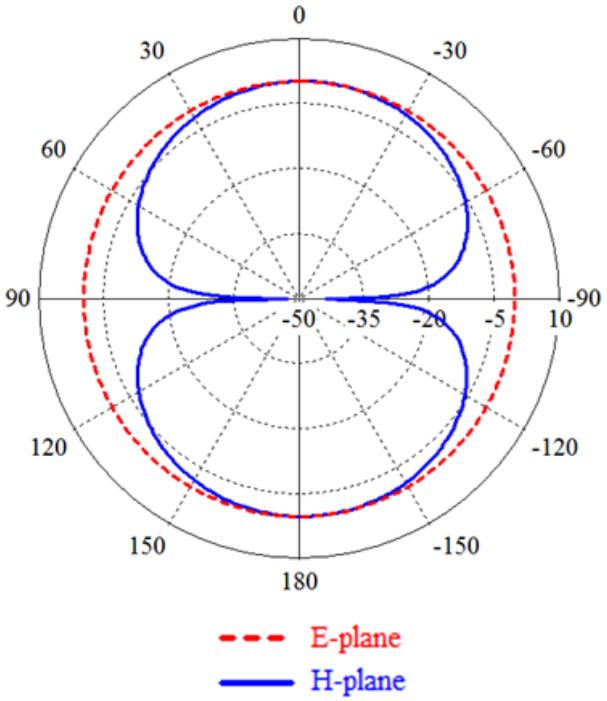

(a) 1.26 GHz

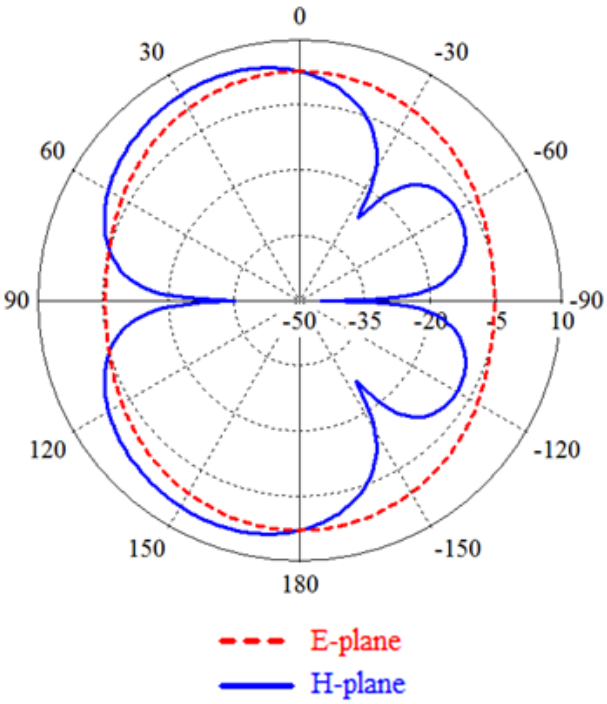

(b) 4 GHz

Figure 3.14 Simulated radiation pattern

Table 3.2 Comparison between the proposed antenna and other broadband antenna designs for RF energy scavenging system

Antenna Design	Simulated Bandwidth	Size
[19]	1.3 GHz (1.7 – 3 GHz)	30×30 mm^2
[16]	135 MHz (840 – 975 MHz)	30×110 mm^2
[17]	2.03 GHz (2.17 – 4.2 GHz)	30×50 mm^2
Proposed	4.5 GHz (1 – 5.5 GHz)	35×80 mm^2

Comparison between the proposed antenna and previously published broadband antenna designs for RF energy scavenging is summarized in Table 3.2. Our proposed antenna has a larger bandwidth compared with the other designs, which covers most of the wireless communication frequency bands such as WLAN and LTE. Although it has a relatively larger size, the thin substrate makes the proposed antenna suitable for implementation in compact electronic devices.

3.2.1.4 Measurement Results

The fabricated antenna is demonstrated in Figure 3.15 and Figure 3.16 illustrates the measured reflection coefficient. According to the measurement results, the operating bandwidth of the antenna is about 4 GHz, from 1.1 GHz to 5.1 GHz, which is 500 MHz smaller than the simulated bandwidth of 4.5 GHz. The discrepancy between the measured and simulated results is caused by the accuracy of the fabrication process. This difference is also attributed to the simplified model used in the simulation which does not include material loss, soldered joints, and the SMA connector. Antenna efficiency was also measured, as shown in Figure 3.17. Within operating frequencies, the lowest efficiency is about 50%, which is the same as the simulation result. But the maximum efficiency is only 82%, 7% lower than the simulated one. As for the

antenna gain (Figure 3.18), between 1.1 GHz and 5.1 GHz, it varies from 2.8 dBi to 4.4 dBi. The maximum value is observed at 3.6 GHz.

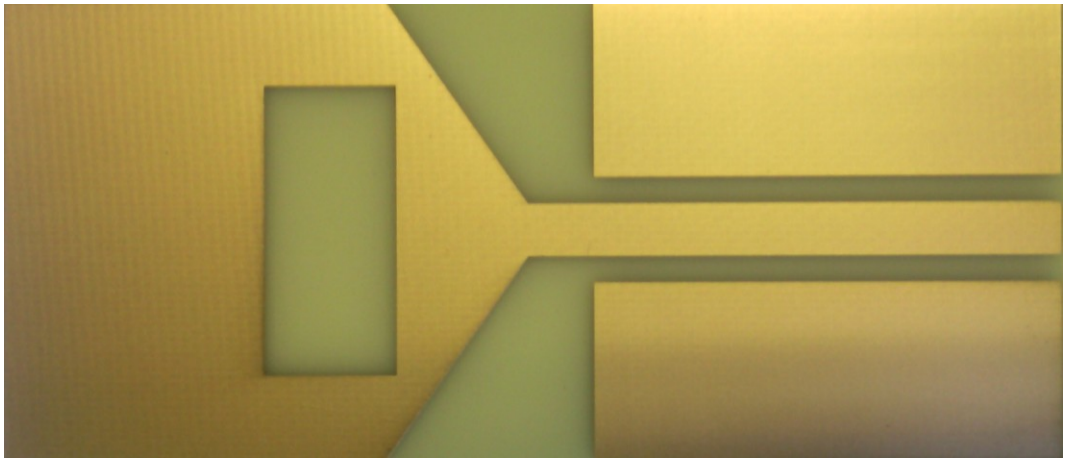

Figure 3.15 Fabricated prototype of the proposed UWB antenna

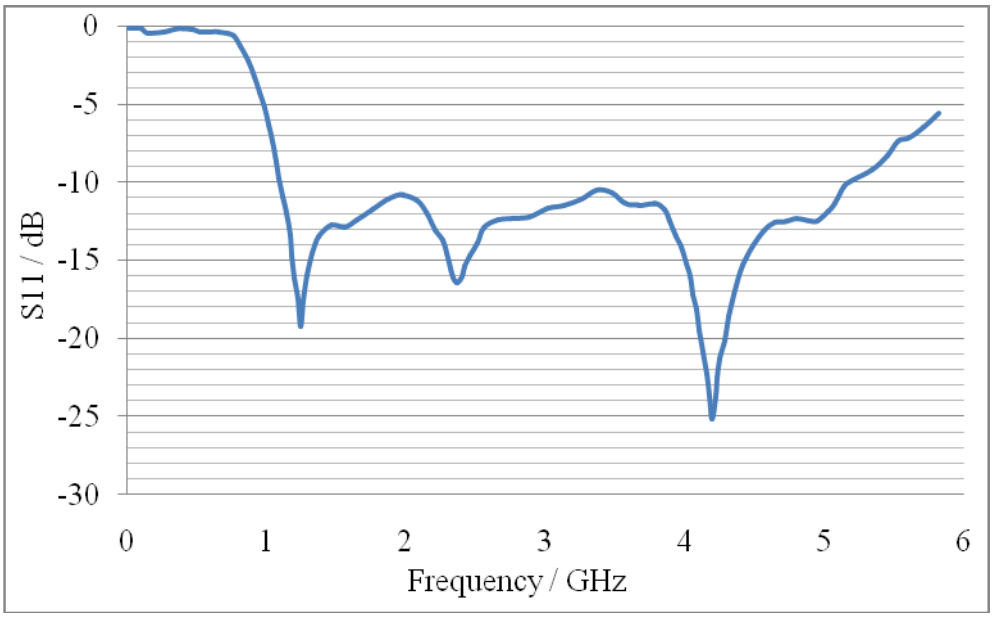

Figure 3.16 Measured reflection coefficient of the proposed UWB microstrip antenna

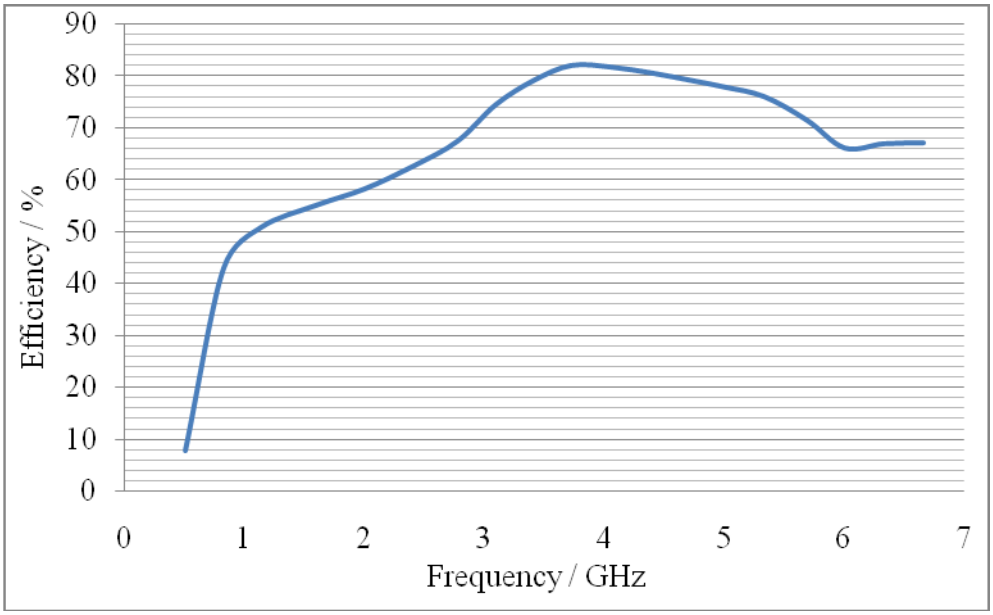

Figure 3.17 Measured antenna efficiency of the proposed UWB microstrip antenna

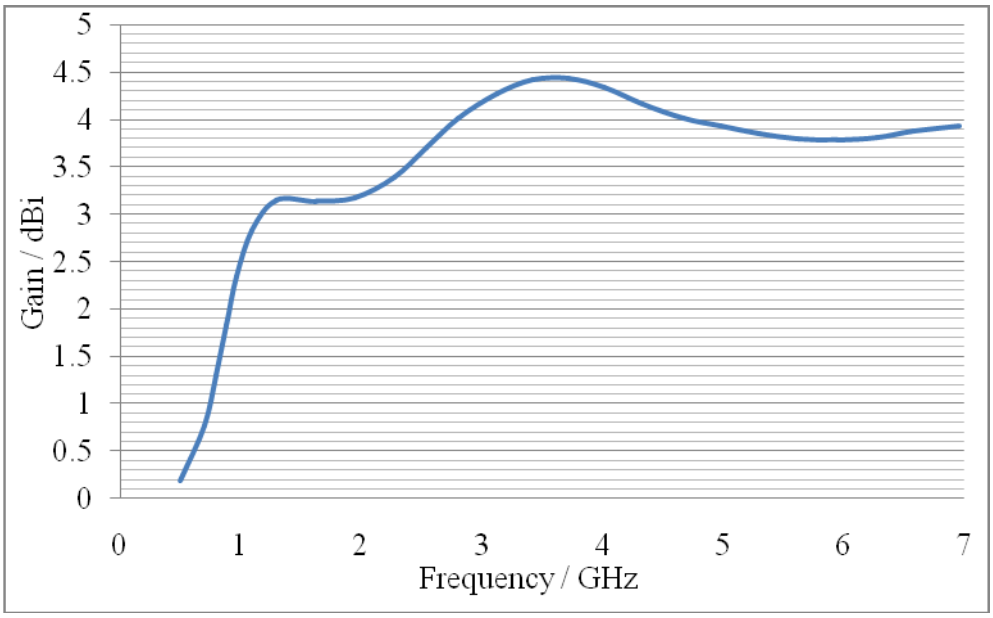

Figure 3.18 Measured antenna gain of the proposed UWB microstrip antenna

3.2.2 Dual-Antenna Array for Differential RF Energy Scavenging

As has been introduced previously, other than antenna, rectifier is another crucial component in RF energy scavenging systems. With low turn-on voltage and fast switching characteristic, Schottky diode is generally considered as an ideal choice for rectifier circuit to achieve both high voltage gain and high power conversion efficiency. However, due to the fact that Schottky diode cannot be implemented in normal CMOS process, CMOS integration of rectifier design is usually realized by utilizing diode-connected MOS transistors. For passive CMOS rectifier, full wave rectifier circuit with differential drive has higher conversion efficiency when compared with half wave design of single input due to its bridge structure. With the cross-coupled differential CMOS configuration, active threshold voltage cancellation scheme can be adopted to obtain both small ON-resistance and small reverse-leakage current, which is impracticable for conventional "static" threshold voltage cancellation scheme. Therefore, in order to achieve high conversion efficiency for maximum output power of RF energy scavenging system, a dual-antenna array based on the proposed single UWB microstrip antenna is developed dedicated for differential RF energy scavenging.

3.2.2.1 Array Geometry

The array geometry is demonstrated in Figure 3.19 and detailed dimensions of the array are presented in Table 3.3. Taking into account the trade-off between antenna size and mutual coupling, the element spacing of the array is optimized to be 15 mm. The width of the slot on the radiating patch of the single antenna element is slightly adjusted from 22 mm to 20 mm for wider bandwidth while the rest of the dimensions remain the same as the single UWB antenna design.

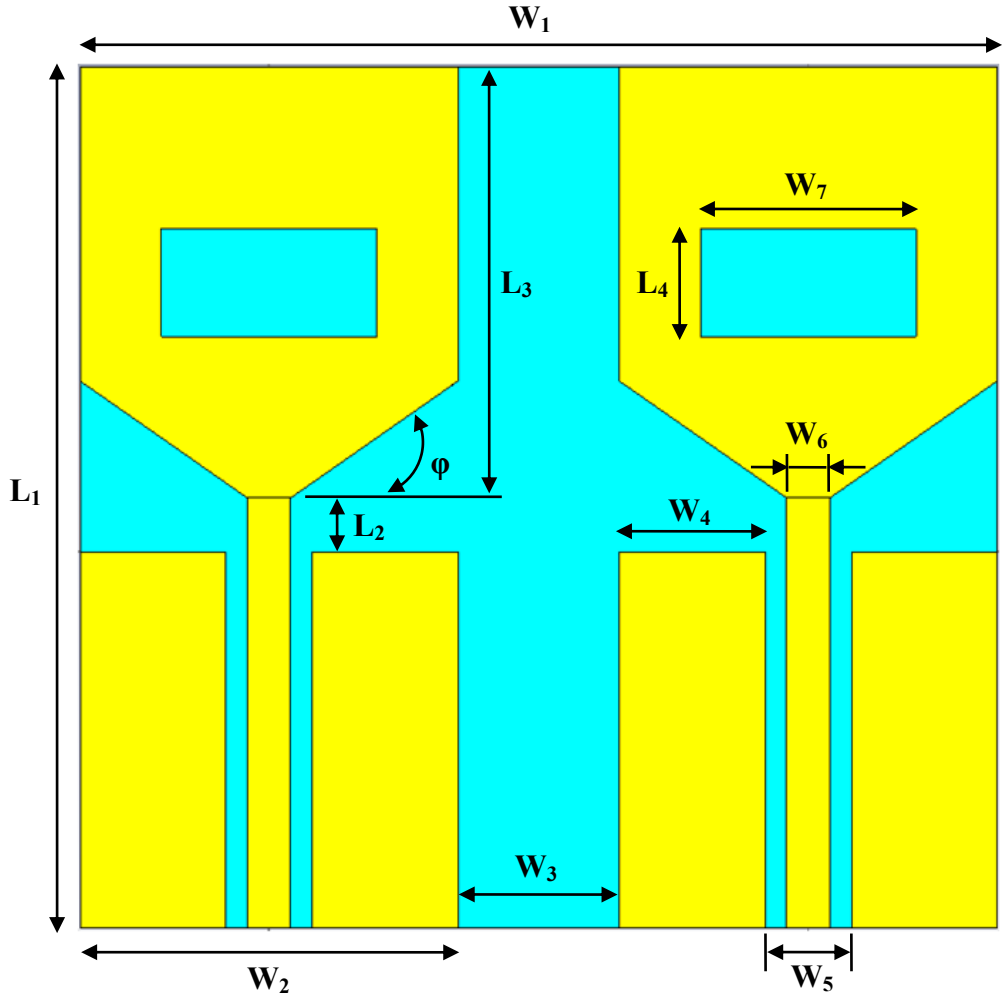

Figure 3.19 Array geometry

Table 3.3 Array dimensions

Parameter	Value	Parameter	Value
W_1	85mm	W_7	20mm
W_2	35mm	L_1	80mm
W_3	15mm	L_2	5mm
W_4	13.5mm	L_3	40mm
W_5	8mm	L_4	10mm
W_6	4mm	Taper Angle φ	35°

3.2.2.2 Simulation Performance

Figure 3.20 shows the simulated scattering parameters of the array configuration. With reference to -10 dB, the simulation results reveal a relatively narrower impedance bandwidth of 3.48 GHz (1.05 – 4.53 GHz) compared with the single antenna. Nevertheless, the bandwidth is still larger than the other published works in Table 3.2. The operating bandwidth covers communication applications including DCS (1710 - 1880 MHz), PCS (1850 - 1990 MHz), UMTS (1920 - 2170 MHz), WiFi / WLAN / Hiper LAN / IEEE 802.11 2.4 GHz (2412 - 2484 MHz), 3.6 GHz (3657.5 - 3690.0 MHz), Bluetooth (2400 - 2484 MHz), WiMAX 2.3 GHz (2.3 - 2.5 GHz), 2.5 GHz (2500 - 2690 MHz), 3.3 GHz, 3.5 GHz (3400 - 3600 MHz) & LTE applications.

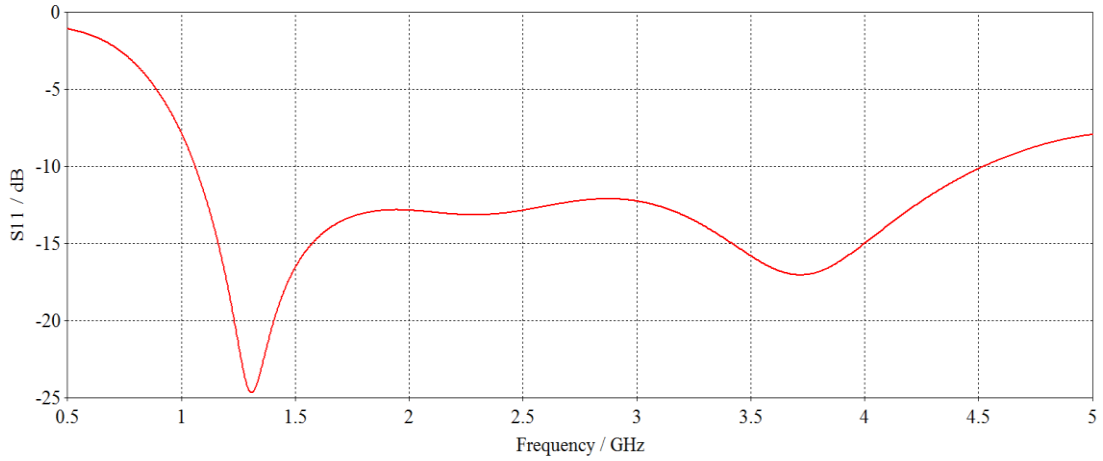

(a)

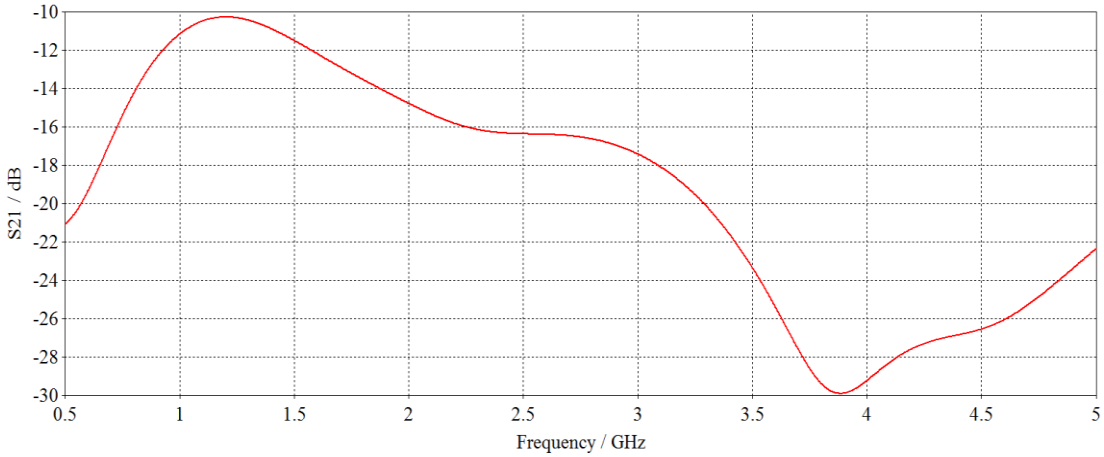

(b)

Figure 3.20 Simulated S-parameters: (a) S_{11}, (b) S_{21}

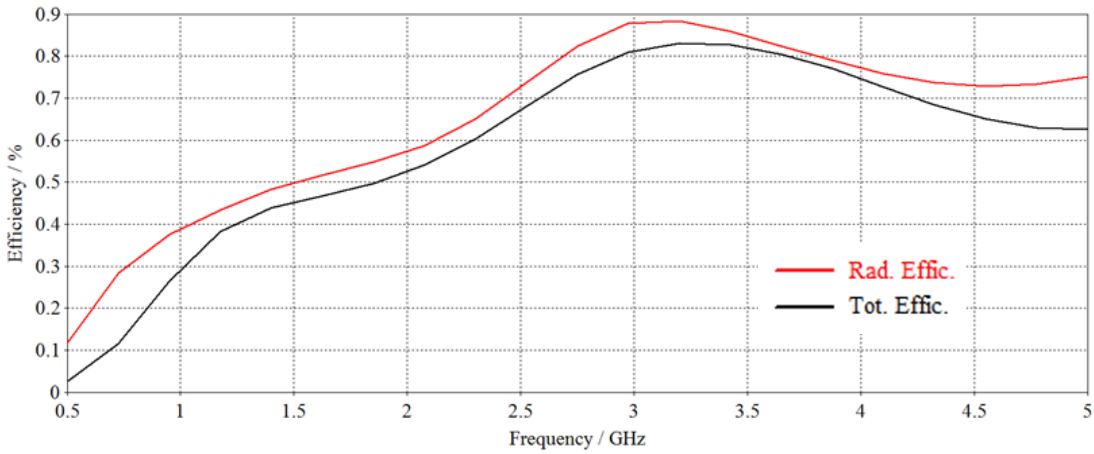

Figure 3.21 Simulated efficiency

The simulated efficiency for single antenna element in the array is shown in Figure 3.21. The maximum radiation efficiency achieves approximately 90% at higher efficiencies around 3.2 GHz. Compared with the single microstrip antenna, the array element has lower efficiency at lower frequencies. The efficiency at lower frequencies can be improved by increasing the element spacing, but it results in a larger size.

Radiation characteristics of single element at various frequencies are also studied, as shown in Figure 3.22. It can be seen from the figures that at low frequencies the radiation patterns are bi-directional, which are similar to those of conventional monopole antennas. While at high frequencies quasi omni-directional behaviour is observed.

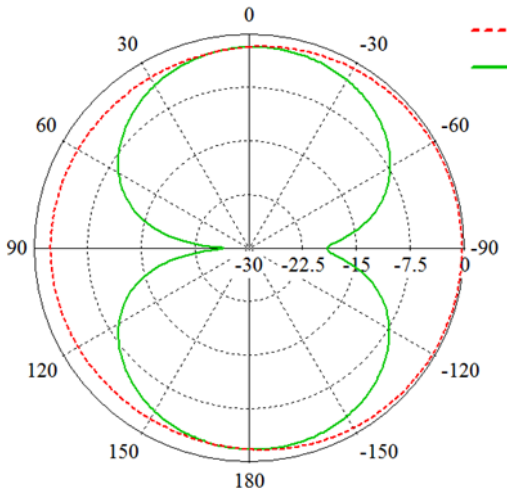

(a) At 1.22 GHz

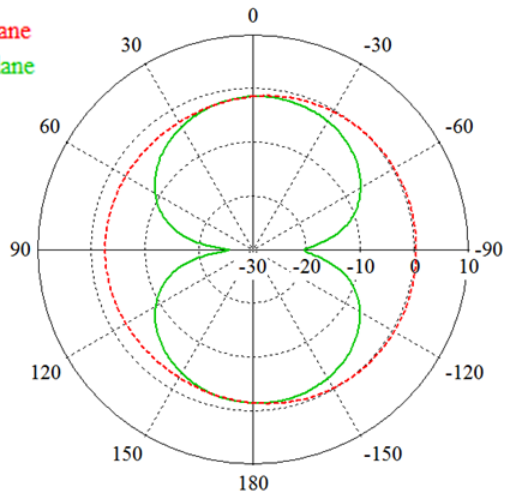

(b) At 1.38 GHz

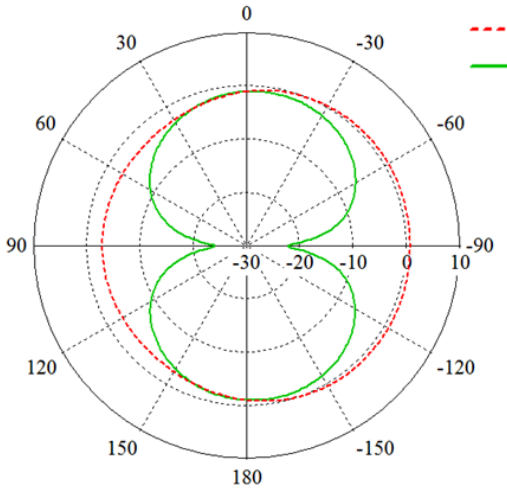

(c) At 1.575 GHz

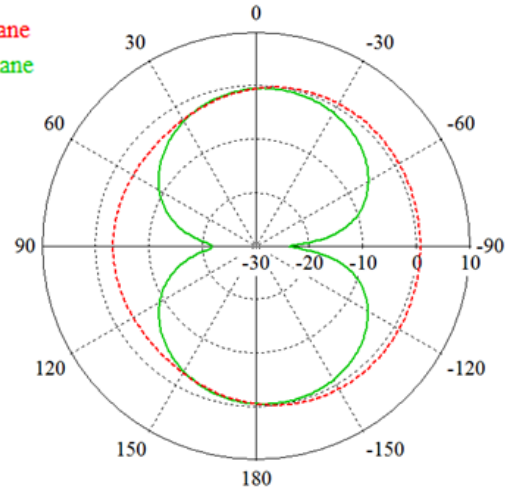

(d) At 1.8GHz

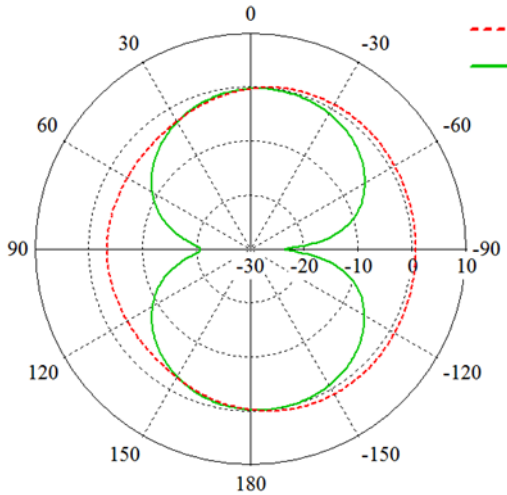

(e) At 1.9 GHz

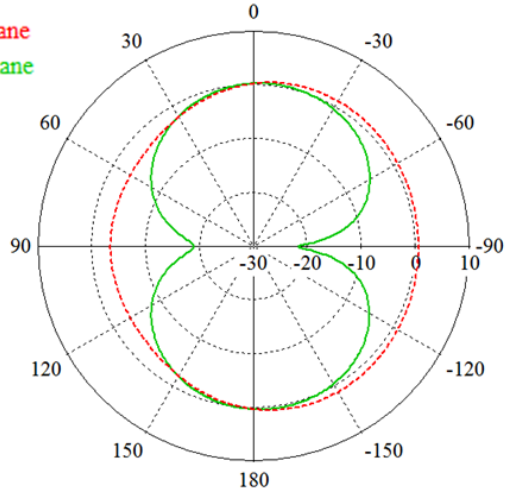

(f) At 2.1 GHz

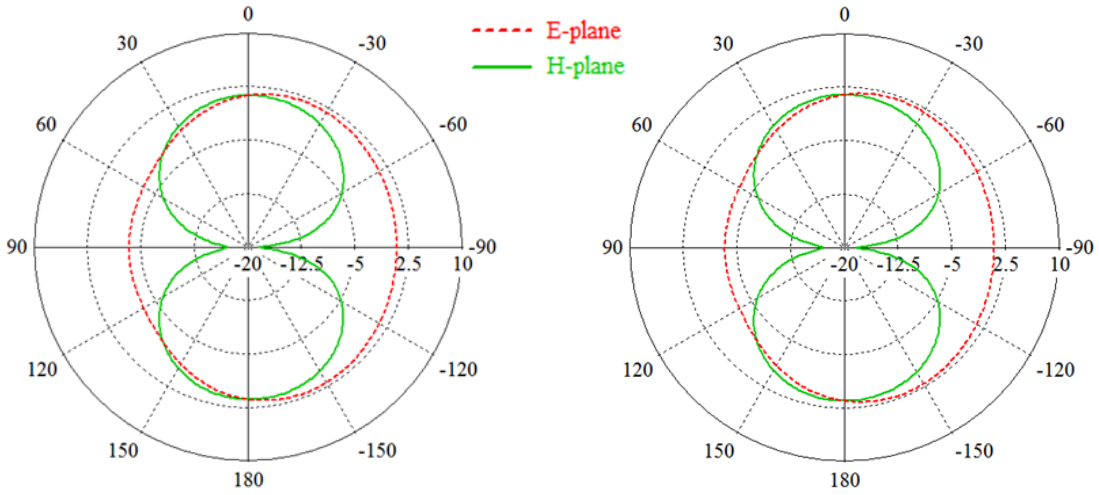

(g) At 2.45 GHz (h) At 2.5 GHz

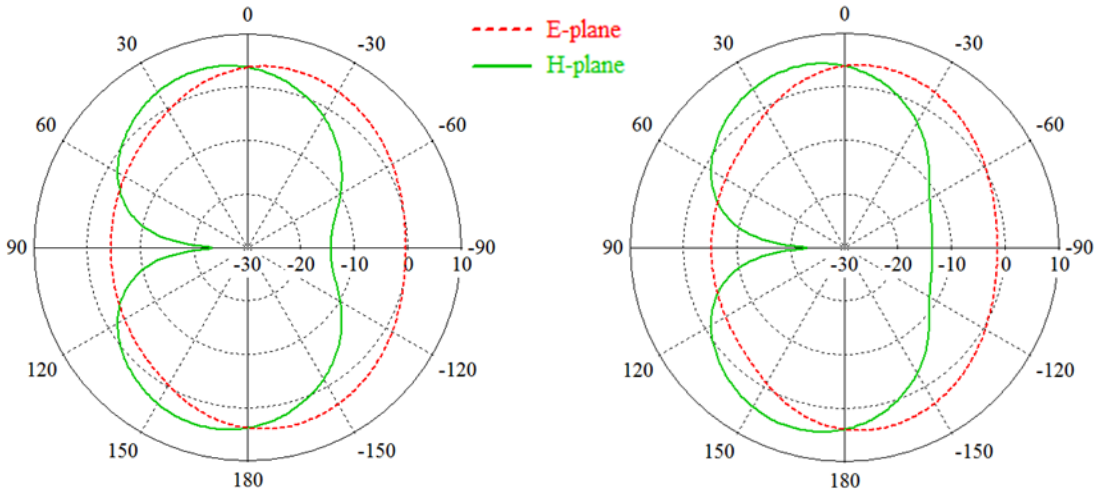

(i) At 3.3 GHz (j) At 3.5 GHz

Figure 3.22 Radiation pattern at various frequencies

3.2.2.3 Parametric Analysis

3.2.2.3.1 Element Spacing Variation

Figure 3.23 shows the simulated reflection coefficient and mutual coupling when the element spacing is varied. Within operating frequencies, as the distance between antenna elements increases, both the reflection coefficient and mutual coupling decrease. A minimum element spacing of 15 mm is observed to maintain the wideband operation based on the reference of -10 dB.

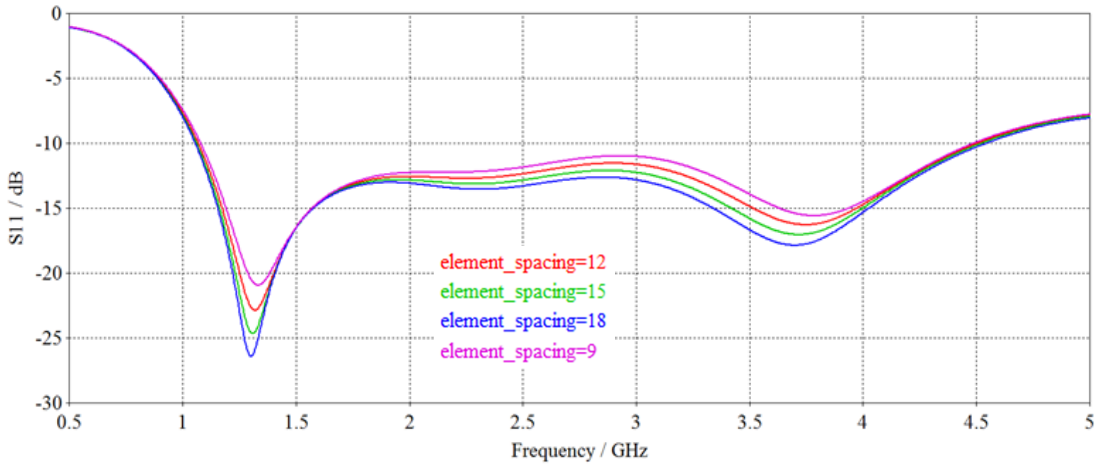

(a) S_{11} plot

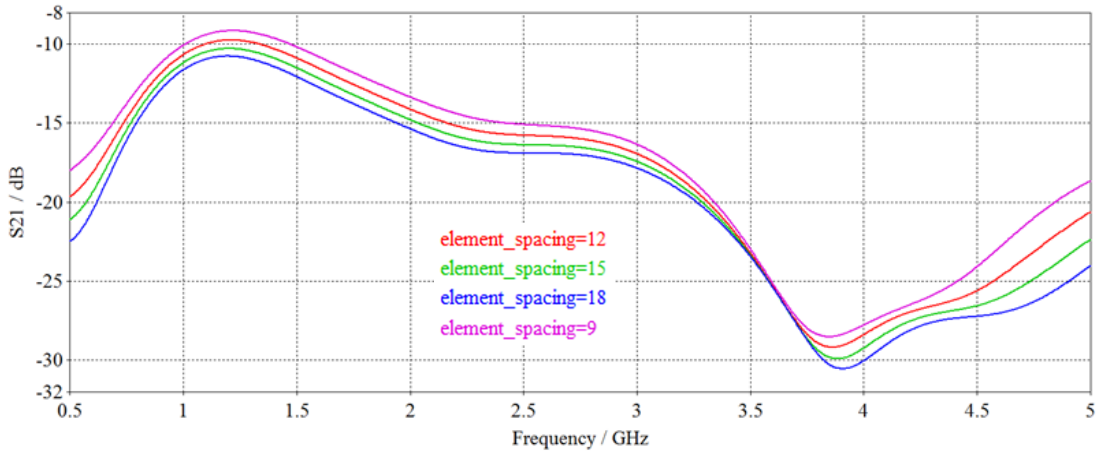

(b) S_{21} plot

Figure 3.23 Parametric analysis of element spacing

3.2.2.3.2 Taper Angle Variation

The simulated results for various taper angles (20°, 35°, 50° and 65°) are plotted in Figure 3.24. It is noted that when the taper angle is smaller than 65°, the simulated S_{11} varies as the taper angle changes while there is no significant variation for the S_{21}. The largest operating bandwidth with relatively low reflection coefficient can be obtained at an optimal taper angle of 35°.

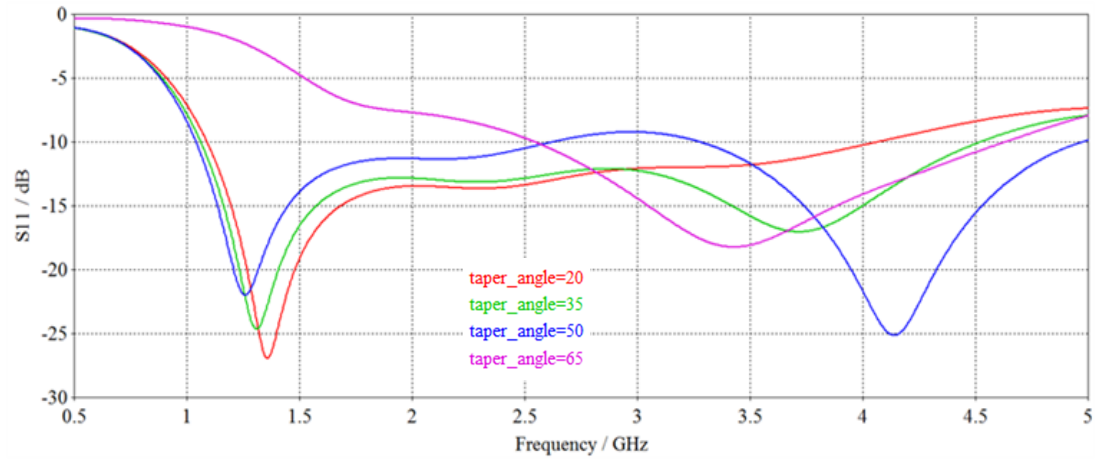

(a) S_{11} plot

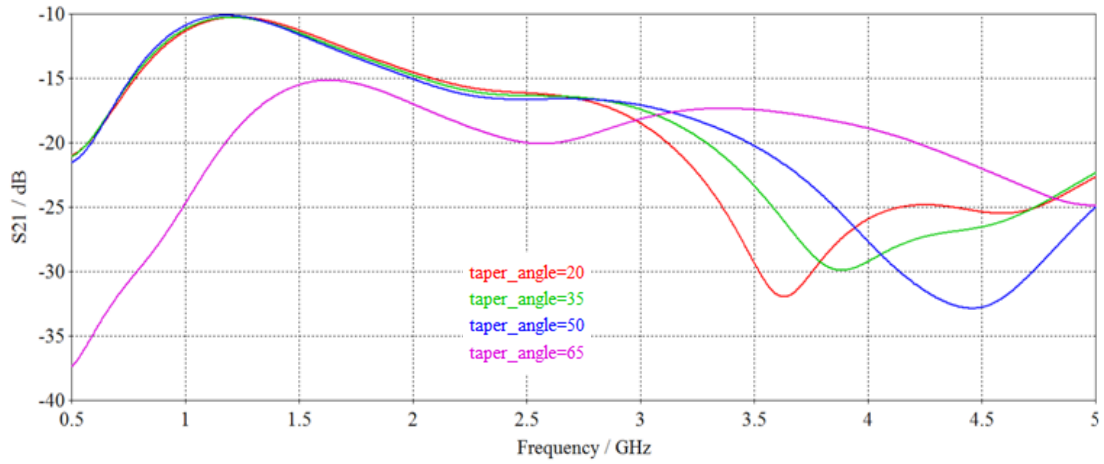

(b) S_{21} plot

Figure 3.24 Parametric analysis of taper angle

3.2.2.3.3 Feed Gap Variation

Another parameter that is studied is the feed gap between the radiating patch and the ground plane. The S-parameter variations due to the change of feed gap are demonstrated in Figure 3.25. Four different values of feed gap, 2 mm, 5 mm, 8 mm and 11 mm are investigated. With the change of the feed gap, notable variations can be observed in the S_{11} plot. An optimal value of 5 mm is selected for the feed gap based on the parametric analysis results.

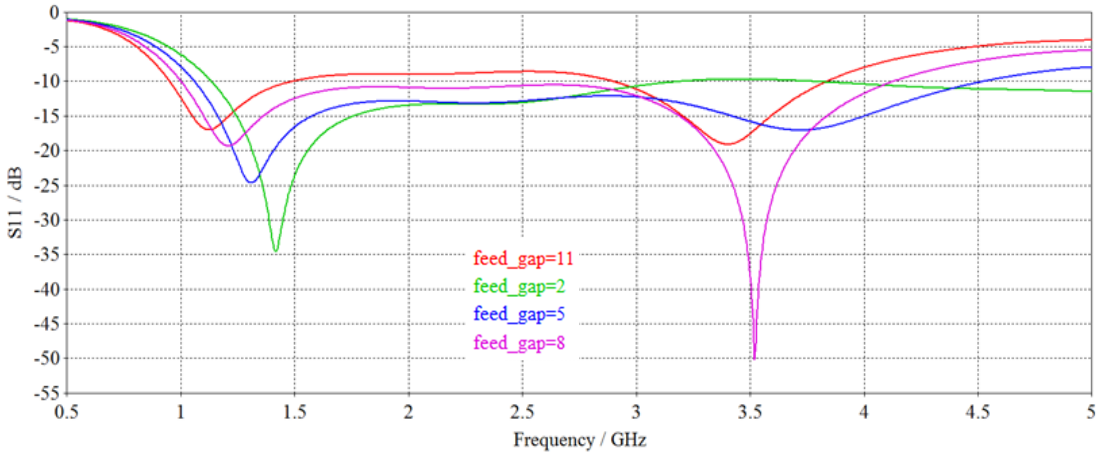

(a) S_{11} plot

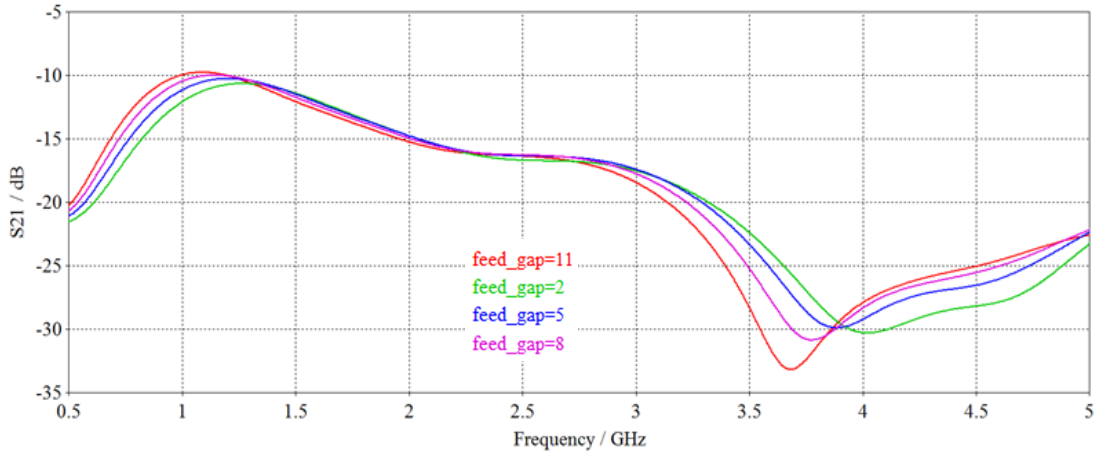

(b) S_{21} plot

Figure 3.25 Parametric analysis of feed gap

3.2.2.3.4 Slot Width Variation

Finally, the width of the slot on the radiating patch is analysed. It can be noticed that the slot width has more significant effect on the radiation performance at higher frequencies than lower frequencies. The operating bandwidth increases as the slot width decreases. In our case the width of the slot on the radiating patch is decided to be 20 mm.

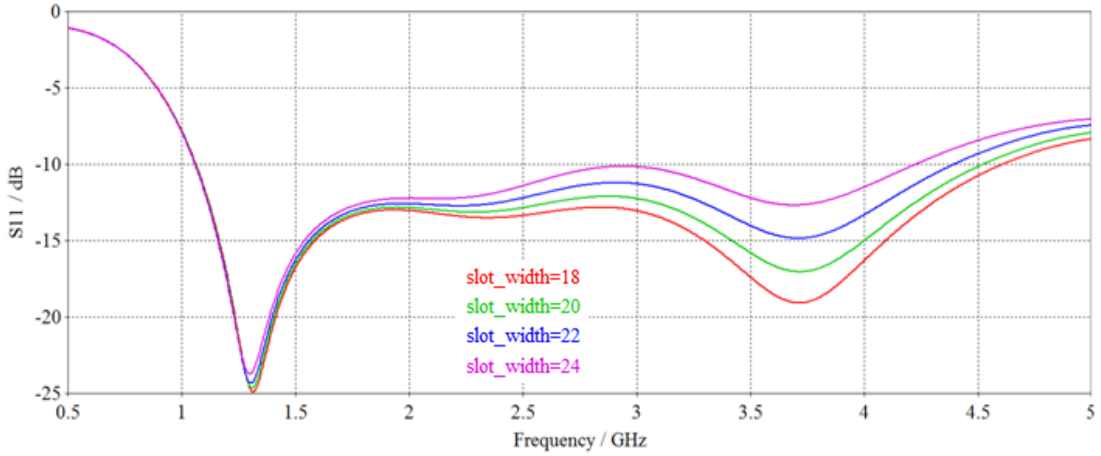

(a) S_{11} plot

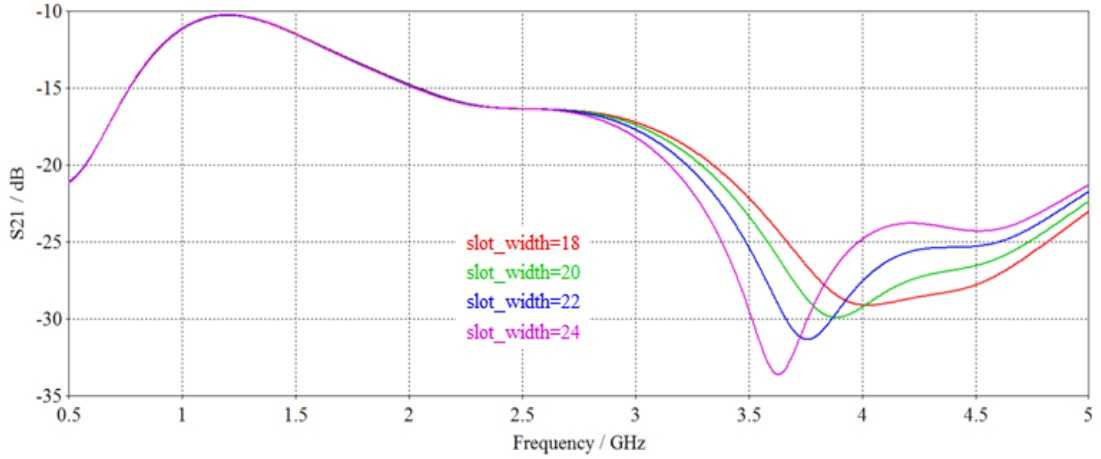

(b) S_{21} plot

Figure 3.26 Parametric analysis of slot width

3.2.2.4 Measurement Results

Figure 3.27 shows the fabricated dual antenna array. The measured reflection coefficient and mutual coupling of the dual array are plotted in Figure 3.28 and Figure 3.29. Compared with the simulated S-parameters in Figure 3.20, a good consistency between the measured and simulated results is revealed. The measured bandwidth with both S_{11} and S_{21} lower than -10 dB is 3.25 GHz, from 1.15 GHz to 4.4 GHz.

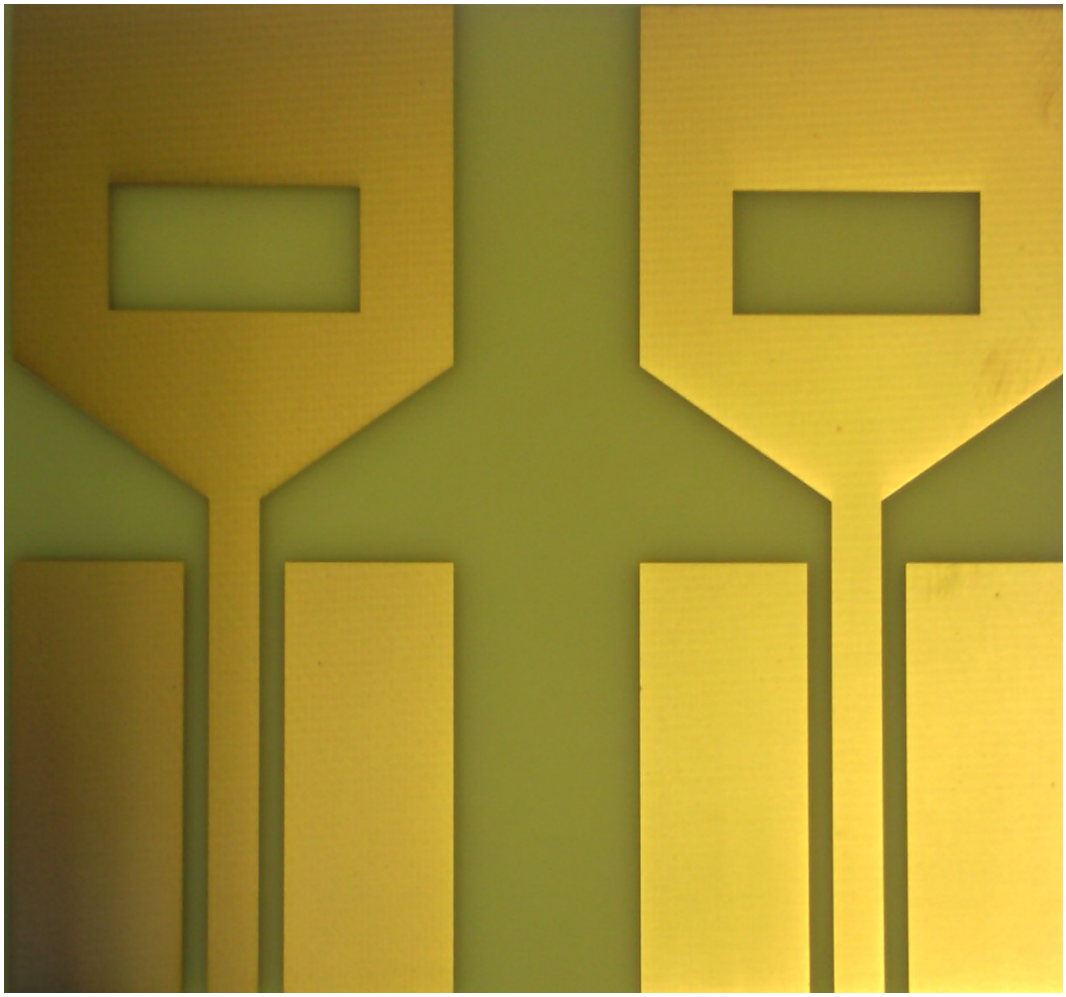

Figure 3.27 UWB dual antenna array fabrication

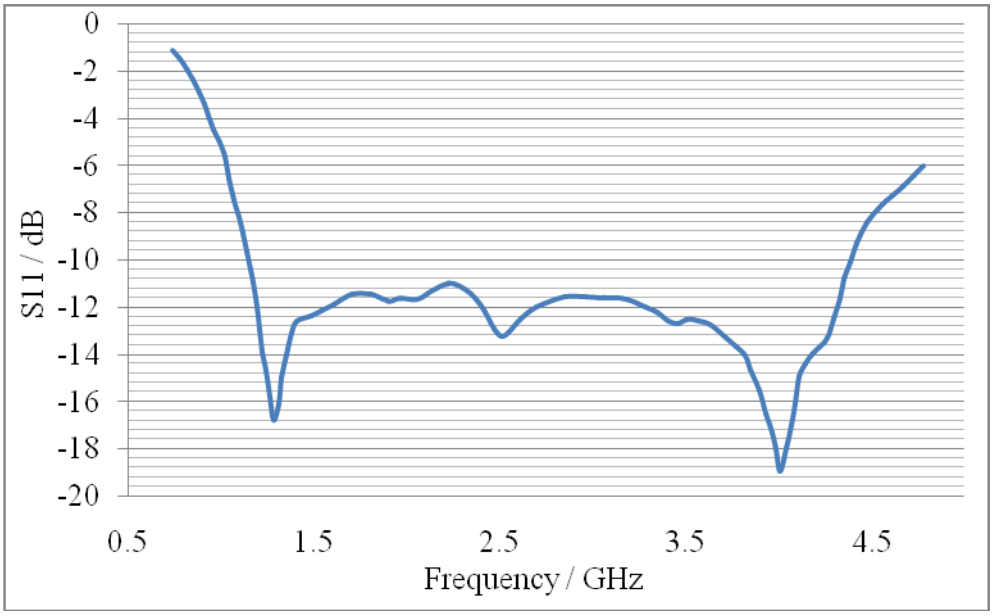

Figure 3.28 Measured reflection coefficient of the dual-antenna array

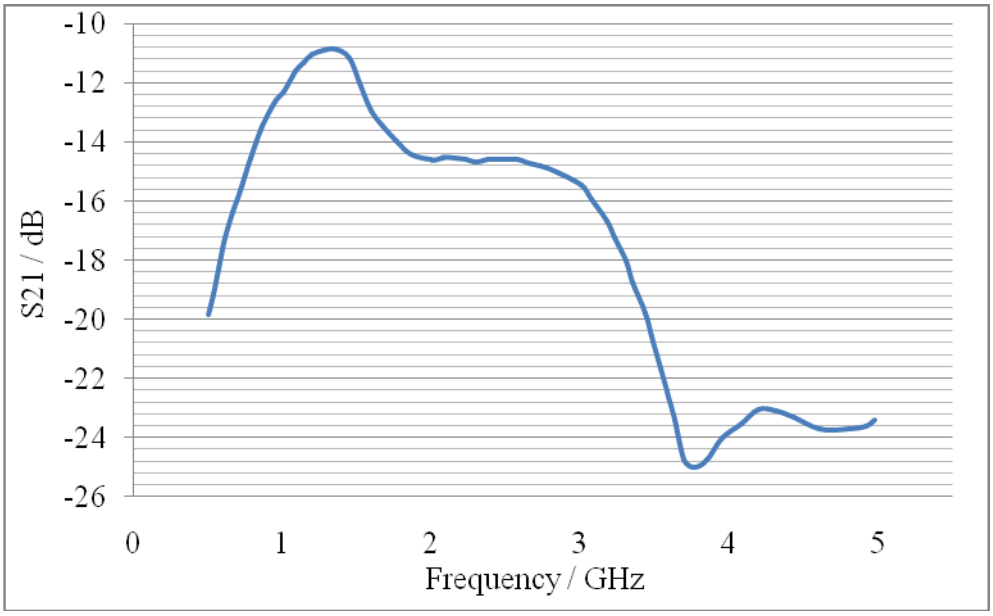

Figure 3.29 Measured mutual coupling of the dual-antenna array

3.3 Summary

In this chapter, firstly, a new UWB microstrip antenna configuration with coplanar waveguide feeding has been presented for wideband RF energy scavenging. The proposed antenna is printed on a thin FR4 substrate of 0.2 mm for easy integration. Etched slot, bevelled edge and partial ground plane are adopted in the design to achieve bandwidth enhancement. According to the measurement results, the antenna has its operating bandwidth covering 1.1 GHz to 5.1 GHz with maximum efficiency reaching 82%. The investigation of the UWB antenna design is demonstrated in Figure 3.30.

Secondly, a dual-antenna array utilising the unit antenna has been designed, simulated, optimized and characterised for full wave RF energy scavenging. Dimension of the slot on the radiating patch is modified for wider bandwidth. An optimized element spacing of 15 mm is selected. Measured reflection coefficient and mutual coupling closely correlate with those obtained from design simulations. The proposed array has its operation in the frequency range from 1.15 GHz to 4.4 GHz, which covers the frequency bands for DCS, PCS, UMTS, Bluetooth, Wi-Fi, WLAN, WiMAX, HIPERLAN and LTE applications.

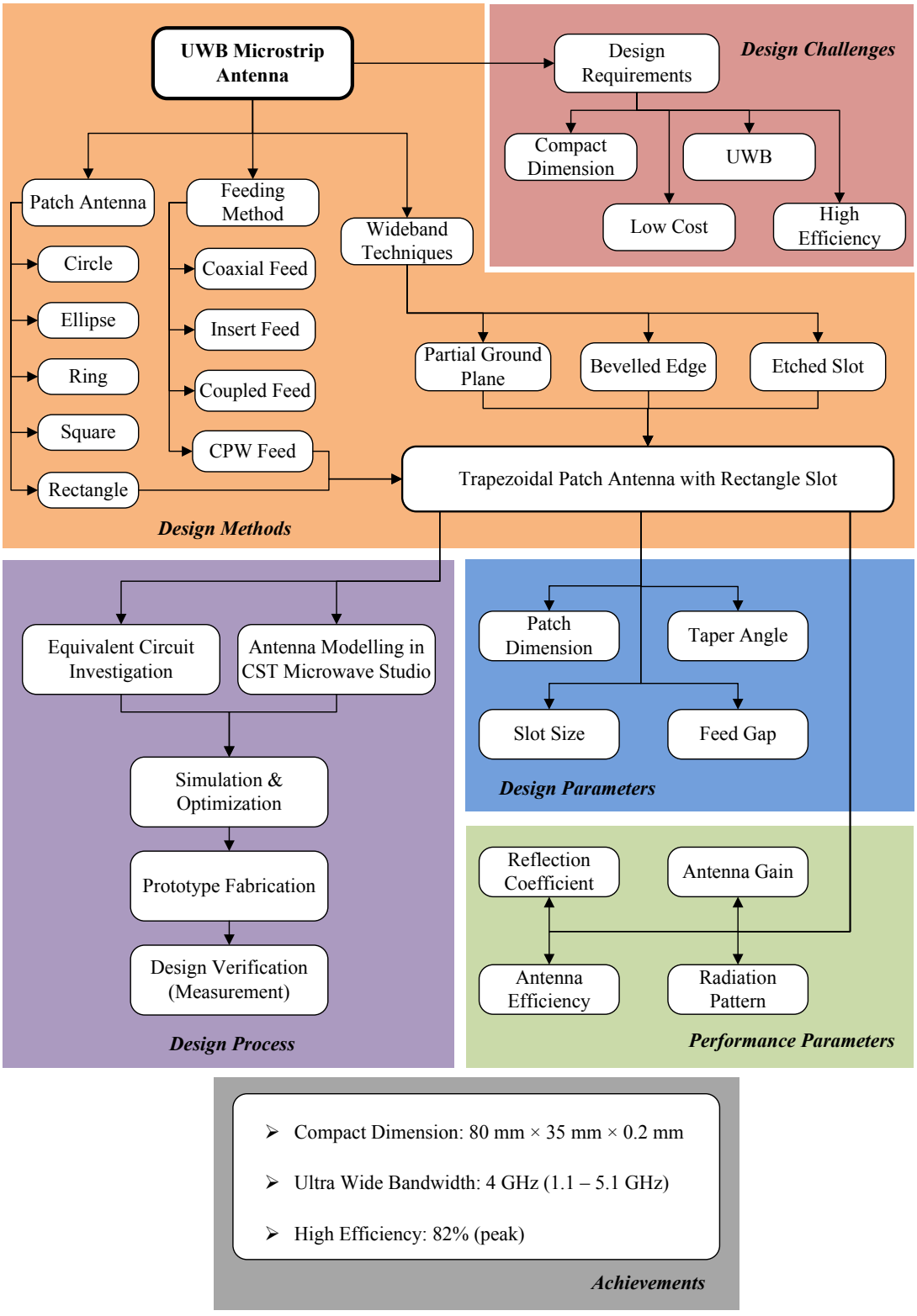

Figure 3.30 The investigation of the UWB microstrip antenna for RF energy scavenging

Chapter 4

Multi-Band PIFA for RF Energy Scavenging

In order to explore the potential for RF energy scavenging and quantify input RF power density levels in urban and semi-urban environment, a citywide RF spectral survey from outside all of the 270 London underground stations was undertaken within ultrahigh frequency range (0.3 GHz to 3 GHz) in the year 2013 [1]. Figure 4.1 demonstrates measurement results from one of the underground stations at street level, where maximum RF power density is identified at spectral bands for GSM 900 and GSM 1800. In the first part of this chapter we introduce a dual-band Planar Inverted-F Antenna (PIFA) printed on 1.6 mm – thick FR4 substrate for scavenging RF energy from ambient GSM 900 (downlink: 935-960MHz) and GSM 1800 (downlink: 1805-1880MHz) signals. Frequency band of GSM 900 is widely used for RF energy scavenging since RF power at this frequency is transmitted more efficiently for longer distance with lower propagation loss compared with higher frequency bands (i.e., 2.4 GHz). On the other hand, GSM 1800 frequency band is also a good choice for RF energy scavenging due to its widespread use in wireless communication (i.e. DCS, LTE application). Although free space path loss (L_p) of 1800 MHz is quadrupled with respect to 900 MHz, its ICNIRP (International Commission on Non-Ionizing Radiation Protection) exposure limit is doubled [84]. Moreover, the actual exposure level of GSM 900 is well below the

ICNIRP exposure limit. Hence, we can expect similar power density level for GSM 1800 MHz, as validated by the survey within Greater London [1]. This is also justified by measurements carried out in UK [85] and in Austria [86] for a mix of GSM-900/1800 base stations.

If we refer to the Wi-Fi 2.4 GHz band, a Wi-Fi router transmit much less power than a GSM base station [87]. But due to the fact that a router is confined to indoor environment, the transmission distance would be much shorter, which results in reduced path loss. This helps to achieve suitable levels of power density. In [65] an ambient Wi-Fi energy harvesting system was demonstrated to generate enough power to drive temperature and humidity meter with LCD display. In the second part of this chapter, the dual-band PIFA is modified and a new triple-band PIFA on standard 0.8 mm – thick FR4 substrate covering GSM 900, GSM 1800 and Wi-Fi 2.4 is proposed for multi-band RF energy scavenging.

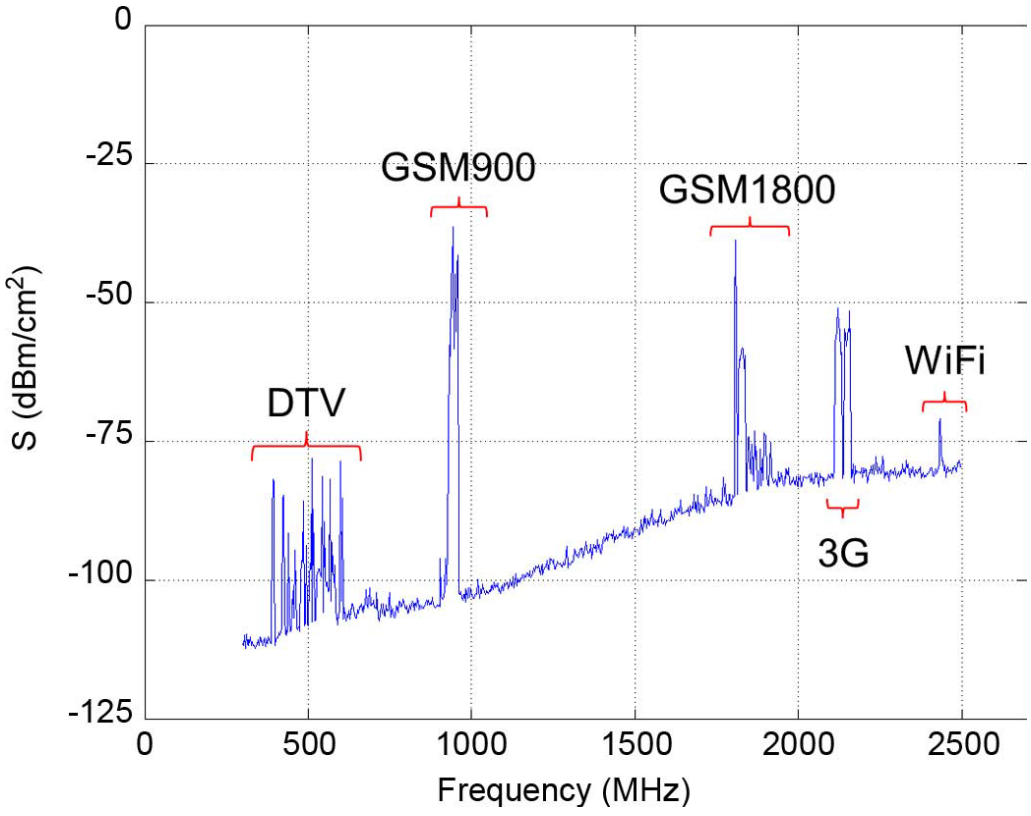

Figure 4.1 Input RF power density measurements outside the Northfields London Underground station [1] © IEEE

4.1 Introduction to Planar Inverted-F Antenna

4.1.1 Inverted-F Antenna

As shown in Figure 4.2, an Inverted-F Antenna (IFA) typically consists of a rectangular planar element (radiating arm) located above a ground, a shorting pin or plate, and a feeding mechanism for the planar element. The feed is placed from the ground to the radiating arm of the IFA. The radiating arm usually has a length of about a quarter – wavelength. To the left of the feed, the radiating arm is shorted to the ground plane.

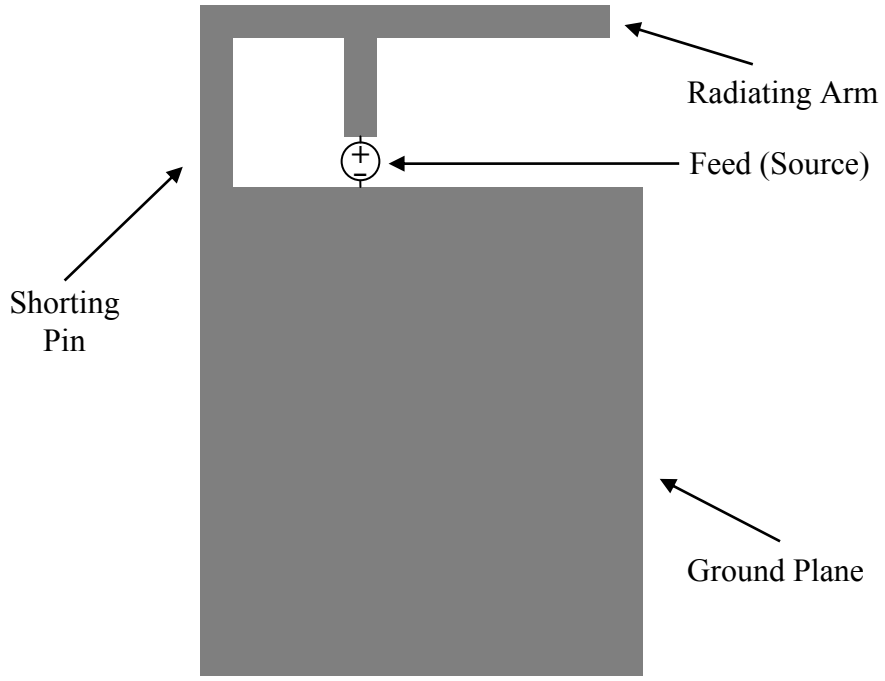

Figure 4.2 A typical Inverted-F Antenna

The IFA is a variant of the monopole where the top radiating section is folded down so as to be parallel with the ground plane. This is done to reduce the height of the antenna while maintaining a resonant trace length. This parallel radiating section with an open end introduces capacitance to the input impedance of the antenna, which is compensated by the inductance provided by the shorting pin.

The ground plane plays a significant role in antenna radiation. Excitation of currents in the upper arm of the IFA causes excitation of currents in the ground plane. The

resulting electromagnetic field is formed by the interaction of the IFA and an image of itself below the ground plane. Its behaviour as a perfect energy reflector is consistent only when the ground plane is infinite. In practice the ground plane are of comparable dimensions to the monopole and act as the other part of a dipole.

4.1.2 Planar Inverted-F Antenna

Planar Inverted-F Antenna (PIFA) can be considered as a kind of linear Inverted-F Antenna (IFA) with the wire radiator element replaced by a plate to increase the bandwidth, as shown in Figure 4.3. The PIFA is resonant at a quarter – wavelength due to the shorting pin or plate at the end. The feed is located between the open and shorted end and its position decides the input impedance.

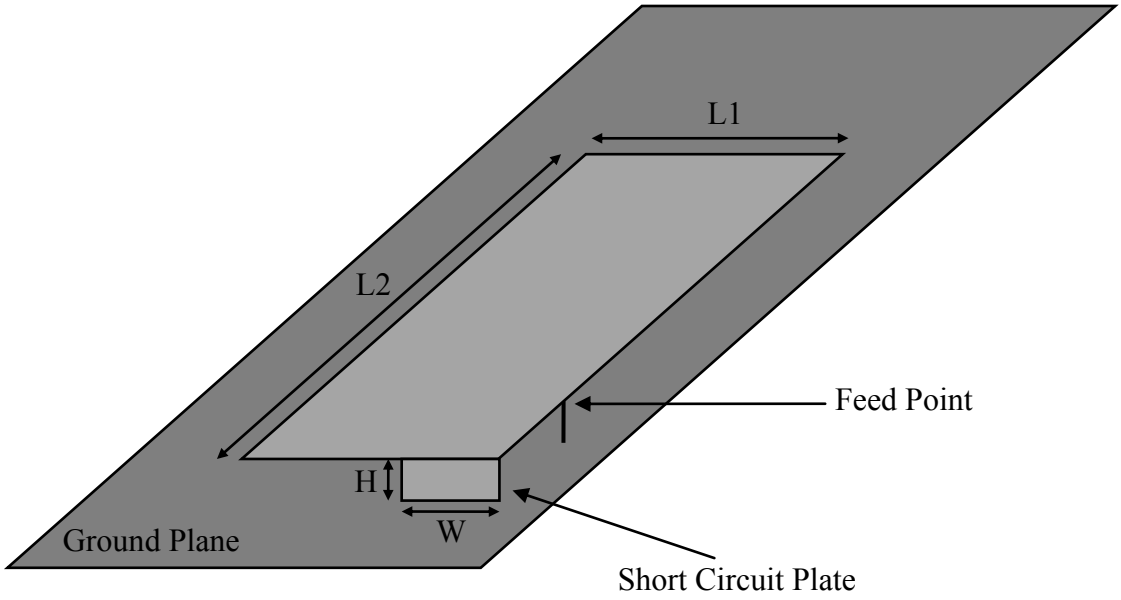

Figure 4.3 Planar Inverted-F Antenna (PIFA) with a shorting plate

The resonant frequency of the PIFA mainly depends on the width of the shorting plate and the size ratio of the planar element. The effect of these two parameters on the effective length of the current distribution is studied in Figure 4.4. The resonant frequency is reversely proportional to the effective current path length. It can be noticed that when the plate width *W* increases, the effective path length of current flow decreases, resulting in higher resonant frequency. On the other hand, with fixed

W and L_2, the effect current path increases with the value of L_1. This leads to lower resonant frequency.

Numerically, the resonant frequency of the PIFA can be approximated by:

$$f = \frac{c}{4\sqrt{\varepsilon_r}\,(L_1+L_2+H-W)} \tag{4.1}$$

where c is the speed of light, L_1 and L_2 are the dimensions of the radiating plate, W is the width of the shorting plate, H is the height of the PIFA and ε_r is the relative permittivity of the substrate on which the radiating plate is placed.

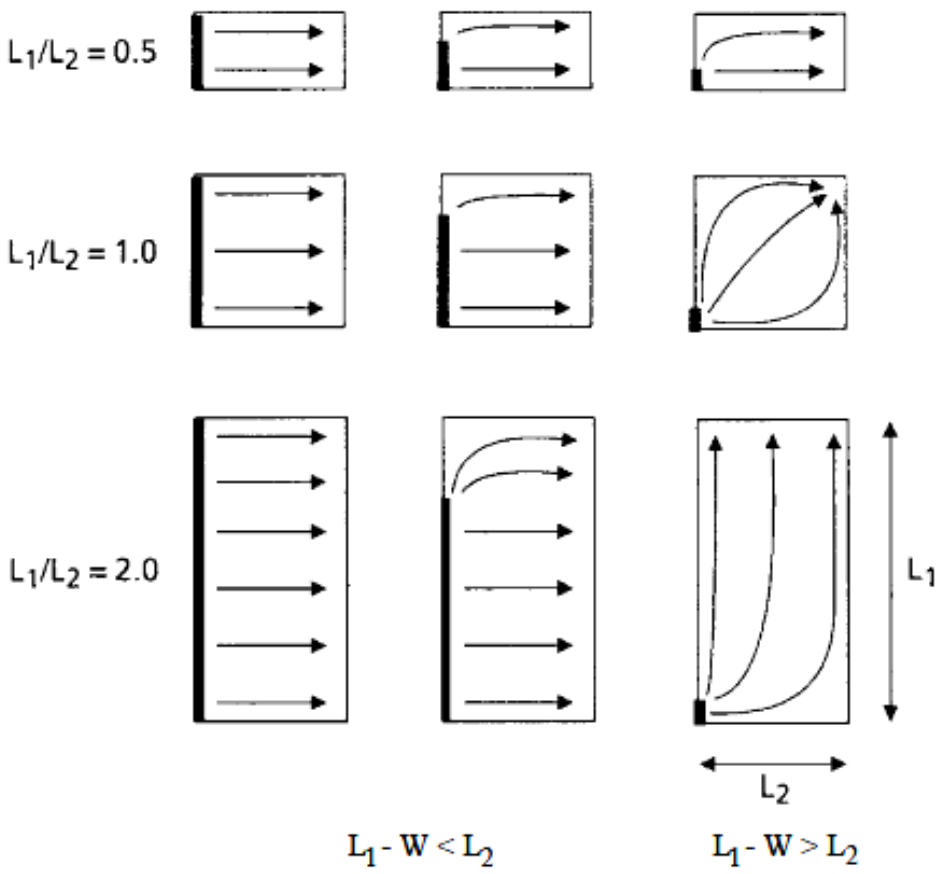

Figure 4.4 Variation of surface current flow underneath the planar element due to size ratio of planar element and width of short-circuit plate [88]

4.2 Dual-Band Planar Inverted-F Antenna

4.2.1 Antenna Structure

Figure 4.5 (a) and (b) illustrate the top view and bottom view of the proposed dual-band PIFA. The PIFA is printed on a 1.6 mm – thick FR4 substrate with relative permittivity of 4.55 and loss tangent of 0.0175. Unlike conventional PIFA designs that require an air gap between substrate and antenna or a very thick substrate to provided expected performance, the proposed antenna is directly printed on a standard substrate. Therefore, the antenna can be easily fabricated at low cost. Moreover, its compact structure makes the antenna more suitable to be integrated in a miniaturized RF energy scavenging system. The total size of the board is 100×40 mm^2, which consists of two areas: ground plane (80×40 mm^2) and no ground area (20×40 mm^2). The radiating antenna with a size of 15×40 mm^2 is located in the no ground area. There is a feed gap of 5 mm from the ground plane of PCB to the radiating patch. Detailed geometry of the radiating antenna is presented in Figure 4.6. The positions of feeding point and shorting pin are indicated using dotted and solid circles, respectively. The shorting pin with radius of 0.4 mm is used to connect between the ground region and the radiating antenna through a via hole.

The proposed PIFA can be thought of as a combination of inverted-F antenna (IFA) and short-circuit microstrip antenna (SC-MSA). In the design, width of the shorting plate is reduced to minimum (shorting pin) so that the resonant frequency becomes lower than that of a conventional short-circuit MSA having the same sized planar element. There is a bended metal strip across the feed gap to short circuit the radiating patch to the ground plane and the shorting pin is located at the end of the metal strip. The bended metal strip has a length of about 20 mm and a width of 1 mm. It behaves like a simple shorting strip loaded with a chip inductor. The bended metal strip is hence considered as an inductive shorting strip here. By incorporating the use of the inductive shorting strip, a wide operating band to cover the frequency range for GSM 900 operation can be generated. Although there are significant effects of the inductive shorting strip on the antenna's lower band, the resonant frequency of the desired upper band is slightly affected.

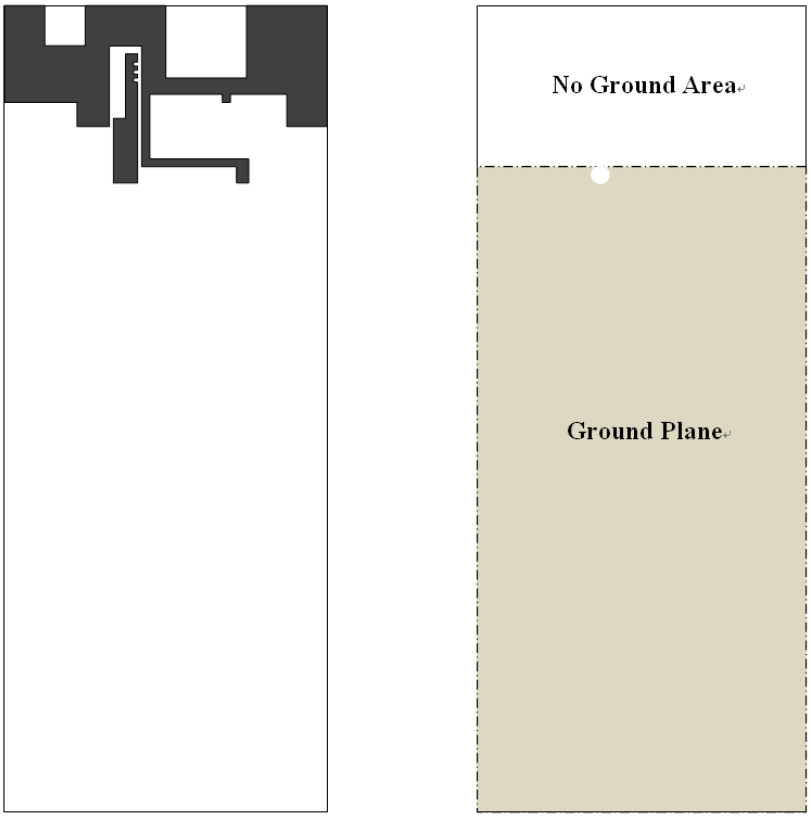

Figure 4.5 Proposed dual-band PIFA: (a) top view, (b) bottom view

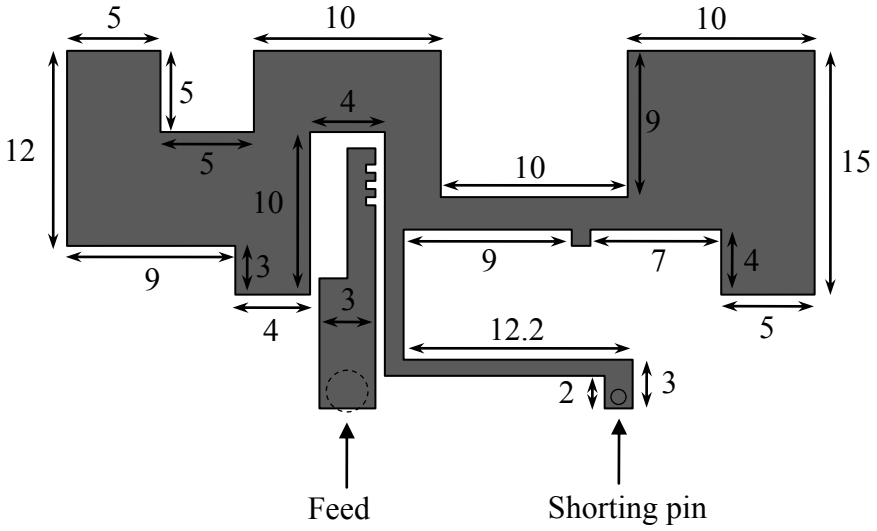

Figure 4.6 Detailed geometry of the proposed dual-band PIFA (unit: mm)

As the effective inductance of the antenna element is increased when the width of the shorting plate is narrower than that of the planar element [89], a coupled feeding line with grooves is applied for inductive compensation. The indirect coupling feed effectively compensates the large inductive reactance introduced by the shorting strip and shorting pin over a wide frequency range so that it helps to improve the antenna bandwidth [90-93].

4.2.2 Simulations and Discussion

Figure 4.7 shows the comparison of the simulated reflection coefficient for the proposed antenna with a coupling feed and a straight shorting pin (type a), the case with a direct feed and a bended shorting strip (type b), and the case with a coupling feed and a straight shorting strip (type c). The corresponding dimensions for the three studied antennas (Figure 4.8) are the same.

Type (a) applies a coupling feed to replace the conventional direct feed used in type (b). From the results of type (a) and type (b), a coupling feed structure affects greatly in the lower and upper frequency ranges. A much wider bandwidth for type (a) than for type (b) is seen.

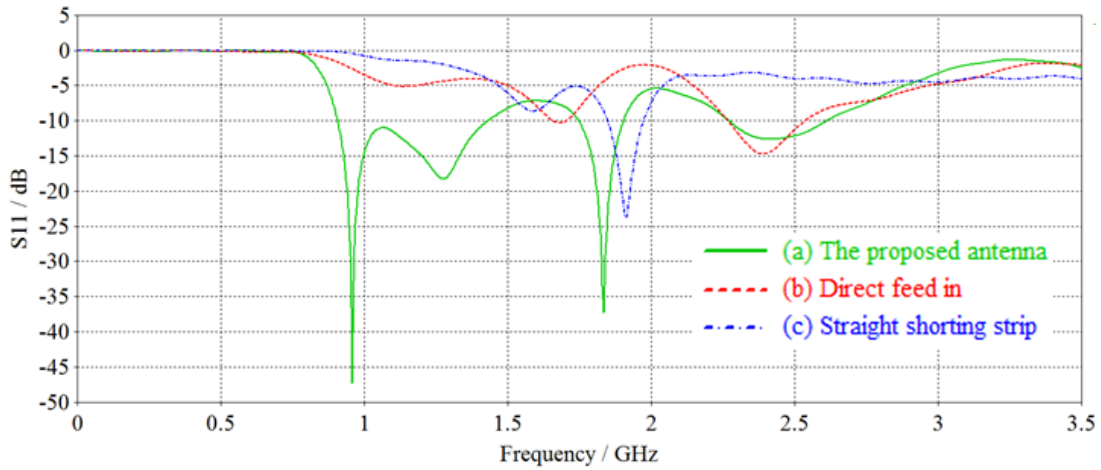

Figure 4.7 Simulated reflection coefficient for the proposed antenna, the corresponding antenna with a direct feed and the corresponding antenna with a straight shorting strip

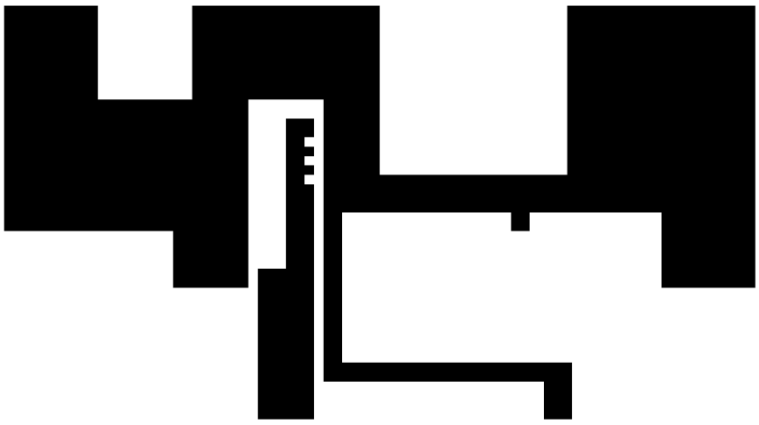

(a) The proposed antenna with a coupling feed and a bended shorting strip

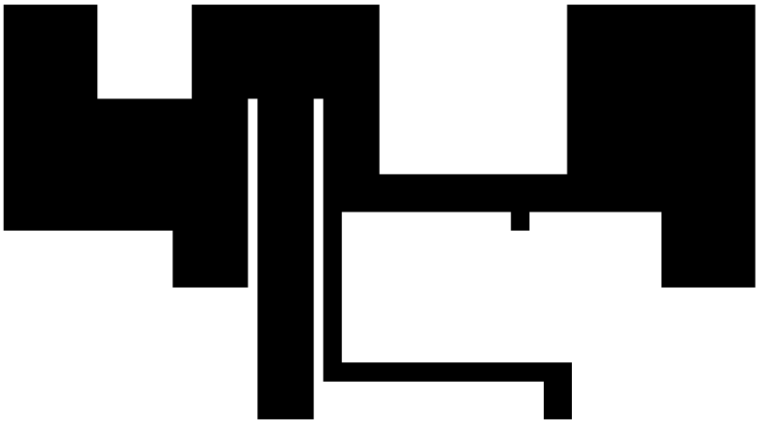

(b) Antenna with a direct feed and a bended shorting strip

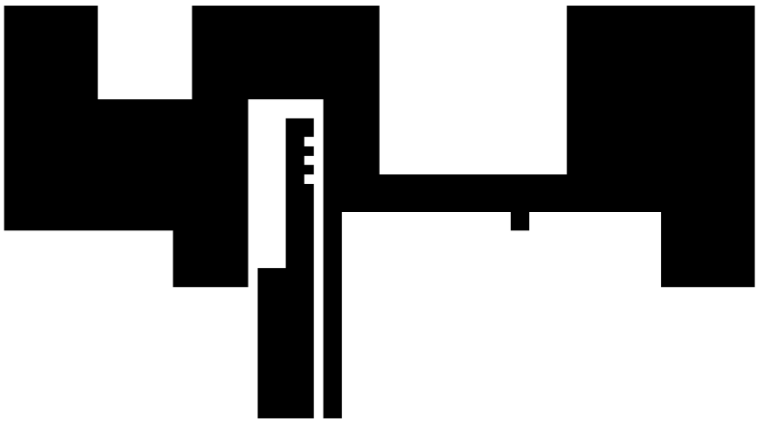

(c) Antenna with a coupling feed and a straight shorting strip

Figure 4.8 (a) the proposed antenna with a coupling feed and a bended shorting strip, (b) antenna with a direct feed and a bended shorting strip, (c) antenna with a coupling feed and a straight shorting strip

From the comparison of reflection coefficient between type (a) and type (c) in Figure 4.7, the shorting strip has a dominant effect on the lower frequency range. A lower band centred at about 900 MHz is generated for the proposed antenna. This is owing to the use of the bended shorting striping that replaces the straight shorting strip in type (c). The bended shorting strip causes the lengthening of the effective resonant path of the antenna, which not only generates a new additional resonant mode at lower band around 900 MHz, but also shifts the 1.9 GHz resonant mode of type (c) to lower frequencies at around 1.8 GHz. It also makes impedance matching easier in the lower and upper bands.

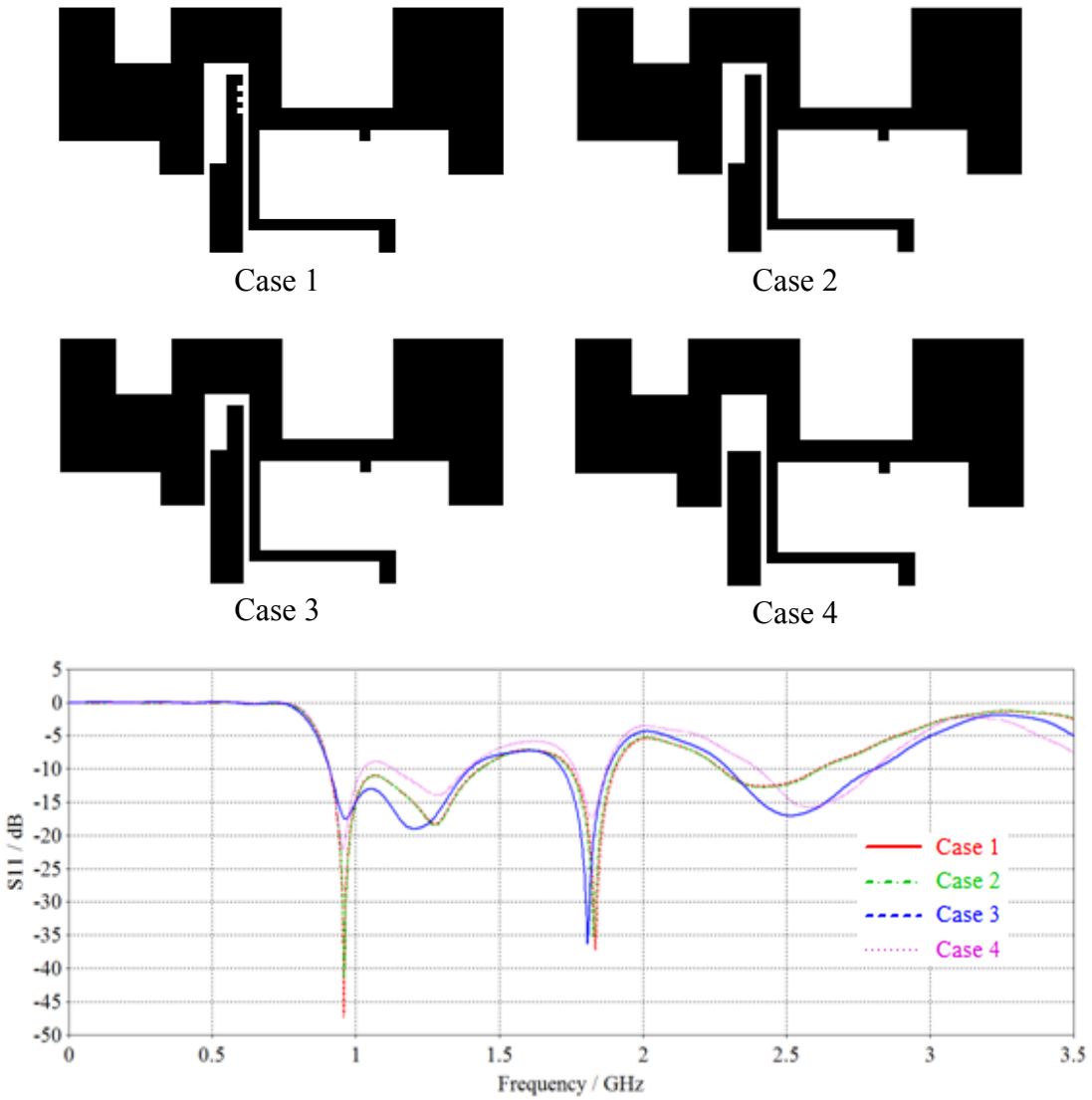

Figure 4.9 Simulated reflection coefficient for antennas with various coupled feeding line structures

Various structures for the coupling feed line are also studied for the proposed dual-band PIFA, as shown in Figure 4.9. It is noted that the feed line structure has no significant effect on the resonant frequencies of the antenna. However, different feed line structures result in different impedance matching condition at the resonant frequencies. The optimised feed line structure with grooves in case 1 is used in our dual-band PIFA design.

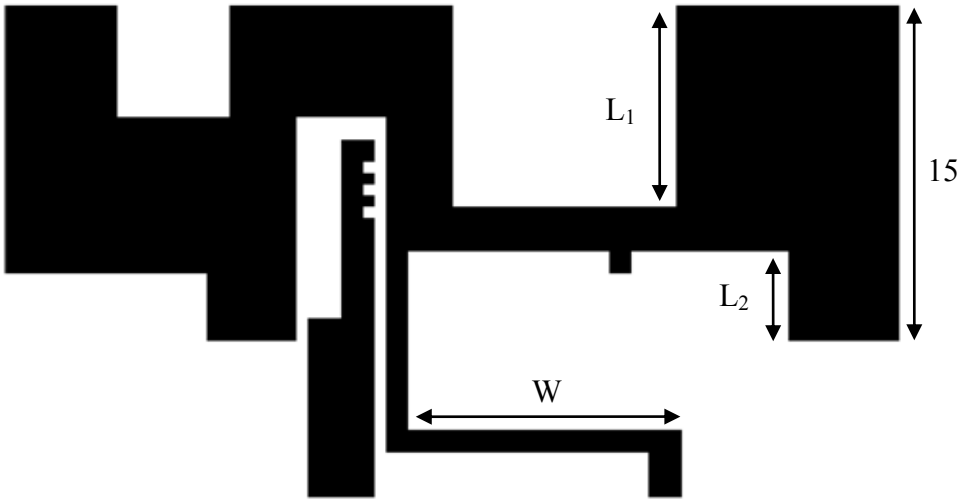

Figure 4.10 Parameters of the PIFA design for analysis

Effects of varying the principle design parameters of L_1 and L_2 (indicated in Figure 4.10) are also studied. The simulated reflection coefficient for L_1 varied from 3 mm to 9 mm and L_2 varied from 2 mm to 5 mm is shown in Figure 4.11 (a) and (b), respectively. Small effects on the antenna's lower band are seen. The operating frequencies of the upper band, however, can be controlled by the length of L_1 and L_2. By increasing the length of L_1 and L_2, the upper band is shifted to lower frequencies. It can be observed from the figures that the increase of L_1 has no effect on the lower frequency band while the lower band is slightly shifted to lower frequencies as the increase of L_2. Nevertheless, the effects of L_2 on the lower band are small compared with those on the upper band. That is, by selecting proper lengths for L_1 and L_2 (9 mm and 4 mm in this study), the upper band can be adjusted to cover the desired frequency range for GSM 1800.

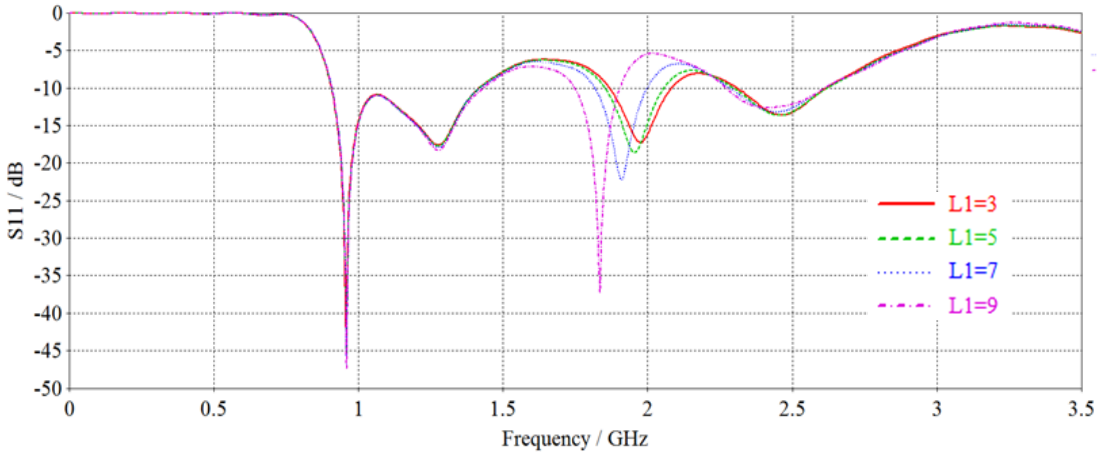

(a) Simulated reflection coefficient for variation of L_1

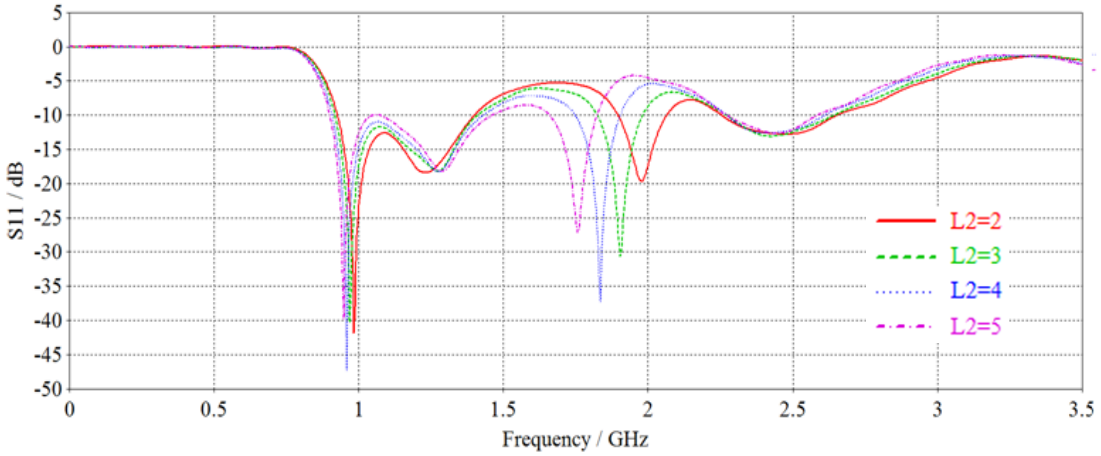

(b) Simulated reflection coefficient for variation of L_2

Figure 4.11 Simulated reflection coefficient as a function of L_1 and L_2

The simulated reflection coefficient for the width W of the bended shorting strip varied from 10 mm to 16 mm is presented in Figure 4.12. Significant effects of the width W on the antenna's lower band are observed. When the width W increases, the lower band is shifted to lower frequencies. However, the obtained bandwidth is decreased. On the other hand, effects of the width W on the upper band are negligible.

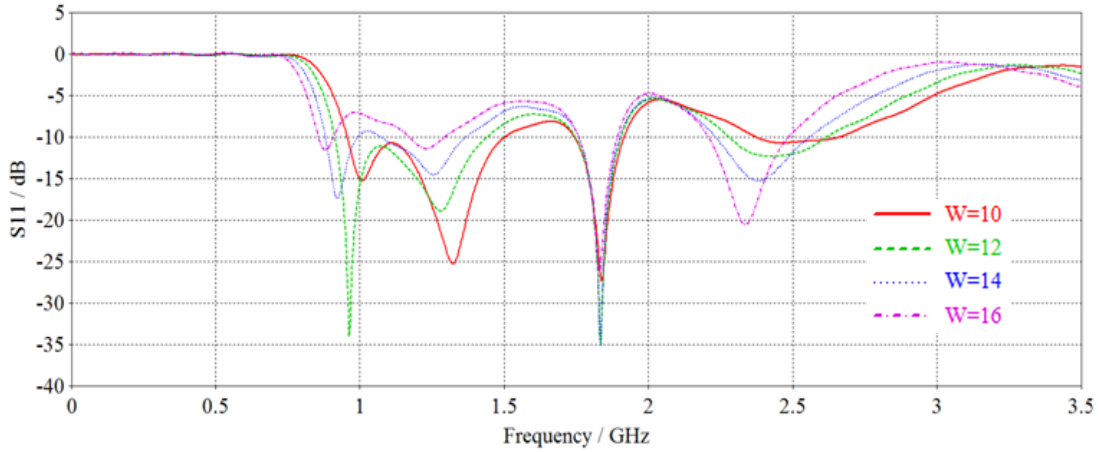

Figure 4.12 Simulated reflection coefficient as a function of the width *W* of the shorting trip

Effects of the ground plane length on the antenna radiation performance are investigated in Figure 4.13. Results of the simulated reflection coefficient for the length varied form 70 mm to 100 mm are shown. The impedance matching at resonant frequencies of both lower band and upper band is strongly affected by the ground plane length. In our design the length of the ground plane is set to be 80 mm for the best impedance matching for spectral bands of both GSM 900 and GSM 1800.

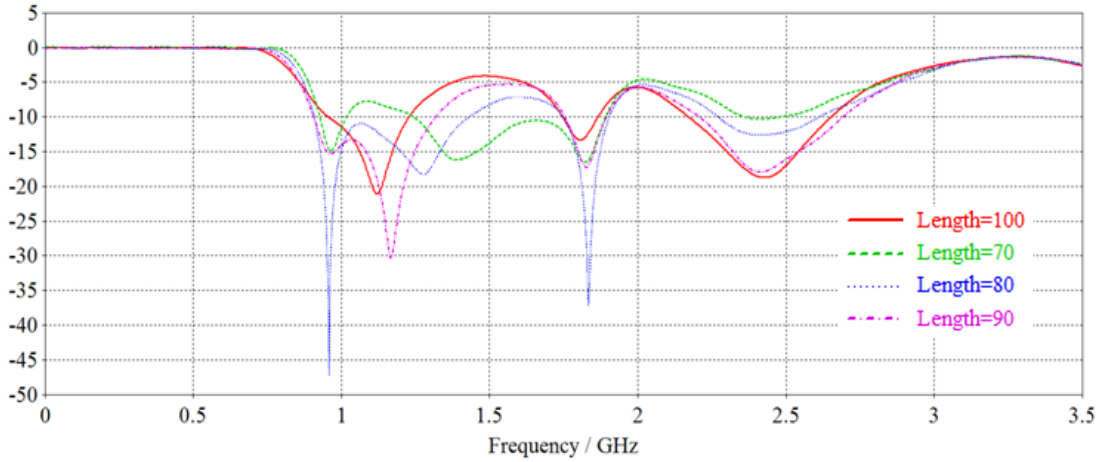

Figure 4.13 Simulated reflection coefficient as a function of the length of the ground plane

4.2.3 Measurement Results

Fabricated prototype of the proposed dual-band PIFA design is presented in Figure 4.14 and the antenna was characterised with an HP8753C vector network analyser (VNA) as shown in Figure 4.15. Figure 4.16 illustrates the measured reflection coefficient which is compared with simulation results using both discrete port and waveguide port in CST microwave studio. In general, the measured and simulated results show good agreement. The discrepancy between measurement and simulation is caused by the simplified feeding to antenna model during simulation. During the simulation of the proposed antenna using waveguide port, the SMA connector is simplified to metal cylinders. The antenna prototype has operation in the frequency bands of 840 – 970 MHz and 1.78 – 1.94 GHz, which covers downlink of both GSM 900 (935-960MHz) and GSM 1800 (1805-1880MHz).

Figure 4.14 Fabricated prototype of the proposed dual-band PIFA

Figure 4.15 HP8753C vector network analyser

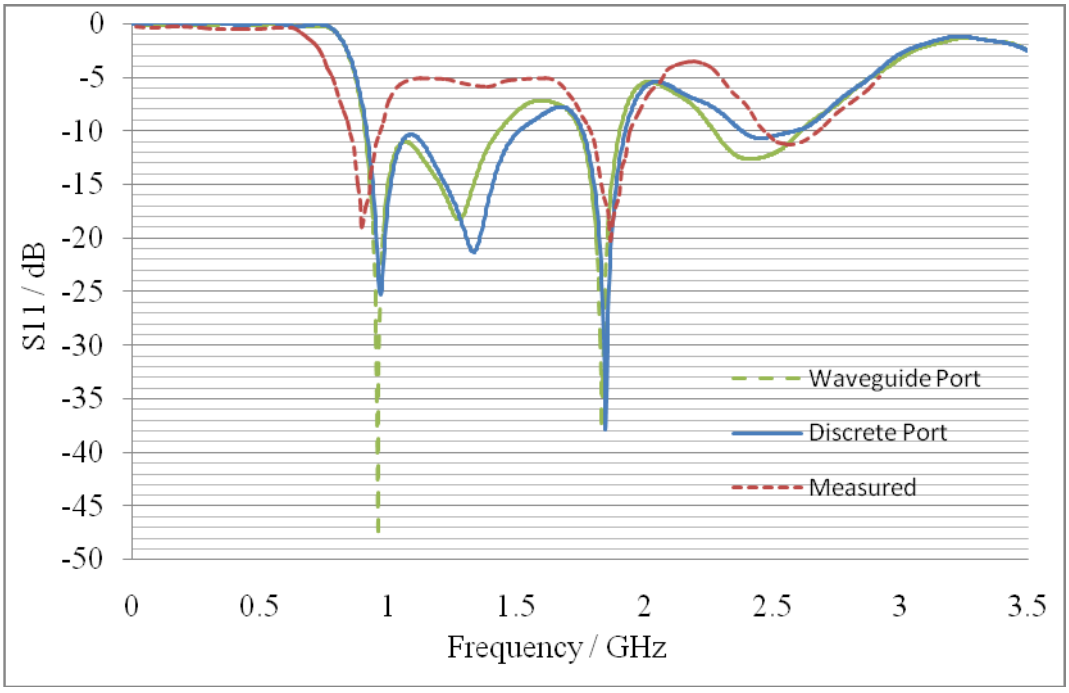

Figure 4.16 Measured and simulated reflection coefficient of the proposed dual-band PIFA

Figure 4.17 illustrates a schematic of the radiation pattern measurement setup. The source antenna and the antenna prototype under test are connected to Port 1 and Port 2 of a network analyser, respectively. To control the azimuth and elevation for the antenna measurement, a computer controlled positioner is used. Data acquisition interface sends the control signal to the position controller to rotate by specific step angle after programmed time interval and acquires the data from the network analyser for each step. The measurements were carried out in an anechoic chamber covered with RF absorbers on the walls, as shown in Figure 4.18.

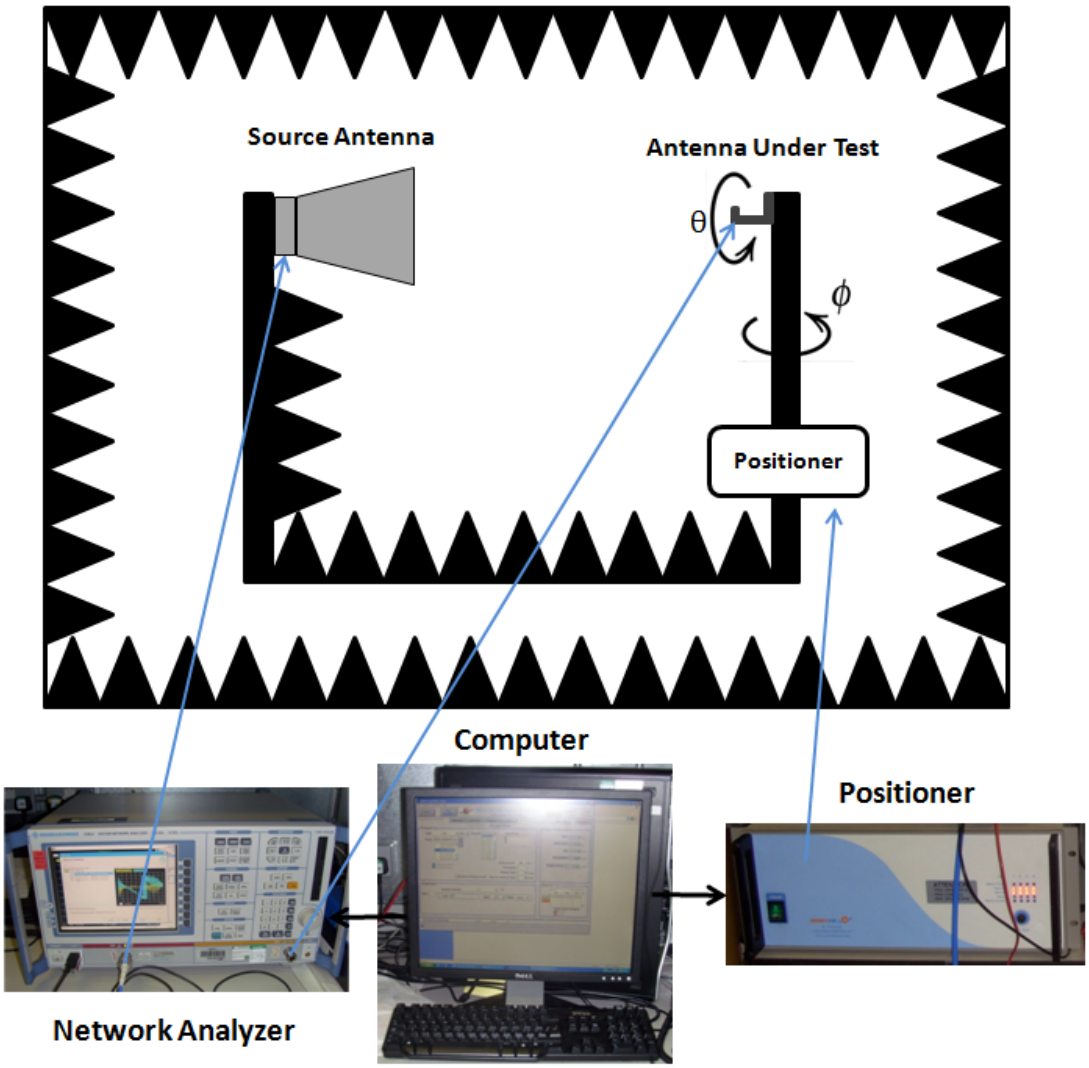

Figure 4.17 Schematic of radiation pattern measurement setup

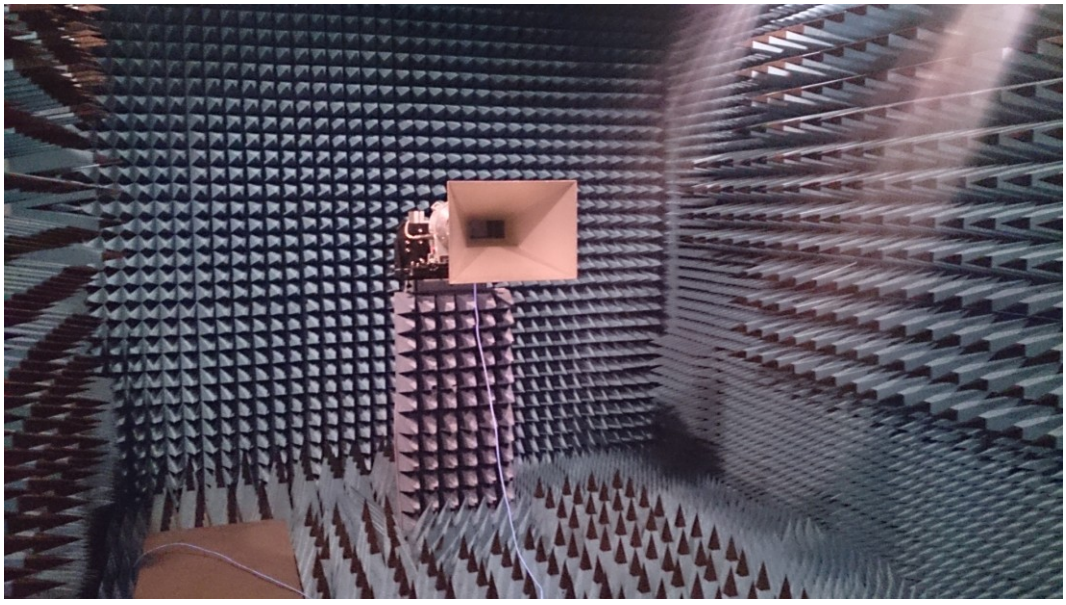

Figure 4.18 Radiation pattern measurement in the anechoic chamber

Measured radiation patterns at typical resonant frequencies of 896 MHz and 1.858 GHz are plotted in Figure 4.19 and Figure 4.20, respectively. At lower frequency of 896 MHz, dipole-like radiation patterns with omni-directional radiation in the azimuth plane (x-z plane) are observed. While at frequency of 1.858 GHz, more variations in the patterns are observed. Also note that measured radiation patterns at other frequencies in the lower and upper bands reveal similar results as those plotted in Figure 4.19 and Figure 4.20. Figure 4.21 illustrates the measured antenna gain and efficiency. Over the 840 – 970 MHz band shown in Figure 4.21 (a), the antenna gain is about 1.6 – 2.3 dBi and the radiation efficiency ranges from about 71% to 86%. As for the 1.77 – 1.94 GHz band in Figure 4.21 (b), the antenna gain is about 3.5 – 4.3 dBi, and the radiation efficiency varies from 73% to 88%.

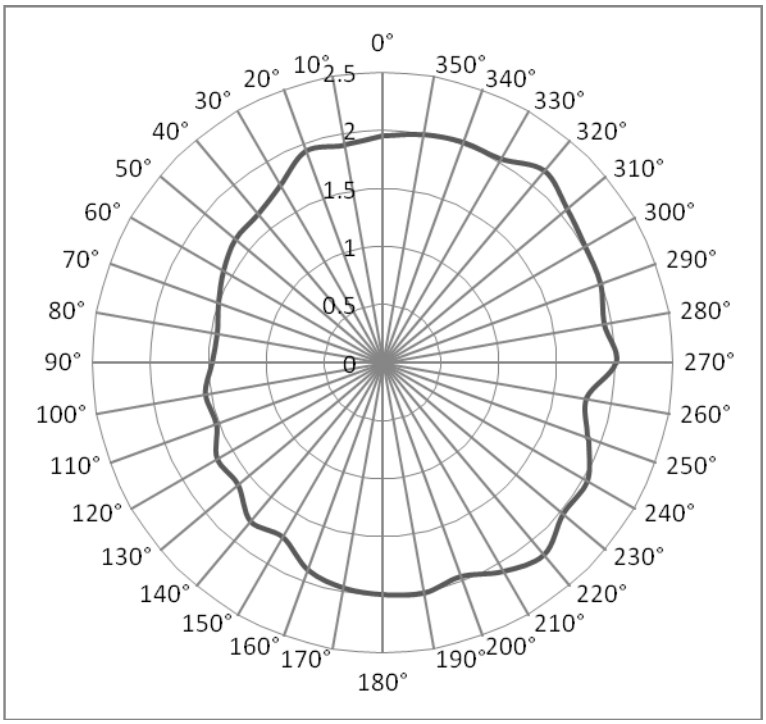

(a) E-Plane

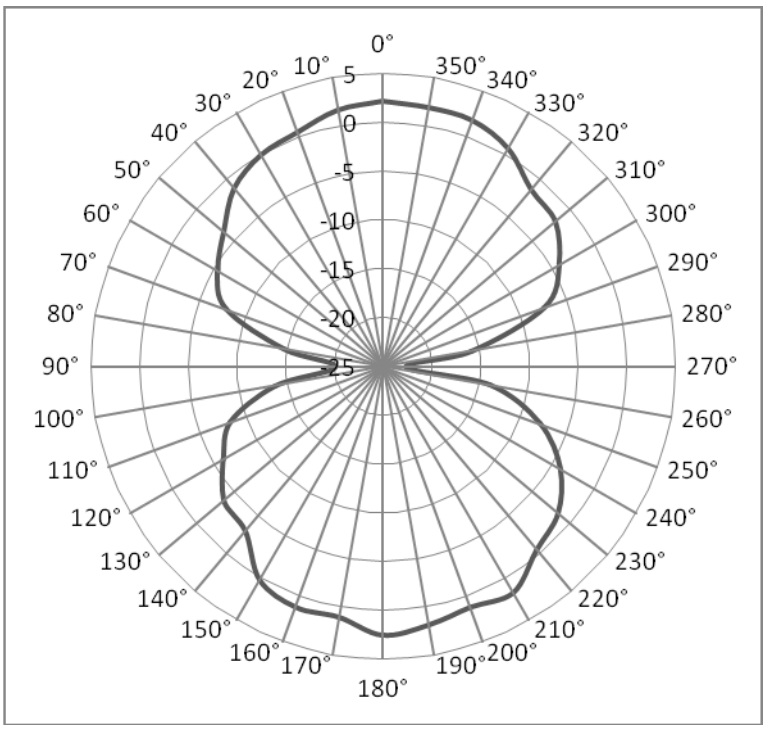

(b) H-Plane

Figure 4.19 Measured radiation patterns at 896 MHz

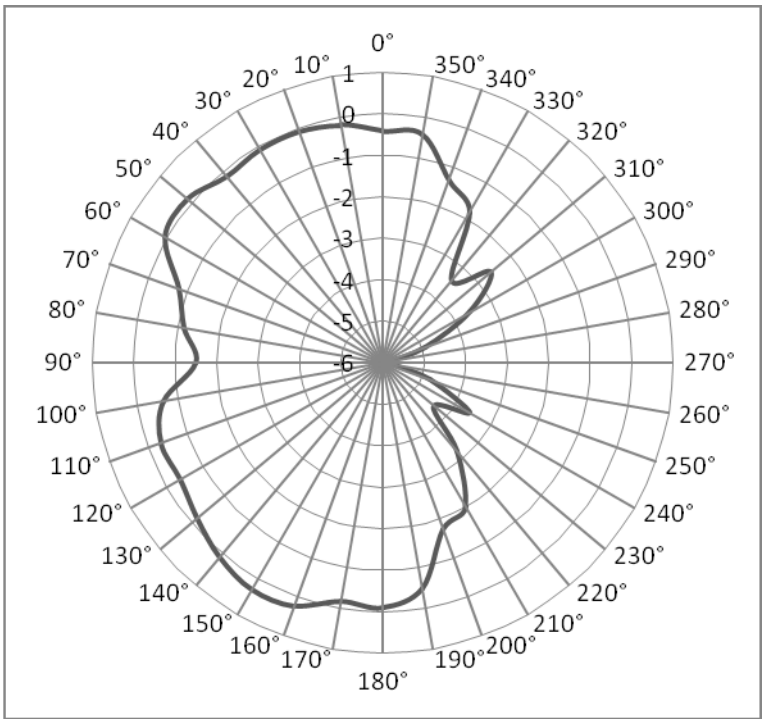

(a) E-Plane

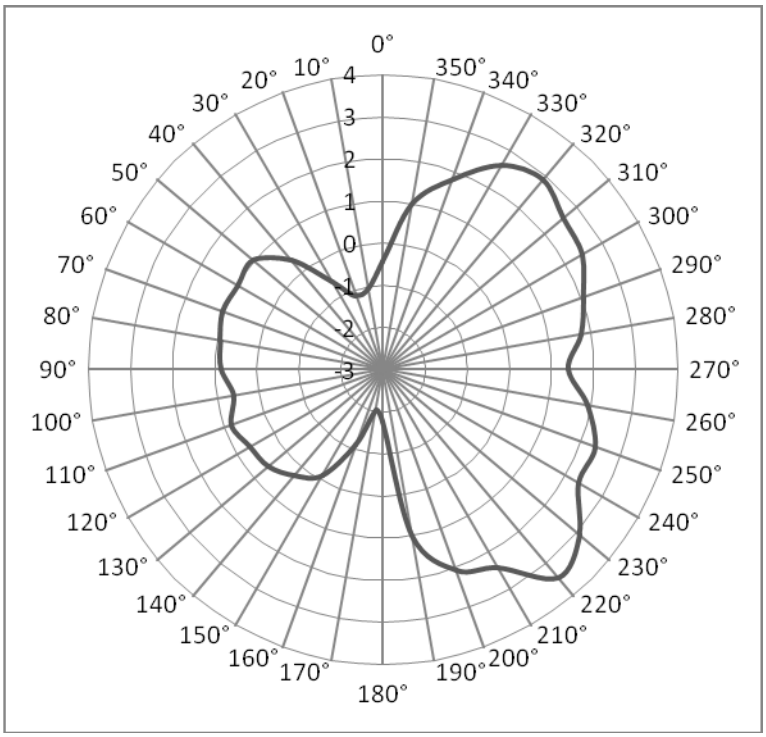

(b) H-Plane

Figure 4.20 Measured radiation patterns at 1.858 GHz

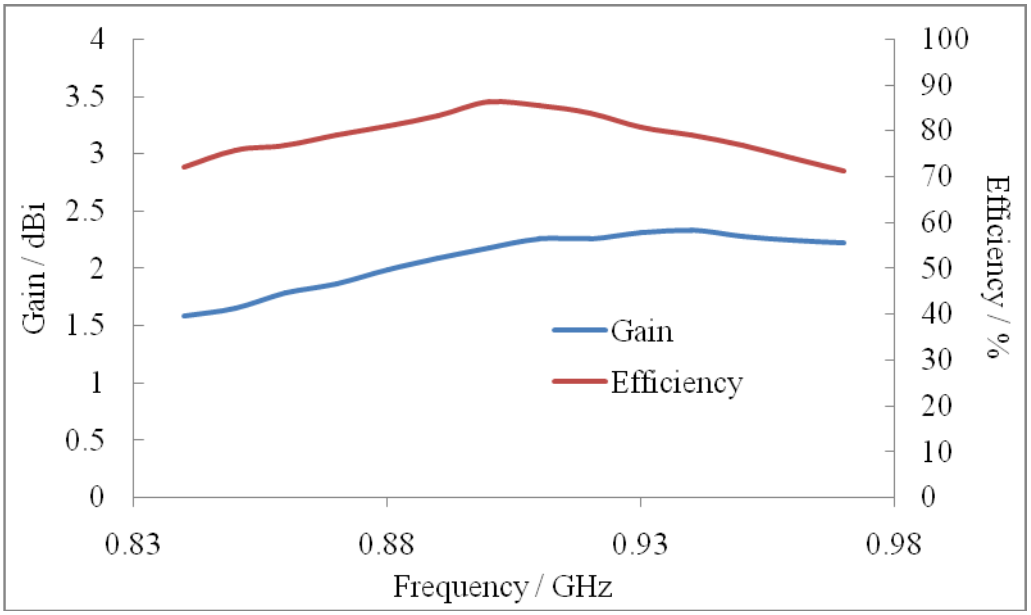

(a)

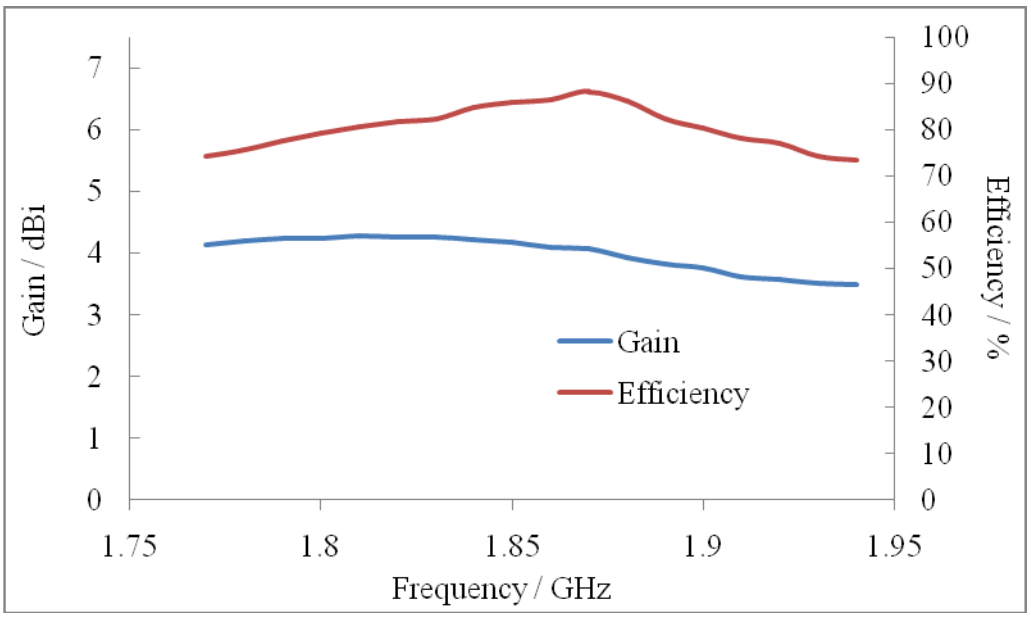

(b)

Figure 4.21 Measured antenna gain and efficiency of the proposed dual-band PIFA: (a) the lower band, (b) the upper band

4.3 Triple-Band Planar Inverted-F Antenna

4.3.1 Antenna Structure

Structure of the proposed triple-band PIFA is demonstrated in Figure 4.22. The radiating antenna has a total size of 15mm × 40mm and resides on a 0.8mm FR4 substrate with relative permittivity $\varepsilon_r \approx 4.5$ and loss tangent $\delta \approx 0.0175$. Although FR4 may experience relatively higher losses compared with other materials, it is the most common and cost effective PCB material.

Same as the dual-band PIFA design, the planar antenna utilizes one metal layer on one side with the ground plane (80×40 mm^2) residing on the other side. Overall dimensions of the board are 100×40 mm^2. Compared with the dual-band PIFA design, as the substrate height of the proposed triple-band PIFA is reduced by half, width of the feeding line is modified from 3 mm to 1.5 mm to maintain 50 Ohm. Meandered shorting strip is applied to obtain resonance at Wi-Fi 2.4 GHz [94]. Detailed dimensions of the proposed triple-band PIFA are presented in Figure 4.23.

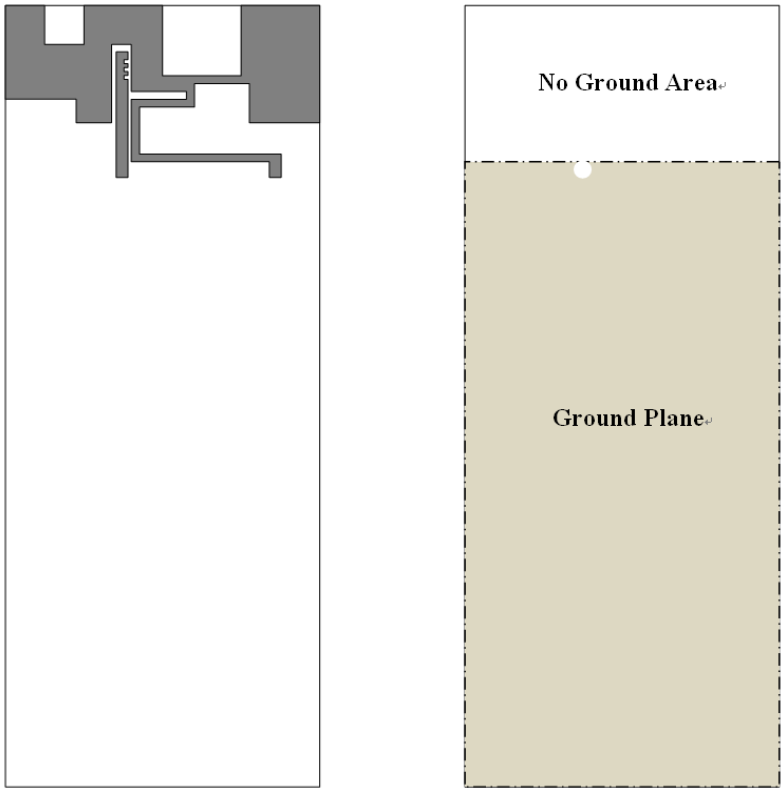

Figure 4.22 Proposed triple-band PIFA

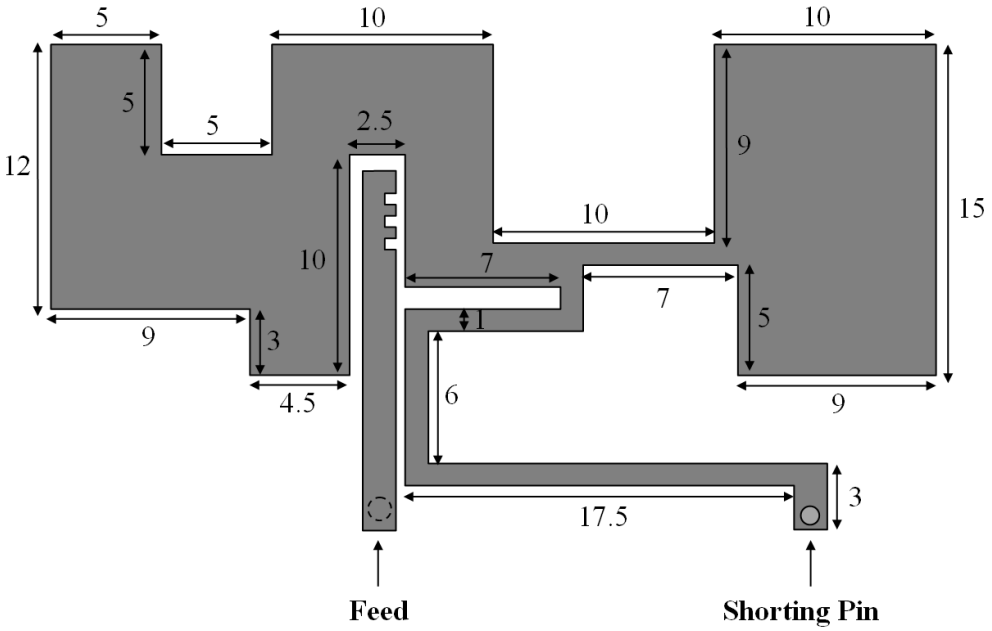

Figure 4.23 Detailed geometry of the proposed triple-band PIFA (unit: mm)

4.3.2 Simulations and Discussion

It can be noticed from the measurement of the dual-band PIFA design in Figure 4.16 that there is a third resonant mode at around 2.6 GHz. To shift it to lower frequencies covering desired Wi-Fi 2.4 GHz band, the shorting strip of the previous designed PIFA is modified. As a result, a well matched resonant frequency at around 2.45 GHz is obtained.

Figure 4.24 demonstrates the comparison of the simulated reflection coefficient for the proposed antenna and the case with a simple bended shorting strip similar to the dual-band antenna design. Owing to the presence of the meandered shorting strip, a third resonant mode at about 2.45 GHz can be observed for the proposed antenna. Compared with the reference antenna, as the length of the shorting strip is increased, the first operating band is shifted to lower frequencies. It can be noticed frequencies of the second resonant mode of the reference antenna is lower than that of the proposed antenna. This is because the reference antenna has longer distance between the shorting position and the right edge of the radiating plate than the proposed antenna. Simulated surface current distribution is presented in Figure 4.25 to illustrate the operation of the proposed antenna.

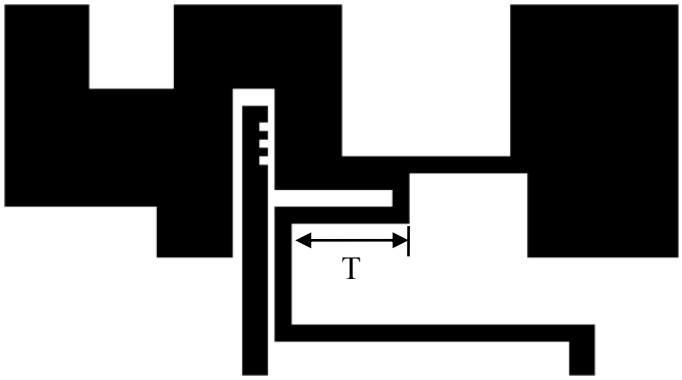

Proposed

(Meandered shorting strip)

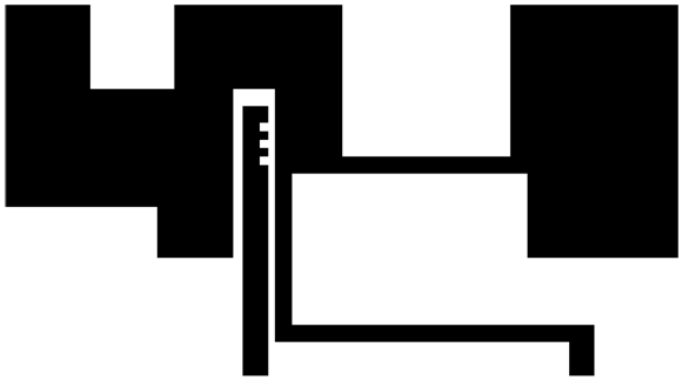

Reference

(Simple bended shorting strip)

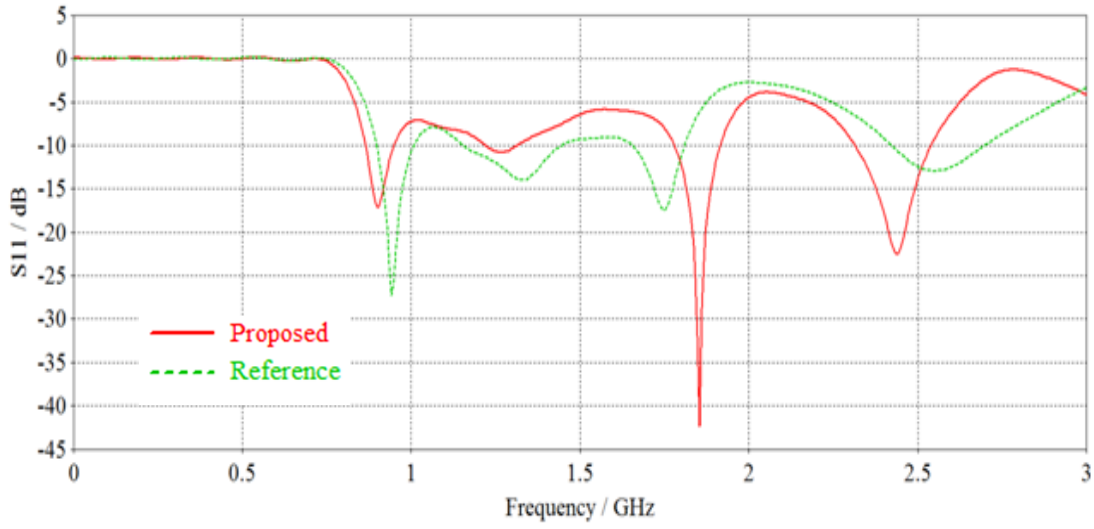

Figure 4.24 Simulated reflection coefficient for the proposed antenna and the corresponding antenna with a simple bended shorting strip (reference)

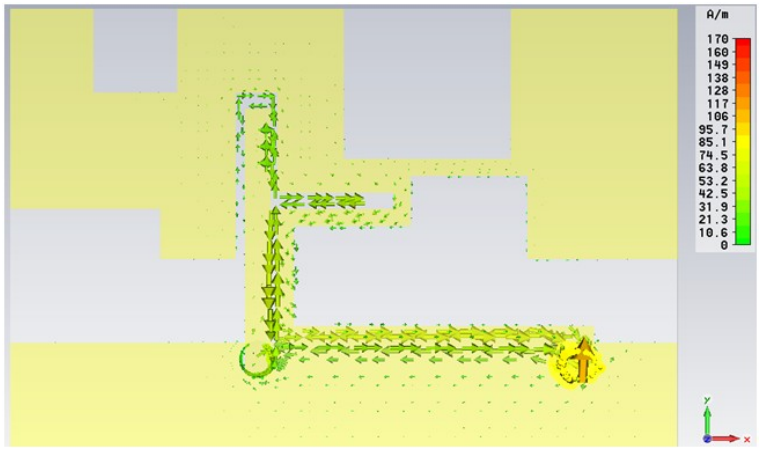

(a) 900 MHz

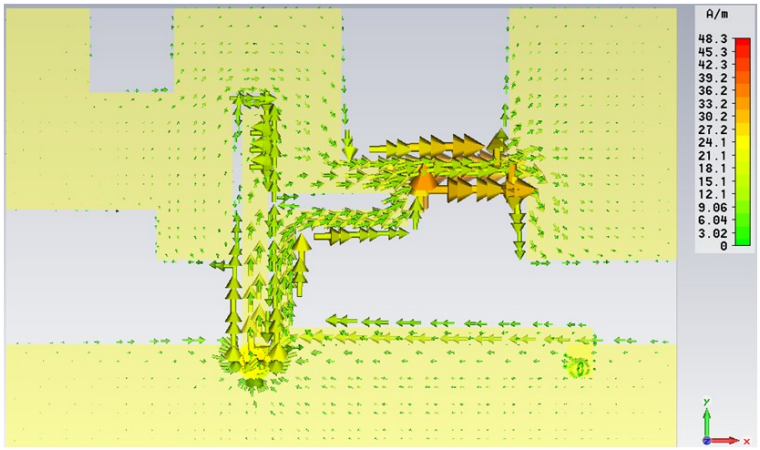

(b) 1.85 GHz

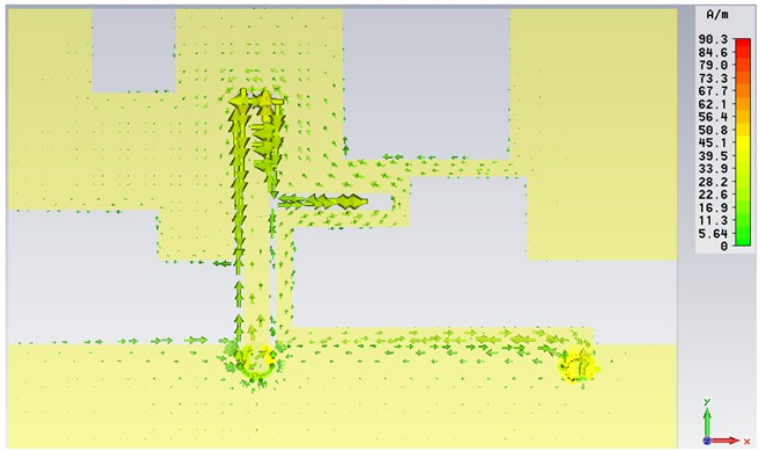

(c) 2.45 GHz

Figure 4.25 Simulated surface current distribution

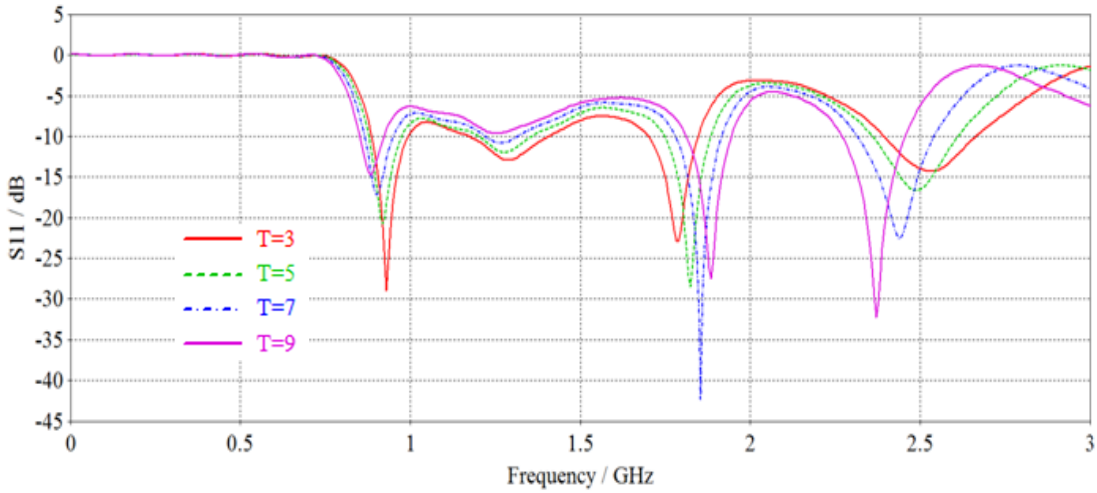

Figure 4.26 Simulated reflection coefficient as a function of *T*

Effects of parameter *T* (indicated in Figure 4.24) of the meandered shorting strip on the resonant frequencies of the proposed antenna are investigated in Figure 4.26. By increasing the length *T*, the first and third resonant modes are shifted to lower frequencies while the bandwidth is reduced. As for the second resonant mode, resonant frequencies decrease with the length of *T*. An optimal value of 7 mm is selected to cover desired frequency bands of GSM 900, GSM 1800 and Wi-Fi 2.4 GHz.

4.3.3 Measurement Results

Figure 4.27 demonstrates fabricated prototype of the proposed triple-band PIFA. Comparison results between the simulated and measured reflection coefficient of the proposed antenna are shown in Figure 4.28. The measured reflection coefficient illustrates satisfactory bandwidth in the resonant frequency bands of 0.91 – 1 GHz, 1.75 – 1.89 GHz and 2.36 – 2.52 GHz that covers downlink of GSM 900 (935-960MHz), GSM 1800 (1805-1880MHz) and the whole Wi-Fi 2.4 GHz band (2.4 – 2.5 GHz). The measured radiation patterns for the designed triple-band antenna in E-plane and H-plane are demonstrated in Figure 4.29. The radiation patterns at 940 MHz have omni-directional characteristic in the azimuth plane which is similar to dipole antennas. At higher frequencies, more various shapes of the radiation patterns with directional behaviors are noticed.

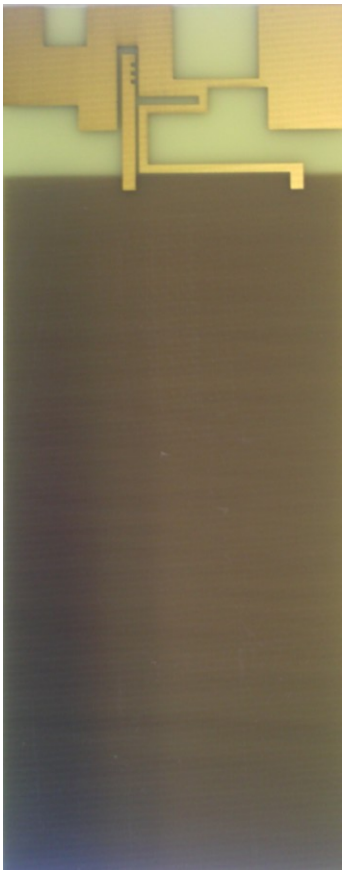

Figure 4.27 Fabricated prototype of the proposed triple-band PIFA

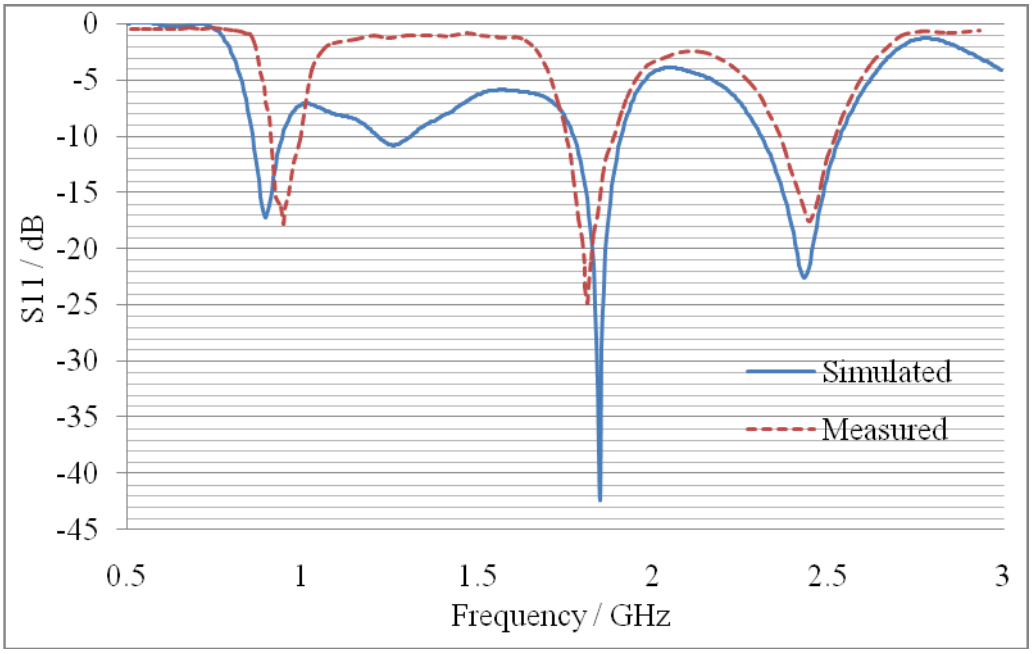

Figure 4.28 Simulated and measured reflection coefficient of the proposed triple-band PIFA

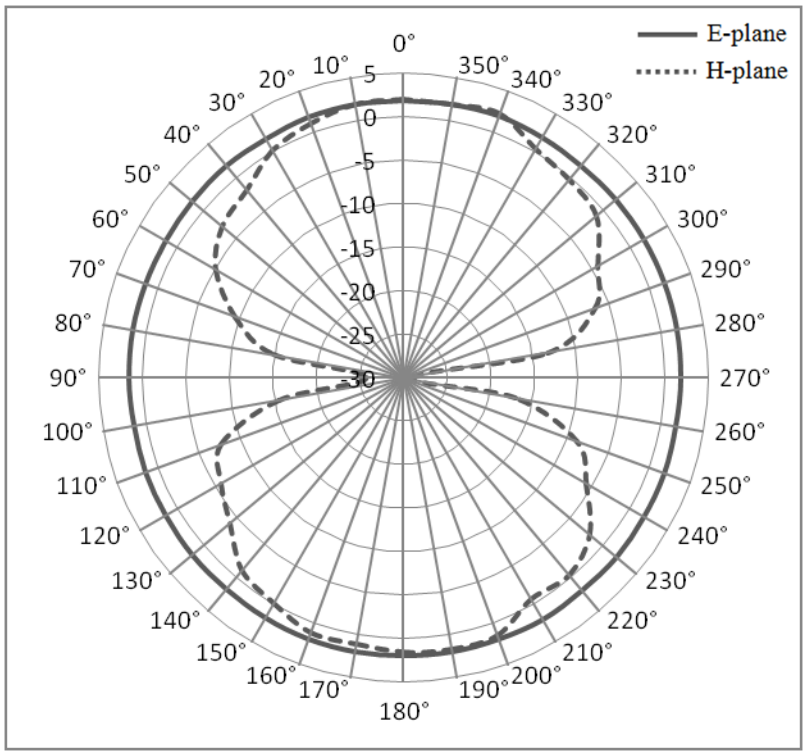

(a) 940 MHz

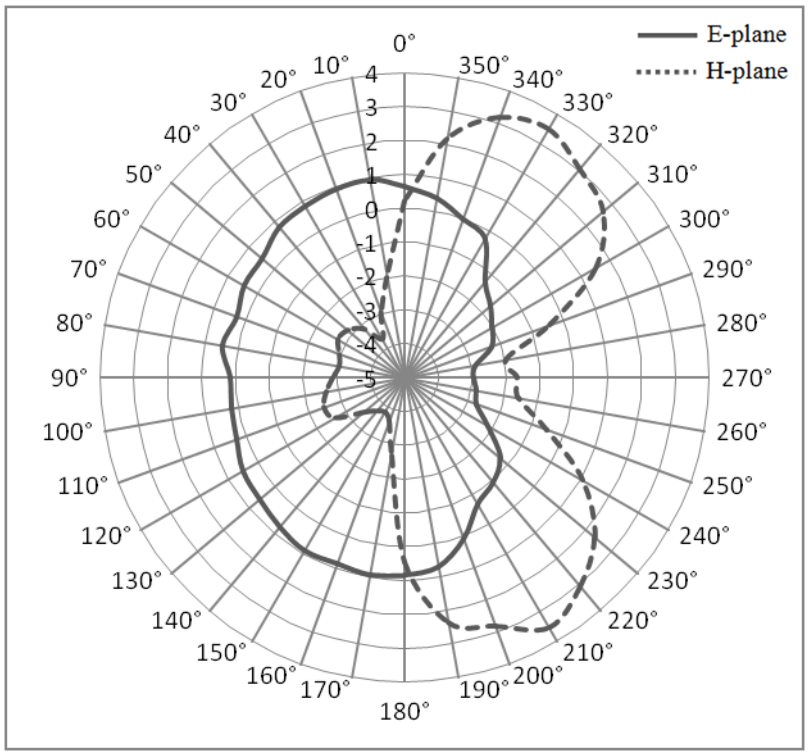

(b) 1.81 GHz

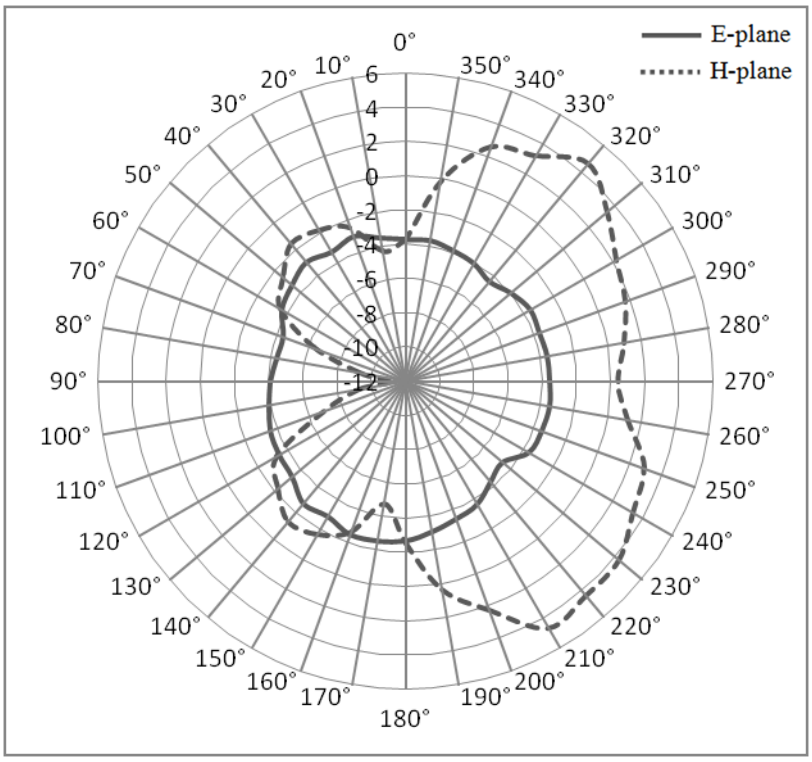

(c) 2.44 GHz

Figure 4.29 Measured radiation patterns at: (a) 940 MHz, (b) 1.81 GHz, (c) 2.44 GHz

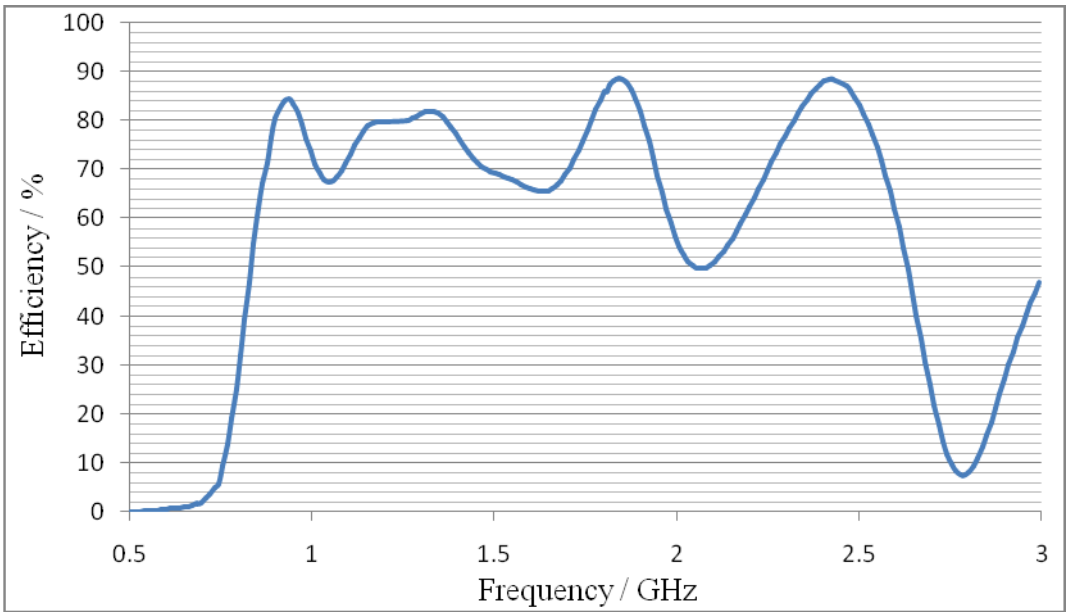

Figure 4.30 Measured antenna efficiency of the proposed triple-band PIFA

Figure 4.30 presents the measured antenna efficiency of the proposed triple-band PIFA. In the resonant frequency bands of 0.91 – 1 GHz, 1.75 – 1.89 GHz and 2.36 – 2.52 GHz, the antenna efficiency varies in the range of 71% - 84%, 77%-89%, and 79%-88%, respectively.

In Table 4.1, Dimensions and antenna gain of the proposed PIFA are compared with those of other triple-band antennas designed for RF energy scavenging and wireless applications. Significant reduction in antenna dimensions has been achieved with our antenna design. Compared with the triple-band PIFA design presented in [95], volume reduction of 81% is achieved for the proposed antenna. Moreover, the proposed antenna has higher antenna gain compared with the other designs, which means the maximum power that is possibly received by the antenna is higher. For RF energy scavenging systems, power extracted by the antenna is critical since the higher the input power level, the higher the output power.

Table 4.1 Comparisons of antenna dimensions and gain among the proposed antenna and other studies

Antenna Design	Proposed	[24]	[96]	[95]
Resonant Frequency (MHz)	940 1810 2440	940 1950 2400	920 1750 2240	890 1800 2400
Antenna Gain (dBi)	2.13 4.31 5.03	0.3 2.3 3.5	2 4	1.47 2.05 2.37
Dimensions (mm^3)	15×40×0.8	40×90×0.2	62×89.6×0.78	12×30×7
Volume Reduction $(1-\frac{\text{Proposed}}{\text{Published}})$		33.3%	88.9%	81.0%

4.3.4 Received Power Estimation

According to *Friis' transmission formula*, power received in wireless power transmission is mainly determined by antenna gain and transmission distance. When expressed on a logarithmic scale, the received power P_r is given by:

$$\boldsymbol{P_r = P_t + G_t + G_r - L_p} \tag{4.2}$$

where P_t is the total transmitted power, G_t and G_r are the antenna gains of the transmitting and receiving antennas, respectively, and L_p is the free space path loss that can be calculated as

$$\boldsymbol{L_p = 32.4 + 20 \times log\,(f) + 20 \times log\,(R)} \tag{4.3}$$

where f is the frequency and R is the transmission distance. The product of $P_t + G_t$ is called *Equivalent Isotropic Radiated Power* (*EIRP*). Therefore,

$$\boldsymbol{P_r = EIRP + G_r - L_p} \tag{4.4}$$

Thus power received in RF energy scavenging using proposed antenna can be estimated if multi path fading is ignored.

Equivalent Isotropic Radiated Power (EIRP) of Wi-Fi signals in EU is limited to 20 dBm (100 mW) and the mobile station maximum output power control level for GSM 900 and GSM 1800 is defined according to its class, as shown in Table 4.2. Power level 3 is used for calculation in our case.

Table 4.2 Mobile Station (Handset) Maximum Output Power *[97]*

Power class	GSM 900	GSM 1800	Tolerance (dB)	
			normal	extreme
1		30 dBm	±2	±2.5
2	39 dBm	24 dBm	±2	±2.5
3	37 dBm	36 dBm	±2	±2.5
4	33 dBm		±2	±2.5
5	29 dBm		±2	±2.5

Based on the formulas mentioned above, calculated maximum received power (peak power) of the proposed triple-band antenna at resonant frequencies is plotted in Figure 4.31. As can be observed, received power decreases with the increase of transmission distance. For distance of 10 meters, received power at frequencies of 940 MHz and 1810 MHz is -12.8 dBm and -17.3 dBm, respectively. If efficiency of conversion circuits is assumed to be 50%, output power of a RF energy scavenging system at these two frequencies is -15.8 dBm and -20.3 dBm. This is enough to power up low power wireless sensors as presented in [98-100] with power consumption ranging from -36.6 dBm to -20 dBm. However, for frequency of 2.44 GHz, the received power at distance of 10 meters is only -35.2 dBm. Therefore, frequency bands of GSM 900 and GSM 1800 could be used for RF energy at short or moderate distance while Wi-Fi 2.4 GHz is restricted to RF energy scavenging at close range.

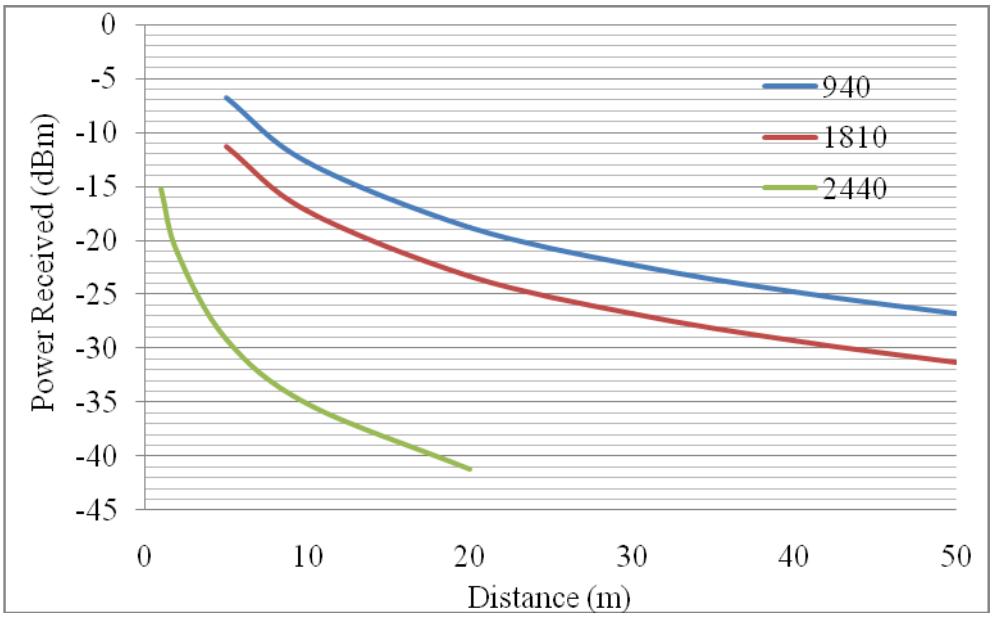

Figure 4.31 Estimated received peak power over distance

4.4 Summary

Although in the ambient environment RF energy is distributed in a wide frequency range, the power level varies greatly with frequency. This means not all of these frequency bands are suitable for RF energy scavenging. For this reason, multi band antennas are presented in this chapter for RF energy scavenging from potential frequencies with highest power level.

Firstly a novel printed dual-band PIFA with a wide radiating plate excited by a coupling feed and short-circuited by an inductive metal strip has been presented for RF energy scavenging. The antenna has its operation at GSM 900 and GSM 1800. Compared to conventional PIFA with relatively large thickness, the printed construction of the antenna is more suitable for compact system integration. Moreover, it makes mass production at low cost possible. Good radiation characteristics are also obtained by the antenna with peak efficiencies at the lower and upper operating bands reaching 86% and 88%, respectively.

Secondly, a triple-band PIFA operating in the frequency bands of GSM 900, GSM 1800 and Wi-Fi 2.4 GHz has been developed from the dual-band antenna design. The bended shorting strip in the dual-band PIFA is replaced by a meandered shorting strip to obtain resonance at around 2.45 GHz. The proposed triple-band PIFA achieves not only physically small and compact structure ($15 \times 40 \times 0.8$ mm^3), but also appreciable efficiency and gain across the operating frequency range. Compared with published researches, the proposed PIFA has smaller dimensions with higher gain. The satisfactory performance of the proposed PIFA with its compact structure, small size and easy, low-cost fabrication makes the antenna very promising for miniaturized RF energy scavenging system.

In summary, the investigation of the multi-band PIFA for RF energy scavenging is shown in Figure 4.32.

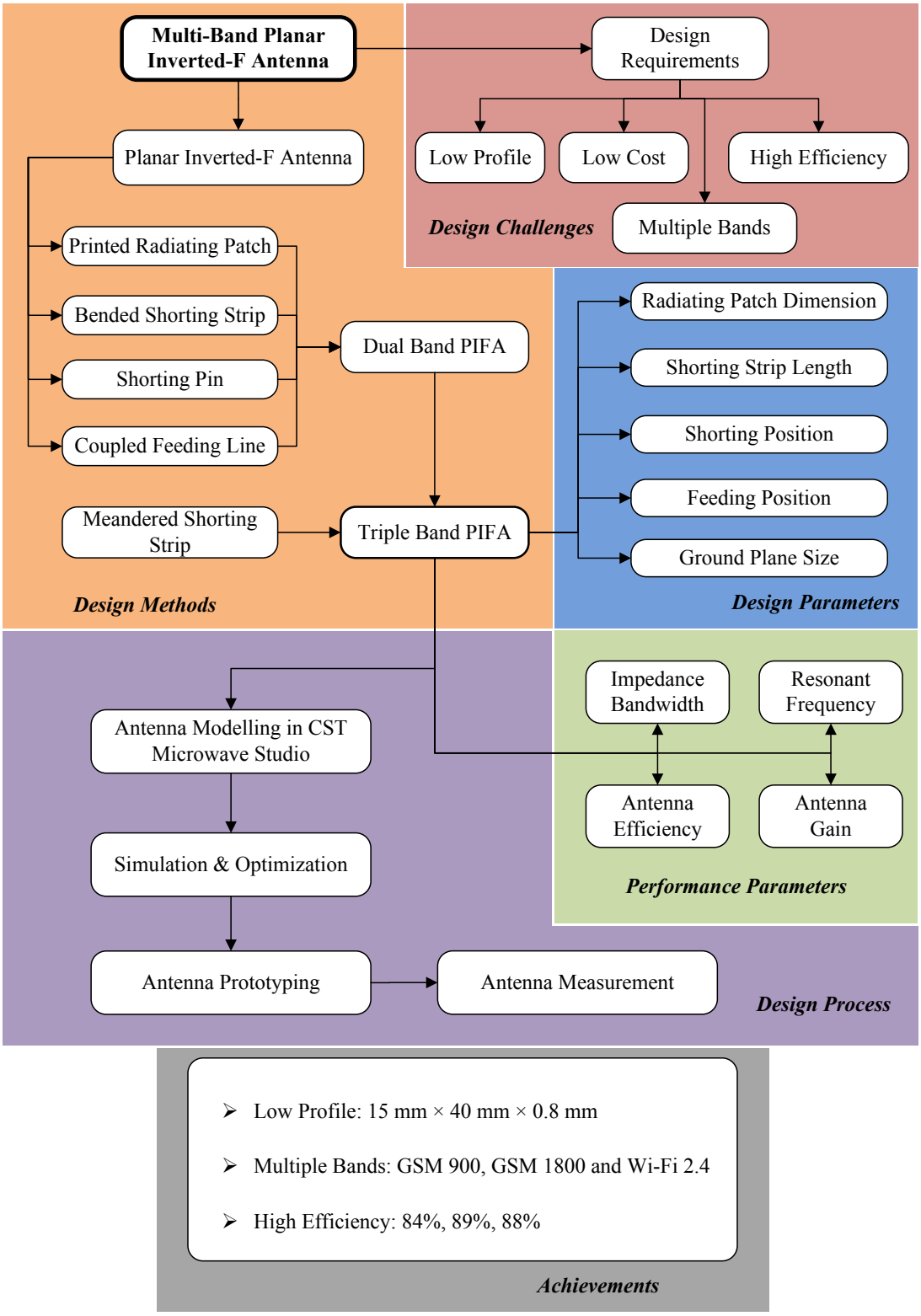

Figure 4.32 The investigation of the multi-band PIFA for RF energy scavenging

Chapter 5

Miniature IFA for Indoor Wi-Fi Energy Scavenging

Modern industrial and residential buildings are equipped with a variety of sensors for human safety and comfort. These sensors include temperature, humidity, motion, smoke, position, light, water, radiation and chemical sensors. Instead of operating continuously, most of these sensors read the desired data at a predetermined frequency or on the principle of sense – on – demand. Therefore, RF energy scavenging that harvest energy from ambient propagating waves and provide the stored energy to power the sensor node for a fixed duration is suitable for various indoor close range sensing applications to solve the problem of power supply.

Previous research on RF energy scavenging usually focus on the ambient broadcast and communication bands of relatively low frequencies due to the fact that the lower frequency, the lower propagation loss. ISM band of 902 – 928 MHz is the most widely used frequency band as RF power in this frequency range transmits more efficiently for longer distance and experiences smaller loss than higher frequency bands. However, with the popularization of indoor Wireless Local Area Network (WLAN, or simply Wi-Fi) and the fact that it operates in the crowded 2.4GHz band (the same as RFID, Bluetooth, ZigBee, cordless phone etc.), Wi-Fi 2.4GHz emerges as another perfect candidate for short – range RF energy scavenging. There are

increased number of Wi-Fi routers and wireless end devices such as laptops. Already, in some urban environments, one can detect tens of Wi-Fi transmitters from a single location [101]. Moreover, global market survey indicated unprecedented growth in Wi-Fi hotspot deployments which are predicted to rise by 350% to a total of 5.8 million by 2015 [102].

Compared with 100-108 MHz FM and 900 MHz GSM signal, lab measurements reveal that for indoor environment the most powerful signal available in close physical proximity of the sensor location is 2.4 GHz Wi-Fi signal [103]. At close range, as is the case of indoor Wireless LAN, it is possible to scavenge energy form a typical Wi-Fi router transmitting at a power level of 20 dBm. Figure 5.1 shows a possible application of Wi-Fi energy scavenging to power up different types of sensor nodes in a hotel room.

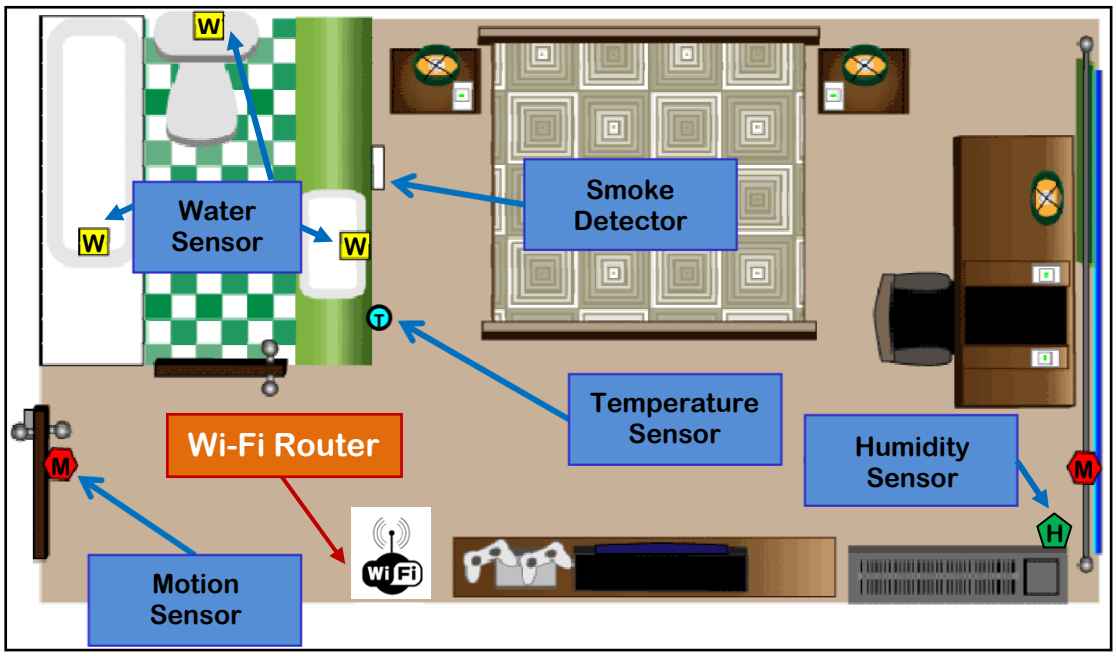

Figure 5.1 Sensors in a hotel room [104] © Powercast Corporation

Among existing RF energy scavenging systems, most of them have significant limitations on mobility since these systems operate only in the presence of physically large antennas. For an indoor Wi-Fi energy scavenging system, with the continuous miniaturization of electronic devices, an antenna effective in both radiation performance and space requirement is a critical part to extract maximum power from the ambient environment.

In this chapter, we discusses the design, simulation, optimisation, fabrication and characterisation of a novel miniaturized Inverted – F Antenna (IFA) operating at centre frequency of 2.45 GHz for Wi-Fi energy scavenging to power indoor sensor networks. Four primary designs with different features and techniques are also presented to introduce the developing process and design considerations of the proposed antenna. Compared with the primary designs, the proposed IFA has advantages on both bandwidth and radiation efficiency.

5.1 Initial IFA Design

Figure 5.2 demonstrates geometry of the initial IFA design. The antenna developed from the PIFA configuration is implemented with one piece of metal patch. The patch is modeled into a 3D structure with overall dimensions of 8 × 4 × 3 mm^3. The antenna is fed from the corner with shorting pin located 4 mm to the left. Meandered line structure is implemented between the feed and the top radiating plate to provide more inductance to the input impedance. The meandered geometry helps to reduce the wavelength and the associated antenna length. A bent slot is etched on the top radiating plate to adjust the operating frequency. Good impedance matching and bandwidth optimization can be achieved through the capacitive coupling. At the end of the top radiating plate a strip section extended to the right surface that provides electrical path for resonance is added to minimize the antenna dimensions. Based on the IFA structure, the resonant length of the antenna is about quarter-wavelength at the operating frequency. Hence, the lowest operating frequency f_l can be estimated by:

$$f_l = \frac{c}{4\sqrt{\varepsilon_r}\,L_l} \tag{5.1}$$

where c is the velocity of light in free space, ε_r is the effective relative permittivity of the medium in between the ground and the radiating patch, Ll is the estimated longest current path. Consequently, the antenna can be designed properly with suitable centre frequency at around 2.45 GHz.

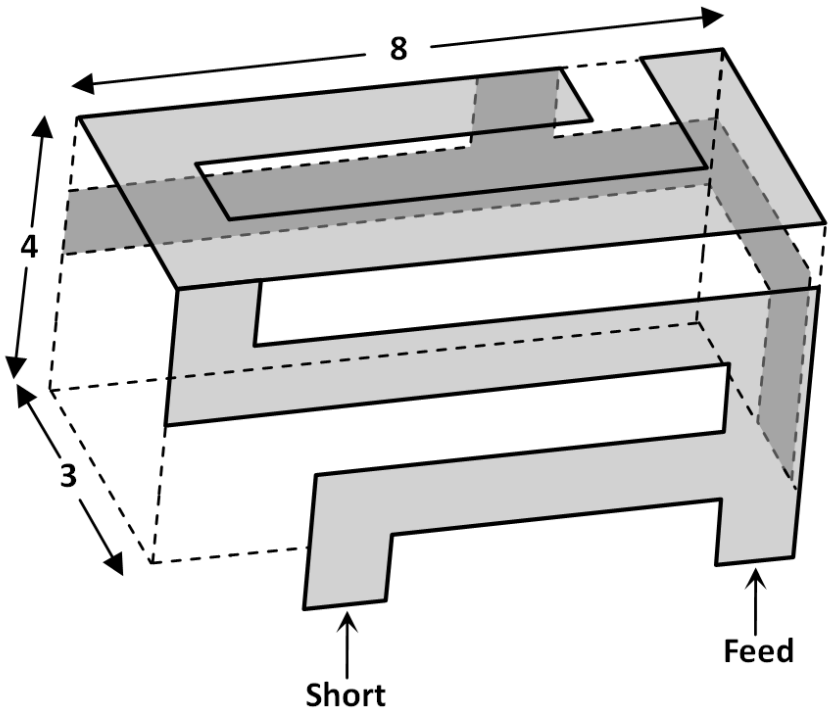

Figure 5.2 Geometry of the initial IFA design

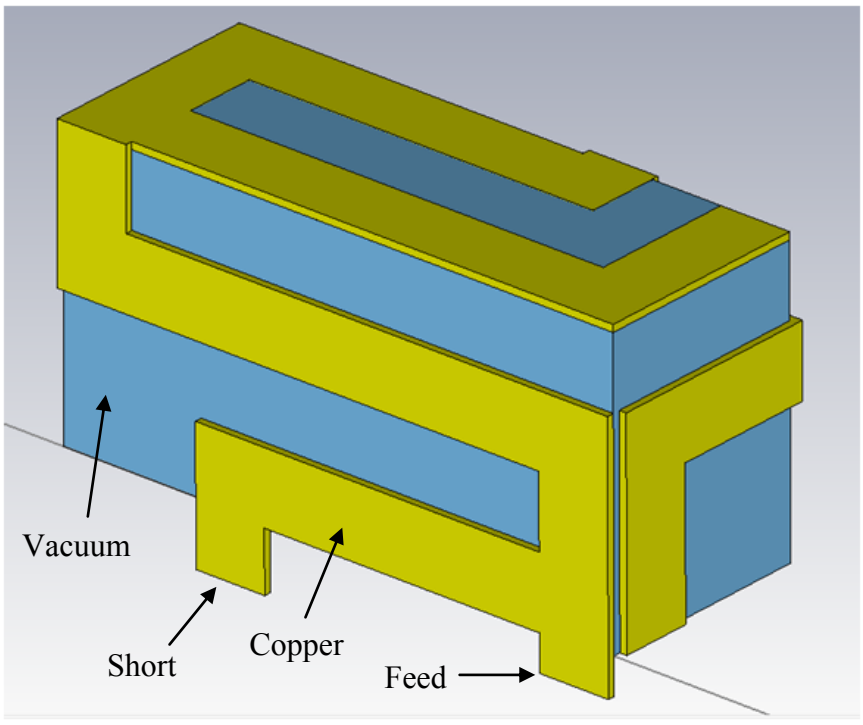

Figure 5.3 Model of the initial IFA design in CST

Figure 5.3 shows the antenna model build in CST. The empty space in the 3D antenna structure is filled with vacuum to reduce the simulation time. To simulate the effect for an integrated miniature device on the antenna, the designed IFA is mounted on a test board of 80 × 40 × 0.8 mm^3 with full ground, as shown in Figure 5.4 (the same to other designs). A minimum size of a quarter wavelength at the operating frequency is recommended for the test board to ensure antenna performance [29].

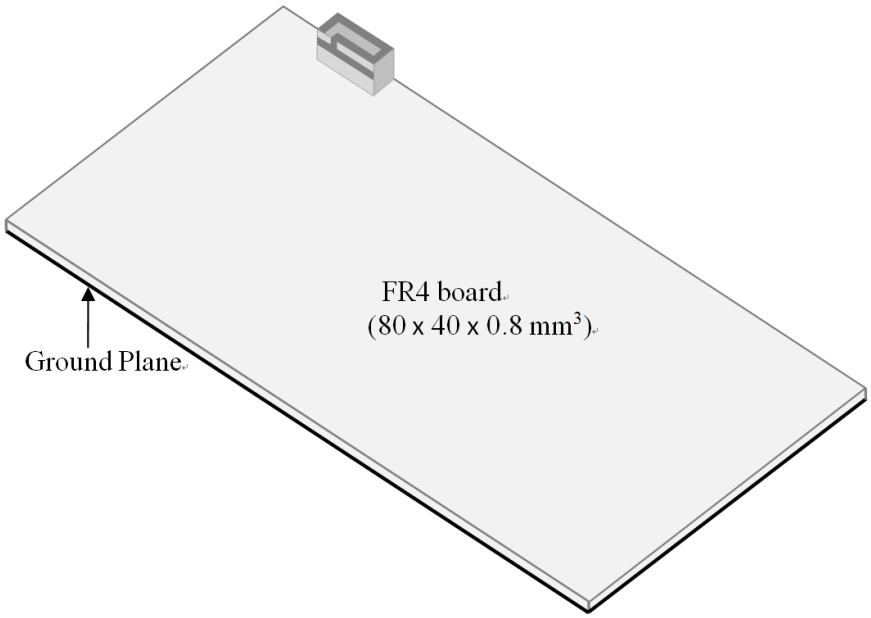

Figure 5.4 Simulation model setup of the initial IFA design on a FR4 board

The simulated reflection coefficient of the antenna embedded on the test board is demonstrated in Figure 5.5 and Figure 5.6 illustrates the surface current distribution at centre frequency. From the simulation results, it is seen that the impedance bandwidth with -10 dB reflection coefficient is 46 MHz, from 2.456 GHz to 2.502 GHz. At centre frequency of 2.48 GHz, the reflection coefficient is approximately -21 dB. For the initial IFA design, its bandwidth is too narrow to cover the whole Wi-Fi frequency band ranging from 2.4 GHz to 2.5 GHz. Moreover, the simulated radiation efficiency at centre frequency is only 77%.

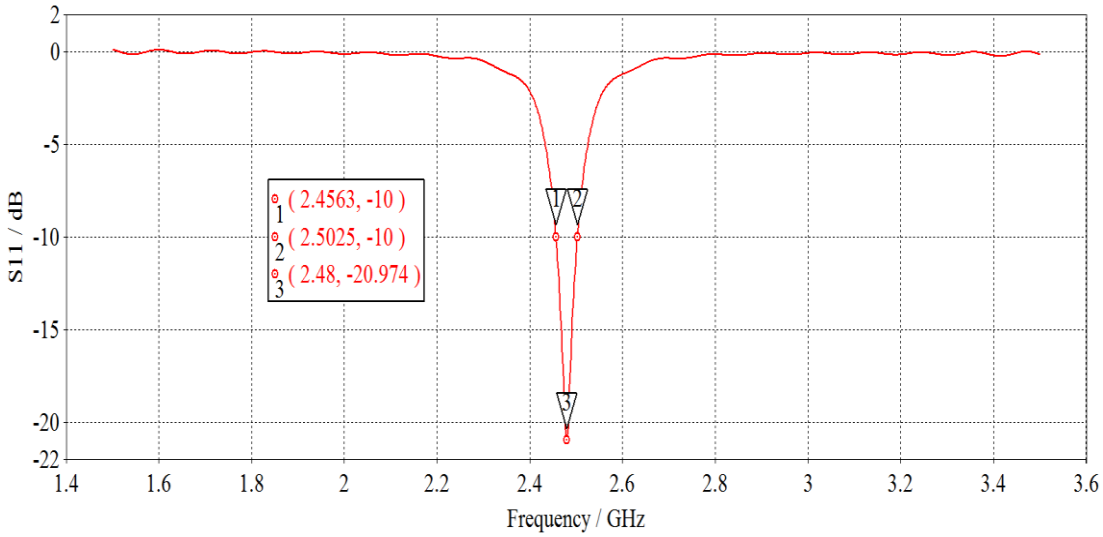

Figure 5.5 Simulated reflection coefficient of the initial IFA design

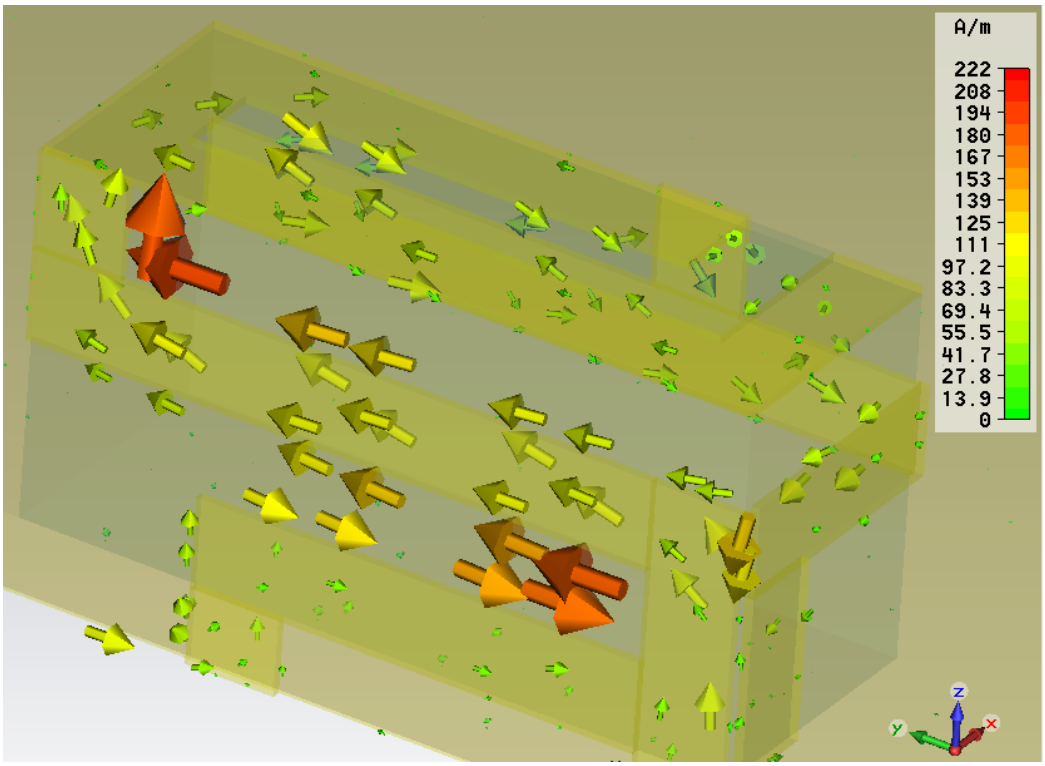

Figure 5.6 Surface current distribution on the initial IFA design

5.2 Second IFA Design

Figure 5.7 depicts geometry of the second design of miniature IFA. The bandwidth of an PIFA depends on a few parameters, specially the size ratio of the planar element and the height of the short – circuit plate [105]. Hence, to broaden the antenna bandwidth, the overall dimensions of the antenna are increased to 10 × 4 × 3 mm^3. The size ratio of the top radiating plate is increased from 8/3 to 10/3. The end strip section is extended to both left and right surface and three slots are etched on the top radiating plate to adjust and control the operating frequency.

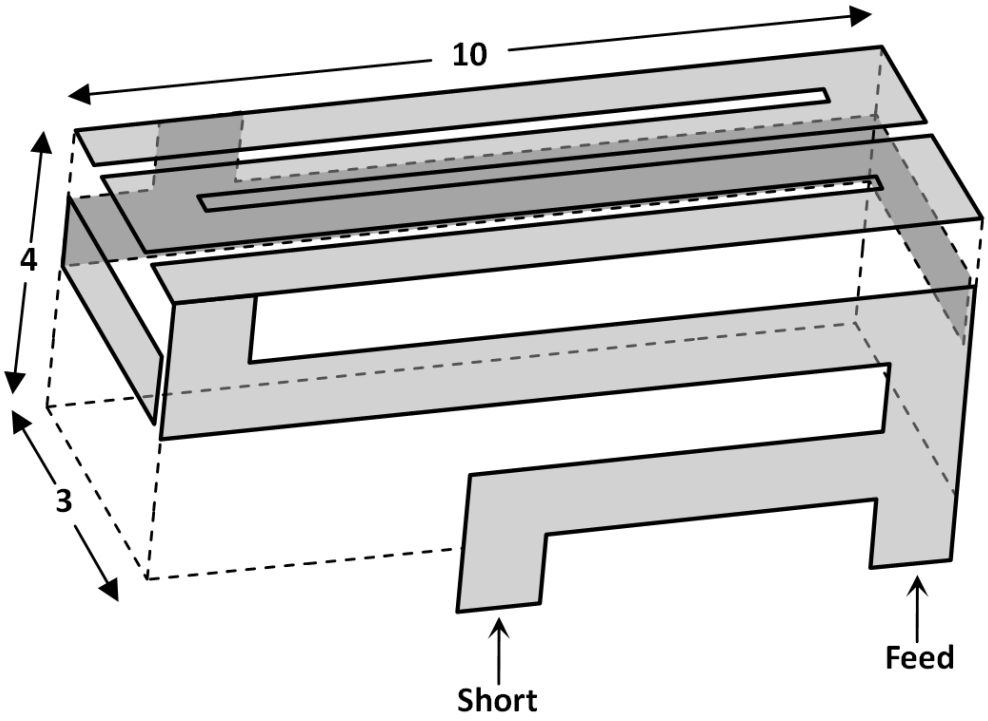

Figure 5.7 Geometry of the second IFA design

The simulation model in CST and its corresponding surface current flow at centre operating frequency are shown in Figure 5.8 and Figure 5.9, respectively. The slots on the top radiating plate increase the current flow path length, which helps to reduce the antenna size. By increasing the length of these slots, the operating frequency can be reduced for the same antenna size. However, this results in a decrease in antenna bandwidth.

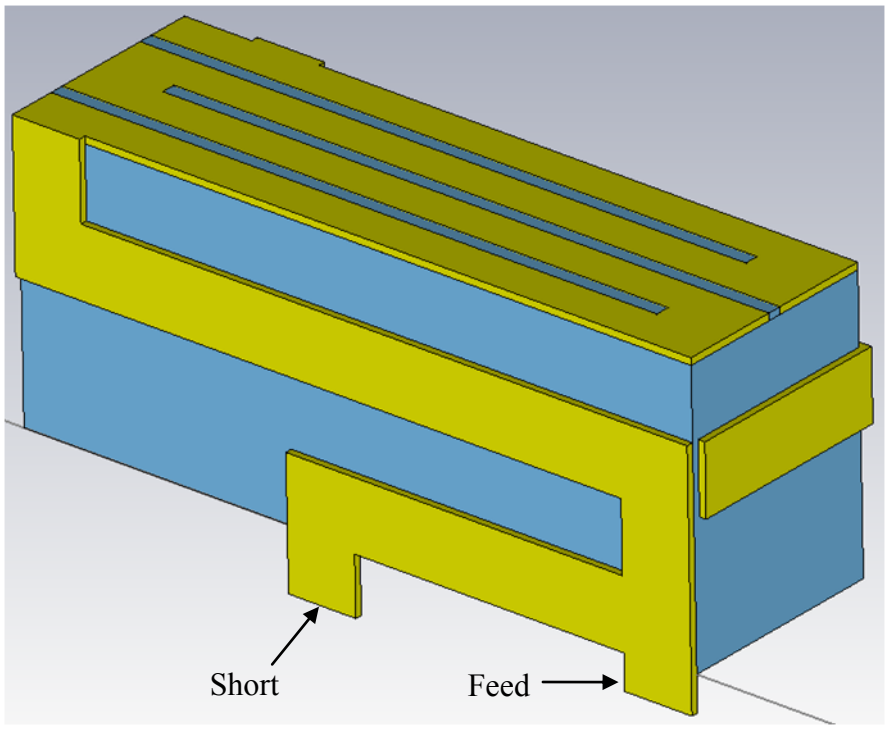

Figure 5.8 Model of the second IFA design in CST

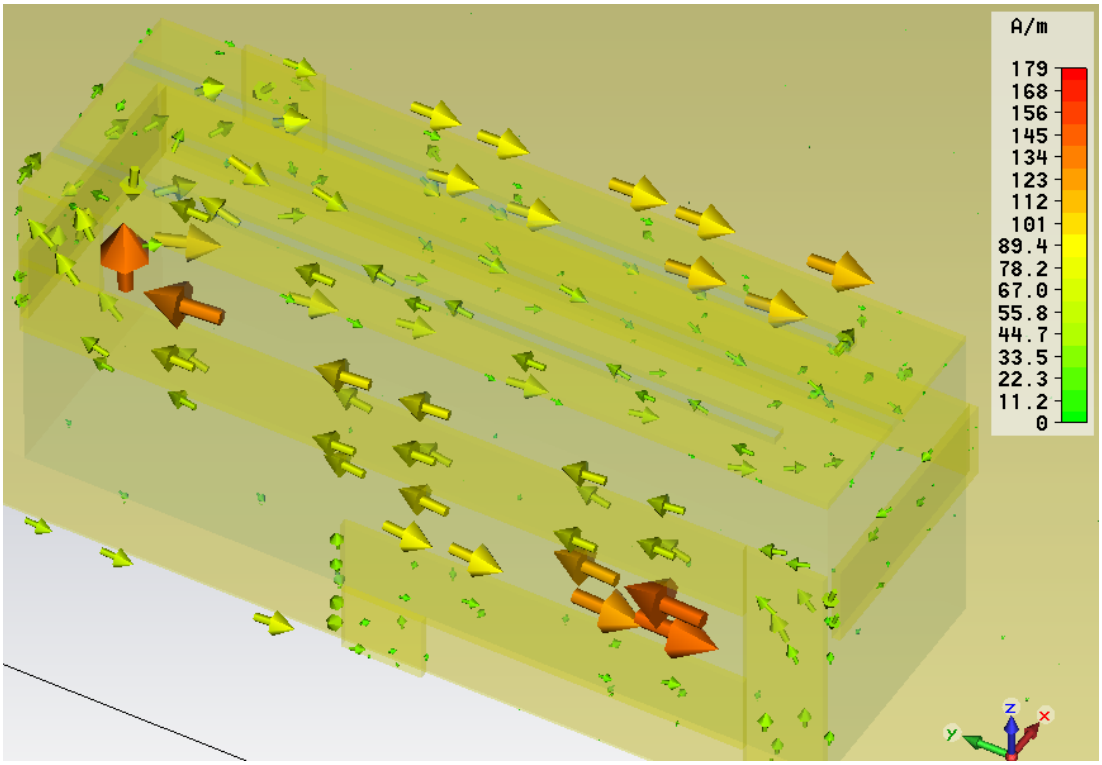

Figure 5.9 Surface current distribution on the second IFA design

The simulated reflection coefficient is plotted in Figure 5.10. According to the simulation result, the second antenna design has an impedance bandwidth of 71 MHz, from 2.425 GHz to 2.496 GHz. The lowest reflection coefficient reaches -49.5 dB at frequency of 2.46 GHz. The bandwidth of the second IFA design is larger than the initial design. However it is still not large enough to cover the 2.4 GHz Wi-Fi frequency band. The simulated radiation efficiency of the second antenna is 92%, which is significantly higher than that of the initial design.

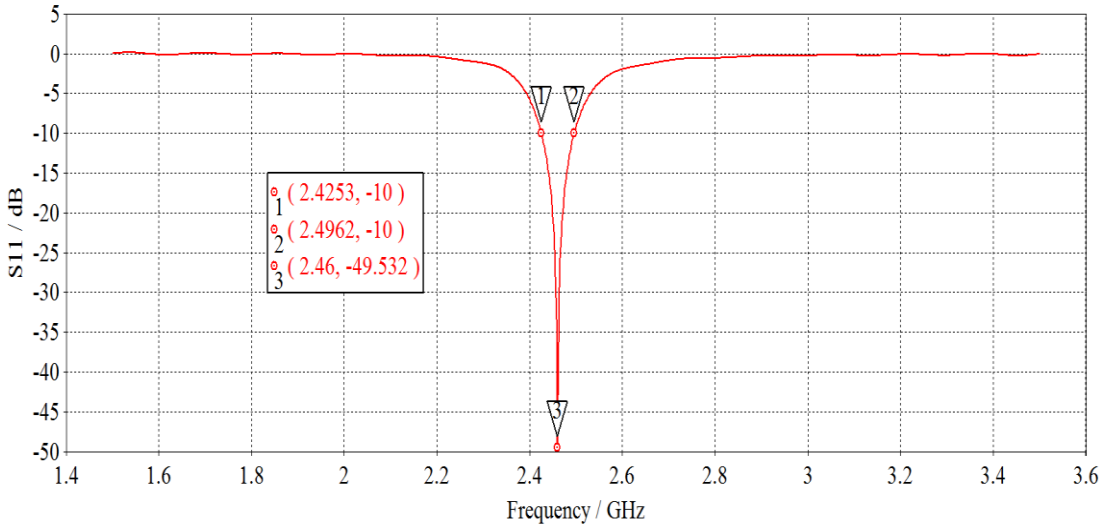

Figure 5.10 Simulated reflection coefficient of the second IFA design

5.3 Third IFA Design

The third IFA design is illustrated in Figure 5.11 and its model for simulation in CST is shown in Figure 5.12. Instead of air substrate, a 4 mm-thick FR4 substrate with relative permittivity of 4.3 and loss tangent of 0.025 is used to avoid interference from the circuit routing on the PCB. Good stability can be achieved by lengthening the distance between the PCB's circuit and the antenna due to the reduced mutual coupling between them. Moreover, with the FR4 substrate, the antenna size can be reduced to achieve the same operating frequency. The overall dimensions are 10 × 4 × 3 mm^3. The end strip section is extended to the left and right surface to increase the resonant length but there is no slot on the top radiating plate. By adjusting the length of the end strip section the operating frequency can be modified.

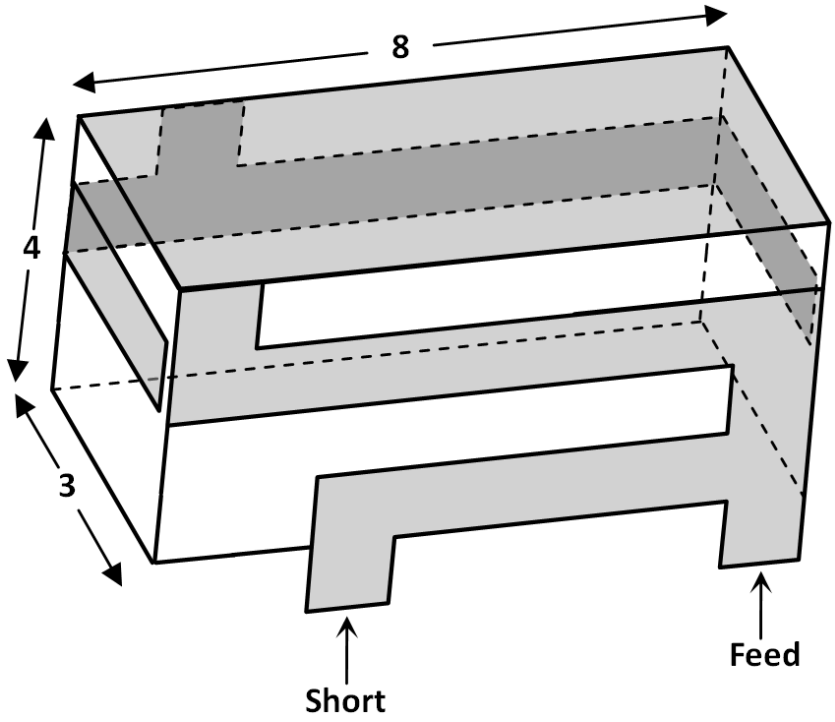

Figure 5.11 Geometry of the third IFA design

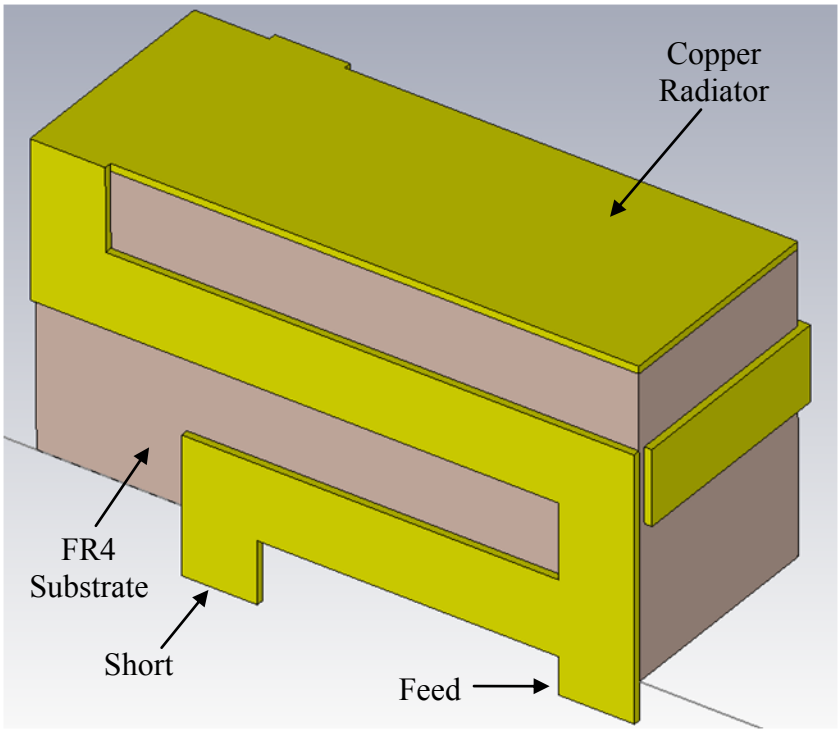

Figure 5.12 Model of the third IFA design in CST

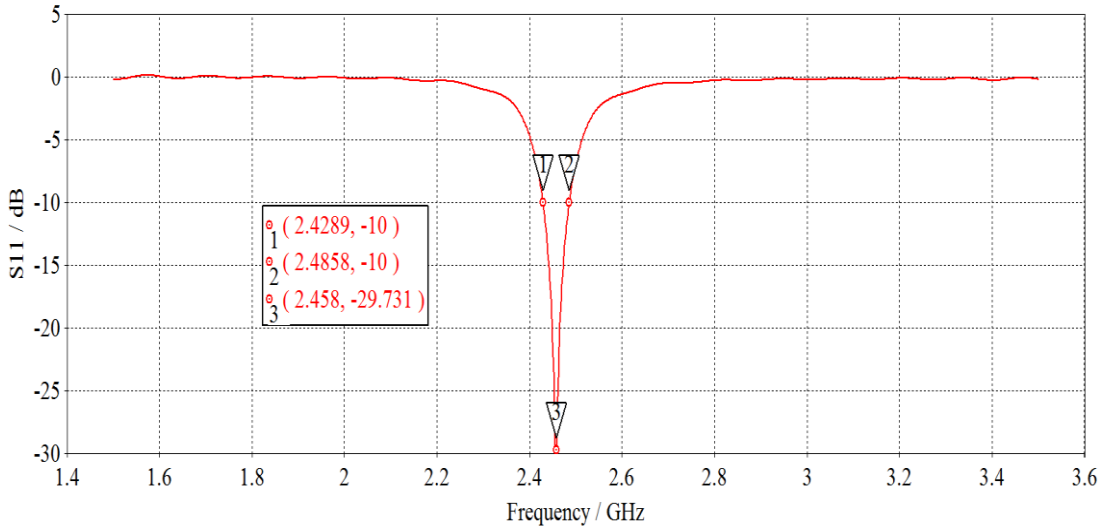

Figure 5.13 Simulated reflection coefficient of the third IFA design

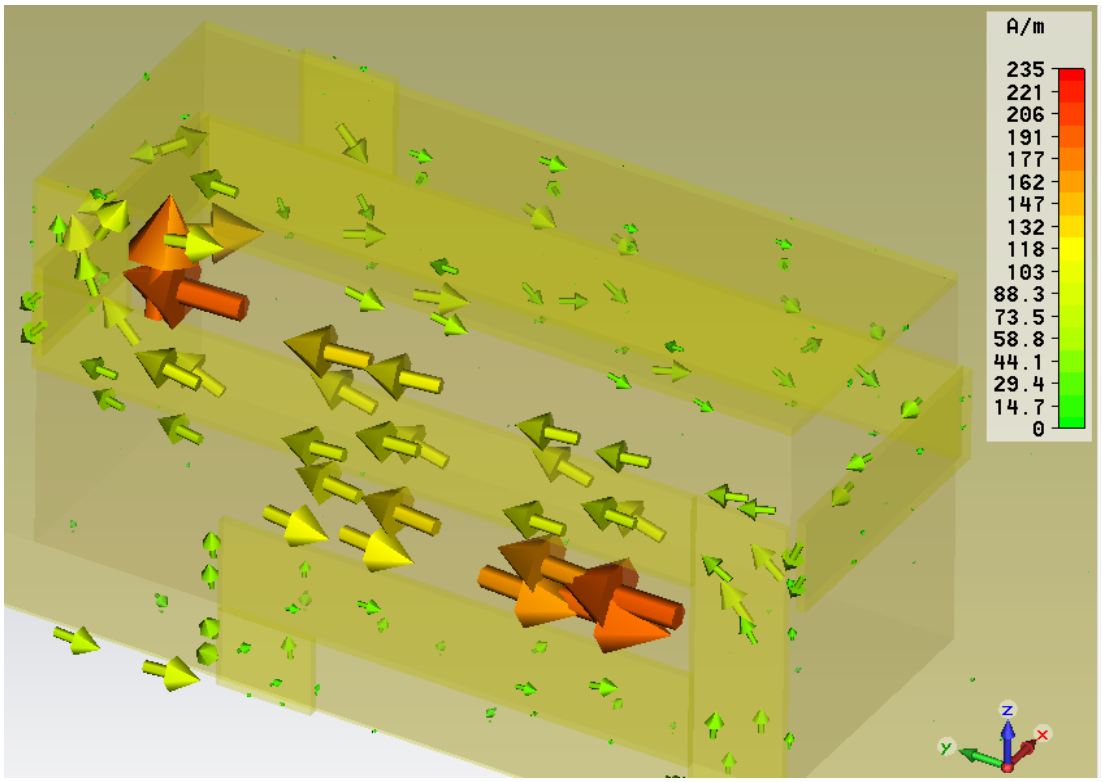

Figure 5.14 Surface current distribution on the third IFA design

Figure 5.13 and Figure 5.14 present the simulated reflection coefficient and the surface current flow of the third IFA design, respectively. It can be seen from the figures, the third antenna design has a resonant frequency of 2.458 GHz with S11 parameter reaching approximately -30dB. The -10 dB reflection bandwidth is about 57 MHz, from 2.429 GHz to 2.486 GHz and the simulated radiation efficiency at resonant frequency is 72%. In the third design, a thick FR4 substrate is employed to support the radiator and provide good stability. However, its radiation performance is not as good as the previous designs. This is because substrate with high relative permittivity tends to store energy more than radiate it, leading to high antenna Q value which is inversely proportional to the antenna bandwidth.

5.4 Fourth IFA Design

The fourth IFA is designed in the presence of a dielectric superstrate loading as shown in Figure 5.15. The layer above the top radiating plate causes a change in the fringing fields between the plate and the ground plane, and this effect is accounted for in terms of the effective relative permittivity [106]. The dimension of the radiating antenna is effectively extended by the fringing fields which are very much dependent on the relative characteristics of the substrate–superstrate combination, as presented by Alexopoulos and Jackson [107]. It is indicated that the surface wave excitation may be reduced to a great extent because of a dielectric cover with relative permittivity higher than that of the substrate at a proper thickness. The presence of the superstrate shifts the resonance to the lower frequency. The higher the relative permittivity, the greater is the effect. Moreover, thicker superstrate leads to a greater decrease in resonant frequency values.

The overall dimensions of the fourth IFA design are $10 \times 4.5 \times 3.6$ mm^3. The substrate is 3.5 mm-thick FR4 with relative permittivity of 4.3 and loss tangent of 0.025. 0.5 mm-thick Rogers RT6010 with relative permittivity of 10.2 and loss tangent of 0.0023 is used as superstrate. The top radiating plate is made of thick copper with thickness of 0.5 mm to provide more capacitance to the input impedance.

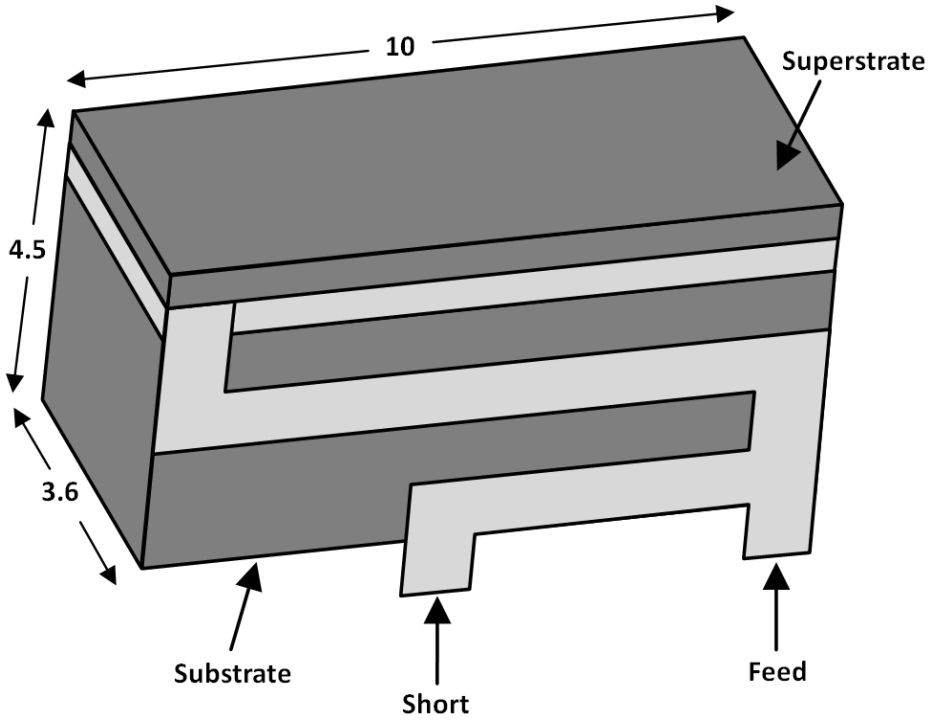

Figure 5.15 Geometry of the fourth IFA design

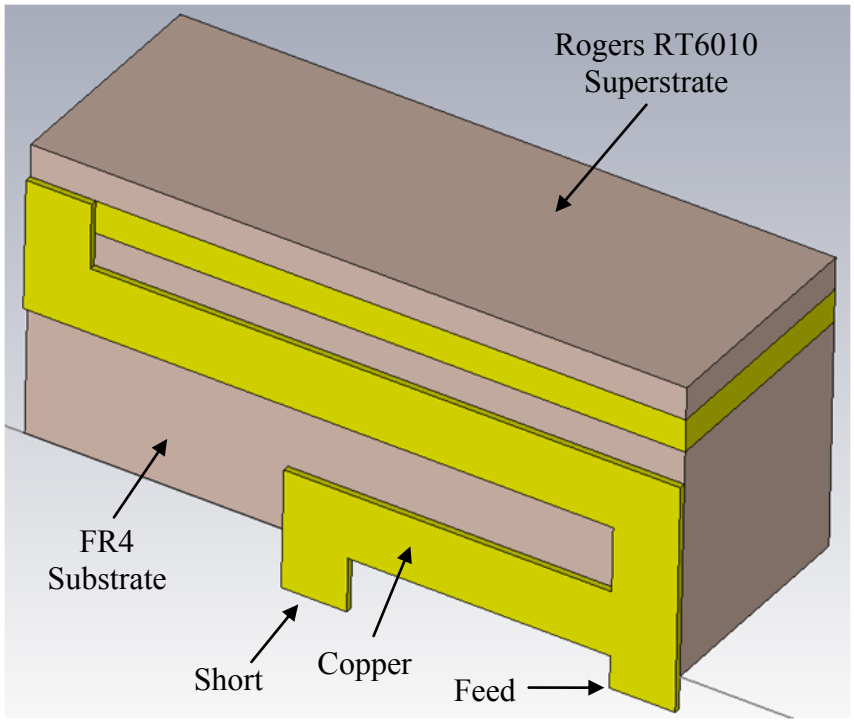

Figure 5.16 Model of the fourth IFA design in CST

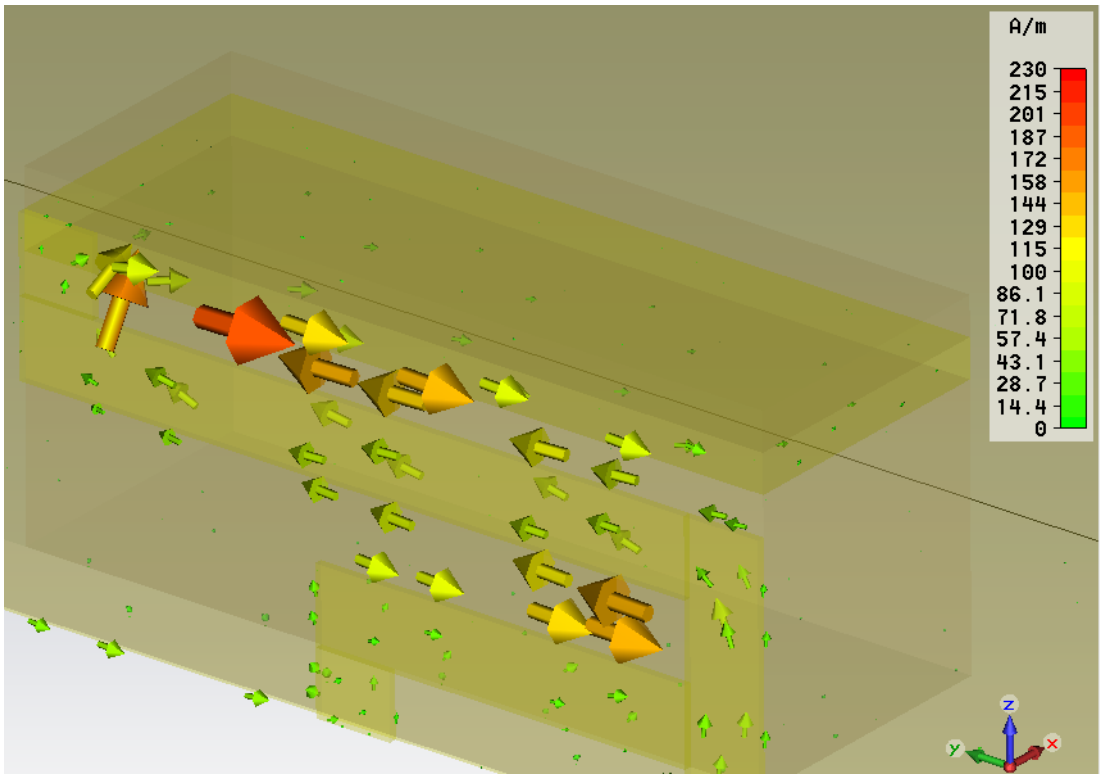

Figure 5.17 Surface current distribution on the fourth IFA design

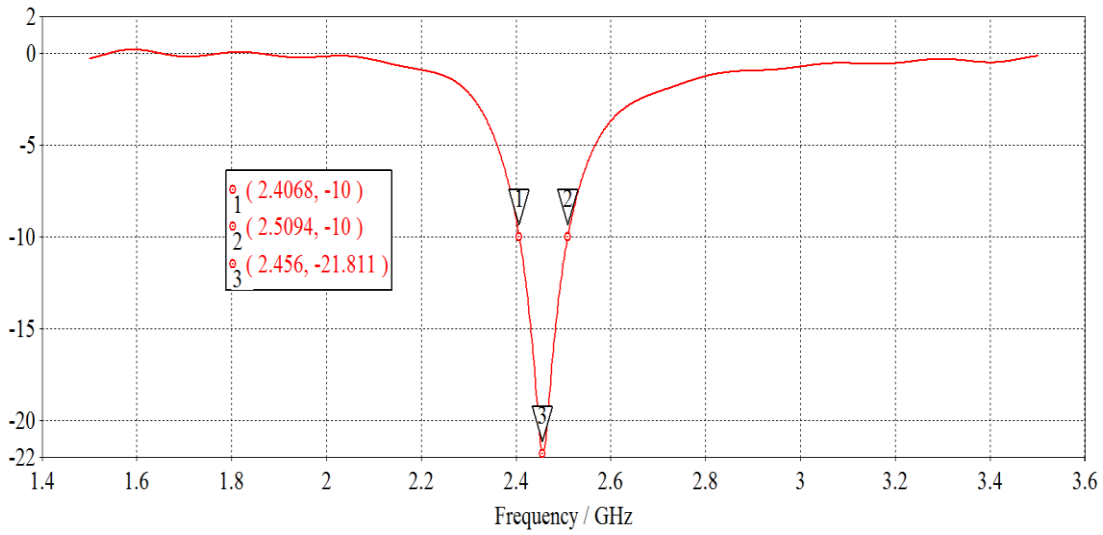

Figure 5.18 Simulated reflection coefficient of the fourth IFA design

Figure 5.16 and Figure 5.17 illustrate the CST model of the fourth IFA design and the corresponding surface current distribution, respectively. The simulated S11 parameter is shown in Figure 5.18. The impedance bandwidth of the antenna is about 102 MHz from 2.407 GHz to 2.509 GHz and the radiation efficiency at resonant frequency is 84%. Compared with the other three designs introduced previously, the fourth IFA design has the largest bandwidth that covers the 2.4 GHz Wi-Fi frequency band. The radiation efficiency is slightly lower than that of the second design, but it is significantly higher than the radiation efficiency of the first and third design. Although the fourth IFA design has the best performance among these designs, its fabrication process is much more difficult than the other designs due to the existence of the superstrate.

5.5 Final IFA Design

5.5.1 Antenna Structure

The proposed final design is depicted in Figure 5.19 with detailed dimensions listed in Table 5.1. Compared with the fourth design, the proposed IFA design has a thicker radiating patch on the substrate with no superstrate. The proposed antenna has small dimensions of 10 (L) $\times$ 5 (H) $\times$ 3.5 (W) mm^3 to be integrated into low power miniaturized devices. The FR4 substrate with relative permittivity of 4.3 and loss tangent of 0.025 has a thickness of 4 mm and the top radiating copper plate is 1 mm-thick. The width and thickness of the meandered line between the feed and the top radiating patch are 1 mm and 0.1 mm, respectively.

The meandered line structure is implemented with extra inductance while the thickness of the top radiating patch is increased for extra capacitance so that the inductance and capacitance can be balanced out. The thick FR4 substrate can support the radiator with good stability. Without additional empty space inside the 3D antenna structure, circuit routing on a multilayer PCB is allowed underneath and around the antenna with no restrictions.

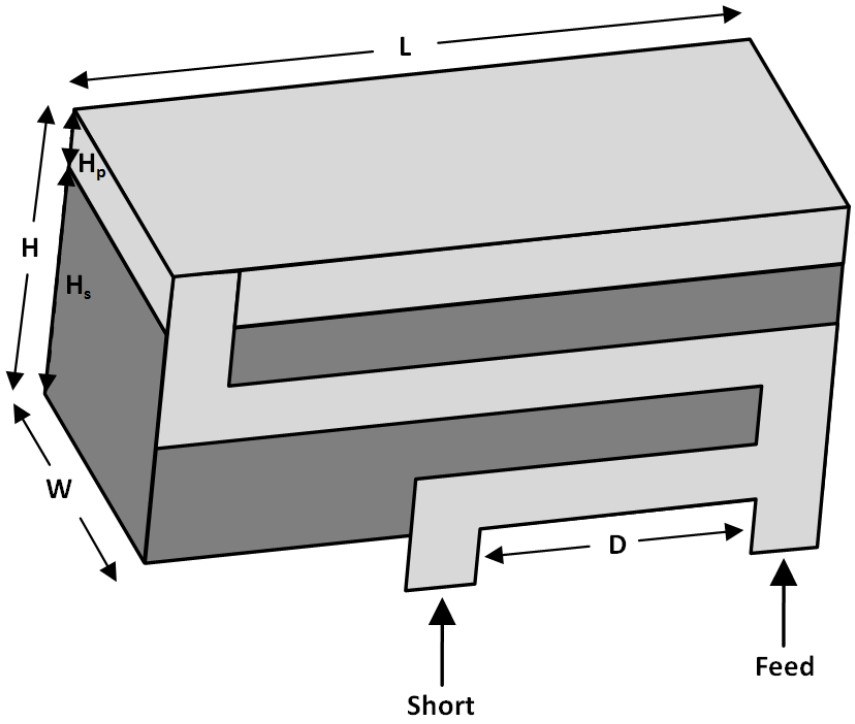

Figure 5.19 Geometry of the final IFA design

Table 5.1 Detailed dimensions of the final IFA design

Parameter	*Value (mm)*
L	10
H	5
W	3.5
H_s	4
H_p	1
D	4

5.5.2 Simulation Performance

The 3D model of the final IFA design build in CST microwave studio is demonstrated in Figure 5.20. Figure 5.21 and Figure 5.22 show the simulated reflection coefficient and surface current distribution, respectively. The impedance bandwidth with -10 dB reflection coefficient is from 2.395 GHz to 2.506 GHz, corresponding to 4.53%, which also covers the 2.4 GHz Wi-Fi band.

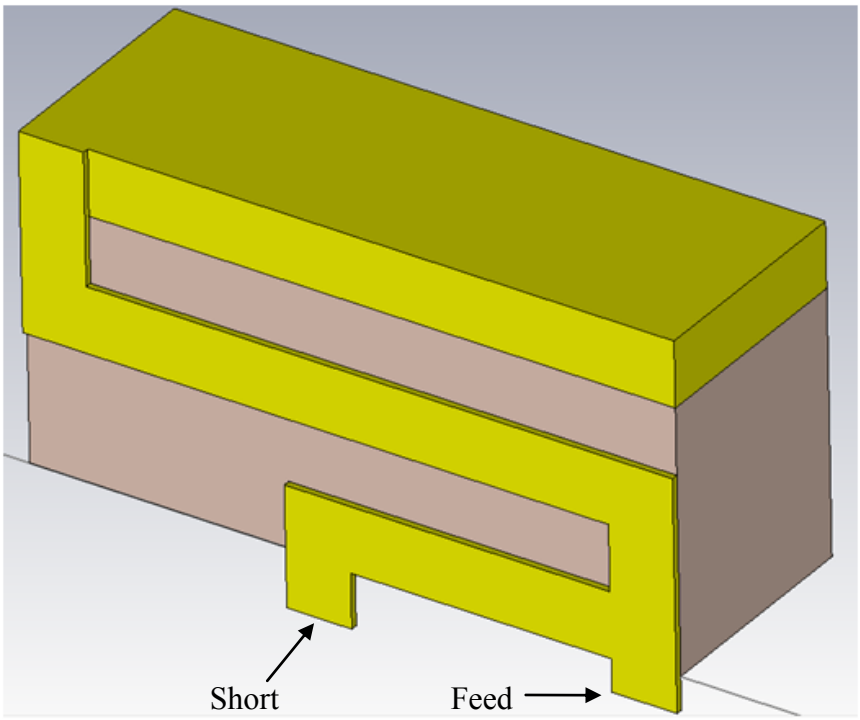

Figure 5.20 Model of the final IFA design in CST

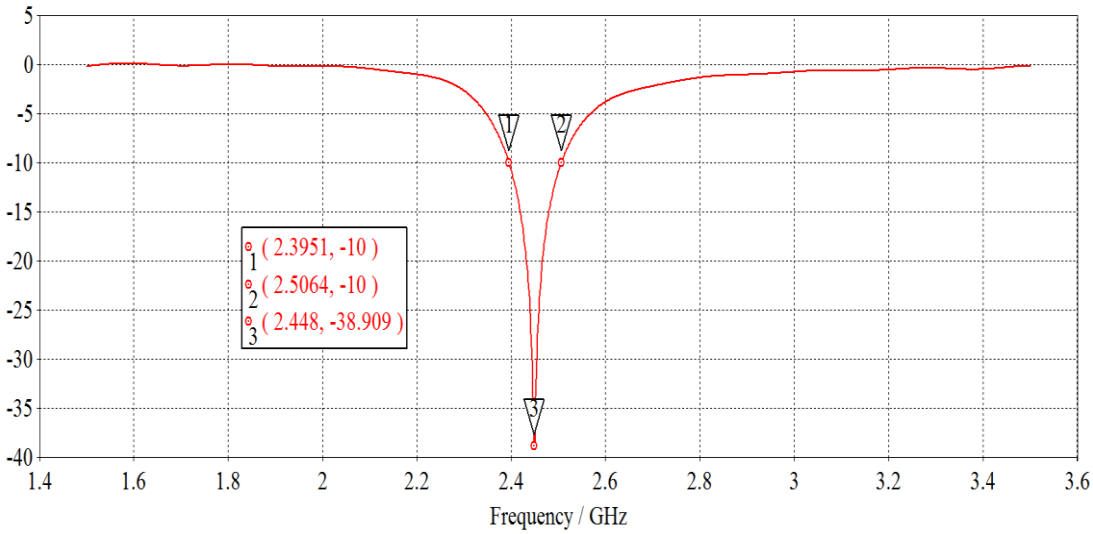

Figure 5.21 Simulated reflection coefficient of the final IFA design

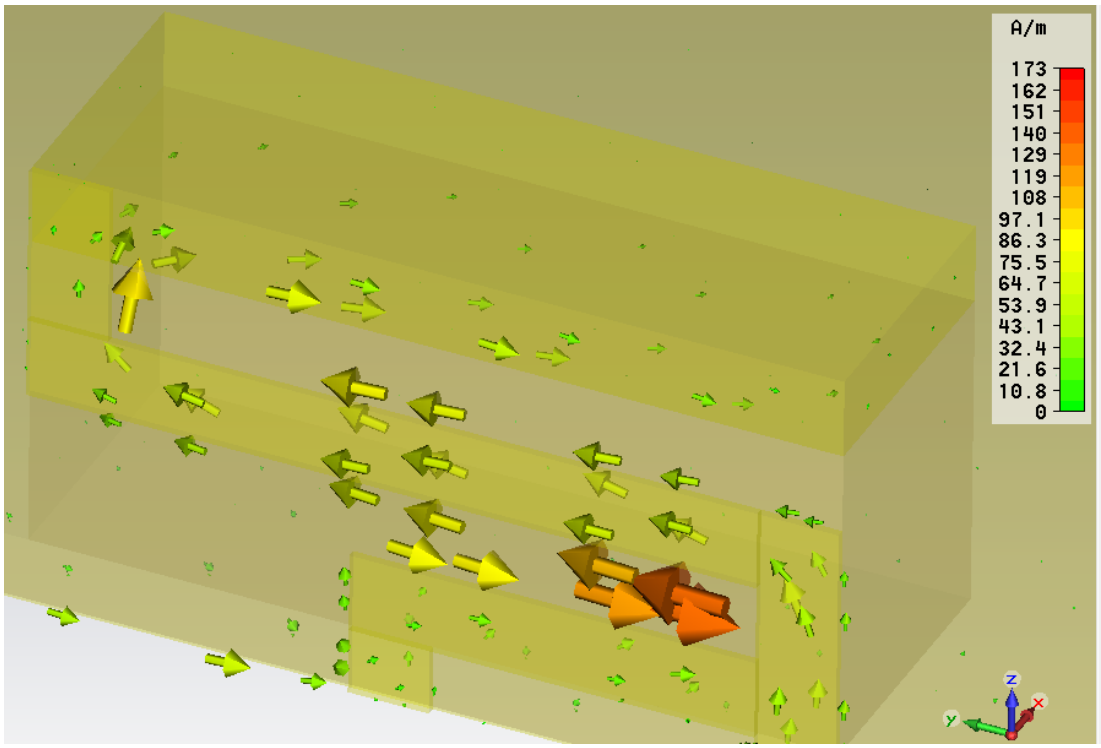

Figure 5.22 Surface current distribution on the final IFA design

A summary of the IFA designs introduced in this chapter is shown in Table 5.2. Compared with the other four designs, although the proposed final design has slightly larger dimensions, it reveals the best radiation performance. The bandwidth of the proposed IFA is notably wider than that of the other designs. Moreover, the proposed design has a high efficiency of 90%, which is only 2% lower than the efficiency of the second design, but higher than the others'.

Table 5.2 Summary of the IFA designs

Antenna Design	*Overall Dimensions* (mm^3)	*Bandwidth*	*Rad. Efficiency (Resonant Freq.)*
Initial Design	8 × 4 × 3	46 MHz	77%
Second Design	10 × 4 × 3	71 MHz	92%
Third Design	8 × 4 × 3	57 MHz	72%
Fourth Design	10 × 4.5 × 3.6	102 MHz	84%
Final Design	10 × 5 × 3.5	111 MHz	90%

5.5.3 Parametric Analysis of Antenna Dimensions

In this section, the effects of different antenna dimensions on the radiation performance of the proposed IFA are investigated. The variation of operating frequency and impedance bandwidth with the change of antenna dimensions is monitored for S_{11} values that are less than -10 dB. The parameters observed include the substrate thickness (H_s), the top radiating metal patch thickness (H_p) and the distance between shorting and feeding (D).

5.5.3.1 Substrate Thickness

The simulated reflection coefficient for various substrate thicknesses are plotted in Figure 5.23. It is noted that the operating frequency decreases as the thickness increase. However, the decrease in frequency is insignificant when the substrate thickness is larger 4 mm. On the other hand, the impedance bandwidth increases with the increase of the substrate thickness. The bandwidth of the proposed antenna is increased from 108 MHz to 116 MHz when the substrate thickness is varied from 3.5 mm to 5 mm. The minimum S_{11} is -39 dB at 2.45 GHz, with substrate thickness of 4 mm.

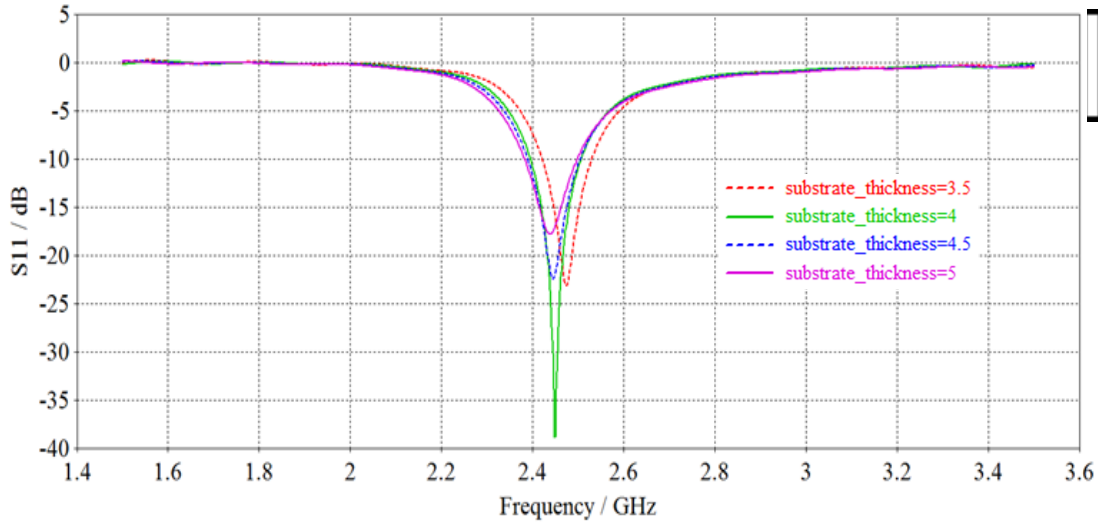

Figure 5.23 The effects of varying substrate thickness on reflection coefficient (radiating patch thickness H_p: 1 mm)

5.5.3.2 Top Radiating Metal Patch Thickness

The simulated S_{11} when the metal thickness is varied is shown in Figure 5.24 and Figure 5.25. Figure 5.24 is the simulation results of the proposed antenna with a constant substrate thickness of 4 mm. Figure 5.25 is obtained from the simulation where the antenna height is set as a constant of 5 mm. In the latter case both metal thickness and substrate thickness are varied accordingly.

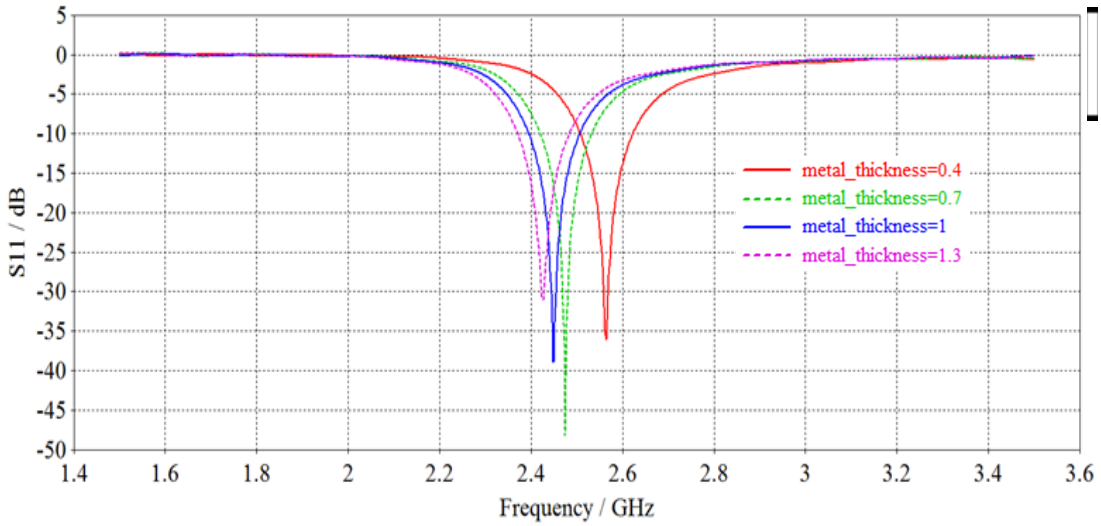

Figure 5.24 The effects of varying radiating patch thickness on reflection coefficient (substrate thickness H_s: 4 mm)

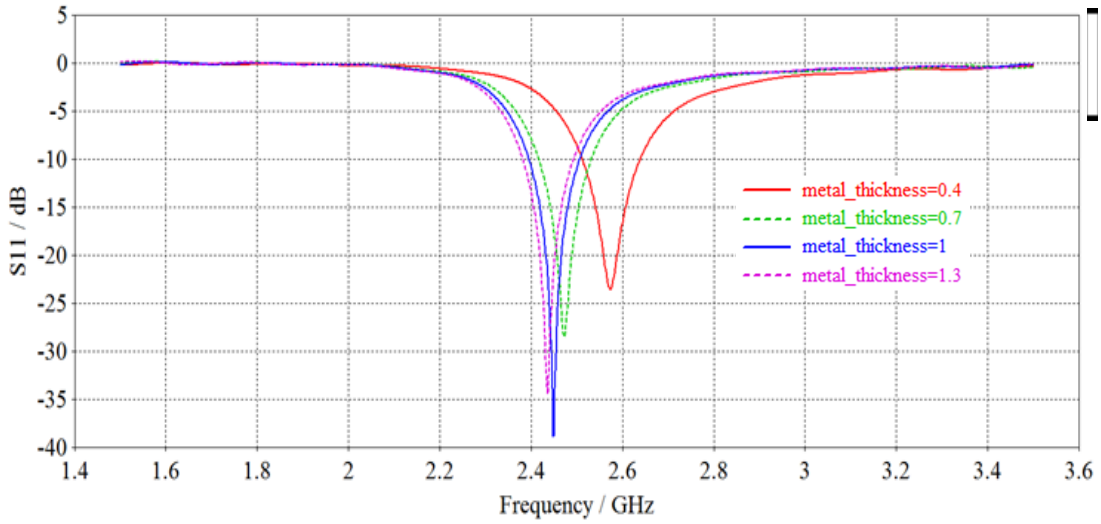

Figure 5.25 The effects of varying radiating patch thickness on reflection coefficient (antenna height H: 5 mm)

As shown in both Figure 5.24 and Figure 5.25, the operating frequency is reduced when the thickness of the radiating patch is increased. However, this also comes with a trade-off in narrower impedance bandwidth.

5.5.3.3 Distance between shorting and feeding

Another parameter that is observed is the distance between shorting and feeding, D, shown in Figure 5.26. The impedance of the proposed IFA can be controlled through the distance of the feed to the shorting point. The closer the feed is to the shorting point, the smaller the impedance is. Therefore, the proposed IFA can have its impedance tuned with this parameter. By adjusting the distance, the antenna bandwidth can be optimized. An optimum distance of 4 mm is selected in our case for the best performance.

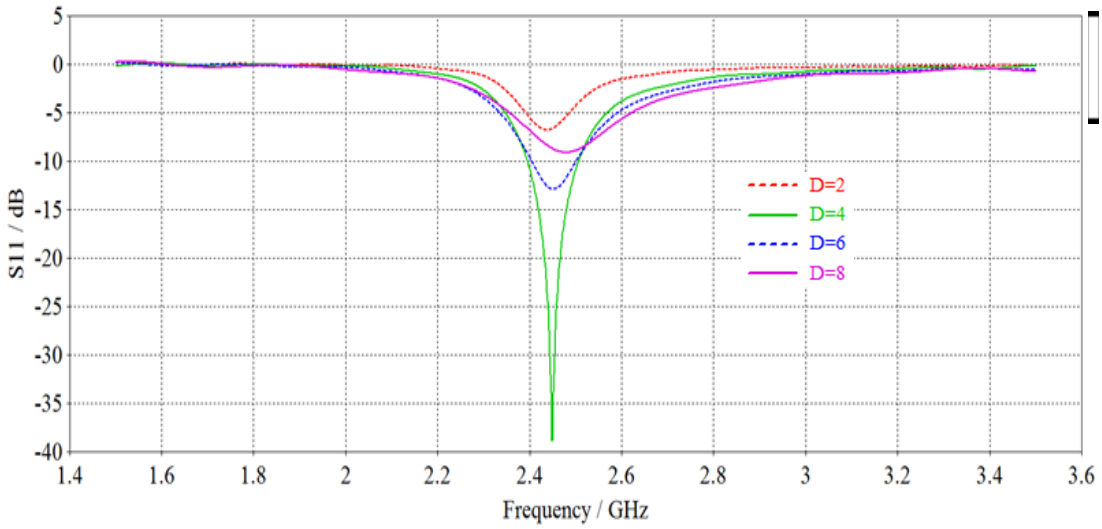

Figure 5.26 The effects of varying distance between shorting and feeding

5.5.4 Test Board and Ground Plane Effects on the Performance of the Proposed IFA

This section studies the effects of size and shape of test board and ground plane on the antenna radiation performance. Results from investigations on the performance of the proposed IFA mounted on a test board (full ground) with various size and shapes will be discussed. Orientation and position of the antenna on a fixed-size test board will be analyzed as well. The purpose of this study is to illustrate the characteristics

of the IFA on a finite test board such as resonant frequency, impedance bandwidth and radiation pattern.

Figure 5.27 demonstrates the model setup of the proposed IFA in CST to simulate the effects of test board and ground plane on the antenna radiation performance. The antenna is placed in the middle of one edge of a FR4 test board (thickness: 0.8 mm) with variable edge length L1. L2 is the length of the test board edge perpendicular to the longer edge of the antenna and D1 is the distance between the antenna feeding and the edge of the test board.

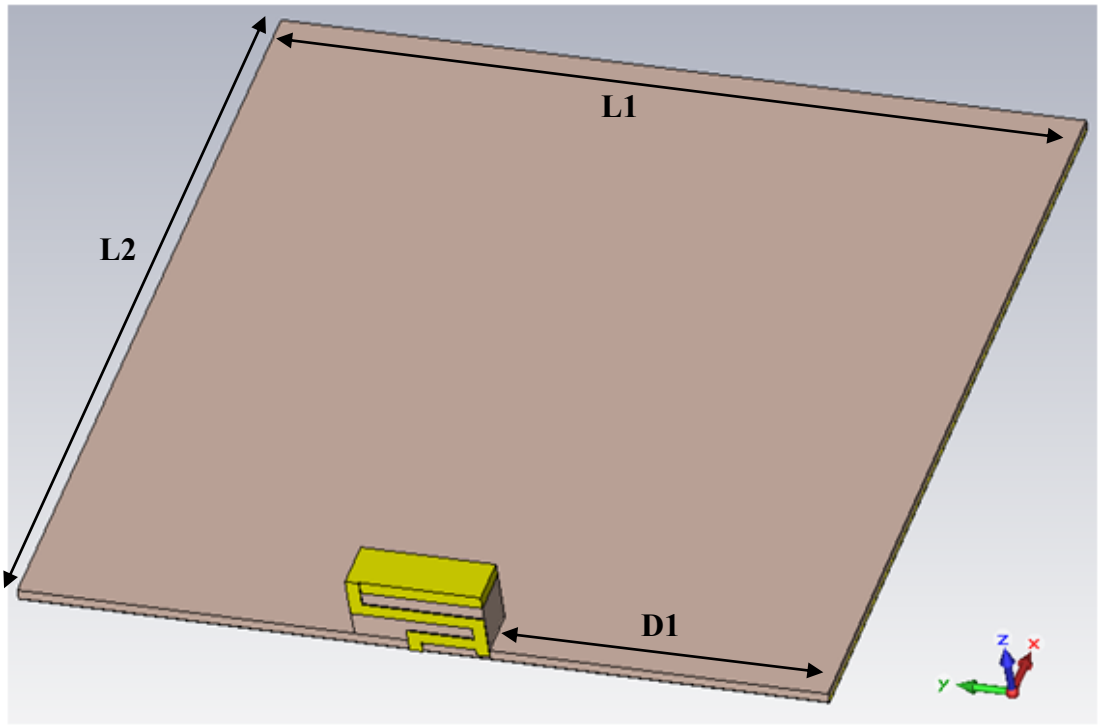

Figure 5.27 Model setup in CST to study the effects of test board and ground plane on the IFA radiation performance

Values ranging from 30 to 130 mm for dimension L1 and L2 are used to simulate the characteristics of the antenna. Simulation results are demonstrated in Figure 5.28 and Figure 5.29 for resonant frequency and impedance bandwidth, respectively. Previous researches from other authors [108-112] showed that the impedance of an antenna is a damped oscillating function of ground plane dimensions. Since resonant frequency and impedance bandwidth are related to the impedance of the antenna, they should have similar behaviours, which can be observed in Figure 5.28 and Figure 5.29.

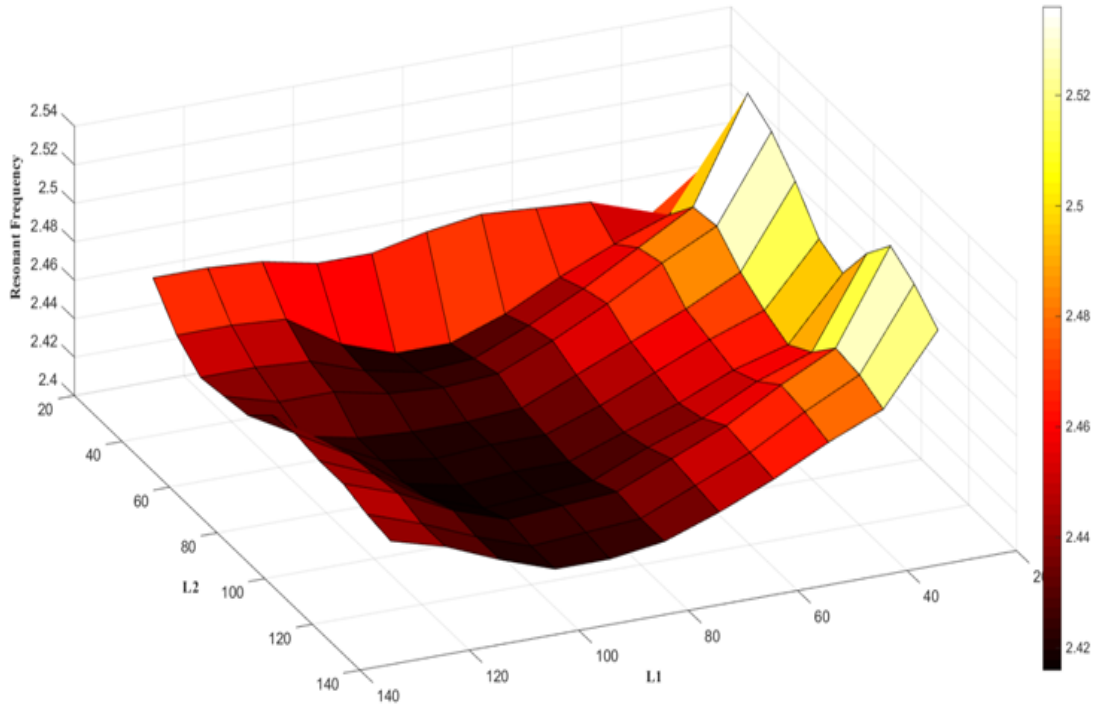

Figure 5.28 Computed resonant frequency versus dimensions of the test board and ground plane

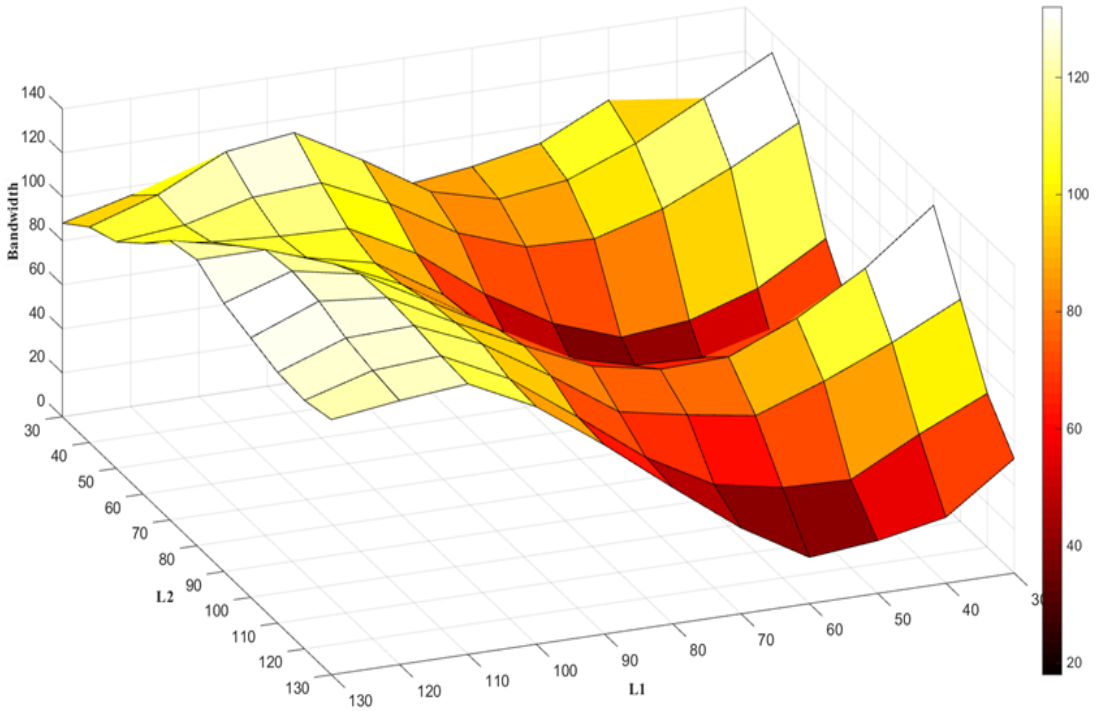

Figure 5.29 Computed impedance bandwidth versus dimensions of the test board and ground plane

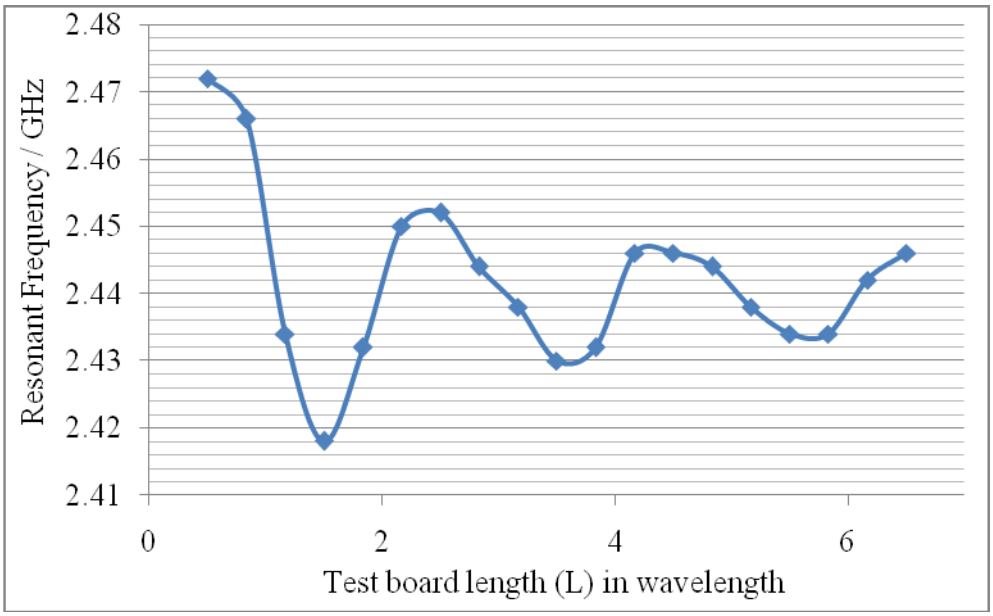

Figure 5.30 Resonant frequency of the proposed IFA mounted on square test board of various sizes

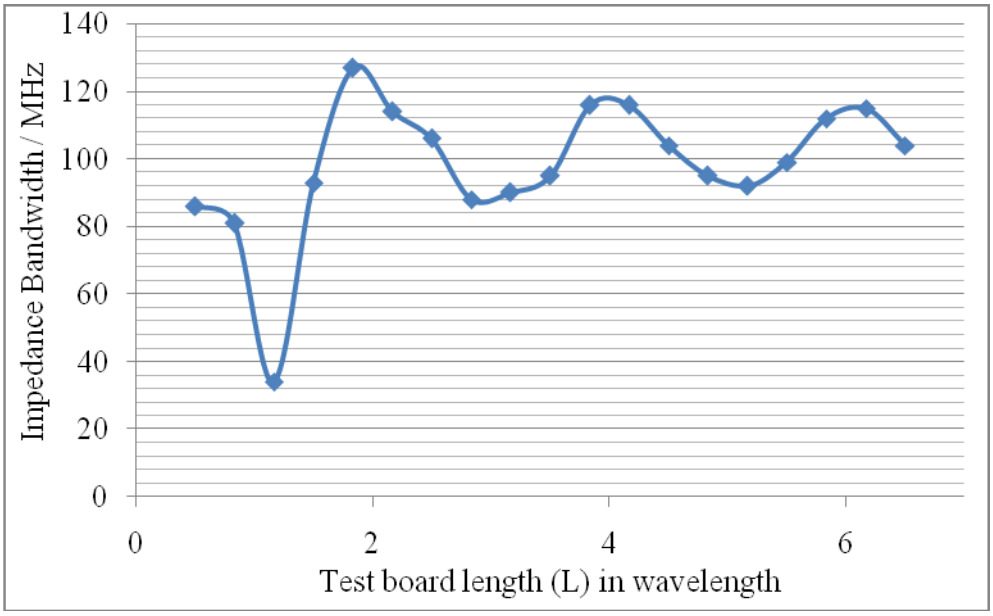

Figure 5.31 Impedance bandwidth of the proposed IFA mounted on square test board of various sizes

In fact, the resonant frequency and bandwidth of the IFA oscillate as the dimensions of test board and ground plane increase and converge to the values for that the IFA mounted on an infinite test board. It should be mentioned that, according to the simulation results, the effects of L2 on resonant frequency and impedance bandwidth are becoming less significant with the increase of L1.

Specially, the resonant frequency and impedance bandwidth of the IFA on a square test board (L1 = L2 = L) with various sizes are studied, as shown in Figure 5.30 and Figure 5.31. The convergence properties can be clearly observed for both resonant frequency and impedance bandwidth of the proposed IFA on a square test board with full ground. As shown in the figure, the resonant frequency and impedance bandwidth oscillate with the test board size and converge toward a value as the test board size increases.

Therefore, without changing the design of the proposed IFA, its operating frequency and bandwidth can be slightly tuned by adjusting the dimensions of the test bench on which the antenna is mounted.

Radiation patterns of the IFA mounted on both rectangular and square test boards are computed at resonance to illustrate the radiation behaviour. As indicated in Figure 5.32 and Figure 5.33, the direction of maximum radiation is significantly affected by the size of test board and ground plane. For both rectangular and square shape, as the test board increases in size, the main lobe and back lobe of the radiation are split into two, respectively. The four lobes form a pattern similar to the clover leaf pattern, seen on centre-fed dipoles that are 3/4-wavelengths long.

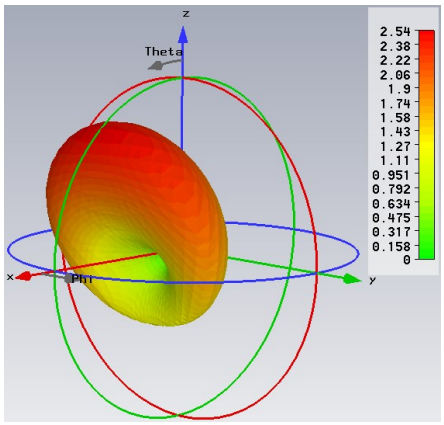

(a) L1 = 40 mm, L2 = 80mm

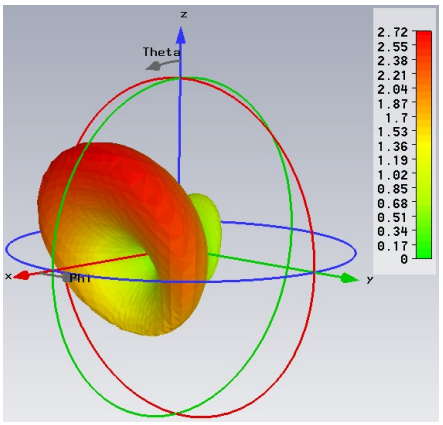

(b) L1 = 40 mm, L2 = 120mm

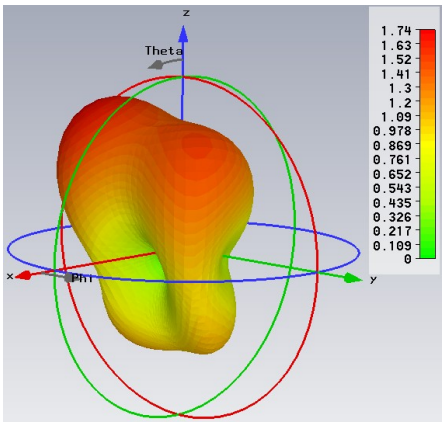

(c) L1 = 80 mm, L2 = 40mm

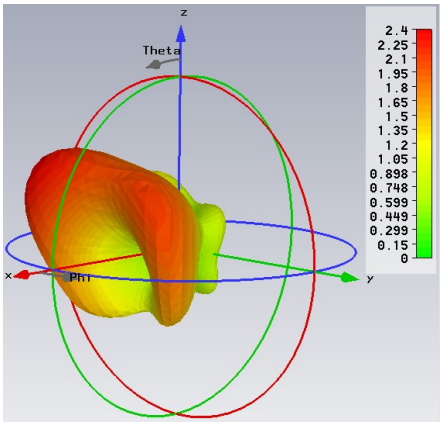

(d) L1 = 80 mm, L2 = 120mm

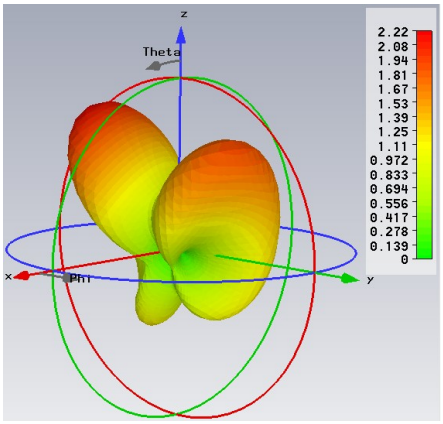

(e) L1 = 120 mm, L2 = 40mm

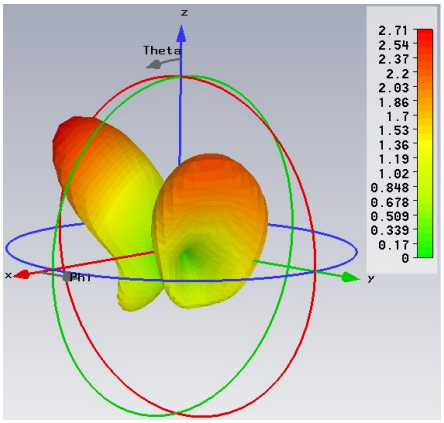

(f) L1 = 120 mm, L2 = 80mm

Figure 5.32 Radiation patterns of the proposed IFA at resonance mounted on rectangular test board of various dimensions

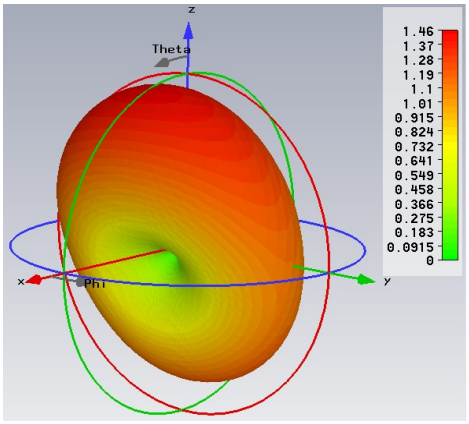

(a) L = 30 mm

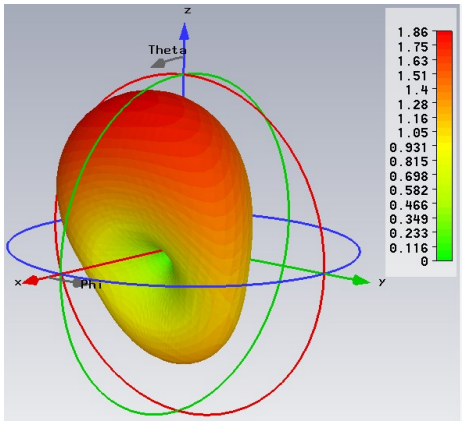

(b) L = 50 mm

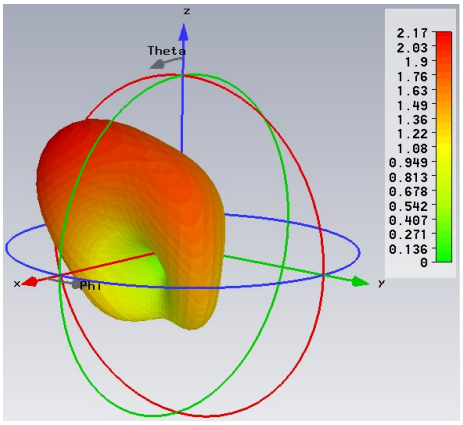

(c) L = 70 mm

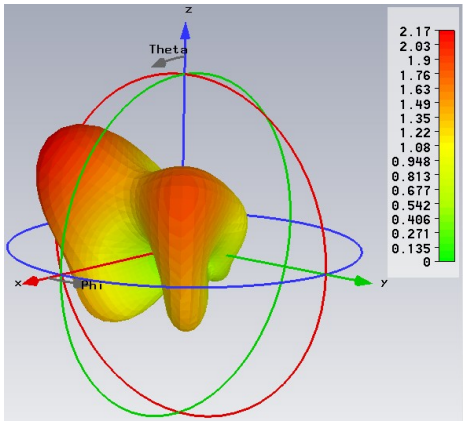

(d) L = 90 mm

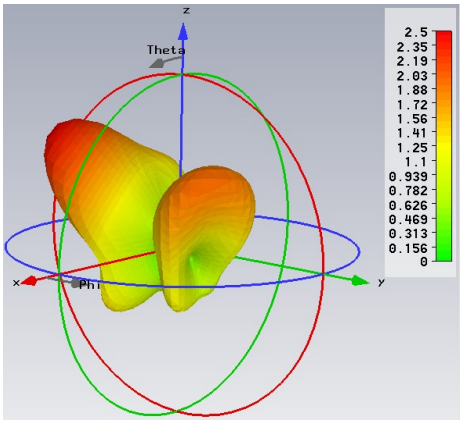

(e) L = 110 mm

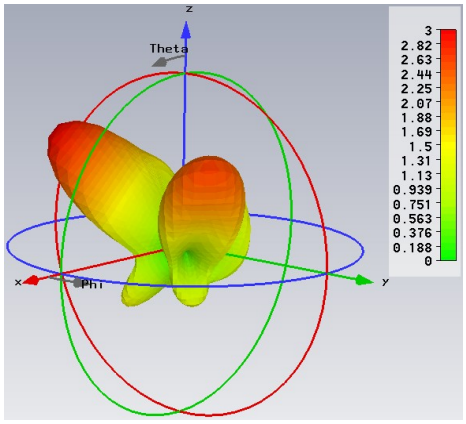

(f) L = 130 mm

Figure 5.33 Radiation patterns of the proposed IFA at resonance mounted on square test board of various sizes

Computations are also performed to study the effect of antenna location on the radiation performance. Simulated resonant frequency and impedance bandwidth of the proposed IFA mounted at various distances (D1, as shown in Figure 5.27) to the edge of a square test board of fixed size (130×130 mm^2) are illustrated in Figure 5.34 and Figure 5.35. Depending on the distance, the values of resonant frequency and impedance bandwidth are approximately "W"-shaped. Higher resonant frequency and larger bandwidth are observed at the centre and both ends. The radiation pattern is affected strongly by the location of the IFA on the test board as shown in Figure 5.36. It should be noted that the direction of main lobe and the number of side lobes vary with the distance (D1) from the antenna feeding to the edge of test board parallel to the shorter edge of the antenna. Therefore, the position of the proposed IFA on the test board should be carefully decided based on the application requirements to obtain suitable radiation performance.

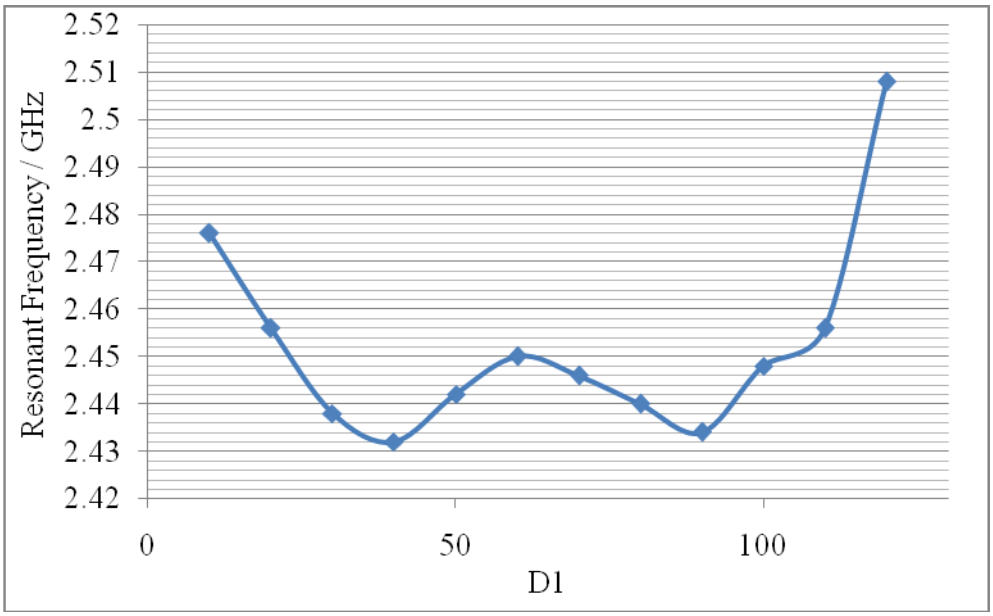

Figure 5.34 Resonant frequency of the proposed IFA mounted at various positions of a square test board of 130×130 mm^2

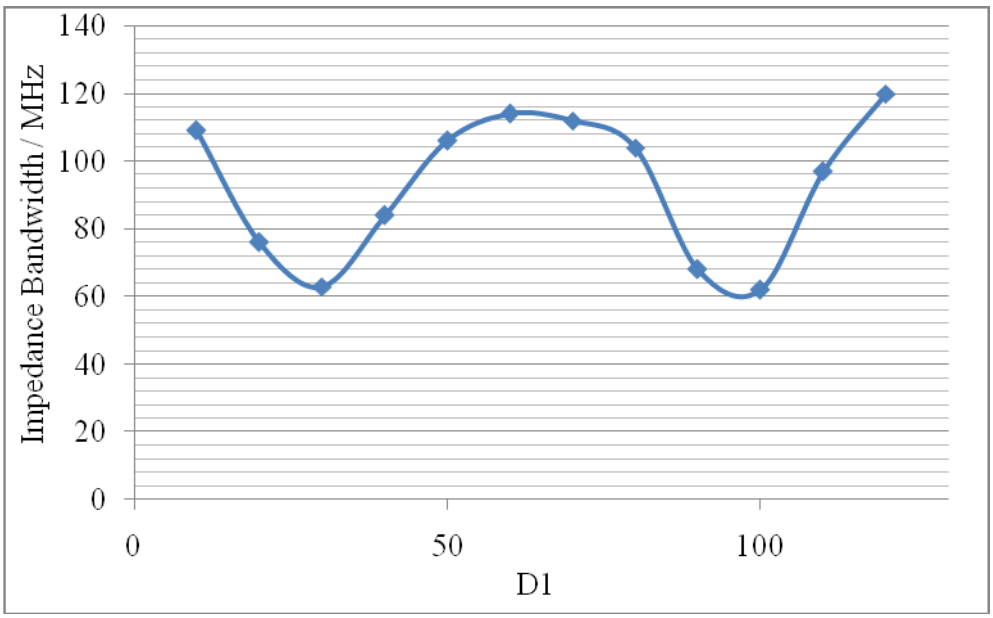

Figure 5.35 Impedance bandwidth of the proposed IFA mounted at various positions of a square test board of 130×130 mm^2

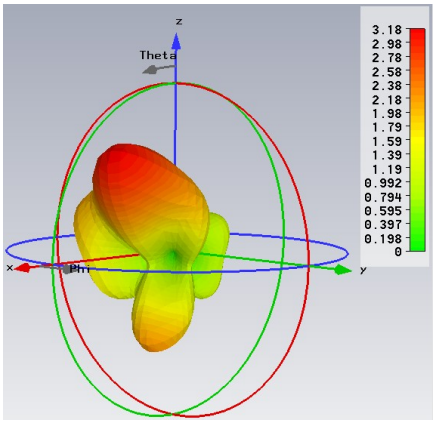

(a) D1 = 10 mm

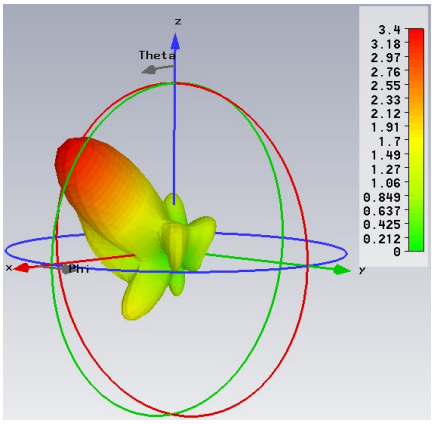

(b) D1 = 30 mm

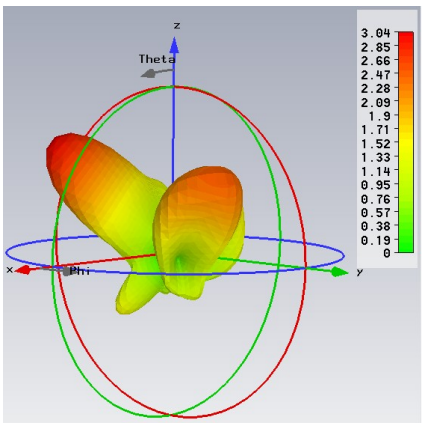

(c) D1 = 50 mm

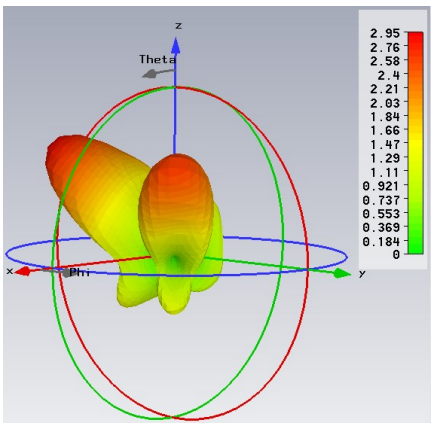

(d) D1 = 70 mm

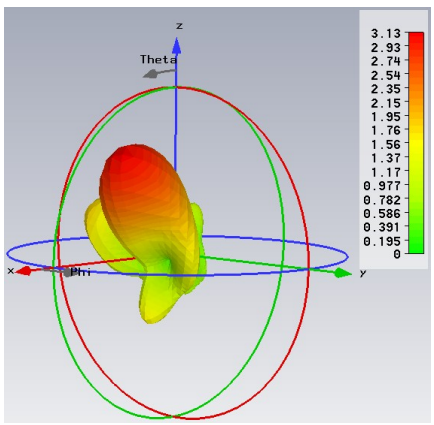

(e) D1 = 90 mm

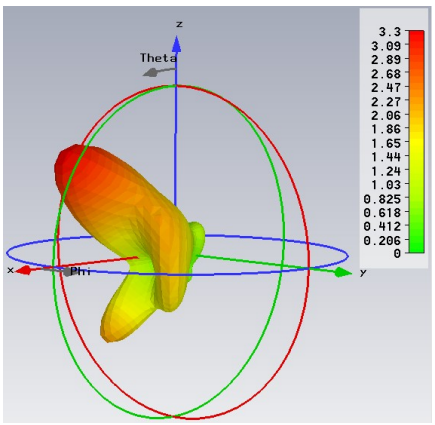

(f) D1 = 110 mm

Figure 5.36 Radiation patterns of the proposed IFA at resonance mounted at various positions of a square test board of 130×130 mm^2

5.5.5 Measurement Results

The fabricated antenna prototype for measurement is shown in Figure 5.37. To measure the radiation performance, the test antenna is mounted on a 0.8 mm-thick FR 4 board (L1 = 80 mm, L2 = 40 mm, D1 = 10 mm). The simulated and measured reflection coefficient is demonstrated in Figure 5.38. It is noted that there is a good consistency between the simulation and measurement results. The proposed IFA operates from 2.38 GHz to 2.5 GHz, which covers the frequency band of Wi-Fi 2.4 GHz. As to the total radiation efficiencies illustrated in Figure 5.39, the values are all larger than 70% across the operating frequency range and the maximum efficiency reaches 82%. Figure 5.40 depicts the measured radiation patterns. The proposed IFA has reduced backward radiation which is suitable for RF energy scavenging to power indoor sensor networks as in most cases the sensors are placed next to a wall.

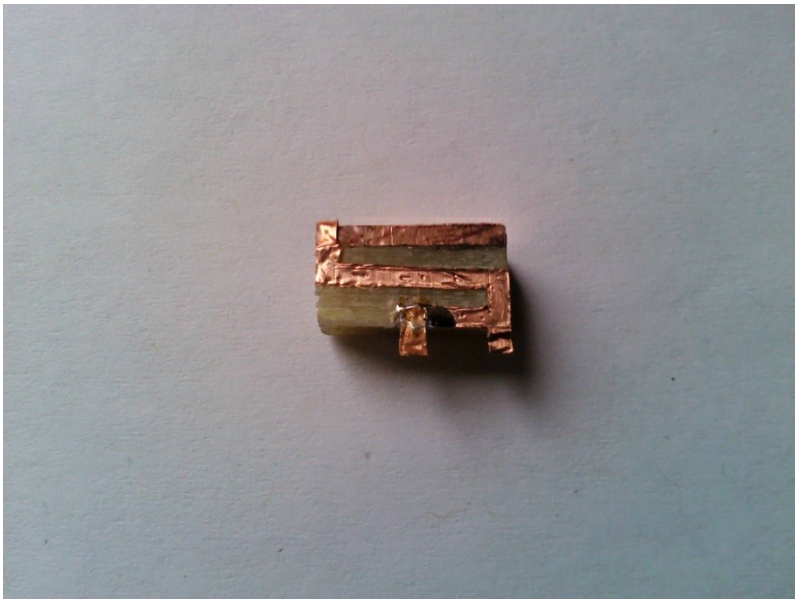

Figure 5.37 Prototype of the proposed miniature IFA

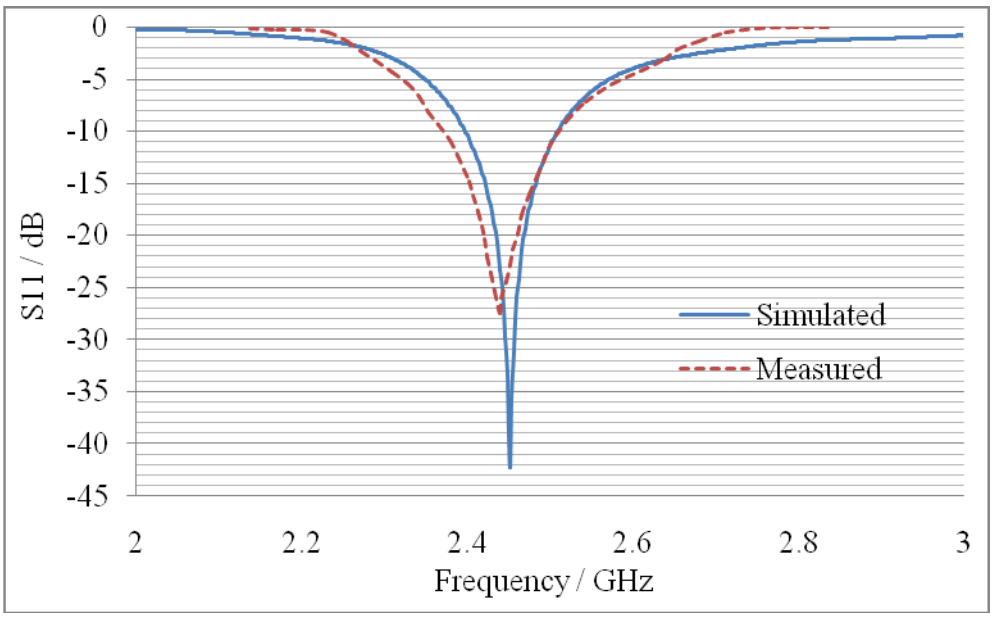

Figure 5.38 Simulated and measured reflection coefficient of the proposed IFA mounted on a test board of 80×40 mm^2

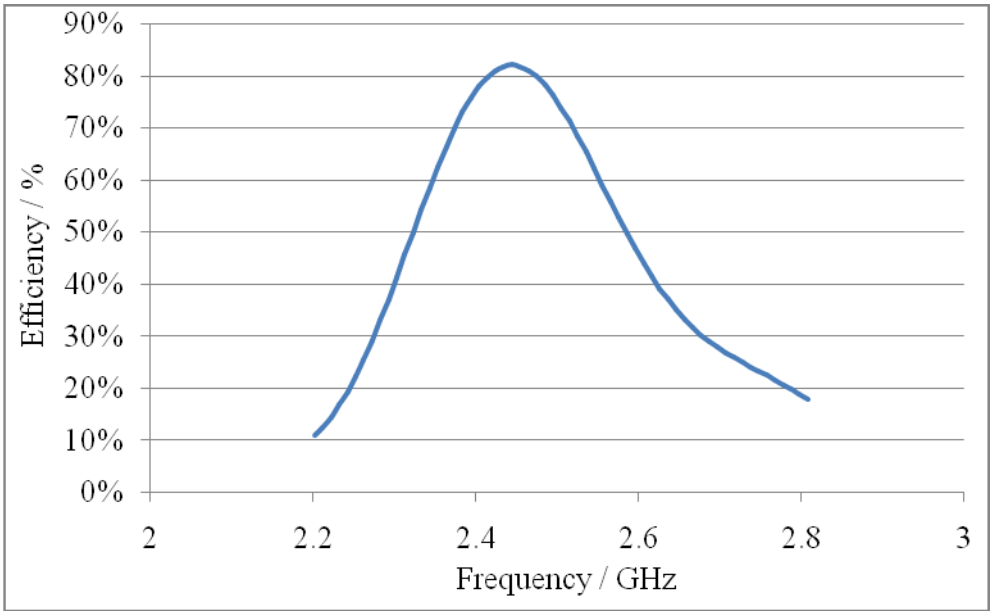

Figure 5.39 Measured Efficiency of the proposed IFA mounted on a test board of 80×40 mm^2

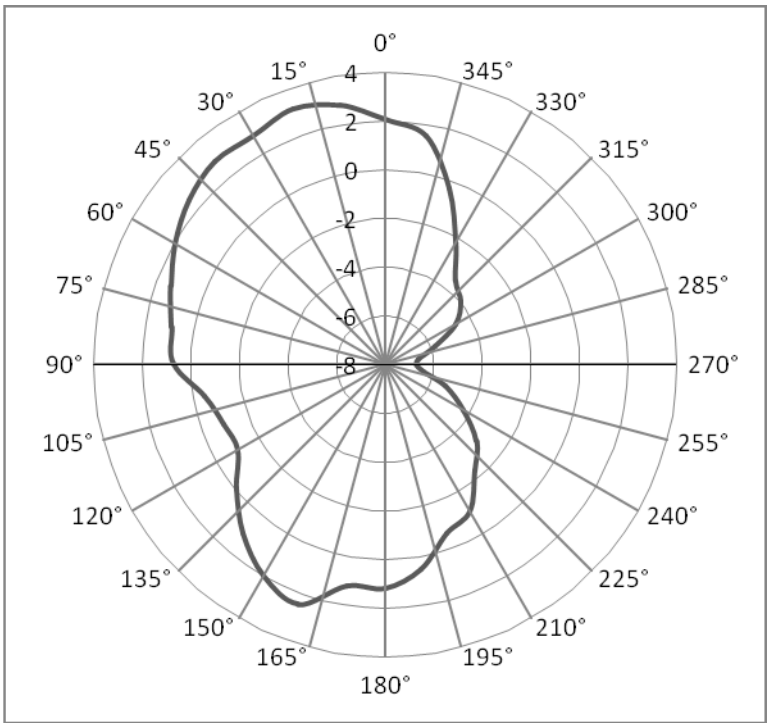

(a) E-plane

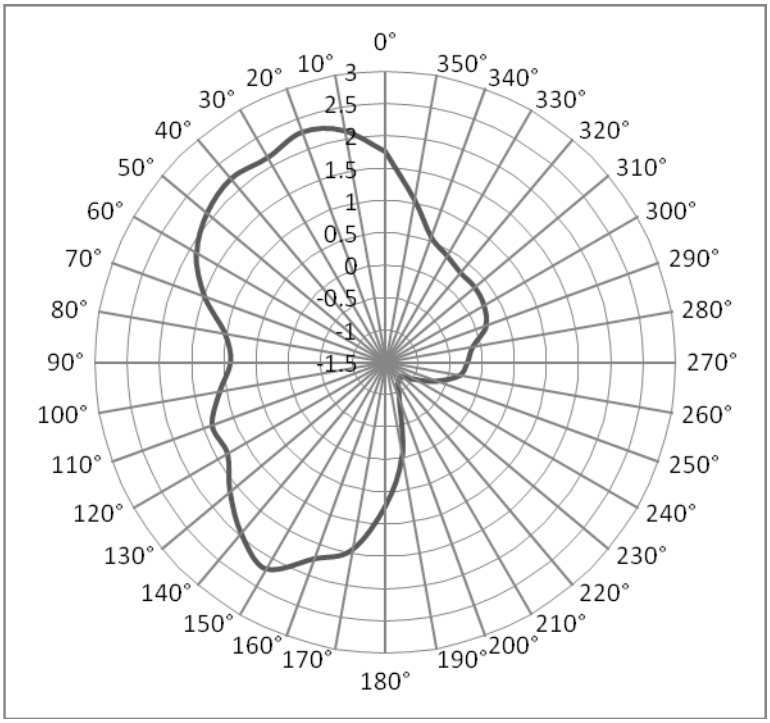

(b) H-plane

Figure 5.40 Measured radiation pattern at resonance of the proposed IFA mounted on a test board of 80×40 mm^2

5.6 Summary

Compared with multi band antennas discussed in chapter 4, Wi-Fi antenna usually has a much smaller size, which makes it possible to achieve small size array with enhanced power extraction ability for RF energy scavenging. Therefore, a novel miniaturized Inverted-F Antenna operating at Wi-Fi 2.4 GHz is proposed for indoor RF energy scavenging.

In summary, the investigation of the miniature IFA without empty space is illustrated in Figure 5.41. In this chapter, several inverted-F antennas designed in 3D structure have been investigated in order to develop a suitable miniature IFA for Wi-Fi energy scavenging to power indoor sensor networks. Different structures and techniques have been studied to enhance the radiation performance while maintain small antenna dimensions. The proposed final antenna design fabricated on a FR4 substrate has an overall size of only 10 (L) × 5 (H) × 3.5 (W) mm^3 to be embedded inside miniaturized systems and devices. Owing to no additional empty space, the circuit routing on the PCB is permitted underneath and around the antenna so that significant reduction in device size can be realized. Meandered lines and thick radiating patch are implemented to introduce additional inductance and capacitance for impedance matching. The effects of ground plane and test board on the radiation performance have also been investigated in this chapter. Dimensions of the test board are selected to be 80 × 40 mm^2 with a thickness of 0.8 mm for antenna measurement to verify the design strategies. The measured impedance bandwidth is about 120 MHz from 2.38 GHz to 2.5 GHz and the maximum efficiency is about 82%. The proposed antenna is of small volume, simple structure, light weight, low cost and requires no clearance region. Moreover, it achieves reduced backward radiation with appreciable efficiency across the operating frequency range. Above features make it suitable for miniaturized Wi-Fi energy scavenging systems.

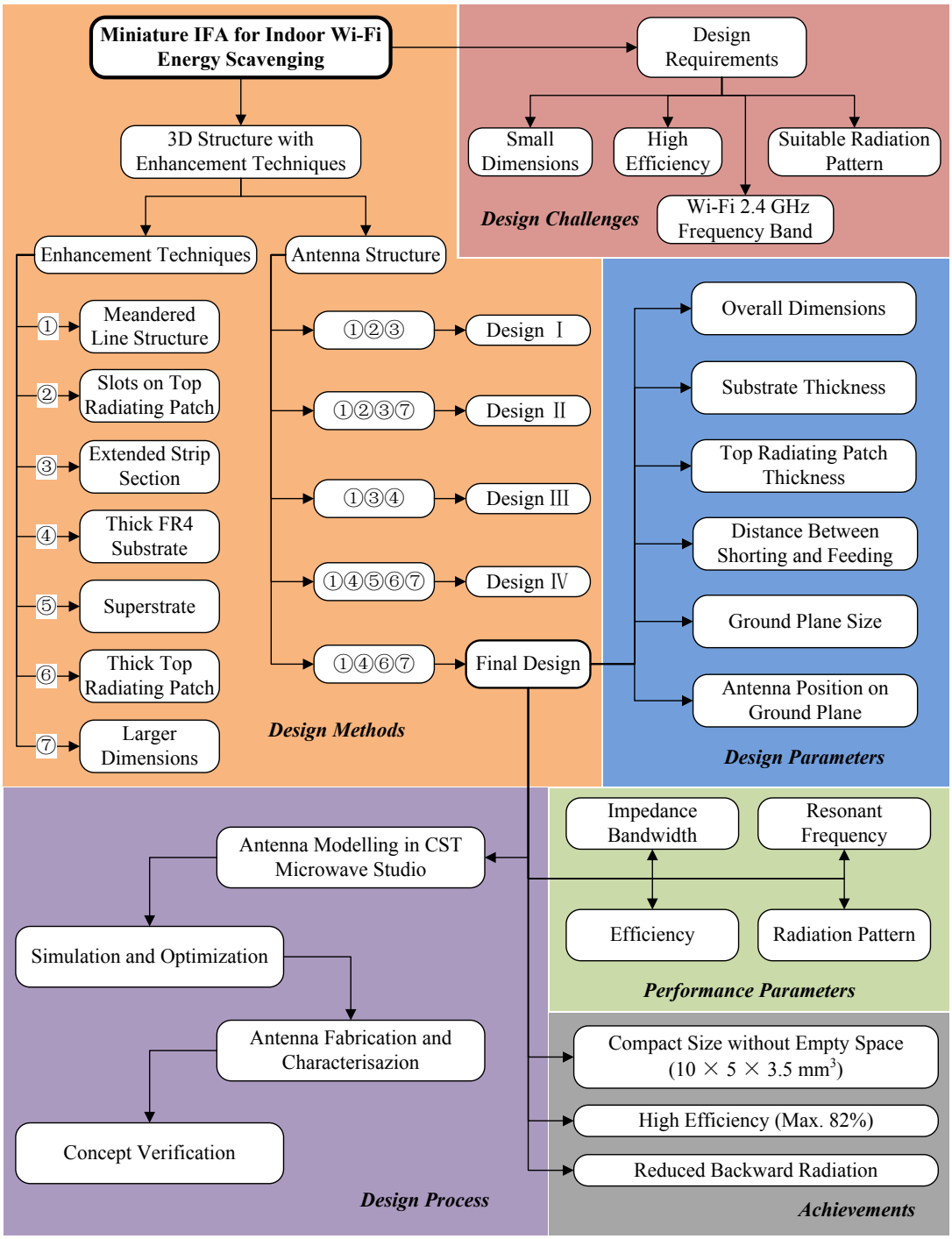

Figure 5.41 The investigation of the miniature IFA for indoor Wi-Fi energy scavenging

Chapter 6

Passive CMOS Charge Pump Rectifier

Non-Ohmic devices are utilized as the basic rectifying elements for all the rectifier designs. The I-V characteristics of these devices are asymmetric about the voltage axis and usually nonlinear. Physically, such structures take a number of forms, including mercury-arc valves, ignitrons, thyratrons, vacuum tube diodes, Silicon Controlled Rectifiers (SCR's), selenium oxide rectifiers and semiconductor diodes. Historically, even synchronous electromechanical switches and motors have been used. Today, semiconductor devices with a wide range of sizes and power handling capabilities dominate in practically all the rectifier applications, except for high power situations, where ignitrons and vacuum diodes are still used [12]. Generally the applications of the rectifier designs can be categorized into two distinct streams. One stream, deals with high frequency and low power level, mostly for microwave mixer and detector applications. The other stream constitutes traditional power electronics at high power level with low frequency. The work described in this chapter focus on the rectifier design at high frequency, low power level for RF energy scavenging.

6.1 Common Rectifier Architecture

6.1.1 Dickson Rectifier

Dickson rectifier consists of a cascade diodes / capacitors cells intended for low voltage purposes. The topology has been used in various applications of charge pumps and rectifiers for years. In RF energy scavenging system designs, Dickson rectifier is one of the most widely used topology.

6.1.1.1 Schottky based Dickson Rectifier

Schottky diodes are widely used in switch-mode power converters. When supplied with a load current, Schottky diodes usually have lower forward voltage drop compared with common semiconductor p-n junction diodes as higher orders of magnitude of reverse saturation currents is achievable for Schottky diodes. The low forward voltage drop results in less energy dissipation as heat, making the Schottky diode an ideal choice for applications sensitive to power efficiency. In addition, the Schottky diode is a "majority carrier" semiconductor device. With no current flow necessary to recover stored charge, smaller device size and faster transition is allowed. This is another reason for adopting the Schottky diode in power converter circuits. Schottky diode based Dickson rectifiers have been used for Passive RFID Tag Chips at UHF-Band [113] and RF-DC conversion in energy harvesting rectenna [114].

Figure 6.1 presents N-stage diode based Dickson rectifier circuit [115]. The RF input is fed into all stages in parallel through pump capacitors, while the final output is produced by adding up the load voltages across each load capacitors. Theoretically, the load voltage of each stage should be $2(V_{in} - V_{th})$. Therefore, the final output voltage of the N-stage rectifier is expressed as

$$\boldsymbol{V_{out} = 2N(V_{in} - V_{th})} \tag{6.1}$$

where V_{out} is the final load voltage, V_{in} is the AC amplitude of the input signal and V_{th} is the forward voltage drop of the diodes. As can be seen, V_{th} need to be as small as possible for higher output voltage (V_{out}). Moreover, the reverse current conducted

by a reverse biased diode is negligible compared with the forward current. Hence, decreasing the value of V_{th} reduces the output resistance while dose not significantly increase the reverse conduction loss. This also applies to, generally, all the other diode based rectifier topologies. Thus, Schottky diodes with low forward voltage drop (V_{th}) are usually used to obtain operation at low input level (V_{in}).

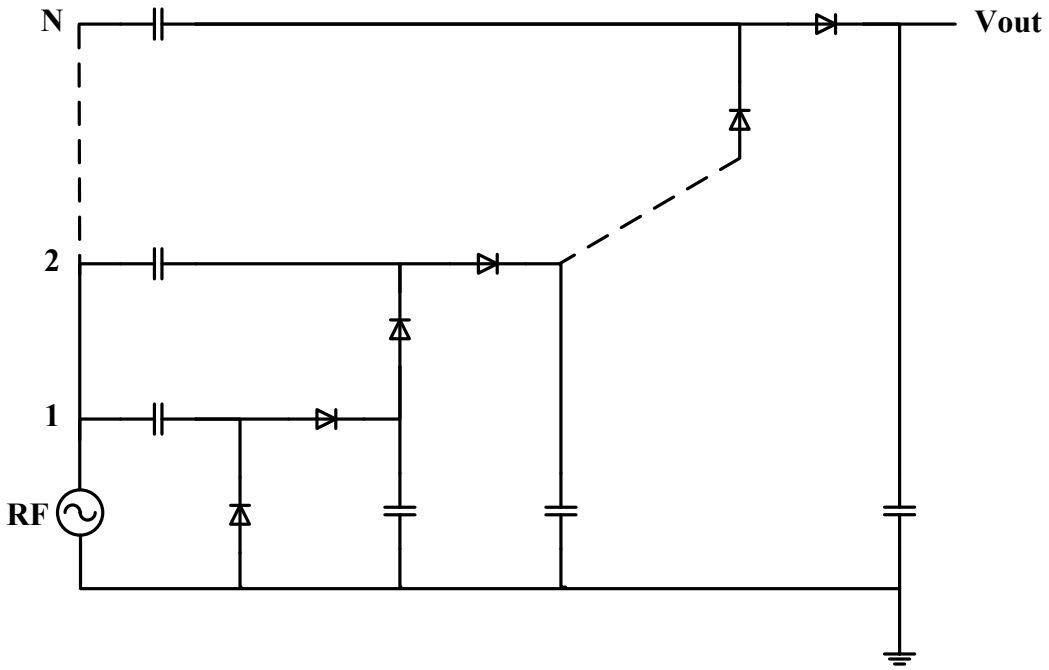

Figure 6.1 N-stage diode based Dickson rectifier circuit [115]

6.1.1.2 CMOS Implementation of Dickson Rectifier

With its particularity of manufacturing, Schottky diode cannot be implemented in standard CMOS process. In most cases, diode-connected MOS transistors are utilized in Dickson rectifier to make the integration of Schottky based rectifier compatible with CMOS implementation. Figure 6.2 depicts the CMOS implementation of Dickson rectifier. Diode-connected MOSFET are switched between saturation region and cutoff region during positive and negative input phases. The rectified output voltage of a N-stage rectifier, V_{out}, is given by

$$\boldsymbol{V_{out} = 2N(V_{in} - V_{ds})} \tag{6.2}$$

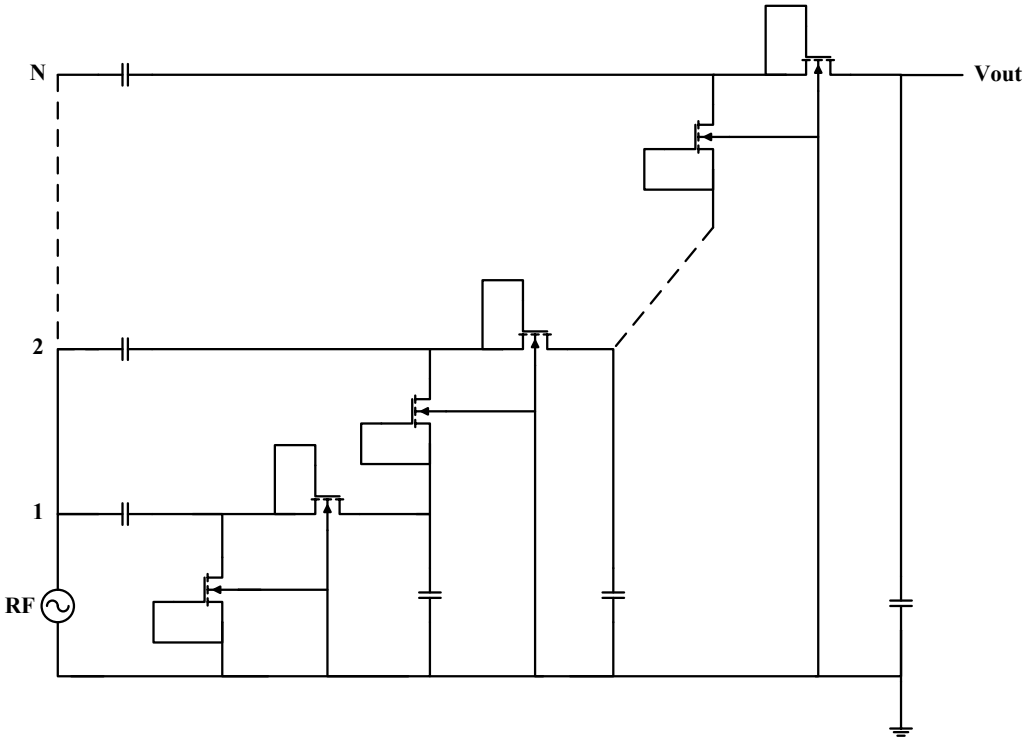

Figure 6.2 CMOS implementation of Dickson rectifier

where V_{in} is the voltage amplitude of the RF input and V_{ds} is the voltage between transistor drain and source terminal. Owing to short connecting between gate and drain, all the transistors operate in saturation region when turned on, therefore

$$\boldsymbol{V_{ds} = V_{gs} = V_{th} + \sqrt{\frac{2I_{ds}}{\mu_n C_{ox}}\left(\frac{L}{W}\right)}} \tag{6.3}$$

where V_{gs} is the voltage between gate and source, V_{th} is the threshold voltage of the transistor, I_{ds} is the drain-source current in saturation region, L/W is the ratio of transistor gate length to width, μ_n is charge-carrier effective mobility and C_{ox} refers to the capacitance (per unit area) of the oxide layer. According to equation (6.2), to obtain higher output voltage, we need V_{ds} to be small as possible. Hence, with limited L/W ratio, MOS transistors with low threshold voltage (V_{th}) should be adopted. However, threshold voltage of less than 100mV is not recommended because all transistors can be turned on simultaneously and result in severe reverse leakage [116].

6.1.2 Bridge Rectifier

Both polarities of AC input signal can be converted to DC signal of the same polarity through a full wave bridge rectifier which requires four diodes as shown in Figure 6.3 (a). If the input voltage is higher than the output voltage, in each signal cycle there will be one pair of diodes operating for rectification. One of the diodes (D_1 / D_3) regulates the current path from the load to the ground while the other one (D_4 / D_2) delivers the power to the load. Although the bridge rectifier has increased output power compared with half wave rectifier, it experiences voltage drop of two diodes in each signal cycle. The bridge topology is usually adopted for power electronics applications of low frequency and high power level, but in some cases the concept could be extended to high frequency, low power 'radio' region for wireless power transmission at radio frequency. Conventional CMOS implementation of the bridge rectifier using diode-connected transistors is illustrated in Figure 6.3 (b). For CMOS bridge rectifier, the power loss is mainly decided by the effective on-resistance of the diode-connected MOS transistors. Generally, small effective on-resistance can be achieved by minimizing the threshold voltage of the transistor.

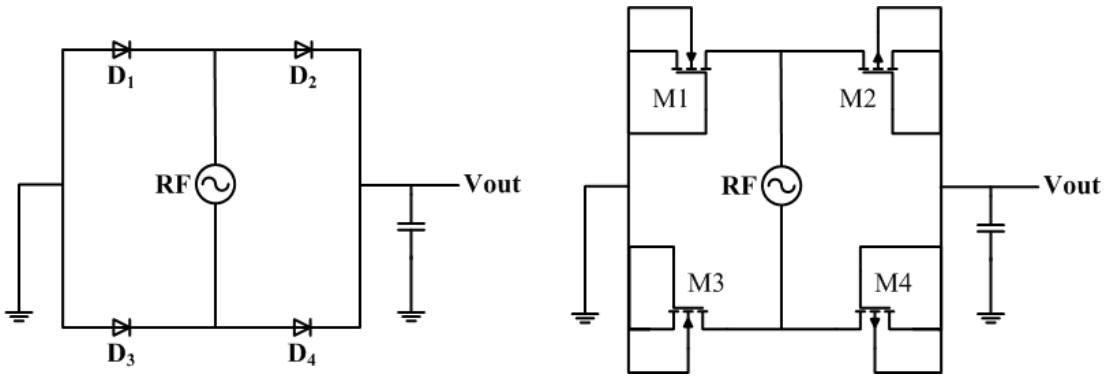

(a) (b)

Figure 6.3 Bridge rectifier: (a) diode bridge rectifier, (b) CMOS bridge rectifier

6.1.3 Threshold Voltage Cancellation Scheme

As threshold voltage (V_{th}) of the MOS transistor is one of the main parameters which affect the performance of the rectifiers, V_{th} – cancellation mechanisms are usually applied in practical design. These include External – V_{th} – Cancellation (EVC)

scheme [31], Internal $-V_{th}$ – Cancellation (IVC) scheme [117], Self $-V_{th}$ – Cancellation (SVC) scheme [118] and Differential $-V_{th}$ – Cancellation (DVC) scheme [119].

6.1.3.1 External – V_{th} – Cancellation Scheme

For CMOS rectifier circuit, maximum output voltage is obtained when the threshold voltage of the MOS transistor is negligible. In the External – V_{th} – Cancellation (EVC) scheme, to compensate the threshold voltage, external bias voltage is applied between the gate and drain terminals of each transistor as demonstrated in Figure 6.4. Thereby the threshold voltage is equivalently changed from V_{th} to $V_{th} - V_{bth}$. If the bias voltage is nearly equal to the threshold voltage, the equivalent threshold voltage can be expected to be approximately zero. Therefore, the power loss due to transistor voltage drop can be minimized and operation with small RF signals is possible. However, the gate bias voltage is generated using switch-capacitor (SC) mechanism which requires external power supply and clocking. This means the EVC scheme is only applicable for active or semi-passive applications.

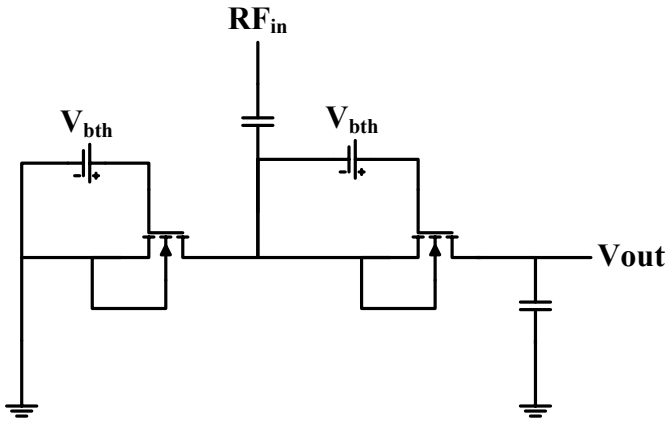

Figure 6.4 External – V_{th} – Cancellation Scheme

6.1.3.2 Internal $-V_{th}$ – Cancellation Scheme

The Internal $-V_{th}$ – Cancellation (IVC) scheme is depicted in Figure 6.5. Unlike the EVC scheme, gate bias voltage of the rectifying transistor is produced internally from the output voltage instead of external voltage supply. An IVC circuit consists of a bias transistor, a bias capacitor and a large bias resistor. The bias capacitor (C_{bp} /

C_{bn}) holds the threshold voltage of the rectifying transistor (M_p / M_n) by replicating the threshold voltage with the bias transistor (M_{pb} / M_{nb}). And the large bias resistor is added to reduce the leakage current in the IVC circuit. Each rectifying transistor should be equipped with one IVC circuit. It should be noted that due to its voltage division mechanism, the IVC scheme requires high RF input power and voltage to obtain high conversion efficiency.

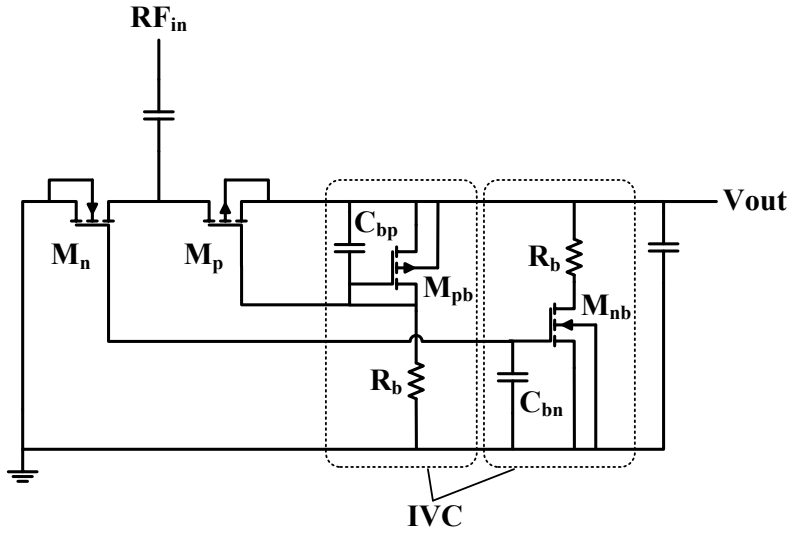

Figure 6.5 Internal –V_{th} – Cancellation Scheme

6.1.3.3 Self –V_{th} – Cancellation Scheme

Figure 6.6 presents the Self –V_{th} – Cancellation (SVC) scheme. It is similar to the conventional diode-connected configuration, but the gate electrodes of the n-type and p-type MOS transistors in the SVC scheme are cross connected to the DC output voltage and ground, respectively. In this way, gate-source voltages of the transistors are boosted by the output voltage which equivalently decreases the effective threshold voltage. Compared with IVC scheme, SVC scheme has a simpler structure and gives better performance at low input power level. However, as the MOS transistor is statically biased by the DC output, the reverse leakage current is increased with the decrease of the effective threshold voltage of the transistor. It is not possible to achieve small on-resistance and small reverse leakage at the same time.

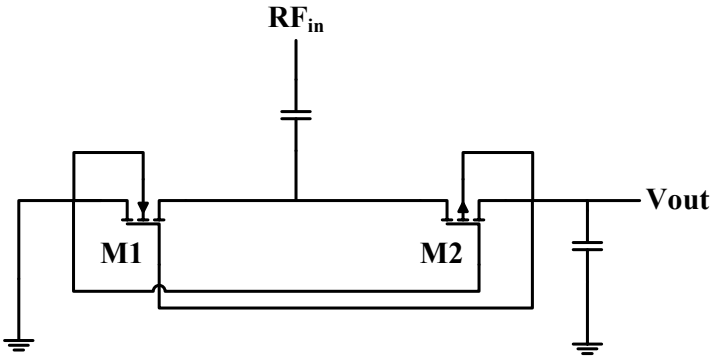

Figure 6.6 Self –V_{th} – Cancellation Scheme

6.1.3.4 Differential – V_{th} – Cancellation Scheme

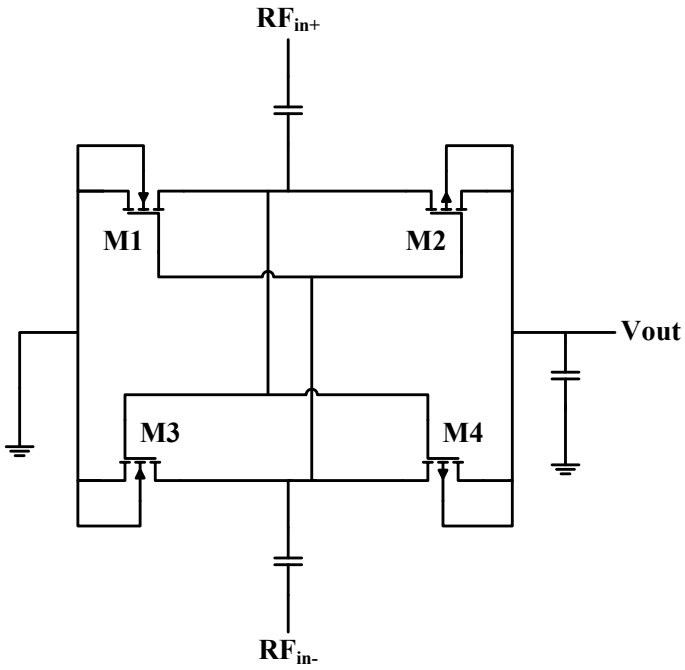

Figure 6.7 Differential –V_{th} – Cancellation Scheme

As has been introduced, if the gate-source voltage of a transistor is statically biased to compensate the threshold voltage constantly, smaller effective on-resistance can be obtained in forward bias condition. Nevertheless, it leads to increased reverse leakage current when the bias voltage is too large or, in other words, the effective threshold voltage is too small. As a result, small on-resistance and small reverse

leakage current cannot be achieved simultaneously by static V_{th} – cancellation techniques. In [119], an active differential $-V_{th}$ – Cancellation (DVC) CMOS rectifier is proposed based on the bridge topology. As shown in Figure 6.7, it consists of a cross-coupled configuration where the gate of the transistor is actively biased by the differential input signal. In the positive input cycle, the gate of n-type transistor M3 (M1) is positively biased, and the effective threshold voltage is effectively decreased, resulting in small on-resistance. Whereas, in the negative input cycle, the gate voltage drops rapidly and the transistor is reversed biased. This equivalently increases the threshold voltage of the transistor and effectively reduces the reverse leakage current. Similar situation applies to the p-type transistor M2 and M4. The combination of two cross-connected gate structures makes a complementary CMOS bridge rectifier. Detailed analysis for the operation of the cross-coupled topology can be found in [120].

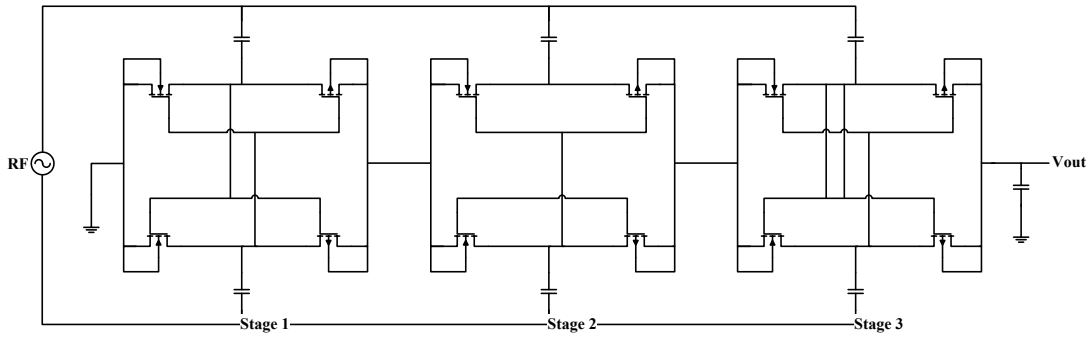

Figure 6.8 Rectifier formed by cascading 3 stages in series.

To increase the output voltage, several cells of the differential drive rectifier can be cascaded in series. Figure 6.8 demonstrates the resultant circuit when 3 cells are adopted. The first cell is connected directly to the RF input and the following stages are capacitively coupled to the RF input, which behaves as a charge pump.

Although the differential drive synchronous bridge rectifier has advantage of high conversion efficiency due to the active V_{th} – cancellation scheme, its application for RF energy scavenging is limited. From the circuit point of view, the input signal should be exactly square wave of large enough amplitude in order to generate the maximum output voltage. Operation with sinusoidal input will result in lower

efficiency since the transistors only turn on for part of the input cycle. From the system point of view, as differential input is required, the space and performance requirements for antenna and circuit design are much stricter. Therefore, the differential drive bridge rectifier is usually considered for power transfer through inductive resonance coupling using magnetic coils. However, in this case the effective distance of the coils has to be maintained within several inches unless larger coils are used to create a stronger magnetic field [121].

6.2 Proposed CMOS Rectifier Topology

6.2.1 Structure and Operation

As Schottky diode is not suitable for practical applications due to its temperature dependence and costly fabrication process, our research interest focus on the CMOS rectifier design for miniature RF energy scavenging system. In order to reduce the effective threshold voltage of MOSFET, bootstrapping capacitors are used. Hence, higher output voltage can be achieved with reduced voltage drop. Moreover, multi-stage topologies are also studied for output voltage enhancement.

The proposed single stage rectifier circuit and its corresponding block diagram are shown in Figure 6.9. It consists of a main path transistor M_1, a bootstrapping circuit (M_{b1} and C_{b1}) and a load capacitor C_1. At start up, the leakage current turns on M_1 in sub-threshold region, forming a path to provide the required current to pre-charge C_{b1} via M_{b1}.

To prevent the reverse leakage current, main paths transistor M_1 is expected to turn on fully when the input voltage V_i is higher than the output voltage V_o and turn off immediately as V_i is lower than V_o. As can be seen, the gate voltage of M_1 and M_{b1}, V_{cap}, is a threshold voltage lower than the output voltage. That is to say, $V_{cap} = V_{out} - |V_{th1}|$, where $|V_{th1}|$ is the threshold voltage of M_{b1}. Thus, M_1 turns on when

$$V_i > V_o - |V_{th1}| + |V_{th}| \tag{6.4}$$

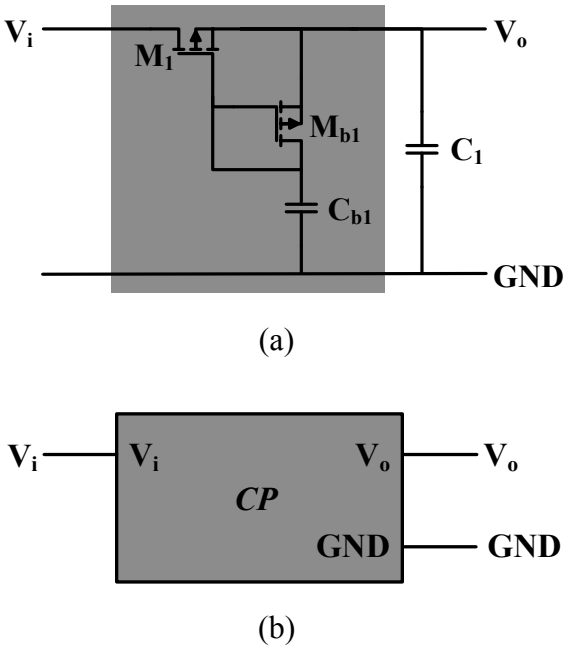

Figure 6.9 Proposed single stage rectifier: (a) circuit, (b) block diagram

where V_{th} is the threshold voltage of M_1. Similarly, M_1 turns off if

$$V_i < V_o - |V_{th1}| + |V_{th}| \tag{6.5}$$

The voltage drop is reduced if $|V_{th1}|$ is close to $|V_{th}|$. Therefore, for a given input voltage source, the use of bootstrapping circuit could result in increasing the output voltage with a typical MOSFET threshold voltage. This becomes increasingly significant to low input CMOS integrated circuit where threshold voltage of MOSFET cannot be ignored compared with input voltage. Figure 6.10 illustrates the waveforms of input and output voltage of the single stage rectifier at steady state.

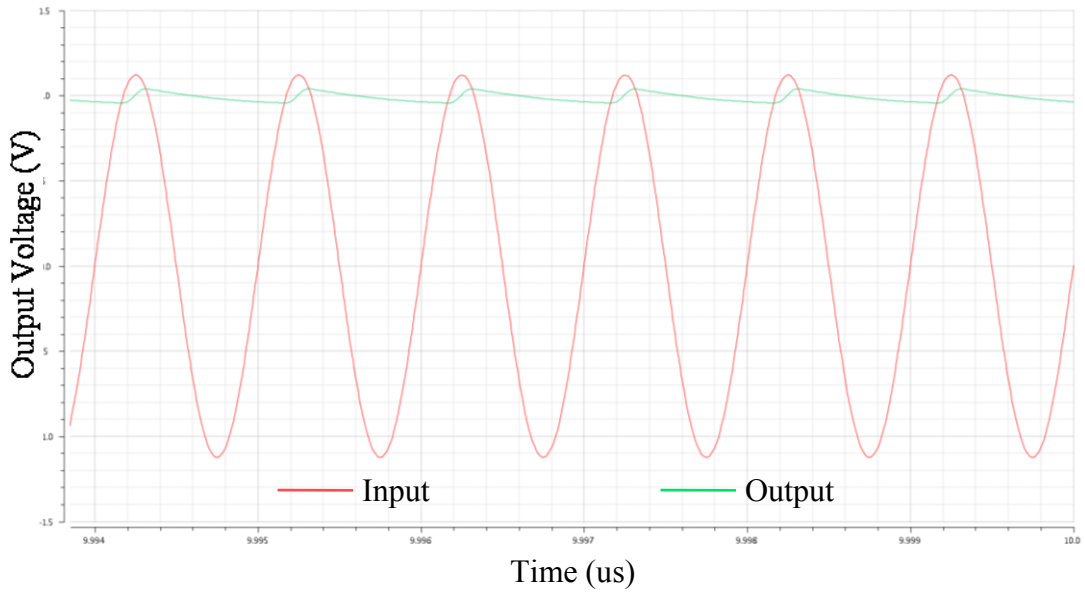

Figure 6.10 Steady-state waveforms of input and output voltage of the single stage rectifier

To further increase the output voltage, an N-stage topology is usually employed at given input power level to produce output voltage roughly N times of that achievable with a single stage. The proposed three-stage charge pump rectifier configuration which includes three stacked single stage rectifiers is depicted in Figure 6.11. The basic operational principle of is indicated by the current flow in red. In the state 1, input RF voltage is transferred to capacitor C_1 through the main path transistor M_1 in positive phase. The maximum output voltage of C_1 is V_{in}. Next, when V_{in} is in negative phase, that is, in the state 2, M_2 transfers both the voltages of C_1 and V_{in} to C_2. The maximum output voltage between two terminals of C_2 is $2V_{in}$. In the state 3, when V_{in} is in positive phase again, the voltages of C_2 and V_{in} are transferred to C_3 via M_3. The maximum output voltage between two terminals of C_3 is $2V_{in}$. Therefore, the maximum output voltage of the three-stage charge pump rectifier via C_1 and C_3 to the ground is $3V_{in}$. Figure 6.12 demonstrates the waveforms of input and output voltage of the three-stage rectifier at steady state. Similarly, if N-stage configuration is adopted, the theoretical DC output voltage should be $N \times V_{in}$. As the main path MOS transistors have reverse leakage when turned off, the bootstrapping circuits are utilised to prevent the voltage drop caused by the reverse leakage.

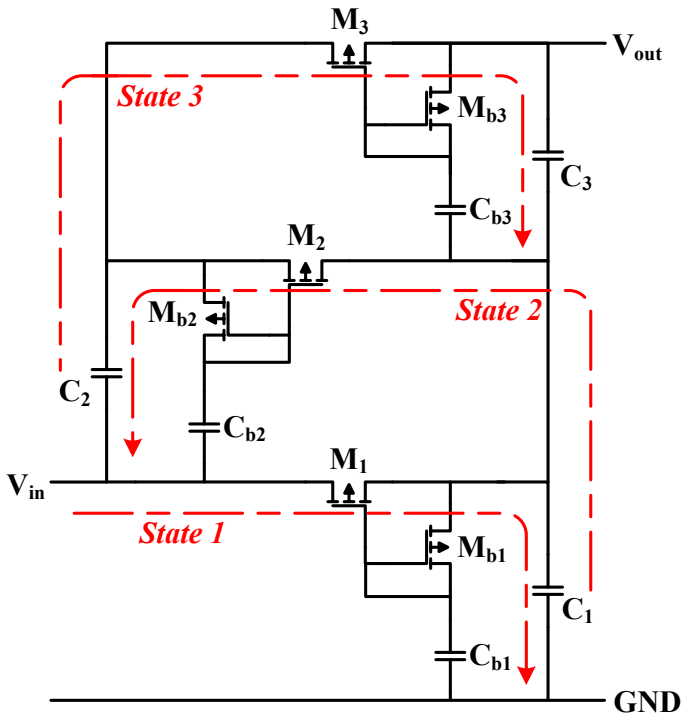

Figure 6.11 Proposed three-stage charge pump rectifier

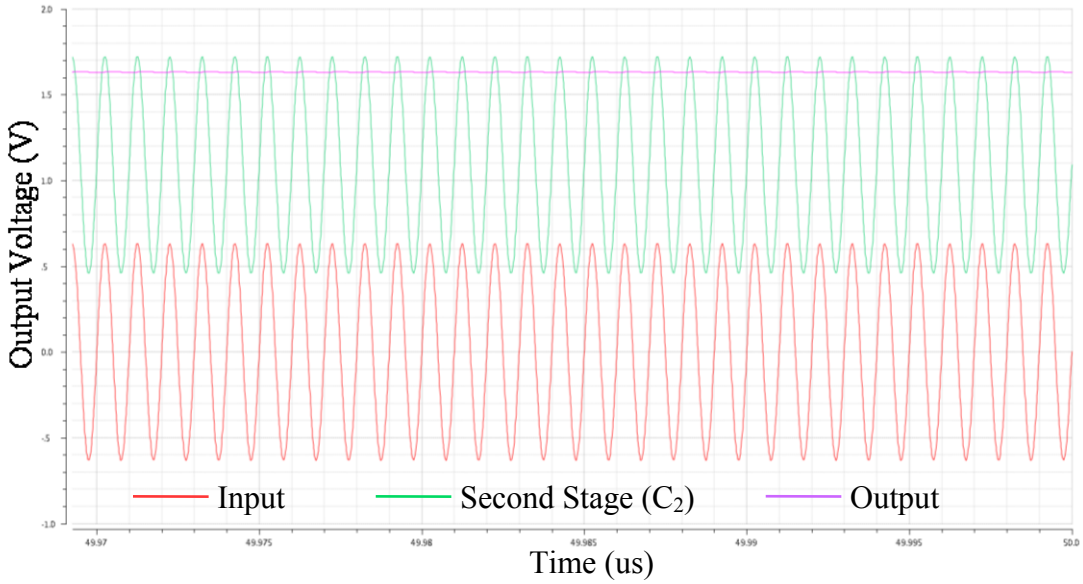

Figure 6.12 Steady-state waveforms of input and output voltage of the proposed three-stage charge pump rectifier

The proposed five-stage charge pump rectifier consisting of five stacked single stage rectifiers is demonstrated in Figure 6.13. Based on the connection of multiplying capacitors, there are four types of configurations. Figure 6.13 (a) shows the first type which is formed by five directly connected single stage rectifier similar to the three stage rectifier configuration in Figure 6.11. Operation of the five stage charge pump rectifier is the same as the same as the three stage one. The charging currents are conducted to the capacitor C_1, C_3 and C_5 in the positive input phase. While in the negative input phase, the voltages of input signal and C_1 are transferred to the capacitor C_2, and the voltages of V_{in}, C_1 and C_3 are transferred to C_4. The maximum output voltages between two terminals of the capacitors are V_{in} for C_1 and $2V_{in}$ for $C_2 - C_5$, respectively. Therefore the maximum output voltage of the rectifier is $5V_{in}$.

Figure 6.13 (b) depicted the second type with five directly connected single stage rectifier. Unlike type I, capacitor C_4 is connected to the input terminal in type II. The maximum output voltage between two terminals of C_4 is $4V_{in}$ instead of $2V_{in}$.

Figure 6.13 (c) demonstrated the third type of configuration for the five stage charge pump rectifier. In type III, capacitors of C_3 and C_5 are connected to the ground directly with the maximum output voltages being $3V_{in}$ and $5V_{in}$, respectively.

Figure 6.13 (d) illustrated the fourth type of the five stage charge pump rectifier topology. Capacitor C_4 is connected to the input terminal while capacitors C_3 and C_5 are connected to the ground. The maximum output voltages between two terminals of C_3, C_4 and C_5 are $3V_{in}$, $4V_{in}$ and $5V_{in}$, respectively.

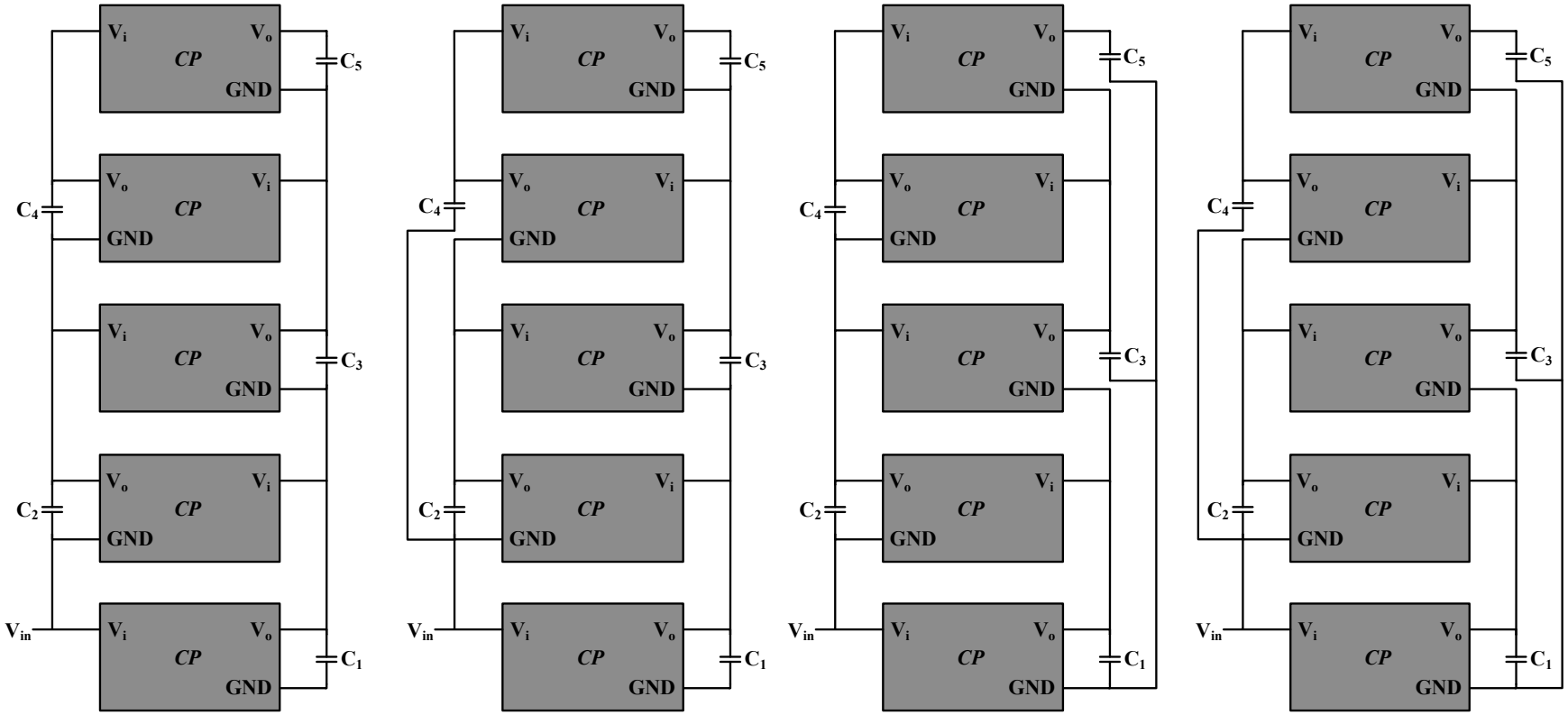

Figure 6.13 Proposed five-stage charge pump rectifier: (a) type I, (b) type II, (c) type III, (d) type IV

6.2.2 Design Strategy

Design strategies of the proposed charge pump rectifier are based on two assumptions: 1. fewer stages, hence fewer power dissipating devices, give higher efficiency; 2. maximum output voltage yields maximum efficiency [122].

6.2.2.1 Tradeoffs

The achievable maximum efficiency depends strongly on tradeoffs between three fundamental factors: transistor size (W/L), leakage current and parasitic capacitance. In the proposed rectifier, for a given input voltage amplitude, the size of the transistors should be raised to reduce the channel resistance in order to achieve a higher output voltage. However, increasing the size increases the reverse leakage current, which soon overtakes the benefits of smaller channel resistance. Furthermore, the capacitance is proportional to the transistor size. This means larger transistor size leads to larger parasitic loss and also limits the number of stages we can cascade. On the other hand, small transistor size leads to incomplete charge transfer, resulting in a low output voltage, hence, low efficiency. Therefore, the size of the transistors in the proposed rectifier has been optimized for maximum efficiency. The only certainty for performance consideration is to use transistors of minimal length. Although the reverse leakage current is usually reduced by increasing the transistor length, the parasitic capacitances and the forward current degrade more rapidly [123].

6.2.2.2 Body Effect

Body effect of the MOS transistor is usually considered in the CMOS rectifier design to achieve high efficiency. The body effect could increase the absolute value of threshold voltage and degrade the output voltage. For pMOS transistor, the dependence of threshold voltage (V_{th}) on source-bulk voltage (V_{SB}) is given by

$$V_{th} = V_{t0} - \gamma \left[\sqrt{(|2\varphi_F| + V_{SB})} - \sqrt{|2\varphi_F|}\right] \tag{6.6}$$

Where V_{t0} is the threshold voltage when source and substrate are at the same voltage, γ is the body effect coefficient, and φ_F is the Fermi potential. For the rectifier design, a common solution for solving the problem is to apply Dynamic Bulk Biasing (DBB)

circuit [124] to avoid potential latch-up and reduce substrate leakage. As illustrated in Figure 6.14, with the dynamic biasing configuration, bulk of the main transistor M_m is selectively connected to the highest available voltage (either input or output) through two small auxiliary transistors (M_x). Source-drain voltage of the auxiliary transistors is close to zero as no sustained current passes through when they are turned off. However, since the proposed rectifier is designed for RF energy scavenging where the input power is small, increased power dissipation caused by extra auxiliary transistors overtakes the advantages of body effect elimination. Therefore, in the proposed rectifier design, bulks of the main transistors are directly connected to the multiplying capacitors without dynamic bulk switching.

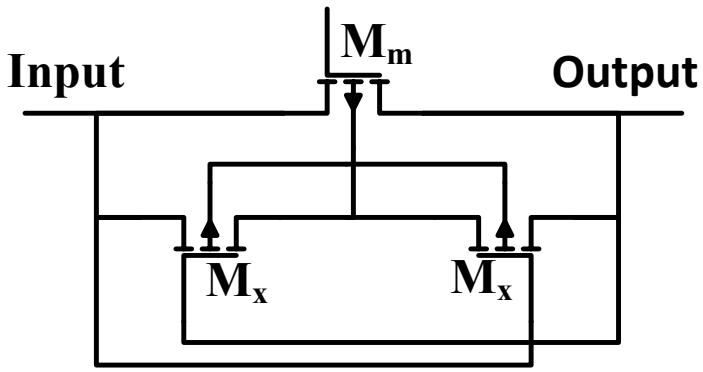

Figure 6.14 Schematic of dynamic bulk biasing circuit

6.2.2.3 Ripple Voltage

It should be noticed that there will be ripple voltage at the output of the rectifier. It is caused by the leakage current and the load current during the conduction time of the neighbouring transistors [122]. This ripple voltage V_r is expressed by

$$V_r = V_{out} / f RC \tag{6.7}$$

where V_{out} is output voltage, f is operating frequency, R is load resistance and C is multiplying capacitance. Thus the ripple voltage can be substantially reduced by increasing input signal frequency, load resistance or multiplying capacitance.

6.2.2.4 Multiplying Capacitor Value

As has been mentioned, using large multiplying capacitors can reduce the output ripple voltage. However, with large multiplying capacitors it would take significantly longer time for the rectifier to reach steady output state while small multiplying capacitors suffer heavier attenuation by parasitic capacitance, hence, reducing the efficiency. Thus, an optimal value of the multiplying capacitors has been set according to the requirements of specific application.

6.2.3 Power Efficiency Optimization

The factual charge transfer mechanism of the proposed rectifier is actually much more sophisticated than that introduced previously. This is because in each cycle the transistor operates in different regions, and transistor resistance, reverse leakage current as well as parasitic capacitance should be taken into consideration. In one cycle, main path transistor experiences four regions, which are subthreshold region, super-threshold region, subthreshold region and reverse biased region.

As the current in the subthreshold region is very small and the duration is very short compared with that of the super-threshold region, charge transfer in the subthreshold region can be neglected without triggering substantial error. However, on the other hand, in the micro-power regime leakage current in the reverse biased region cannot be neglected, especially for our case, where threshold voltage reduction is applied. This is because the leakage current increases exponentially with the decrease of threshold voltage. Hence, MOS transistor consumes significant amount of power as it stays in the reverse biased region for a considerable period of time [122].

The current of main path transistor in the subthreshold region using BSIM3 transistor model is given by [125]

$$I_{dsub} = I_{so} \frac{W}{L} \left(1 - e^{-V_{ds}/V_T}\right) e^{V_{gs}/nV_T} \tag{6.8}$$

with

$$I_{so} = \mu_p \sqrt{\frac{q\varepsilon_{si}N_{ch}}{2\varphi_s}} V_T^2 \, e^{(-V_{tp}-V_{off})/nV_T} \tag{6.9}$$

where V_T is the thermal voltage, n is the subthreshold swing parameter, V_{off} is the offset voltage, V_{tp} is the threshold voltage of the pMOS transistor, φ_s is the surface potential, N_{ch} is the doping concentration, ε_{si} is the silicon permittivity, q is the hole charge, and μ_p is the hole mobility.

Thus, the reverse leakage current is the subthreshold current with $V_{gs} = 0$ and is equal to

$$I_{leak} = I_{so} \frac{W}{L} \left(1 - e^{-V_{ds}/V_T}\right) \tag{6.10}$$

Efficiency of the rectifier is closely related to the equilibrium between small transistor resistance and low leakage current. Hence, an optimum value of the aspect ratio (W/L) of pMOS transistor should satisfy both (6.10) and (6.11) simultaneously.

$$R_{on} = \frac{1}{\mu_p C_{ox} \frac{W}{L} (V_{gs} - V_{tp})} \tag{6.11}$$

The power consumption of the single stage rectifier is the sum of power consumed in all the four regions

$$P_{loss} = P_{sub1} + P_{sup} + P_{sub2} + P_{leak} \tag{6.12}$$

As the power consumption and duration of the two subthreshold regions is negligibly small, the approximation is made

$$P_{loss} \approx P_{sup} + P_{leak} \tag{6.13}$$

$$\approx \frac{1}{T}\int_0^{\frac{T}{2}} I_d\, V_{ds}\, dt + \frac{2}{T}\int_{\frac{T}{2}}^{T} I_{leak}\, V_{ds}\, dt$$

$$\approx \frac{1}{T}\int_0^{\frac{T}{2}} \frac{1}{2}\mu_p C_{ox}\frac{W}{L}\left(V_{gs} - V_{tp}\right)^2 V_{ds}\, dt +$$

$$\frac{1}{T}\int_{\frac{T}{2}}^{T} I_{so}\,\frac{W}{L}\left(1 - e^{-V_{ds}/V_T}\right) V_{ds}\, dt$$

The input signal to the rectifier, V_{in}, is assumed to be sinusoidal wave with frequency of f_m and amplitude of V_m.

$$V_{in}(t) = V_m \sin(2\pi f_m t) \tag{6.14}$$

In super-threshold region, $V_{ds} = V_o - V_{in}$, $V_{gs} = V_o - V_{in} + V_{tp}$ and $i_c = C_o \frac{dV_o}{dt}$, where V_o is the output voltage and C_o is the output capacitor. In reverse bias region, $V_{ds} = V_{in} - V_m$.

By substituting V_{ds} and V_{gs} in saturation and reverse bias regions by their values in (6.13), the total power consumption of the single stage rectifier in one cycle will be

$$P_{loss} = \frac{1}{T}\int_0^{\frac{T}{2}} \frac{1}{2}\mu_n C_{ox}\frac{W}{L}[V_o - V_m \sin(2\pi f_m t)]^3 dt +$$

$$\frac{1}{T}\int_{\frac{T}{2}}^{T} I_{so}\,\frac{W}{L}\left(1 - e^{V_m\frac{[1-\sin(2\pi f_m t)]}{V_T}}\right) V_m[\sin(2\pi f_m t) - 1]\, dt \tag{6.15}$$

Therefore, the power conversion efficiency η can be calculated as it is given by

$$\eta = \frac{P_{out}}{P_{in}} = \frac{P_{out}}{P_{out} + P_{loss}} \tag{6.16}$$

Also, by taking the derivate of efficiency according to (6.17) over the aspect ratio (*W/L*), an optimum size of the transistor can be decided.

$$\frac{\partial(\eta)}{\partial(W/L)} = \mathbf{0} \tag{6.17}$$

At input amplitude of 0 dBm, an optimum width of 228μm is obtained to achieve high output voltage while the length of transistor is set to be 0.5μm to reduce the area.

6.2.4 Simulations and Results

The validity of the proposed rectifier design is confirmed with Virtuoso Spectre Circuit Simulator under Cadence environment using AMS 0.35um CMOS process. No electrostatic discharge (ESD) protection is considered in the design due to the fact that it brings extra parasitic capacitance which decreases the power conversion efficiency. Performance of the proposed rectifier with input signal of sine wave at 915 MHz is investigated.

6.2.4.1 Investigation on Transistor Size

The effect of transistor size on power conversion efficiency (PCE) is investigated in Figure 6.15. With input power amplitude of 0 dBm, the proposed single stage rectifier achieves maximum power efficiency of 35% when the aspect ratio (W / L) of the main path transistor is 400. The simulated optimum transistor size is a little smaller then that obtained from the calculation (228 / 0.5). It is because the channel length modulation is not considered during the calculation. Therefore, an aspect ratio of 400 is chosen to increase the output voltage and reduce the reverse leakage simultaneously as illustrated previously. The sizes of the main path transistors are set to be 200 / 0.5 μm. Small size pMOS transistors (0.5 / 0.5 μm) are employed in the bootstrapping circuits to reduce energy dissipation.

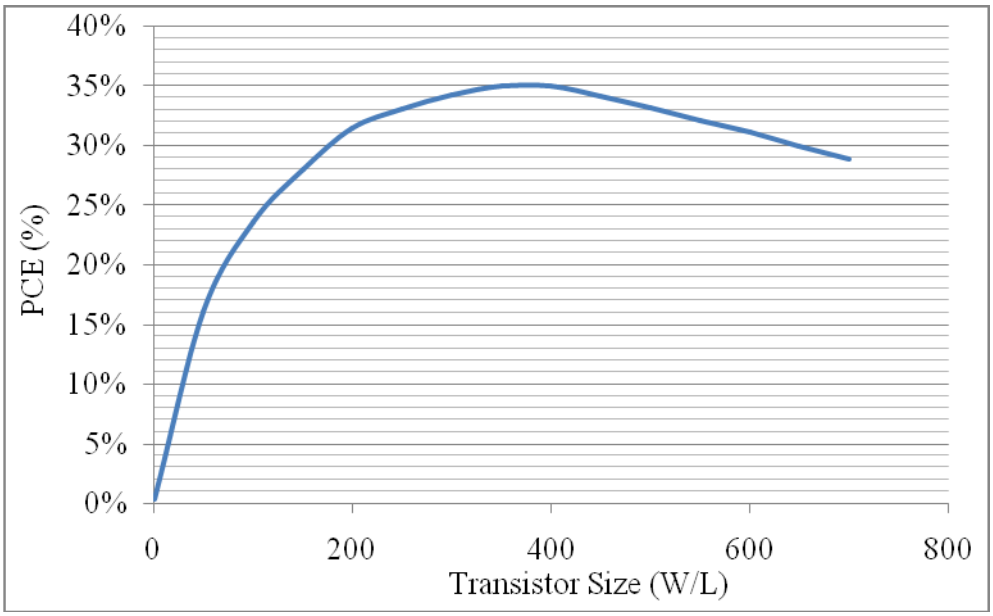

Figure 6.15 PCE vs. Transistor size

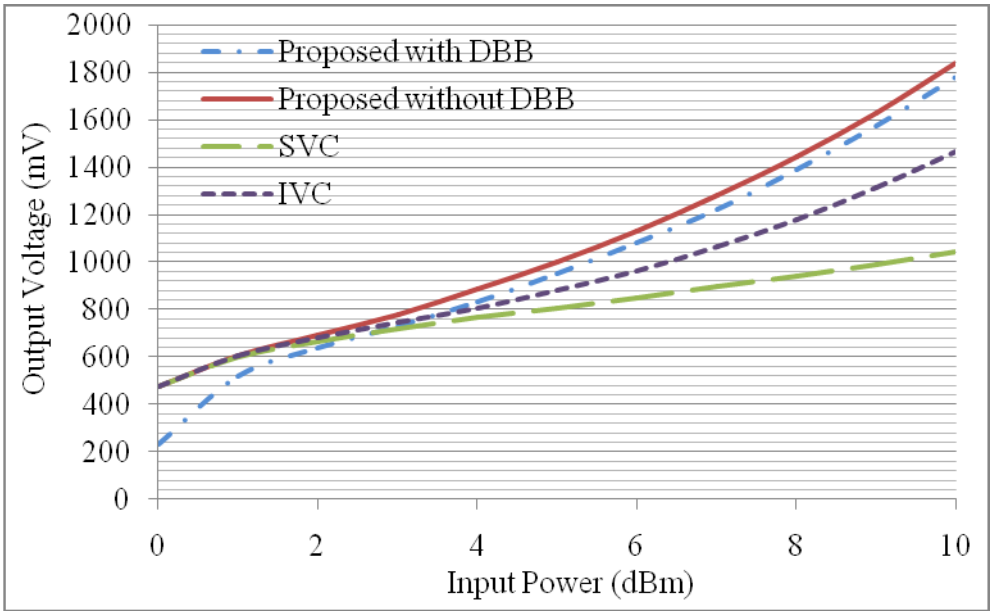

Figure 6.16 Output voltages of different V_{th} – cancellation schemes

6.2.4.2 Comparison with Different V_{th} – Cancellation Schemes

In this section, we compare simulation results of the Internal - V_{th} - Cancellation (IVC) scheme [117] and the Self - V_{th} - Cancellation (SVC) scheme [118] with the proposed single stage rectifier with / without Dynamic Bulk Biasing (DBB). The other two schemes introduced earlier, External - V_{th} - Cancellation (EVC) scheme [31] and Differential - V_{th} - Cancellation (DVC) scheme [119], are not included in the comparison as they require more than one power input terminal, which is not practical for RF energy scavenging. Figure 6.16 plots the simulation results characterizing the output voltage verse input power for these different structures. To make fair comparison, transistors, capacitors and load resistors of the same size are used. With the same load resistance, higher output voltage reveals higher output power, hence higher power conversion efficiency.

As can be seen, applying dynamic bulk biasing circuit leads to higher parasitic loss, hence, lower output voltage for the proposed rectifier in comparison with the case where no DBB circuit is used. The reduction in the output voltage due to DBB circuit is more noticeable when the input power is lower than 2 dBm. With input power higher than 2 dBm, the output voltage of the proposed rectifier with DBB circuit is approximately 55 mV lower than that without DBB circuit, while the difference increases to 245 mV at 0 dBm input.

The proposed rectifier without DBB circuit presents significantly higher output voltage than that of the other two schemes over a wide range of input power greater than 2 dBm. With a input amplitude of 8 dBm, the proposed rectifier generates a output voltage of 1443 mV, which corresponds to an improvement by up to 501 mV and 264 mV compared with SVC and IVC schemes, respectively.

6.2.4.3 Comparison with 2-Stage Dickson Topology

For most of the case, multi-stage rectifier topology is adopted in low power RF energy scavenging to obtain a relatively high output voltage at low input voltage level. Voltage Conversion Efficiency (VCE) of the proposed 3-stage charge pump rectifier is compared with that of 2-stage Dickson rectifiers.

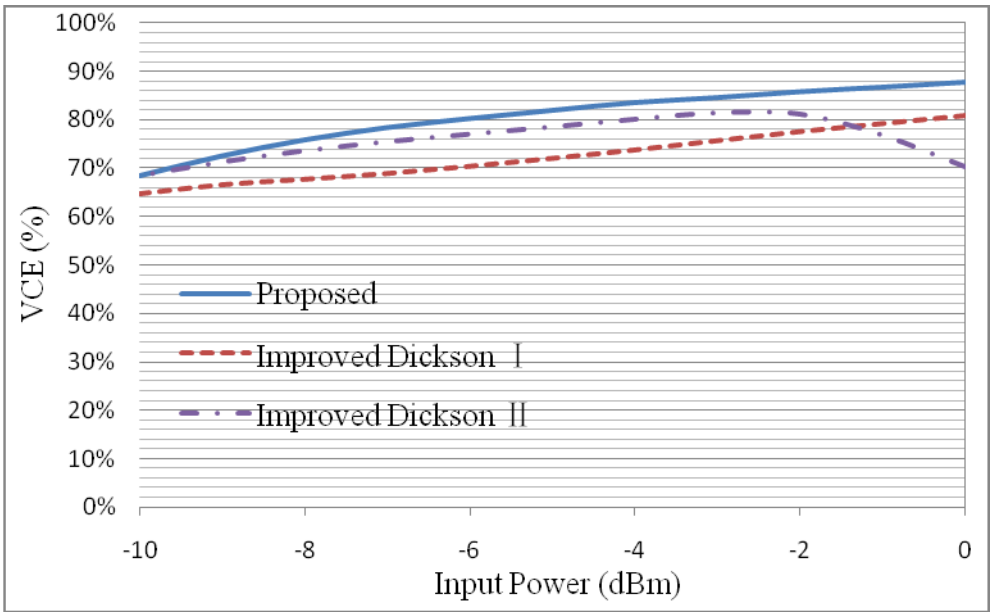

Figure 6.17 VCE vs. Input power

In previous researches, different threshold voltage cancellation technologies were applied in Dickson rectifier topology to improve the conversion efficiency. Essel [126] adopted Internal $-V_{th}$ – Cancellation (IVC) scheme in the Dickson rectifier to achieve high conversion efficiency without the use of Schottky diodes. MOS transistors are used in their subthreshold operating region as active high impedance resistors to replace the large bias resistors in the IVC scheme. In [127], a new diode-connected MOS transistor for ultra-high-frequency (UHF) micro-power rectifiers was designed and implemented in the Dickson topology for high efficiency N-stage charge pump voltage rectifier.

Figure 6.17 depicts the voltage conversion efficiency of type I [127] and type II [126] Dickson rectifier as well as the proposed rectifier topology. During the input range of -10 – 0 dBm, conversion efficiencies of type I Dickson rectifier and the proposed charge pump rectifier increase with the input power. For type II Dickson rectifier, the conversion efficiency increases until it reaches the maximum at -2 dBm input power level and drops dramatically afterwards. With input power of -2 dBm, conversion efficiency of the proposed rectifier is 86%, while type I and type II Dickson rectifier have efficiency of 78% and 81%, respectively.

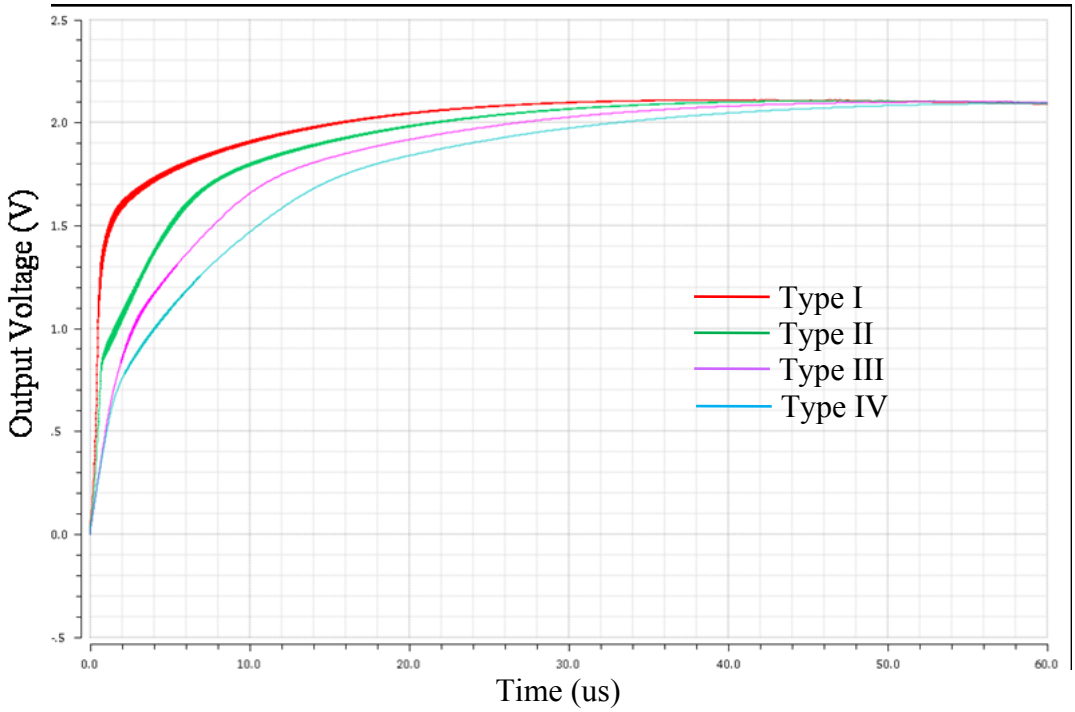

Figure 6.18 Output voltage of the proposed five-stage charge pump rectifiers with different multiplying capacitor connection

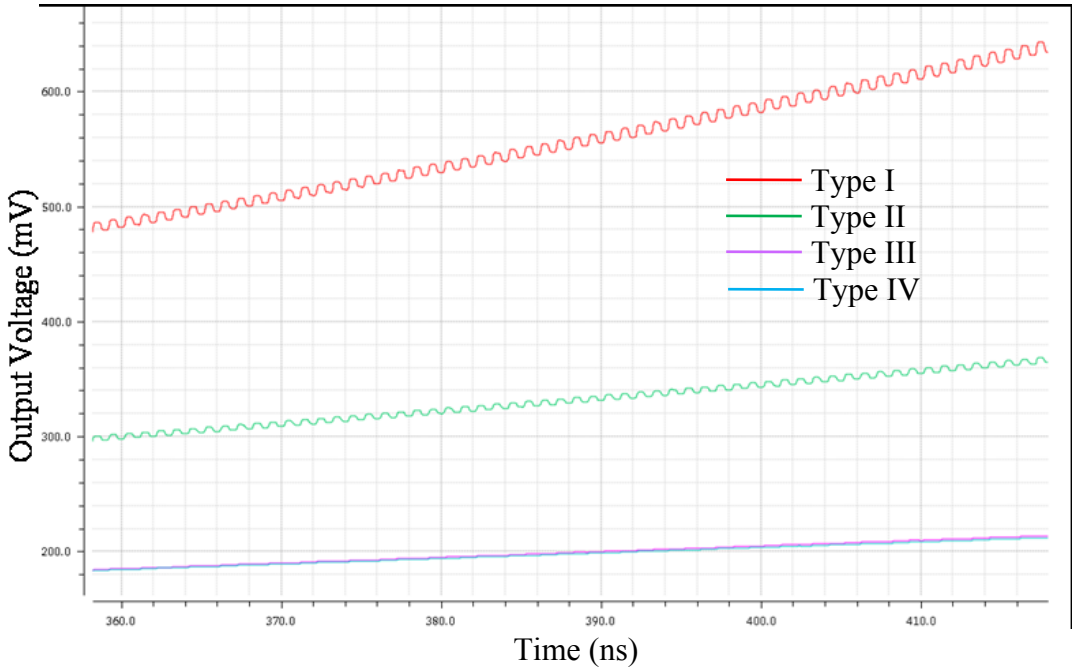

Figure 6.19 Output voltage of the proposed five-stage charge pump rectifiers during the period from 358 ns to 418 ns

6.2.4.4 Simulation of the Proposed Five-Stage Charge Pump Rectifiers

Figure 6.18 and Figure 6.19 demonstrate the schematic simulation results of the proposed five-stage charge pump rectifiers with different multiplying capacitor connection. Transient output voltage at input power amplitude of 0 dBm for types I - IV rectifier configurations (Figure 6.13) are plotted in the figures.

There is no significant difference for the maximum output voltages between different types, while the ripple voltage and the time to reach steady output state vary. As shown in Figure 6.18, type I rectifier takes the shortest time to reach steady output while type IV rectifier consumes the longest time to achieve maximum output. On the other hand, the ripple voltage of type I rectifier (Figure 6.19) is larger than that of the other three types. This is because the multiplying capacitors in both odd and even stages of type I rectifier are connected in series, which equivalently decrease the total capacitance. According to the discussion in the design strategy, smaller multiplying capacitor results in larger ripple voltage and shorter time to reach steady output state. Similarly, the equivalent capacitance of type IV is increased as the multiplying capacitors in both odd and even stages are connected in parallel, leading to smaller ripple voltage and longer time to obtain maximum output voltage. As can be noticed, multiplying capacitors in odd stages of type III rectifier are connected in parallel while multiplying capacitors in even stages are connected in series. This leads to relatively smaller ripple voltage than type I and type II, as shown in Figure 6.19. Moreover, type III rectifier requires shorter time for steady output compared with type IV rectifier. Therefore, the five-stage charge pump rectifier of type III is selected as an optimum choice in this situation.

6.3 Summary

In summary, the investigation on the rectifier design for RF energy scavenging discussed in this chapter is illustrated in Figure 6.20. This chapter has addressed the design of passive CMOS charge pump rectifier topology for AC to DC conversion. The rectifier configuration in 0.35 μm CMOS technology does not require complex circuit design. It employs pMOS switches equipped with bootstrapping capacitors to reduce the effective threshold voltage, hence, yield high conversion efficiency. The effect of main path transistor size on the power conversion efficiency has been studied and an optimum value of 200/0.5 μm has been selected. Multiple stages are cascaded in order to obtain high output voltage at low voltage input. Different configurations for multi-stage topology have also been investigated. Compared with previously reported designs, the proposed charge pump rectifier has advantages on both power conversion efficiency and voltage conversion efficiency. Such performance might open promising perspective for the deployment of passive CMOS rectifier in miniaturized RF energy scavenging system.

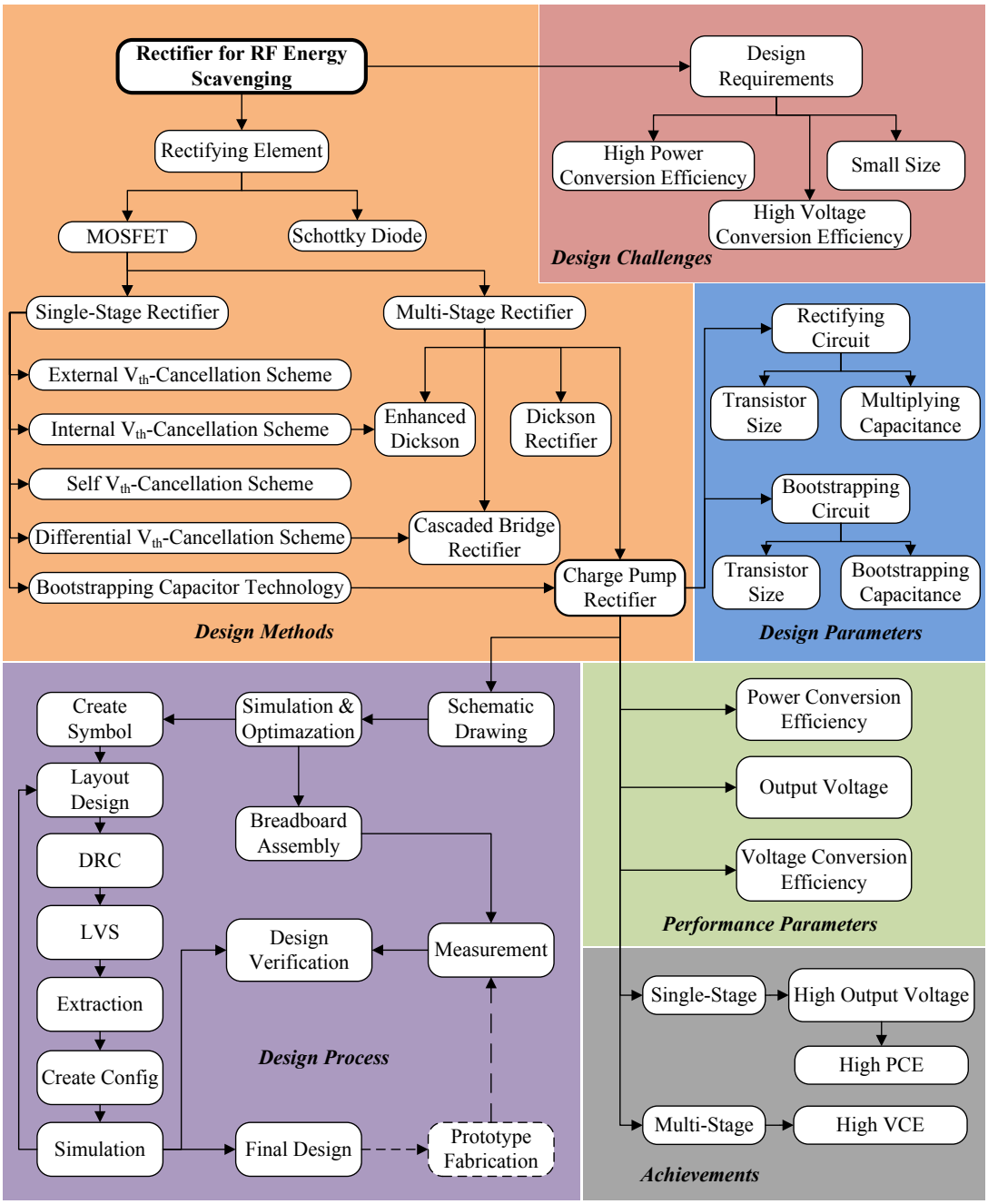

Figure 6.20 The investigation of the rectifier for RF energy scavenging

Chapter 7

Conclusions

This thesis covers the research studies of antenna and rectifier designs for RF energy scavenging in order to achieve efficient and miniaturized energy scavenging systems that convert RF energy to storable electrical energy for charging low power sensors and devices. This chapter summarises the study presented in this thesis. The main objectives of each chapter are reviewed and the goal of the research is assessed and evaluated. The main achievements are then highlighted and future developments that could follow on from this study are suggested. This chapter is organised as follows. Section 7.1 discusses the conclusion of each chapter in the thesis and the main contributions of the thesis are summarised in Section 7.2. Section 7.3 suggests future work and development based on the research presented in this thesis and, finally, Section 7.4 concludes the chapter.

7.1 Summary and Conclusions

Chapter 2 introduces the general principles of energy scavenging with a broad review on several common energy scavenging techniques including solar energy scavenging, thermoelectric energy scavenging, wind energy scavenging, piezoelectric energy scavenging, radio frequency energy scavenging as well as hybrid energy scavenging. Advantages and disadvantages of each technique are investigated and discussed in this chapter. Unlike other energy sources, RF energy is more human dependent rather than natural environment dependent. With ample radio transmitters scattered throughout urban landscape, plenty of RF energy is available throughout the day in both indoor and outdoor environments. Compared with other energy scavenging systems, RF energy scavenging systems usually have smaller volume with higher power density. A typical RF energy scavenging system has two most important components: antenna and rectifier. Depending on the rectifying elements, current RF energy scavenging systems can be categorized to two groups, which are Schottky diode based rectenna and rectenna with CMOS based rectifier. In this chapter, existing rectenna designs from these two groups are summarized.

One of the limitations on RF energy scavenging is the low output power in long distance operation. In order to improve the output power level, wideband RF energy scavenging is a good choice to extract RF energy from a broad frequency range. Since antenna occupies most of the area in a RF energy scavenging system, it is critical to have an antenna with both small size and good radiation characteristics to achieve miniature and effective RF energy scavenging system. In chapter 3, a compact ultra wideband microstrip antenna is proposed for wideband RF energy scavenging. The antenna fed by a coplanar waveguide transmission line is developed from rectangular patch antenna. Partial ground plane is introduced to broaden antenna bandwidth. A rectangular slot is etched on the radiating patch for further bandwidth enhancement. To achieve good impedance matching over a wide range of frequencies, two edges of the rectangular radiating antenna are bevelled to form a tapered structure. The proposed antenna has a compact size of $35 \times 80 \times 0.2$ mm^3

and demonstrates a wide bandwidth from 1.1 GHz to 5.1 GHz. The maximum efficiency in the operation range reaches 82%. A dual antenna array is also designed, simulated and optimized utilizing the unit antenna for full-wave RF energy scavenging. Different inter-element spacing values are investigated and compared. When the spacing is 15 mm, the array geometry displays bandwidth of 3.25 GHz, from 1.15 GHz to 4.4 GHz, covering DCS, PCS, UMTS, Bluetooth, Wi-Fi, WLAN, WiMAX, HIPERLAN and LTE applications.

As wideband RF energy scavenging requires complex impedance matching circuit, power conversion circuit and control circuit with wideband characteristic, multiband and single band RF energy scavenging are considered as more practical alternatives. In chapter 4, planar inverted-F antennas are investigated for multi-band RF energy scavenging. In the first stage, a low profile PIFA antenna with coupled feeding line and bended shorting strip is presented. The antenna has dual band operation that covers GSM 900 (downlink: 935-960MHz) and GSM 1800 (downlink: 1805-1880MHz). Maximum efficiencies and gains in these two bands are 86%, 88% and 2.3 dBi, 4.3 dBi, respectively. In the second stage, the antenna is modified to triple band PIFA with a meandered shorting strip in order to obtain operation in Wi-Fi 2.4 GHz. The antenna with a small size (15×40 mm^2) is printed on 0.8 mm – thick FR4 substrate. Compared with other triple band antenna designs, the proposed antenna achieves not only smaller volume, but also higher gain (2.13 dBi, 4.31 dBi, 5.03 dBi). Estimated output power illustrates that it is possible to power wireless sensors through RF energy scavenging using the proposed triple band PIFA.

Chapter 5 presents a novel miniaturized inverted-F antenna design without empty space for indoor RF energy scavenging at Wi-Fi 2.4 GHz. Five different designs are analyzed and compared. The proposed IFA has a meandered structure with thick substrate and radiating plate. The antenna with dimensions of $10 \times 5 \times 3.5$ mm^3 is placed on a test board ($80 \times 40 \times 0.8$ mm^3) with full ground. Measurement results reveal that impedance bandwidth of the antenna is about 120 MHz, covering the whole Wi-Fi 2.4 GHz band. Across the operating range, antenna efficiencies are all above 70%, with a maximum value of 82%. Reduced backward radiation is also

achieved by the proposed IFA, which makes it suitable for indoor applications. Effects of test board dimensions and antenna positions on the test boards are also simulated and analyzed. It is observed that resonant frequency and impedance bandwidth of the antenna oscillate as the dimensions of test board and ground plane increase and converge to the values for that the IFA mounted on an infinite test board.

The rectifier is another crucial component in a RF energy scavenging system that decides the efficiency of the conversion circuits. In chapter 6, firstly conventional rectifier configurations for RF energy scavenging are reviewed. Four threshold voltage cancellation schemes for CMOS rectifier design, including External – V_{th} – Cancellation (EVC) scheme, Internal –V_{th} – Cancellation (IVC) scheme, Self –V_{th} – Cancellation (SVC) scheme and Differential –V_{th} – Cancellation (DVC) scheme are also discussed. Then a new passive CMOS rectifier is designed in 0.35 μm CMOS technology. With bootstrapping capacitor implemented, effective threshold voltage of MOS transistor is reduced, which results in higher conversion efficiency. Multiple stage topologies are also investigated to obtain high output voltage. At input level of 0 dBm, size of main path transistor is optimized to 200/0.5 μm. Compared with conventional rectifier topologies, improvements on power conversion efficiency and voltage conversion efficiency are achieved by the proposed charge pump rectifier.

7.2 Summary of Contributions

This section summarizes the areas and the challenges in designing miniaturized RF energy scavenging systems that have been addressed in this thesis. In particular, the research areas include antenna designs with wideband, multiband and single band operation and efficient CMOS rectifier design, which are discussed as follows.

7.2.1 Compact Ultra Wideband Antenna Design

Wideband RF energy scavenging extracts ambient RF energy from a wide frequency range in order to generate enough power to charge electronic devices. Hence, it is important for the antenna in the system to have a broad bandwidth. Microstrip antennas are widely used in RF energy scavenging because they can be printed

directly onto a circuit board, which means low cost, low profile and easy fabrication. However, the bandwidth of the patch antenna is usually small. For this reason, a microstrip antenna is designed with enhanced bandwidth in order to achieve ultra wideband operation with a relatively small size for wideband RF energy scavenging. The proposed microstrip antenna (35 mm × 80 mm) is printed on 0.2 mm substrate, and a wide bandwidth of 4 GHz (1.1 – 5.1 GHz) is obtained.

7.2.2 Compact Ultra Wideband Dual Antenna Array

An effective RF energy scavenging system requires not only a high performance antenna, but also an efficient rectifier. For passive CMOS rectifier, full wave rectifier topology with active threshold voltage cancellation scheme has its merit of high conversion efficiency compared with half wave rectifier. Therefore, an ultra wideband dual antenna array is developed from the proposed UWB microstrip antenna for wideband full wave RF energy scavenging. The optimized array covers most of the communication bands including DCS (1710 - 1880 MHz), PCS (1850 - 1990 MHz), UMTS (1920 - 2170 MHz), WiFi / WLAN / Hiper LAN / IEEE 802.11 2.4 GHz (2412 - 2484 MHz), 3.6 GHz (3657.5 - 3690.0 MHz), Bluetooth (2400 - 2484 MHz), WiMAX 2.3 GHz (2.3 - 2.5 GHz), 2.5 GHz (2500 - 2690 MHz), 3.3 GHz, 3.5 GHz (3400 - 3600 MHz) & LTE applications.

7.2.3 Low Profile Dual Band Planar Inverted-F Antenna

One of the methods to improve performance used in microstrip antenna design is to introduce shorting pins (from radiating patch to ground), which helps to reduce the antenna size by half. In this research, planar inverted-F antenna, which can be considered as a combination of inverted-F (IFA) and short-circuit microstrip antenna (SC-MSA), is investigated for multiband RF energy scavenging. A dual band PIFA with low profile (15×40 mm^2) is proposed in this thesis. With a coupled feeding line and a bended shorting strip, the antenna achieves dual band operation at GSM 900 and GSM 1800. The reason for using these two bands in our RF energy scavenging design is that they have the highest power density in outdoor environment. Peak

efficiencies of the antenna at lower and upper bands reach 86% and 88%, respectively.

7.2.4 Low Profile Triple Band Planar Inverted-F Antenna

A triple band planar inverted-F antenna is presented in this research for RF energy scavenging from signals of GSM 900, GSM 1800 and Wi-Fi 2.4 GHz. The antenna is developed from the proposed dual band PIFA. Operation at Wi-Fi 2.4 GHz is obtained by replacing the bended shorting strip with a meandered shorting strip. As the radiating patch is printed directly on 0.8 mm substrate, the antenna is suitable for mass production at low cost. Moreover, with a small size of 15 × 40 mm^2, the proposed triple band PIFA can be integrated into compact and miniaturized RF energy scavenging systems.

7.2.5 Miniaturized Inverted-F Antenna Design

With the popularization of indoor wireless local area network, there are increased numbers of Wi-Fi routers and wireless end devices. This makes Wi-Fi energy scavenging a perfect approach for indoor applications to power wireless sensor networks. This research demonstrates a novel miniaturized inverted-F antenna without empty space for indoor Wi-Fi energy scavenging. The proposed antenna has dimensions of only 8 (L)× 3 (W) × 4 (H) mm^3 to be embedded in low power miniaturized devices. Moreover, owing to no additional empty space, circuit routing on a multilayer PCB is allowed underneath and around the antenna with no restrictions. With reduced backward radiation and appreciable efficiency, the proposed miniaturized IFA is suitable for indoor Wi-Fi energy scavenging.

7.2.6 Efficient Passive CMOS Rectifier Design

Although Schottky diode with low forward voltage and high switching speed is usually considered for rectifier design in RF energy scavenging researches, its temperature dependence and costly fabrication process make it unsuitable for practical applications. Hence, diode-connected MOS transistor is usually used in CMOS integration. To reduce the effective threshold voltage of MOS transistors for

high conversion efficiency, a passive CMOS charge pump rectifier with bootstrapping capacitors is proposed for RF energy scavenging in this research. Simulation results in 0.35um CMOS technology manifests that the output voltage and conversion efficiency of the proposed rectifier at low-voltage power supply is significantly improved compared with previously published designs.

7.3 Future Work

This thesis points to several areas that require further investigation:

7.3.1 Wideband Impedance Matching Network Design

Impedance matching network is necessary for RF energy scavenging system to fine tune the impedance match between the antenna and the rectifier to reduce transmission loss and increase the voltage gain. Coarse impedance matching is done through circuit and antenna design but fine impedance matching must be done on the PCB for more accurate matching [32]. An ultra wideband microstrip antenna is presented in this thesis. To realize wideband RF energy scavenging, a wideband impedance matching network with microstrip element also needs to be developed in the future study.

7.3.2 Wi-Fi Antenna Array Design

In this research, miniaturized IFA has been designed for indoor Wi-Fi energy scavenging. However, energy scavenged using single antenna element is quite limited. In order to improve the output power level and increase the effective range of the RF energy scavenging system, more antenna elements are required. Further study involves the design of antenna array utilizing the proposed antenna. Interactions between adjacent antenna elements in the array need to be minimized.

7.3.3 Filter Design

To complete the RF energy scavenging system design, filters are also needed. A band pass filter placed between antenna and rectifier is necessary to reject higher order

harmonics generated by the rectifier from radiating through the antenna. Moreover, a DC filter following the rectifier helps to remove unwanted voltage transient. In the future research, design strategies of low pass filter and band pass filter should be investigated.

7.3.4 Further Investigation on the Rectifier Design

For the proposed charge pump rectifier, further work can be done to improve the layout design and reduce the power dissipation. The long term reliability and operating condition of the rectifier remains to be evaluated. Also, more experiments can be performed to further characterize each stage of the charge pump rectifier.

7.4 Final Comment

With the growing demand for wireless devices, the need to adopt inexpensive, green communication strategies has captured significant interests as it is of paramount importance. One approach is to implement the capability of scavenging ambient energy from a variety of natural and man-made sources. It leads to significant reduction in maintenance cost associated with periodically replacing battery. Among various energy scavenging techniques, RF energy scavenging holds a promising future for generating small amounts of electrical energy from propagating radio waves to fully or partially power wireless electronics. However, the large size and high cost of conventional RF energy scavenging system has limited its realization in commercial applications. This thesis demonstrated several techniques to overcome these problems for establishing miniaturized RF energy scavenging systems.

The research presented in this thesis makes its contributions to future wireless devices, which are implemented with the ability of ambient energy scavenging for sustained operation with extended battery life, advancing towards the vision realization of perennially operating wireless device.

References

[1] M. Pinuela, P. D. Mitcheson, and S. Lucyszyn, "Ambient RF Energy Harvesting in Urban and Semi-Urban Environments " *IEEE Transactions on Microwave Theory and Techniques,* vol. PP, pp. 1-12, 2013.

[2] T. Le, K. Mayaram, and T. Fiez, "Efficient Far-Field Radio Frequency Energy Harvesting for Passively Powered Sensor Networks," *IEEE Journal of Solid-State Circuits,* vol. 43, pp. 1287-1302, 2008.

[3] S. Monfray, O. Puscasu, G. Savelli, U. Soupremanien, E. Ollier, C. Guerin*, et al.*, "Innovative thermal energy harvesting for zero power electronics," in *2012 IEEE Silicon Nanoelectronics Workshop (SNW)*, 2012, pp. 1-4.

[4] V. Leonov, T. Torfs, P. Fiorini, and C. V. Hoof, "Thermoelectric converters of human warmth for self-powered wireless sensor nodes," *IEEE Sensors Journal,* vol. 7, pp. 650-657, 2007.

[5] S. P. Beeby, R. N. Torah, M. J. Tudor, P. G. Jones, T. O'Donnell, C. R. Saha*, et al.*, "A micro electromagnetic generator for vibration energy harvesting," *Journal of Micromechanics and microengineering,* vol. 17, p. 1257, 2007.

[6] H. B. Fang, J. Q. Liu, Z. Y. Xu, L. Dong, L. Wang, D. Chen*, et al.*, "Fabrication and performance of MEMS-based piezoelectric power generator for vibration energy harvesting," *Microelectronics Journal,* vol. 37, pp. 1280-1284, 2006.

[7] B. O'regan and M. Grfitzeli, "A low-cost, high-efficiency solar cell based on dye-sensitized colloidal TiO2 films," *nature,* vol. 353, pp. 737-740, 1991.

[8] J. B. Lee, Z. Z. Chen, M. G. Allen, A. Rohatgi, and R. Arya, "A miniaturized high-voltage solar cell array as an electrostatic MEMS power supply," *Journal of Microelectromechanical Systems,* vol. 4, pp. 102-108, 1995.

[9] J. P. Thomas, M. A. Qidwai, and J. C. Kellogg, "Energy scavenging for small-scale unmanned systems," *Journal of Power Sources,* vol. 159, pp. 1494-1509, 2006.

[10] M. Hatay, "Empirical formula for propagation loss in land mobile radio services," *IEEE Transactions on Vehicular Technology,* vol. 29, pp. 317-325, 1980.

[11] H. T. Friis, "A Note on a Simple Transmission Formula," *Proceedings of the IRE,* vol. 34, pp. 254-256, 1946.

[12] S. Mandal, "Far field RF power extraction circuits and systems," Massachusetts Institute of Technology, 2004.

[13] H. A. Wheeler, "Small antennas," *IEEE Transactions on Antennas and Propagation,* vol. 23, pp. 462-469, 1975.

[14] D. Bouchouicha, F. Dupont, M. Latrach, and L. Ventura, "Ambient RF energy harvesting," in *International Conference on Renewable Energies and Power Quality*, 2010, pp. 1-4.

[15] F. Congedo, G. Monti, L. Tarricone, and M. Cannarile, "Broadband bowtie antenna for RF energy scavenging applications," in *Proceedings of the 5th European Conference on Antennas and Propagation (EUCAP)*, 2011, pp. 335-337.

[16] L. Vincetti, M. Maini, E. Pinotti, L. Larcher, S. Scorcioni, A. Bertacchini*, et al.*, "Broadband printed antenna for radiofrequency energy harvesting," in *International Conference on Electromagnetics in Advanced Applications (ICEAA)*, 2012, pp. 814-816.

[17] N. A. Zainuddin, Z. Zakaria, M. N. Husain, B. M. Derus, M. Z. A. A. Aziz, M. A. Mutalib*, et al.*, "Design of wideband antenna for RF energy harvesting system," in *2013 3rd International Conference on Instrumentation,*

Communications, Information Technology, and Biomedical Engineering (ICICI-BME), 2013, pp. 162-166.

[18] A. Buonanno, M. D'Urso, and D. Pavone, "An ultra wide-band system for RF Energy harvesting," in *Proceedings of the 5th European Conference on Antennas and Propagation (EUCAP)*, 2011, pp. 388-389.

[19] Z. Jingwei, H. Y, and C. Ping, "A wideband cross dipole rectenna for rf wireless harvesting," in *2013 7th European Conference on Antennas and Propagation (EuCAP)*, 2013, pp. 3063-3067.

[20] B. Li, X. Shao, N. Shahshahan, N. Goldsman, T. Salter, and G. M. Metze, "An antenna co-design dual band RF energy harvester," *IEEE TRANSACTIONS ON CIRCUITS AND SYSTEMS—I: REGULAR PAPERS,* vol. 60, pp. 3256-3266, 2013.

[21] D. Masotti, A. Costanzo, and S. Adami, "Design and realization of a wearable multi-frequency RF energy harvesting system," in *Proceedings of the 5th European Conference on Antennas and Propagation (EUCAP)*, 2011, pp. 517-520.

[22] M. Arrawatia, M. S. Baghini, and G. Kumar, "RF energy harvesting system at 2.67 and 5.8 GHz," in *Asia-Pacific Microwave Conference Proceedings (APMC)*, 2010, pp. 900-903.

[23] A. Costanzo, A. Romani, D. Masotti, N. Arbizzani, and V. Rizzoli, "RF/baseband co-design of switching receivers for multiband microwave energy harvesting," *Sensors and Actuators A: Physical,* vol. 179, pp. 158-168, 2012.

[24] B. L. Pham and A. V. Pham, "Triple bands antenna and high efficiency rectifier design for RF energy harvesting at 900, 1900 and 2400 MHz," in *2013 IEEE MTT-S International Microwave Symposium Digest (IMS)*, 2013, pp. 1-3.

[25] H. Kanaya, S. Tsukamaoto, T. Hirabaru, D. Kanemoto, R. K. Pokharel, and K. Yoshida, "Energy Harvesting Circuit on a One-Sided Directional Flexible Antenna," *IEEE Microwave and Wireless Components Letters,* vol. 23, pp. 164-166, 2013.

[26] S. Keyrouz, H. J. Visser, and A. G. Tijhuis, "Ambient RF energy harvesting from DTV stations," in *2012 Loughborough Antennas and Propagation Conference (LAPC)*, 2012, pp. 1-4.

[27] T. C. Hong, S. W. Su, and F. S. Chang, "A compact, one‐piece, metal‐plate patch PIFA for 2.4‐GHz WLAN operation," *Microwave and Optical Technology Letters,* vol. 53, pp. 1757-1761, 2011.

[28] K. K. A. Devi, S. Sadasivam, N. M. Din, and C. K. Chakrabarthy, "Design of a 377Ω patch antenna for ambient RF energy harvesting at downlink frequency of GSM 900," in *17th Asia-Pacific Conference on Communications (APCC)*, 2011, pp. 492-495.

[29] H. W. Liu and C. F. Yang, "Miniature PIFA without empty space for 2.4 GHz ISM band applications," *Electronics Letters,* vol. 46, pp. 113-115, 2010.

[30] U. Karthaus and M. Fischer, "Fully integrated passive UHF RFID transponder IC with 16.7-μW minimum RF input power," *IEEE Journal of Solid-State Circuits,* vol. 38, pp. 1602-1608, 2003.

[31] T. Umeda, H. Yoshida, S. Sekine, Y. Fujita, T. Suzuki, and S. Otaka, "A 950-MHz rectifier circuit for sensor network tags with 10-m distance," *IEEE Journal of Solid-State Circuits,* vol. 41, pp. 35-41, 2006.

[32] T. T. Le, "Efficient power conversion interface circuits for energy harvesting applications," Electrical and Computer Engineering, Oregon State University, 2008.

[33] S. Mandal and R. Sarpeshkar, "Low-Power CMOS Rectifier Design for RFID Applications," *IEEE Transactions on Circuits and Systems I: Regular Papers,* vol. 54, pp. 1177-1188, 2007.

[34] S. Guo and H. Lee, "An efficiency-enhanced CMOS rectifier with unbalanced-biased comparators for transcutaneous-powered high-current implants," *IEEE Journal of Solid-State Circuits,* vol. 44, pp. 1796-1804, 2009.

[35] G. Lazzi, "Thermal effects of bioimplants," *IEEE Engineering in Medicine and Biology Magazine,* vol. 24, pp. 75-81, 2005.

[36] S. Roundy, D. Steingart, L. Frechette, P. Wright, and J. Rabaey, "Power sources for wireless sensor networks," in *Wireless sensor networks*, ed: Springer, 2004, pp. 1-17.

[37] D. Steingart, S. Roundy, P. K. Wright, and J. W. Evans, "Micropower materials development for wireless sensor networks," *MRS bulletin,* vol. 33, pp. 408-409, 2008.

[38] A. Luque and S. Hegedus, *Handbook of Photovoltaic Science and Engineering*: John Wiley and Sons, 2003.

[39] M. A. Green, K. Emery, Y. Hishikawa, W. Warta, and E. D. Dunlop, "Solar cell efficiency tables (version 43)," *Progress in photovoltaics: research and applications,* vol. 22, pp. 1-9, 2014.

[40] Z. W. Sim, "Radio Frequency Energy Harvesting for Embedded Sensor Networks in the Natural Environment," Electrical and Electronic Engineering, University of Manchester, 2012.

[41] E. Koutroulis, K. Kalaitzakis, and N. C. Voulgaris, "Development of a microcontroller-based, photovoltaic maximum power point tracking control system," *IEEE Transactions on Power Electronics,* vol. 16, pp. 46-54, 2001.

[42] P. Zhao, "Energy Harvesting Techniques for Autonomous WSNs/RFID with a Focus on RF Energy Harvesting," Elektrotechnik und Informationstechnik, der Technischen Universit¨at Darmstadt, 2012.

[43] M. R. Patel, *Wind and solar power systems: design, analysis, and operation*: CRC press, 2012.

[44] J. L. Stone, "Photovoltaics: Unlimited electrical energy from the sun," *Physics Today,* vol. 46, pp. 22-29, 2008.

[45] D. G. F. Sonnenenergie, *Planning and installing photovoltaic systems: a guide for installers, architects and engineers*: Earthscan, 2008.

[46] C. Knight, J. Davidson, and S. Behrens, "Energy options for wireless sensor nodes," *Sensors,* vol. 8, pp. 8037-8066, 2008.

[47] S. Dalola, M. Ferrari, V. Ferrari, M. Guizzetti, D. Marioli, and A. Taroni, "Characterization of thermoelectric modules for powering autonomous sensors," *IEEE Transactions on Instrumentation and Measurement,* vol. 58, pp. 99-107, 2009.

[48] H. J. Goldsmid, "Conversion efficiency and figure-of-merit," *CRC Handbook of Thermoelectrics,* pp. 19-25, 1995.

[49] R. E. Wilson and P. B. S. Lissaman, "Applied aerodynamics of wind power machines," *NASA STI/Recon Technical Report N,* vol. 75, p. 22669, 1974.

[50] R. Morais, S. G. Matos, M. A. Fernandes, A. L. G. Valente, S. F. S. P. Soares, P. J. S. G. Ferreira*, et al.*, "Sun, wind and water flow as energy supply for small stationary data acquisition platforms," *Computers and electronics in agriculture,* vol. 64, pp. 120-132, 2008.

[51] P. D. Mitcheson, E. M. Yeatman, G. K. Rao, A. S. Holmes, and T. C. Green, "Energy harvesting from human and machine motion for wireless electronic devices," *Proceedings of the IEEE,* vol. 96, pp. 1457-1486, 2008.

[52] B. Ozerdem and H. M. Turkeli, "Wind energy potential estimation and micrositting on Izmir Institute of Technology Campus, Turkey," *Renewable Energy,* vol. 30, pp. 1623-1633, 2005.

[53] G. Gautschi, *Piezoelectric sensorics: force, strain, pressure, acceleration and acoustic emission sensors, materials and amplifiers*: Springer, 2002.

[54] S. J. Roundy, "Energy scavenging for wireless sensor nodes with a focus on vibration to electricity conversion," University of California, Berkeley, 2003.

[55] C. C. B. Williams, C. C. Shearwood, M. M. A. Harradine, P. P. H. Mellor, T. T. S. Birch, and R. R. B. Yates, "Development of an electromagnetic micro-generator," in *IEE Proceedings-Circuits, Devices and Systems*, 2001, pp. 337-342.

[56] H. Nishimoto, Y. Kawahara, and T. Asami, "Prototype implementation of wireless sensor network using TV broadcast RF energy harvesting," in *Proceedings of the 12th ACM international conference adjunct papers on Ubiquitous computing-Adjunct*, 2010, pp. 373-374.

[57] C. Viehweger, M. Baldauf, T. Keutel, and O. Kanoun, "Hybrid energy harvesting for autonomous sensors in building automation," in *2012 IEEE International Instrumentation and Measurement Technology Conference (I2MTC)*, 2012, pp. 610-613.

[58] Y. K. Tan and S. K. Panda, "Energy harvesting from hybrid indoor ambient light and thermal energy sources for enhanced performance of wireless sensor nodes," *IEEE Transactions on Industrial Electronics,* vol. 58, pp. 4424-4435, 2011.

[59] V. Raghunathan, A. Kansal, J. Hsu, J. Friedman, and M. Srivastava, "Design considerations for solar energy harvesting wireless embedded systems," in *Proceedings of the 4th international symposium on Information processing in sensor networks*, 2005, p. 64.

[60] T. Le, K. Mayaram, and T. S. Fiez, "Efficient Far-Field Radio Frequency Power Conversion System for Passively Powered Sensor Networks," in *IEEE 2006 Custom Integrated Circuits Conference (CICC)*, 2006, pp. 293-296.

[61] S. Roundy, P. K. Wright, and J. M. Rabaey, *Energy scavenging for wireless sensor networks*: Springer, 2003.

[62] J. A. Paradiso and T. Starner, "Energy scavenging for mobile and wireless electronics," *IEEE Pervasive Computing,* vol. 4, pp. 18-27, 2005.

[63] R. Venkatasubramanian, C. Watkins, D. Stokes, J. Posthill, and C. Caylor, "Energy harvesting for electronics with thermoelectric devices using nanoscale materials," in *IEEE International Electron Devices Meeting (IEDM)*, 2007, pp. 367-370.

[64] C. C. Federspiel and J. Chen, "Air-powered sensor," in *Proceedings of IEEE Sensors*, 2003, pp. 22-25.

[65] U. Olgun, C. C. Chen, and J. L. Volakis, "Design of an efficient ambient WiFi energy harvesting system," *IET Microwaves, Antennas & Propagation,* vol. 6, pp. 1200-1206, 2012.

[66] H. C. Sun, Y. X. Guo, M. He, and Z. Zhong, "Design of a high-efficiency 2.45-GHz rectenna for low-input-power energy harvesting," *IEEE Antennas and Wireless Propagation Letters,* vol. 11, pp. 929-932, 2012.

[67] D. Masotti, A. Costanzo, M. D. Prete, and V. Rizzoli, "Genetic-based design of a tetra-band high-efficiency radio-frequency energy harvesting system," *IET Microwaves, Antennas & Propagation,* vol. 7, pp. 1254-1263, 2013.

[68] G. Papotto, F. Carrara, and G. Palmisano, "A 90-nm CMOS threshold-compensated RF energy harvester," *IEEE Journal of Solid-State Circuits,* vol. 46, pp. 1985-1997, 2011.

[69] T. Salter, K. Choi, M. Peckerar, G. Metze, and N. Goldsman, "RF energy scavenging system utilising switched capacitor DC-DC converter," *Electronics letters,* vol. 45, pp. 374-376, 2009.

[70] P. Nintanavongsa, U. Muncuk, D. R. Lewis, and K. R. Chowdhury, "Design optimization and implementation for RF energy harvesting circuits," *IEEE Journal on Emerging and Selected Topics in Circuits and Systems,* vol. 2, pp. 24-33, 2012.

[71] U. Olgun, C. C. Chen, and J. L. Volakis, "Efficient ambient WiFi energy harvesting technology and its applications," in *2012 IEEE Antennas and Propagation Society International Symposium (APSURSI)*, 2012, pp. 1-2.

[72] C. A. Balanis, *Antenna Theory: Analysis and Design (Third Edition)*: John Wiley & Sons, 2005.

[73] Y. Huang and K. Boyle, *Antennas: from theory to practice*: John Wiley & Sons, 2008.

[74] Y. C. Lin and K. J. Hung, "Compact ultrawideband rectangular aperture antenna and band-notched designs," *IEEE Transactions on Antennas and Propagation,* vol. 54, pp. 3075-3081, 2006.

[75] K. L. Wong, "Compact and broadband microstrip antennas," *Wiley-interscience,* vol. 168, 2004.

[76] J. Powell, "Antenna design for ultra wideband radio," Massachusetts Institute of Technology, 2004.

[77] W. L. Chen, G. M. Wang, and C. X. Zhang, "Bandwidth Enhancement of a Microstrip-Line-Fed Printed Wide-Slot Antenna With a Fractal-Shaped Slot," *IEEE Transactions on Antennas and Propagation,* vol. 57, pp. 2176-2179, 2009.

[78] B. C. Wadell, *Transmission line design handbook*: Artech House, 1991.

[79] Q. X. Chu and Y. Y. Yang, "A compact ultrawideband antenna with 3.4/5.5 GHz dual band-notched characteristics," *IEEE Transactions on Antennas and Propagation,* vol. 56, pp. 3637-3644, 2008.

[80] I. Pele, A. Chousseaud, and S. Toutain, "Simultaneous modeling of impedance and radiation pattern antenna for UWB pulse modulation," in *IEEE Antennas and Propagation Society International Symposium*, 2004, pp. 1871-1874 Vol.2.

[81] X. X. Zhang and F. Yang, "Study of a slit cut on a microstrip antenna and its applications," *Microwave and optical technology letters,* vol. 18, pp. 297-300, 1998.

[82] S. Chauhan and P. K. Singhal, "Enhancement of Bandwidth of Rectangular Patch Antenna Using Multiple Slots in The Ground Plane," *International Journal of Research in Electronics and Communication Technology,* vol. 1, pp. 30-33, 2014.

[83] W. Wiesbeck, G. Adamiuk, and C. Sturm, "Basic properties and design principles of UWB antennas," *Proceedings of the IEEE,* vol. 97, pp. 372-385, 2009.

[84] I. Guidelines, "Guidelines for Limiting Exposure to Time-Varying Electric, Magnetic and Electromagnetic Fields (up to 300GHz)," in *International Commission on Non-Ionizing Radiation Protection*, Oberschleissheim, Germany, 1998.

[85] S. M. Mann, T. G. Cooper, S. G. Allen, R. P. Blackwell, and A. J. Lowe, *Exposure to radio waves near mobile phone base stations*: National Radiological Protection Board, 2000.

[86] S. I. Henderson and M. J. Bangay, "Survey of RF exposure levels from mobile telephone base stations in Australia," *Bioelectromagnetics,* vol. 27, pp. 73-76, 2006.

[87] H. J. Visser, A. C. F. Reniers, and J. A. C. Theeuwes, "Ambient RF Energy Scavenging: GSM and WLAN Power Density Measurements," in *Proceedings of the 38th European Microwave Conference* 2008, pp. 721-724.

[88] K. Hirasawa and M. Haneishi, *Analysis, design, and measurement of small and low-profile antennas*: Artech House on Demand, 1992.

[89] Y. T. Lo and S. W. Lee, *Antenna Handbook*: Van Nostrand Reinhold Company Inc., 1988.

[90] K. L. Wong and C. H. Huang, "Bandwidth‐enhanced internal PIFA with a coupling feed for quad‐band operation in the mobile phone," *Microwave and Optical Technology Letters,* vol. 50, pp. 683-687, 2008.

[91] B. N. Kim, S. O. Park, J. K. Oh, and G. Y. Koo, "Wideband built-in antenna with new crossed C-shaped coupling feed for future mobile phone application," *IEEE Antennas and Wireless Propagation Letters,* vol. 9, pp. 572-575, 2010.

[92] C. T. Lee and K. L. Wong, "Planar monopole with a coupling feed and an inductive shorting strip for LTE/GSM/UMTS operation in the mobile phone," *IEEE Transactions on Antennas and Propagation,* vol. 58, pp. 2479-2483, 2010.

[93] W. Y. Li and K. L. Wong, "Seven‐band surface‐mount loop antenna with a capacitively coupled feed for mobile phone application," *Microwave and Optical Technology Letters,* vol. 51, pp. 81-88, 2009.

[94] P. W. Chan, H. Wong, and E. K. N. Yung, "Dual-band printed inverted-F antenna for DCS, 2.4GHz WLAN applications," in *Loughborough Antennas and Propagation Conference (LAPC)*, 2008, pp. 185-188.

[95] K. Won-Il, P. Seong-Ook, and J. S. Kim, "A Folded Planar Inverted-F Antenna for GSM/DCS/Bluetooth Triple-Band Application," *IEEE Antennas and Wireless Propagation Letters,* vol. 5, pp. 18-21, 2006.

[96] R. S. Aziz, M. A. S. Alkanhal, and A. F. A. Sheta, "Triple band fractal-like antennas," in *2011 41st European Microwave Conference (EuMC)*, 2011, pp. 886-889.

[97] E. T. S. Institute, "Digital cellular telecommunications system (Phase 2+)-Radio transmission and reception (GSM 05.05)," March 1996.

[98] Y. S. Lin, D. Sylvester, and D. Blaauw, "An ultra low power 1V, 220nW temperature sensor for passive wireless applications," in *IEEE Custom Integrated Circuits Conference (CICC)* 2008, pp. 507-510.

[99] A. Khairi, C. Y. Wu, Y. Rabin, G. Fedder, J. Paramesh, and D. Schwartzman, "Ultra-low power frequency and duty-cycle modulated implantable pressure-temperature sensor," in *2013 IEEE Biomedical Circuits and Systems Conference (BioCAS)*, 2013, pp. 226-229.

[100] N. Heidmann, N. Hellwege, D. Peters-Drolshagen, S. Paul, A. Dannies, and W. Lang, "A low-power wireless UHF/LF sensor network with web-based remote supervision—Implementation in the intelligent container," in *2013 IEEE SENSORS*, 2013, pp. 1-4.

[101] Y. C. Cheng, Y. Chawathe, A. LaMarca, and J. Krumm, "Accuracy characterization for metropolitan-scale Wi-Fi localization," in *Proceedings of the 3rd international conference on Mobile systems, applications, and services*, 2005, pp. 233-245.

[102] *Wireless Broadband Alliance Ltd., "Global developments in public Wi-Fi", Available at http://www.wballiance.com/wba/wp-content/uploads/downloads/2012/07/16_WBA-Industry-Report-2011-_Global-Developments-in-Public-Wi-Fi-1.00.pdf, Accessed on Dec. 22, 2014.*

[103] F. Alneyadi, M. Alkaabi, S. Alketbi, S. Hajraf, and R. Ramzan, "2.4GHz WLAN RF energy harvester for passive indoor sensor nodes," in *2014 IEEE International Conference on Semiconductor Electronics (ICSE)*, 2014, pp. 471-474.

[104] *Powercast Corporation, "Practical Applications of RF Energy Harvesting", Available at http://powercastco.com/PDF/Practical-Applications-of-RF-Energy-Harvesting.pdf, Accessed on Dec. 22, 2014*.

[105] M.-C. T. Huynh, "A numerical and experimental investigation of planar inverted-F antennas for wireless communication applications," Virginia Polytechnic Institute and State University, 2000.

[106] M. Biswas and D. Guha, "Input impedance and resonance characteristics of superstrate-loaded triangular microstrip patch," *IET microwaves, antennas & propagation,* vol. 3, pp. 92-98, 2009.

[107] N. Alexopoulos and D. R. Jackson, "Fundamental superstrate (cover) effects on printed circuit antennas," *IEEE Transactions on Antennas and Propagation,* vol. 32, pp. 807-816, 1984.

[108] A. S. Meier and W. P. Summers, "Measured Impedance of Vertical Antennas over Finite Ground Planes," *Proceedings of the IRE,* vol. 37, pp. 609-616, 1949.

[109] G. A. Thiele and T. Newhouse, "A hybrid technique for combining moment methods with the geometrical theory of diffraction," *IEEE Transactions on Antennas and Propagation,* vol. 23, pp. 62-69, 1975.

[110] K. H. Awadalla and T. S. M. Maclean, "Input impedance of a monopole antenna at the center of a finite ground plane," *IEEE Transactions on Antennas and Propagation,* vol. 26, pp. 244-248, 1978.

[111] M. Weiner, "Monopole element at the center of a circular ground plane whose radius is small or comparable to a wavelength," *IEEE Transactions on Antennas and Propagation,* vol. 35, pp. 488-495, 1987.

[112] J. H. Richmond, "Monopole antenna on circular disk," *IEEE Transactions on Antennas and Propagation,* vol. 32, pp. 1282-1287, 1984.

[113] J. W. Lee, B. Lee, and H. B. Kang, "A High Sensitivity, $CoSi_2$ –Si Schottky Diode Voltage Multiplier for UHF-Band Passive RFID Tag Chips," *IEEE Microwave and Wireless Components Letters,* vol. 18, pp. 830-832, 2008.

[114] K. K. A. Devi, M. D. Norashidah, C. K. Chakrabarty, and S. Sadasivam, "Design of an RF-DC conversion circuit for energy harvesting," in *2012 IEEE International Conference on Electronics Design, Systems and Applications (ICEDSA)*, 2012, pp. 156-161.

[115] H. Gao, M. Matters-Kammerer, D. Milosevic, J. P. M. G. Linnartz, and P. Baltus, "A design of 2.4GHz rectifier in 65nm CMOS with 31% efficiency," in *2013 IEEE 20th Symposium on Communications and Vehicular Technology in the Benelux (SCVT)*, 2013, pp. 1-4.

[116] M. Ebrahimian, K. El-Sankary, and E. El-Masry, "Enhanced RF to DC CMOS rectifier with capacitor-bootstrapped transistor," in *Proceedings of 2010 IEEE International Symposium on Circuits and Systems (ISCAS)*, 2010, pp. 1655-1658.

[117] H. Nakamoto, D. Yamazaki, T. Yamamoto, H. Kurata, S. Yamada, K. Mukaida*, et al.*, "A Passive UHF RF Identification CMOS Tag IC Using Ferroelectric RAM in 0.35-um Technology," *IEEE Journal of Solid-State Circuits,* vol. 42, pp. 101-110, 2007.

[118] K. Kotani and T. Ito, "High efficiency CMOS rectifier circuit with self-Vth-cancellation and power regulation functions for UHF RFIDs," in *IEEE Asian Solid-State Circuits Conference*, 2007, pp. 119-122.

[119] K. Kotani, A. Sasaki, and T. Ito, "High-efficiency differential-drive CMOS rectifier for UHF RFIDs," *IEEE Journal of Solid-State Circuits,* vol. 44, pp. 3011-3018, 2009.

[120] S. Y. Wong and C. H. Chen, "Power efficient multi-stage CMOS rectifier design for UHF RFID tags," *INTEGRATION, the VLSI journal,* vol. 44, pp. 242-255, 2011.

[121] Y. W. S. , "Wireless Power Transmission (WPT) Application at 2.4 GHz in Common Network," Doctor of Philosophy, School of Electrical and Computer Engineering, RMIT University, 2010.

[122] J. Yi, W. H. Ki, and C. Y. Tsui, "Analysis and Design Strategy of UHF Micro-Power CMOS Rectifiers for Micro-Sensor and RFID Applications," *IEEE Transactions on Circuits and Systems I,* vol. 54, pp. 153-166, 2007.

[123] J. P. Curty, N. Joehl, F. Krummenacher, C. Dehollain, and M. J. Declercq, "A model for μ-power rectifier analysis and design," *IEEE Transactions on Circuits and Systems I: Regular Papers,* vol. 52, pp. 2771-2779, 2005.

[124] M. Ghovanloo and K. Najafi, "Fully integrated wideband high-current rectifiers for inductively powered devices," *IEEE Journal of Solid-State Circuits,* vol. 39, pp. 1976-1984, 2004.

[125] "BSIM3v3.3 MOSFET Model Users' Manual," T. D. E. E. C. S. BSIM Res. Group, Univ. of California, Ed., ed.

[126] J. Essel, D. Brenk, J. Heidrich, G. Hofer, G. Holweg, and R. Weigel, "Design of a highly efficient CMOS rectifier for passive communication systems," in *2010 Asia-Pacific Microwave Conference Proceedings (APMC)*, 2010, pp. 896-899.

[127] D. S. Liu, X. C. Zou, K. Dai, S. Z. Li, X. M. Hui, Y. Liu*, et al.*, "New design of RF rectifier for passive UHF RFID transponders," *Microelectronics Journal,* vol. 41, pp. 51-55, 2010.